A numerical study of fin and jet propulsions involving fluid-structure interactions

Yang Luo

A thesis submitted in fulfillment of the requirements for the degree of Doctor of Philosophy

Department of Naval Architecture, Ocean and Marine Engineering
University of Strathclyde
Glasgow, United Kingdom
September 2021

Declaration

I hereby declare that this thesis and all materials contained herein is a record of work carried out in the Department of Naval Architecture, Ocean and Marine Engineering at the University of Strathclyde. This thesis is the results of original research by the author except where otherwise indicated. It has been composed by the author and has not been previously submitted for any examination which led to the award of a degree.

The copyright of this thesis belongs to the author under the terms of the United Kingdom Copyright Acts as qualified by University of Strathclyde Regulation 3.50. The due acknowledgment must always be made of the use of any material contained in, or derived from, this thesis.

Yang Luo

Signature: Yang Luo Date: September 2021

This is dedicated to my grandmother, and I wish her to get well soon and enjoy her twilight years.

竹石

清·郑燮

咬定青山不放松，
立根原在破岩中。
千磨万击还坚劲，
任尔东西南北风。

The Rock Bamboo

Zheng Xie (Poet of Qing Dynasty)

The bamboo clings firmly to the mountain steep,
In the chasm of rock it plants its root so deep.
In spite of all beats, it stands still, not bending low,
whether from east, west, south or north the wind does blow.

Acknowledgments

I would like to express my deepest gratitude to my supervisors Dr. Qing Xiao and Dr. Zhiming Yuan for their kind guidance throughout my doctoral journey.

Dr. Xiao is a strict but professional and experienced supervisor. She can always provide help and inspiration when I feel puzzled or depressed. She uses her expertise in computational fluid dynamics and fluid-structure interaction simulation techniques to guide me to solve practical problems and discover new insights. Her efforts in supervising me during my Ph.D. study will be always appreciated.

I would like to thank Prof. Qiang Zhu at the University of California San Diego (UCSD). Prof. Zhu is a professional and wise researcher who can always inspire me with novel ideas. Working with Prof. Zhu is a pleasant experience for me which taught me to think differently and never fall into the conventions.

Special thanks to Prof. Benjamin Uekermann at the University of Stuttgart, Mr. Gerasimos Chourdakis at the Technical University of Munich, and the preCICE team. Prof. Benjamin Uekermann and preCICE team members are always friendly and efficient in providing suggestions to find the bugs during my coding work. Without the kind and professional help from them, I would not be able to accomplish the coupling between the in-house code and CalculiX, nor the development of the FSI solver which lies the foundation of this thesis work.

I would like to thank Dr. Wendi Liu, Dr. Guangyu Shi, Dr. Ruoxin Li, Dr. Yuanchuan Liu, Dr. Zhengkai Zhao, Mr. Yang Zhou, Mr. Marvin Wright, and other group members. I appreciate their help and accompany during my Ph.D. study, which makes me feel the group is a big family.

I also want to thank Prof. Guang Pan and Dr. Qiaogao Huang at Northwestern Polytechnical University (China) for their persistent support even before I started my Ph.D. study. Without them, I would never be able to come to the UK to pursue a Ph.D. degree.

I appreciate Dr. Hong Yue at the Department of Electronic & Electrical Engineering, the University of Strathclyde for her kind help and helpful discussion during my Ph.D. study.

I also would like to thank Prof. Li Wen at Beihang University and Dr. Mark Post at York University. Their help during my Ph.D. is highly appreciated.

Thanks to the hard-working staff at the Department of Naval Architecture, Ocean & Marine Engineering for providing a safe and cozy research environment for me.

I acknowledge China Scholarship Council (CSC) for financial support during my study in the UK. I also thank ARCHIE-WeSt HPC based at the University of Strathclyde and Cirrus HPC based at the University of Edinburgh which provided valuable computational resources that makes this thesis work possible.

Finally, I am indebted to my beloved family for their unconditional love and support. Supporting a Ph.D. study is not easy for a disadvantaged family. I am grateful that my family always support me to pursue my dream and aspiration although they may bear more burdens during this period. I also deeply appreciate my beloved wife, Hui Lai, who always understands me and stands with me to face all the happiness and loss. She gave up a good working opportunity in China and chose to be with me. This sacrifice will be always engraved and appreciated in my deep mind.

List of Publications

Journal Articles

[1] **Luo, Y**., Xiao, Q., Shi, G., 2020. A fluid-structure interaction study on a bionic fish fin with non-uniform stiffness distribution. *Journal of Offshore Mechanics and Arctic Engineering* 142. (Based on the developed FSI solver in Chapter 3 of this thesis)

[2] **Luo, Y**., Xiao, Q., Shi, G., Wen, L., Chen, D., Pan, G., 2020. A fluid-structure interaction solver for the study on a passively deformed fish fin with non-uniformly distributed stiffness. *Journal of Fluids and Structures* 92, 102778. (Based on section 4.1 of this thesis)

[3] **Luo, Y**., Xiao, Q., Shi, G., Pan, G., Chen, D., 2020. The effect of variable stiffness of tuna-like fish body and fin on swimming performance. *Bioinspiration & Biomimetics* 16, 016003. (Based on section 4.2 of this thesis)

[4] **Luo, Y**., Xiao, Q., Zhu, Q., Pan, G., 2020. Pulsed-jet propulsion of a squid-inspired swimmer at high Reynolds number. *Physics of Fluids* 32, 111901. (Based on section 5.1 of this thesis)

[5] **Luo, Y**., Xiao, Q., Zhu, Q., Pan, G., 2021. Jet propulsion of a squid-inspired swimmer in the presence of background flow. *Physics of Fluids* 33, 031909. (Based on section 5.2 of this thesis)

[6] **Luo, Y**., Wright, M., Xiao, Q., Yue, H., Pan, G., 2021. Fluid-structure interaction analysis on motion control of a self-propelled flexible plate near a rigid body utilizing PD control, *Bioinspiration & Biomimetics* 16, 066002. (Based on Chapter 6 of this thesis)

[7] Gorma, W., Post, M.A., White, J., Gardner, J., **Luo, Y**., Kim, J., Mitchell, P.D., Morozs, N., Wright, M., Xiao, Q., 2021. Development of modular bio-inspired autonomous underwater vehicle for close subsea asset inspection. *Applied Sciences* 11, 5401.

Conference Papers

[1] **Luo, Y**., Xiao, Q., Shi, G., Yuan, Z., Wen, L., 2019. A Fluid-Structure Interaction Study on a Passively Deformed Fish Fin, *ASME 2019 38th International Conference on Ocean, Offshore and Arctic Engineering*, Glasgow, UK.

[2] **Luo, Y**., Xiao, Q., Shi, G., 2019. A fluid-structure interaction solver for the study of the propulsion of a passively deformed fish fin, *VIII International Conference on Coupled Problems in Science and Engineering*, Barcelona, Spain.

[3] Wright, M., **Luo, Y**., Xiao, Q., Post, M., Gorma, W., Durrant, A., & Yue, H., 2020. CFD-FSI analysis on motion control of bio-inspired underwater AUV system utilizing PID control. *Paper presented at 2020 IEEE OES Autonomous Underwater Vehicle Symposium*, St. John's, Canada.

[4] Wright, M., Gorma, W., **Luo, Y**., Post, M., Xiao, Q., & Durrant, A., 2020. Multi-actuated AUV body for windfarm inspection: lessons from the bio-inspired RoboFish field trials. *Paper presented at 2020 IEEE OES Autonomous Underwater Vehicle Symposium*, St. John's, Canada.

Abstract

Fish swimming is elegant and efficient, which inspires humans to learn from them to design high-performance artificial underwater vehicles. Research on aquatic locomotion has made extensive progress towards a better understanding of how aquatic animals control their flexible body and fin for propulsion. Although the structural flexibility and deformation of the body and fin are believed to be important features to achieve optimal swimming performance, studies on high-fidelity deformable body and fin with complex material behavior, such as non-uniform stiffness distributions, are rare.

In this thesis, a fully coupled three-dimensional high-fidelity fluid-structure interaction (FSI) solver is developed to investigate the flow field evolution and propulsion performance of caudal fin and jet propulsion involving body and/or fin deformation. Within this FSI solver, the fluid is resolved by solving unsteady and viscous Navier-Stokes equations based on the finite volume method with a multi-block grid system. The solid dynamics are solved by a nonlinear finite element method. The coupling between the two solvers is achieved in a partitioned approach in which convergence check and sub-iteration are implemented to ensure numerical stability and accuracy. Validations are conducted by comparing the simulation results of classical benchmarks with previous data in the literature, and good agreements between them are obtained.

The developed FSI solver is then applied to study the bio-inspired fin and jet propulsion involving body deformation. Specifically, the effect of non-uniform stiffness distributions of fish body and/or fin, key features of fish swimming which have been excluded in most previous studies, on the propulsive performance is first investigated. Simulation results of a sunfish-like caudal fin model and a tuna-inspired swimmer model both show that larger thrust and propulsion efficiency can be achieved by a non-uniform stiffness distribution (e.g., increased by 11.2% and 9.9%, respectively, for the sunfish-like model) compared with a uniform stiffness profile. Despite the improved propulsive e performance, a bionic variable fish body stiffness does not yield fish-like midline kinematics observed in real fish, suggesting that fish movement involves significant active control that cannot be replicated purely by passive deformations.

Subsequent studies focus on the jet propulsion inspired by squid locomotion using the developed numerical solver. Simulation results of a two-dimensional inflation-deflation jet propulsion system, whose inflation is actuated by an added external force that mimics the muscle constriction of the mantle and deflation is caused by the release of elastic energy of the structure, suggest larger mean thrust production and higher efficiency in high Reynolds number scenarios compared with the cases in laminar flow. A unique symmetry-breaking instability in turbulent flow is found to stem from irregular internal body vortices, which cause symmetry breaking in the wake. Besides, a three-dimensional squid-like jet propulsion system in the presence of background flow is studied by prescribing the body deformation and jet velocity profiles. The effect of the background flow on the leading vortex ring formation and jet propulsion is investigated, and the thrust sources of the overall pulsed jet are revealed as well.

Finally, FSI analysis on motion control of a self-propelled flexible swimmer in front of a cylinder utilizing proportional-derivative (PD) control is conducted. The amplitude of the actuation force, which is applied to the swimmer to bend it to produce thrust, is dynamically tuned by a feedback PD controller to instruct the swimmer to swim the desired distance from an initial position to a target location and then hold the station there. Despite the same swimming distance, a swimmer whose departure location is closer to the cylinder requires less energy consumption to reach the target and hold the position there.

Table of Contents

Nomenclature

Roman Symbols

Δt	Physical time step
$\overline{\Delta t}$	Dimensionaless physical time step
a_s	Sound speed
C	Circulation of the leading vortex ring
C_d	Drag force coefficient
$\overline{C_d}$	Time-averaged drag force coefficient
C_{ef}	Actuation force coefficient
C_P	Power expenditure coefficient
$\overline{C_P}$	Time-averaged power expenditure coefficient
C_T	Thrust coefficient
$\overline{C_T}$	Time-averaged thrust coefficient
C_{Ta}	Added mass effect-related thrust coefficient
C_{Tj}	Jet momentum flux-related thrust coefficient
C_{Tm}	Thrust coefficient attributed to horizontal momentum change of the fluid inside the chamber
C_{Tp}	Over-pressure-related thrust coefficient
C_x	Force coefficient in *x*-direction
C_y	Force coefficient in *y*-direction
$\overline{C_y}$	Time-averaged force coefficient in *y*-direction
C_z	Force coefficient in *z*-direction
$\overline{C_z}$	Time-averaged force coefficient in *z*-direction
c_p	Specific heats at constant pressure
c_v	Specific heats at constant volume
$\mathbf{D}$	Artificial dissipation term
D	Nozzle size of the 3D squid-like model
$\mathbf{E}$	Green–Lagrange strain tensor
E	Young’s modulus
E_f	Total energy of the flow
e	Eccentricity of the ellipse

e_0	Eccentricity of the ellipse at inflated state
e_1	Eccentricity of the ellipse at deflated state
e_f	Internal energy of the flow
F_a	Added mass effect related force
$\boldsymbol{F}_{bs}$	Fluidic force on the body surface
$\mathbf{F}_c$	Convective flux tensor
$\mathbf{F}_d$	Diffusion flux tensor
F_{ef}	Externally added force
F_j	Thrust force by jet momentum flux out of the nozzle plane
F_m	Thrust force by change rate of the horizontal momentum of the fluid inside the chamber
$\boldsymbol{F}_o$	Fluid solver operator
F_p	Over-pressure-related thrust
$\mathbf{F}_s$	Global force vector
F_x	Fluid force component in x-direction
F_y	Fluid force component in y-direction
F_z	Fluid force component in z-direction
$\mathbf{f}$	Body force
f	Locomotion frequency
f_{ef}	Actuation force frequency
f^*	Dimensionaless locomotion frequency
$\boldsymbol{f}_i$	Dynamic solution vector at the interface
$\boldsymbol{f}_k^n$	Fluid force at the interface after post-processing
$\tilde{\boldsymbol{f}}_k^n$	Fluid force at the interface before post-processing
G	Gap between the current swimmer position and the target
H_0	Maximum heave amplitude
I	Area moment of inertia of the cross-sectio
I_j	Momentum flux impulse
I_p	Over-pressure related impulse
K	Bending stiffness
$\mathbf{K}_s$	Global stiffness matrix
k	Turbulence kinetic energy
k_d	Tuning gain of derivative term

k_p	Tuning gain of proportional term
m	Mass of the structure
m^*	Mass ratio
m_a	Added mass
m_b	Mass of the swimmer in self-propulsion
Ma	Mach number
$\mathbf{M}_s$	Global mass matrix
$\mathbf{n}$	Unit normal vector in the outward direction
$\mathbf{P}$	Second PiolaKirchoff stress tensor
P_{inp}	Overall energy input during jetting
p	Fluid pressure
p_∞	Fluid pressure in the far-field
P_s	Overall energy expenditure to swim to the target
$\mathbf{Q}$	Flux tensor
$\boldsymbol{q}$	Heat fluxes
$\mathbf{R}$	Residual
R	Nozzle size of the 2D squid-like model
R_f	Gas constant
Re	Reynolds number
Re_j	Jet based Reylnolds number
$\boldsymbol{r}_f$	Force residual
$\boldsymbol{r}_s$	Displacement residual
$\boldsymbol{S}_o$	Structural solver operator
S	Reference area
St	Strouhal number
$\boldsymbol{s}_i$	Kinematic solution vector at the interface
$\boldsymbol{s}_k^n$	Structural solution at time step n and k_{th} subiteration
t	Time
t^*	Pseudo-time
T	Locomotion period
T_d	Body deflation period
T_h	Reference period of the swimmer holding the position at the target

T_s	Time required to swim to the target
T_{ef}	Actuation force period
T_{set}	A constant period used to tune the magnitude of the set swimming velocity
T_t	Temperature
U_0, U_∞	Incoming flow velocity
$\boldsymbol{u}$	Velocity vector
u	Velocity component in x-direction
u_{set}	Desired velocity for motion control
V	Mantle cavity volume
V_j	Jet velocity
V_{jm}	Maximum jet velocity
v	Velocity component in y-direction
$\mathbf{W}$	Conservative variable vector
w	Velocity component in z-direction
$\mathbf{X}$	Position vector in material coordinates
$\mathbf{x}$	Grid coordinates
x_i	Initial position
x_t	Target position
y_0	Maximum heave amplitude in y-direction

Greek Symbols

α	Adjustment factor of actuation force
γ_h	Ratio of specific heats
$\boldsymbol{\delta}$	Unit tensor
$\delta_{\alpha\beta}$	Kronecker function
ε	Relative convergence measure
η	Propulsion efficiency
θ_m	Maximum rotation angle
κ	Thermal conductivity
Λ	Volume difference of the mantle cavity
Γ	Stroke ratio

Γ_b	Whole body surface
Γ_f	Fluid boundary
Γ_i	Coupling interface
Γ_m	Maximum stroke ratio
Γ_s	Structure boundary
λ	Relative tip deformation
μ	Fluid dynamic viscosity
v	Fluid kinematic viscosity
v_s	Possion’s ratio
Π_1	Effective stiffness
ρ, ρ_f	Fluid density
ρ_s	Structure density
Φ	Velocity potential
Φ_b	Velocity potential due to body motion
Φ_v	Velocity potential due to vorticity wake
Ω_f	Fluid domain
Ω_s	Structural domain
φ	Phase shift of the actuation force
φ_i	Shape function
ω	Specific rate of dissipation
ω_z	Z-vorticity

Abbreviations

2D	Two-dimensional
3D	Three-dimensional
μCT	Micro-computed tomography
ALE	Arbitrary Lagrangian-Eulerian
API	Application program interface
AUV	Autonomous underwater vehicle
BCF	Body caudal fin
CF	Cupping style fin segments
CFD	Computational fluid dynamics

CM	Circular muscle
CMP	Central mitochondria poor fibers
CSD	Computational structural dynamics
CSS	Conventional serial staggered
DD	Drift downstream
DPIV	Digital particle image velocimetry
DU	Drift upstream
FSI	Fluid-structure interaction
HD	Holding stationary
HF	Heterocercal style fin segments
IBM	Immersed boundary method
IBQN-LS	Interface-block-quasi-Newton technique with two least-squares reduced-order models
IHC	Implicit hole cutting
IQN	Interface quasi-Newton methods
IQN-ILS	Interface quasi-Newton with inverse Jacobian from a least-square model
LES	Large-eddy simulations
LEV	Leading-edge vortices
LSM	Lattice spring model
MPI	Message Passing Interface
MPF	Median and/or paired fin
NU	Non-uniform
NACA	National Advisory Committee for Aeronautics
N-S	Navier-Stokes
PBV	Posterior body vortices
PID	Proportional-integral-derivative
PIV	Particle image velocimetry
RANS	Reynolds-averaged Navier–Stokes equations
RBF	Radial basis functions
RM	Radial muscle
ROV	Remotely operated vehicle
SMR	Superficial mitochondria-rich fibers

TEV	Trailing-edge vortices
TFI	Trans-finite interpolation
UB	Uniform along the body length
UF	Uniform fin segment
UUV	Unmanned underwater vehicle

List of Figures

List of Tables

Chapter 1 Introduction

1.1 Background

The ocean covers about 70.9 % of Earth’s surface, and it reserves abundant natural resources like the land where the human lives on. Many kinds of minerals, such as salt, copper, nickel, iron, etc are ready for mining. Energy resources, e.g., wave power, tide power, current power, thermal power, crude oil, and natural gas are also found within the ocean (Isaacs and Seymour, 1973). These treasured resources may contribute to the well-being of humans. However, most of them lie underwater even in deep water, making it difficult to explore and finally acquire. This drives people to design and manufacture vehicles that can operate in the underwater environment.

Remotely operated vehicle (ROVs) is the pioneering device used for underwater missions, e.g., oil and gas explorations and underwater biological sampling. They usually have an open-frame design due to the simplicity to manufacture and equipment installation. Nevertheless, this makes it hydrodynamically inefficient and unstable during operations, especially in more complex turbulent flow conditions with currents and surrounding vortices. Subsequently, autonomous underwater vehicle (AUVs) which normally has a torpedo shape is developed. It is pre-programmed to carry out specific tasks, and therefore, it possesses certain autonomy compared with ROV which depends on in-time human control. Their streamlined shape also reduces the hydrodynamic drag force during the voyage. Despite this, they mainly rely on a screw thruster propulsion, which would cause large noise during working and becomes inefficient while maneuverability, especially at low speed (Low, 2011).

In comparison, aquatic animals, the residents of the ocean for more than 600 million years, present elegant swimming with high efficiency, low footprint, and agile maneuverability (Fish, 2020). These aquatic animals provide great prototypes for people to get inspiration to design efficient underwater vehicles and robots that may not present shortcomings existing in the present typical unmanned underwater vehicles (UUVs). On the other hand, biologists are also keen on studying fish swimming as fish’s morphology, physiology, and behavior adaptions are deeply influenced by the interaction between fish and immersed fluid. Therefore, the research on fish swimming mechanisms is of interest to researchers and engineers among a variety of disciplines. In this section, the classifications of biological aquatic propulsion are introduced, followed by the key features. i.e., structural flexibility and deformation, of aquatic locomotion.

1.1.1 Classifications of biological aquatic propulsion

Before introducing the classifications of biological aquatic propulsion, the terminology about the fin types used in this study is depicted in Fig. 1.1 for clarification. In an early review work by Sfakiotakis et al. (1999), fish swimming modes are summarized as two main types, one is the body and/or caudal fin (BCF) locomotion, and the other is termed median and/or paired fin (MPF) locomotion. A fish that mainly generates thrust by bending a propulsive wave that extends to its caudal fin uses the BCF locomotion mode. Alternatively, a fish would be categorized as the MPF mode if it involves the use of median and pectoral fins. Nevertheless, in reality, fishes may use the caudal fin and pectoral fin simultaneously during swimming. Besides, the methodology to classify aquatic locomotion excludes the unique jet propulsion used by the cephalopod which is an indispensable member of aquatic animals.

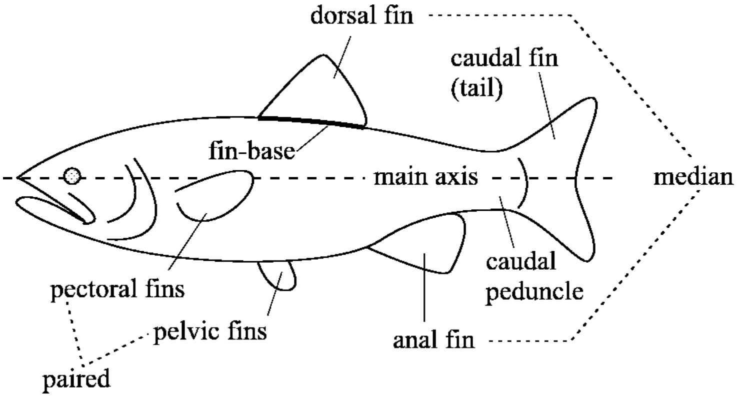

Fig. 1.1. The terminology used in this thesis of the fin types of a fish (Sfakiotakis et al., 1999).

A subsequent study divided underwater locomotion into three main categories, i.e., fin oscillation, fin undulation, and jet propulsion (Salazar et al., 2018), as shown in Fig. 1.2. Distinct from the method to differentiate the used fin types proposed by Sfakiotakis et al. (1999), fin propulsion is categorized by the movement characteristics. Namely, undulatory motion involves at least one complete propulsive wave along the propulsor, while an oscillation propulsor swivels its base without presenting a distinct complete wave formation (Sfakiotakis et al., 1999). Fin oscillation is the most used locomotion by aquatic animals, represented by the caudal fin swimmers. The pectoral fin is usually involved with fin undulation in this category. Although jet propulsion is the smallest classification, its mechanism is quite different from the other two and presents unique features which are worth studying.

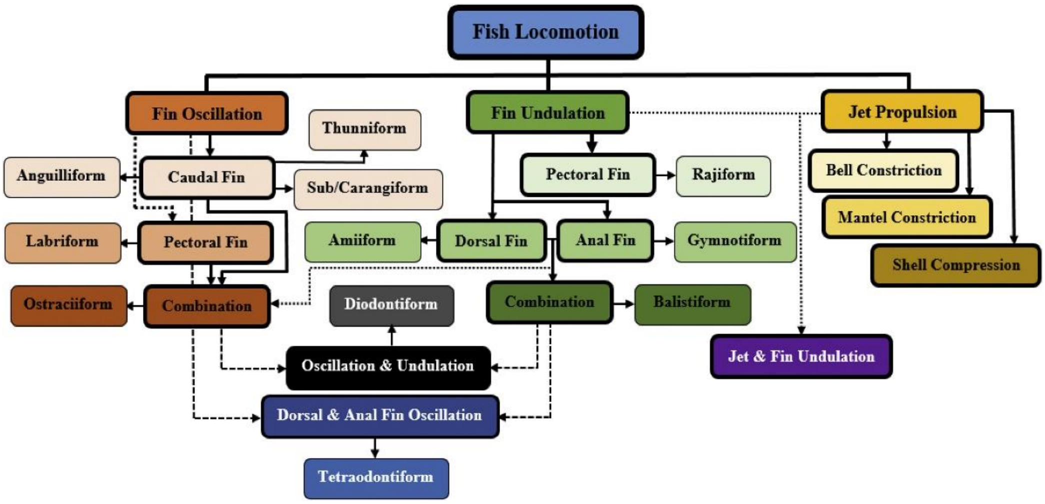

Fig. 1.2. Classifications of biological aquatic locomotion (Salazar et al., 2018).

1.1.1.1 Fin oscillation

The largest category in aquatic locomotion shown in Fig. 1.2, fin oscillation, is firstly introduced in this section. Within the fin oscillation category, most fishes rely on the caudal fin to produce thrust, and other fins are more utilized for maneuverability. A fish that uses a caudal fin tends to be a faster swimmer and a large majority of these fishes are much likely to be predatory in the food chain (Salazar et al., 2018). Besides, some caudal fin propulsion based fishes have impressive swimming endurance which can make a migration of thousands of miles (van Ginneken et al., 2005).

The caudal fin propulsion mode can be further categorized into four modes according to the degree of body motion during oscillating the tail, as shown in Fig. 1.3. Among the four modes, the largest body undulation with at least one complete propulsive wave is presented in the anguilliform pattern. This impressive body flexibility is supported by a large number of vertebrae. For example, the sea snake (*Pelamis*), one of the typical examples of anguilliform swimmers, has 186 vertebrae (Gillis, 1996; Salazar et al., 2018). Some anguilliform swimmers can reverse the swimming direction from forward to backward by changing the propulsive wave propagating direction.

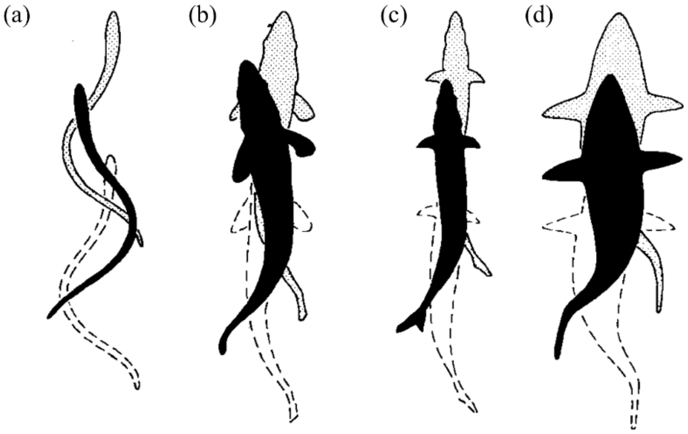

Fig. 1.3. Demonstration diagrams of the body motion during caudal fin oscillation for anguilliform (a), subcarangiform (b), carangiform (c), and thunniform (d) mode (Lindsey, 1978).

The subcarangiform and carangiform are similar and the difference between these two is not distinct. In comparison, the anterior body movement of carangiform swimmers is more limited than that of subcarangiform, as shown in Fig. 1.3. Carangiform swimmers are thought to be faster than anguilliform and subcarangiform swimmers. Nevertheless, their turning ability is reduced compared to the other two modes as the bodies are stiffer. Rainbow trout and Salmon fish are members of the subcarangiform category, while bluegill sunfish and shad fish are examples of carangiform swimmers.

The thunniform swimmers are characterized by a stiff body and rigid tail. The body movement during swimming is more limited and the oscillation only occurs in the last quarter of the body. Therefore, most of the thrust (more than 90%) is produced by the caudal fin (Sfakiotakis et al., 1999). Typical thunniform swimmers include tuna fishes, sharks, and dolphins, which are thought to be highly efficient and fast. They have streamlined bodies that reduce the drag force significantly and can swim fast with long endurance (Guinet et al., 2007). These advantages enable them to be effective predators.

In addition to the caudal fin, other fin types can also be used as the main propulsor. For example, fishes like wrasse, cales, and parrotfishes, utilize their pectoral fins for flapping or rowing motion to produce propulsive thrust. This pectoral-fin-based propulsion mode is termed labriform locomotion. The caudal fin is auxiliary in this propulsion pattern. The dorsal fin and anal fin can also be the main propulsors for the tetraodontiform swimmers, represented by fishes such as spikefishes and ocean sunfishes.

1.1.1.2 Fin undulation

Compared with fin oscillation, undulating fins have more flexibility and tend to present more observable propulsive waves along the fin due to more fine-tuned individual rib excitations. Aquatic animals in this classification can use fin undulation both for thrust generation and maneuvrability (Salazar et al., 2018). Although fishes that solely use fin undulation for locomotion are thought to be low-speed swimmers, they can control the directions and phase shift of the undulating waves, allowing agile forward and backward movement and even turning at zero swimming speed.

Rajiform is the largest category in fin undulation locomotion. This mode can be found in fishes like rays and skates. These fishes rely on the undulation of paired pectoral fins for locomotion, which shows a certain resemblance to the flight of bird wings. Many rajiform swimmers have a large diamond-like body shape, as shown in Fig. 1.4(a), with a wingspan exceeding several meters.

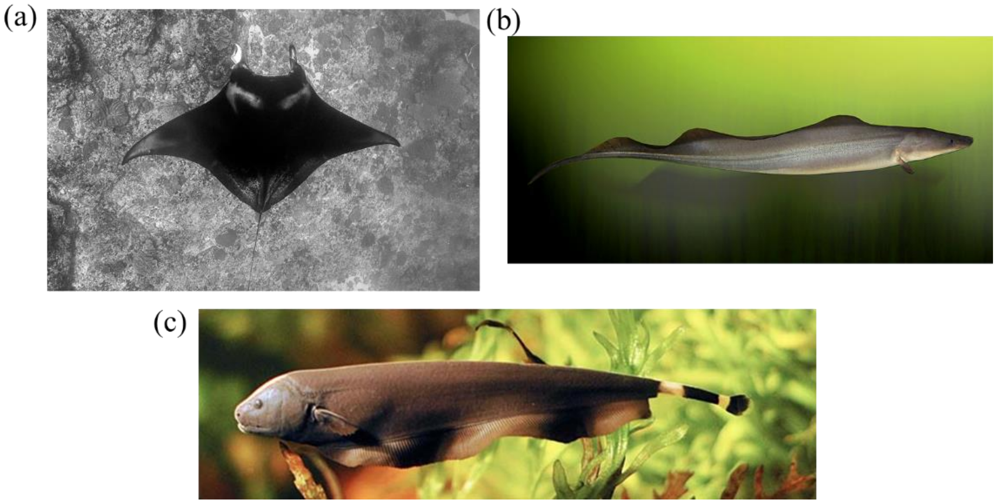

Fig. 1.4. A manta ray (a) (Photo by Emma Li from Pexels (https://www.pexels.com/photo/sea-beach-people-art-5327815/)), the aba knife fish (b) (By Wiki-Harfus; modified by Wildfeuer, CC BY-SA 3.0), and a black ghost knife fish (c) (MacIver et al., 2010).

Fishes that belong to amiiform mode undulate their dorsal fins for locomotion, as classified in Fig. 1.2. They often have an elongated dorsal fin. Examples of these amiiform swimmers include African aba knife fish and bowfin, as shown in Fig. 1.4(b). The gymnotiform swimmers are comparable to amiiform fishes, but the former utilizes the undulation of an elongated anal fin. One example of this category is the black ghost knife fish, as depicted in Fig. 1.4(c). Fishes using these two locomotion modes can easily change the swimming direction by varying the undulation wave directions and attack angle of the fin, thus achieving complex maneuverability (Youngerman et al., 2014). Nevertheless, they are not considered as fast swimmers.

1.1.1.3 Jet propulsion

Jet propulsion is the smallest category of the three main locomotion types shown in Fig. 1.2. It is distinct from the other two as it does not mainly rely on fin movement during the thrust production. Jet propulsion can be divided into three main types, i.e., bell constriction, mantle constriction, and shell compression. Bell constriction is mainly utilized by jellyfish which involves the contraction and relaxation of subumbrella muscles in the bell (Salazar et al., 2018), as shown in Fig. 1.5(a). But swimmers that use bell constriction are highly influenced by ocean current and surrounding hydrodynamic disturbance, as the produced thrust is not sufficiently large to withstand environmental perturbing force. In comparison, swimmers that constrict the body mantle can produce much larger pulsed propulsive thrust by discharging the water from the cavity at a high speed. Cephalopods, such as octopus and squid, as shown in Fig. 1.5(b) and (c), respectively, fall into the mantle constriction category. Compared with jellyfish, cephalopods have a well-formed pressure cavity and a funnel that serves as a nozzle to separate the internal and external flows. Thus, they have a superior capability to compress the entrained fluid and create a stronger jet wake. Besides, the octopus has more developed arms that enable them to walk on the seafloor. A squid also utilizes fin undulation for low-speed swimming and maneuverability in addition to jet propulsion.

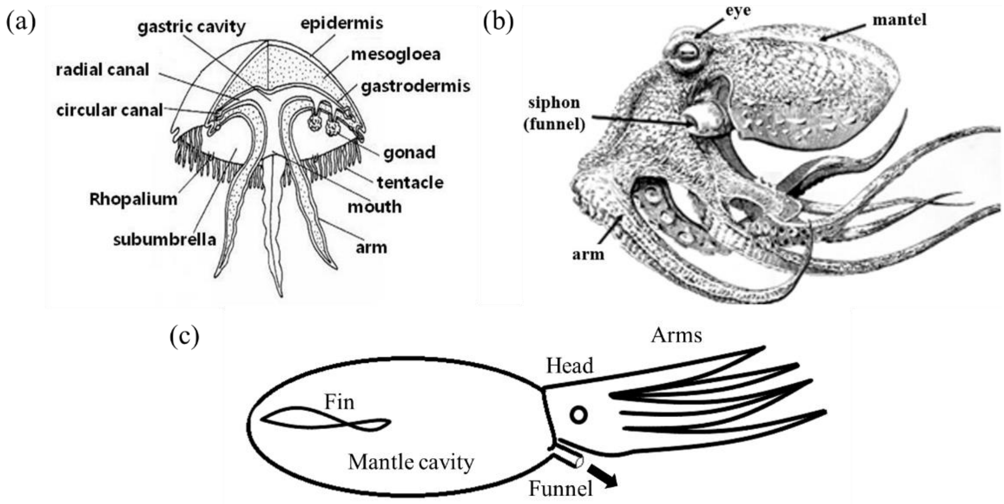

Fig. 1.5. Schematic of a Jellyfish (a) (Salazar et al., 2018; Yeom and Oh, 2009), octopus (b) (Salazar et al., 2018), and squid (c).

Shell compression locomotion is specially used by the mollusk. It involves the opening and closing of two rigid shell halves to produce thrust (Salazar et al., 2018). Nevertheless, the shell compression requires much energy for a mollusk, like a scallop. Thus, it is mainly used for escape which is not endurable.

1.1.2 Deformation and flexibility in biological aquatic propulsion

Through the above biological locomotion classifications, it is understood that deformation of body and/or fin may be the most common feature during these fishes swimming, with one exception is that the rigid shell compression utilized by mollusks. This deformation is not monotonous among different locomotion modes or specifies. One evident difference can be seen between fin propulsion and jet propulsion. The deformation during swimming mainly occurs in the appendages, e.g., the caudal fin and pectoral fin, for the former mode; while for the jet propulsion, the body mantle deforms with periodic inflation-deflation cycles.

As the thickness of the fish fin (including all the different fin types shown in Fig. 1.1) is small compared with other dimensions, i.e., chordwise and spanwise length, it can be termed propulsive surface following Lauder and Madden (2006). The deformation patterns of these propulsive surfaces are rather complex, which cannot be replicated by a simple two-dimensional conformation like that in Fig. 1.3. Taking the caudal fin oscillation, the largest sub-category of fin oscillation mode, as an example, the pectoral fin shapes of a swimming bluegill sunfish are presented in Fig. 1.6. These propulsive surface deformations are three-dimensional and time-varying depending on the swimming speed and maneuverability behaviors, exhibiting a considerable change in shape and area. Even without the dynamic change of caudal fin shapes by the fish itself, the fishtail shapes vary much among different species, as demonstrated in Fig. 1.7. The aspect ratio of the caudal fin, defined as the ratio of the square of the span to the surface area, increases from snakehead to tuna and shark. The tail of tuna (symmetrical about the midline) and shark (asymmetrical about the midline) are highly forked, forming a lunate profile, as shown in Fig. 1.7(c) and (d). Likewise, the pectoral fins of many fin undulation swimmers also show a variety of fin shapes (see Fig.1 in Rosenberger (2001)). These propulsive surfaces with various shapes show complex three-dimensional movement (or deformation) changing with time and space, which are key elements for computational fluid mechanics (CFD) modeling and kinematics design of bio-inspired robotics (Lauder, 2010).

In comparison, the body cavity of jet swimmers, such as jellyfish, octopus and squid, has less variety of morphological shapes. They often have an ellipsoid-like main body with some appendages, as shown in Fig. 1.5. The deformation pattern of the body shape is relatively simple compared with the complex fin conformation change observed in fin-based swimmers. For example, only the diameter of the squid mantle changes while the mantle length remains almost unchanged during the inflation-deflation cycles (Ward, 1972), as shown in Fig. 1.8.

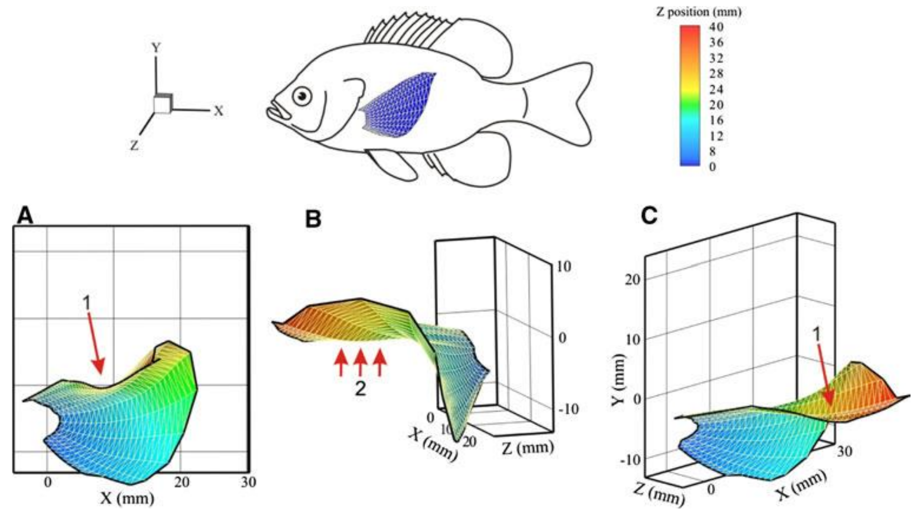

Fig. 1.6. Three views of a pectoral fin of a swimming bluegill sunfish at a single time. Arrow 1 indicates the bending wave from the root to the tip of the fin, and arrow 2 denotes the fin surface which generates thrust during the outstroke (Lauder, 2010).

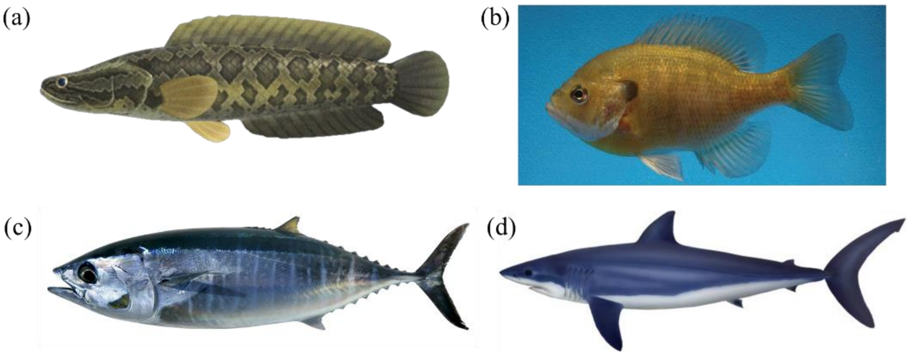

Fig. 1.7. Different caudal fin shapes of a snakehead fish (from https://nookipedia.com/wiki/File:Giant_Snakehead_NH.png#filelinks, CC BY-SA 3.0) (a), bluegill sunfish (Esposito et al., 2012) (b), tuna (with permission from lunamarina (/https://stock.adobe.com)) (c), and mako shark (© State of New South Wales through NSW Department of Industry) (d).

The above deformations of swimmer bodies and/or appendages are closely related to the flexibility of their material properties. It is important for thrust production and force vectoring (Lauder and Madden, 2006). Due to this flexibility, the dynamic interaction between the flexible body and/or fin and surrounding flow during its movement is inevitable. Therefore, the observed various conformation changes in fish body and fin are thought to be the results of complex fluid-structure interaction, complex partly attributed to nonlinear material properties (Lauder, 2010). However, it is unclear if the body and propulsive surfaces deformations are primarily active or passive, as fish can actively control these conformations. For example, flexible fin rays of bluegill sunfish have a bilaminar structure, and muscles are attached to the based of the two halves (Lauder, 2015). A different muscle activity from either side of the hemitrich can cause a curvature of the flexible fin rays. Thus, the complex overall conformation of the fin is presented with individual control of rays along the fin surface. In comparison, the deflation of the squid mantle is actuated by the constriction of circular muscles which causes the reduction of mantle circumference. Its inflation may be caused by the constriction of radial muscles to form hyper-inflation during a short time. Nevertheless, during these procedures, fluidic force is also playing a role in deforming the body and fins. This makes it challenging to interpret the correlation between the deformations and the surrounding flow pattern, given that fishes can, meanwhile, dynamically vary the stiffness of the body and propulsive surfaces (Lauder, 2010).

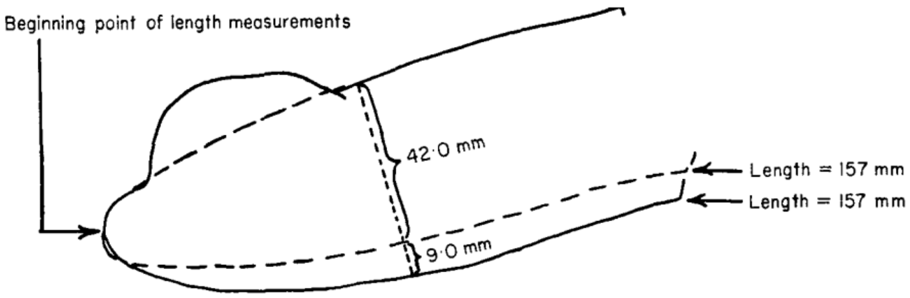

Fig. 1.8. Schematic of the deflation of the squid mantle in lateral view, and the dashed line denotes the deflated state (Ward, 1972).

Most fishes operate in the altered fluid environment as opposed to still or steady flow, either caused by surrounding structures or other swimming fishes. Their deformation patterns change in response to environmental fluid stimuli. To take advantage of these flow stimuli, fish can actively tune their propulsive surface movement to capture energy (Liao, 2007). The flexible deformation of the body and fins under these scenarios may become more complex as it is a collective result of fishes' active response to the altered flow and passive impact of the fluid stimuli which is absent in a still or uniform flow.

1.2 Objectives of the Thesis

Deformation attributed to complex fluid-structure interaction between the flexible body and/or propulsive surfaces and the immersed fluid plays a key role in biological aquatic locomotion. Therefore, the main goal of this thesis is to enhance the understanding of the underlying mechanism of caudal fin propulsion and jet propulsion involving flexible deformations through numerical modeling and simulations. This thesis aims at answering these fundamental questions of fish swimming:

- *What are the hydrodynamic effects of complex propulsor deformations during locomotion?*

- *What are the three-dimensional vortex structures of aquatic animal wakes involving complex propulsor deformations?*
- *To what extent are the observed body and propulsor deformations actively controlled and passively deformed?*
- *What are the vortices' evolution and propulsive performance of jet propulsion at high Reynolds numbers?*
- *How are the vortex ring formation and pulsed-thrust production of squid-like jets via body deformation affected by the background flow and jet velocity profile?*
- *What are the hydrodynamic benefits when fish swims and holds the station in altered flows under feedback locomotion control?*

In order to find the answers to these questions, more specific objectives are targeted:

- Development of a three-dimensional FSI solver which is capable of handling the complex dynamic interaction between the flexible body and fin with complex non-linear material properties and the immersed fluid. Compared with some previously reported FSI solvers based on finite-element method (FEM) structural code specialized in thin-walled structures (Nakata and Liu, 2012; Tian et al., 2014), the used structural solver here, CalculiX, is featured as a more universal FEM code with broader materials and geometrical applicability (Dhondt, 2004). Also, some state-of-art coupling algorithms, such as improved partitioned IQN-ILS algorithm with filtering techniques (Haelterman et al., 2016) and parallel coupling techniques (Mehl et al., 2016) would be utilized for efficient and stable simulations. The development of a universal FSI solver by coupling an in-house solver with a FEM code through a coupling library, preCICE, is one of the main contributions of this thesis which would enrich the database of the numerical tools for bio-inspired studies in the literature and lay the foundation of the following objectives.
- Investigation of the effect of stiffness and its distribution on the kinematics and propulsive performance of caudal fin propulsion based swimmer utilizing the developed FSI solver. As aforementioned, flexibility (or stiffness) is a key feature of fish fins and plays a significant role during locomotion. Through the numerical FSI studies of chordwise and spanwise stiffness distribution of the fish body and tail, it is aimed at answering the first three questions proposed above. They are all related to the stiffness and deformation of the fish fins. And FSI simulations are an indispensable alternative to experimental studies, in which these variables are not easy to measure, to find possible answers.

- Examination of pulsed-jet propulsion of squid-inspired swimmer involving body deformation. As one of the three main locomotion types along with fin oscillation and undulation modes, jet propulsion receives much less attention from researchers. Under the jet propulsion category, bell constriction mode, represented by jellyfish locomotion, has been much more extensively studied compared with the mantle constriction mode of squids and other cephalopods. However, jet propulsion of squid shows superior pulsed thrust production compared with fish fin locomotion and jellyfish bell constriction, which deserves our attention to elucidating its mechanism. The specific goal considered here is to investigate the jet propulsive performance involving body deformation in turbulent flow conditions and in the presence of background flow, respectively. These two scenarios are not studied previously but are indeed the real conditions where live squids are operating in nature.
- Investigation of motion control of a self-propelled flexible swimmer near a rigid body utilizing PD control. As mentioned in section 1.1.2, fishes may change their swimming behavior in response to surrounding fluid stimuli. Thus, distinct from the above uniform flow conditions, the swimmer is freely swimming near a rigid cylinder where the fluid field is altered compared with a uniform flow. By specifying the swimming target using motion control, it is aimed at exploring how a self-propelled flexible swimmer would tune the required actuation force amplitude to swim to the target position and hold the station there. The energy consumption of swimming near a rigid body will be evaluated to compare the energy savings during the “flow refuging” of fish.

1.3 An Outline of the Thesis

This thesis consists of seven chapters and the outline of the thesis is as follows.

The background and motivation of the present study are presented in Chapter 1, including the classification of biological aquatic propulsion and its key feature, i.e., deformation and flexibility. The research objectives are defined as well in this chapter.

Chapter 2 presents the literature review of previous studies relevant to this thesis. Previous biological studies, mechanism studies by robotic devices, and numerical studies of caudal fin propulsion, jet propulsion, and fish swimming in altered fluid conditions will be revisited, respectively. The numerical techniques used by existing FSI solvers are summarized as well.

The mathematical models and numerical approaches to resolving the governing equations are described in Chapter 3. To be more specific, fluid dynamics and structural dynamics are first introduced. Next, the coupling between the fluid and structural solver to form an FSI solver is presented. The developed FSI solver is then validated by comparing the present results with the counterparts from previous experimental and numerical studies.

Chapter 4 to Chapter 6 concentrate on the application of the above numerical solver and present the main results of the thesis. It started with the numerical simulations of a sunfish caudal fin model and a tuna-like swimmer in Chapter 4. The effect of variable stiffness along the spanwise and chordwise direction on the kinematics and propulsive performance is investigated.

Following the study of caudal fin-based propulsion in Chapter 4, Chapter 5 focuses on squid-inspired jet propulsion. A two-dimensional and three-dimensional squid-like model are considered, respectively. The study of the 2D squid-like jet system involves flexible inflation-deflation actuated by externally added force, which mimics circular muscle constriction of squid mantle, with fluid-structure interaction being considered. In comparison, the deformation of the 3D squid-inspired model is prescribed in an attempt to study the effect of jet velocity profile and stroke ratio of the jet flow on propulsive thrust production.

In Chapter 6, the FSI solver is further applied to the study of a self-propelled 2D swimmer in front of a fixed cylinder in the uniform flow. The motion is controlled by a feedback PD controller to tune the actuation force. The effect of initial position relative to the cylinder on the energy consumption during traveling a specified distance to the target location under the PD control is investigated.

To summarize this thesis, conclusions and recommendations for future work are provided in Chapter 7.

Chapter 2 Literature Review

In this chapter, previous studies of fish swimming and the used numerical methods of FSI solvers relevant to the present work are reviewed thoroughly. As mentioned in section 1.1, there are a large variety of fish species and locomotion modes. It is not possible to cover all of these aspects. Thus, the literature review is limited to the relatively large categories of locomotion patterns, i.e., carangiform and thunniform of caudal fin propulsion, and mantle constriction mode of jet propulsion, represented by sunfish and tuna fish, and squid, respectively. They are also among the most popular biological prototypes of bio-inspired engineering applications in underwater robotics. The review of these two locomotion patterns includes biological studies, mechanism studies by robotic devices, and numerical simulations. The last part of the literature review focuses on previous research on fish swimming mechanics and behaviors in altered flow conditions and motion control on fish swimming using PID control.

2.1 Caudal Fin Propulsion

2.1.1 Biological studies of fish

2.1.1.1 Taking sunfish as the example

Structure of sunfish tail

Many fishes utilizing caudal fin propulsion are ray-finned fishes. Ray-finned fishes are featured by their webs-like fins supported by bony spines (rays) (Lauder, 1989). Bluegill sunfish (*Lepomis macrochirus*) is a typical example of the ray-finned fish family, as it has a well-developed caudal fin supported by rays. It has a homocercal tail with dorsal-ventrally symmetric external morphology, as shown in Fig. 2.1(a). Anatomical studies revealed that the tail skeleton consists of median flattened hypural bones, flattened haemal and neural spines (Gosline, 1997; Lauder, 1982; Lauder and Drucker, 2004). The distal edges of the hypural bones support a cartilage pad where the roots of the caudal fin rays attach (Lauder and Drucker, 2004), as shown in Fig. 2.1(c). It was also found that the fish fin rays are bilaminar in structure and neighboring rays are connected by thin membranes (Fig. 2.1(b)). Each fin ray has two halves (hemitriches) that can slide past each other under the constriction of the tendons actuated by muscles at the base. When the base of one hemitrich is pulled past the other, the caused offset yields curvature of the fin ray, as demonstrated in Fig. 2.1(c). Each fin ray can have a fine control of its flexing, which form the morphological and mechanical basis of complex fin configuration movement on the whole.

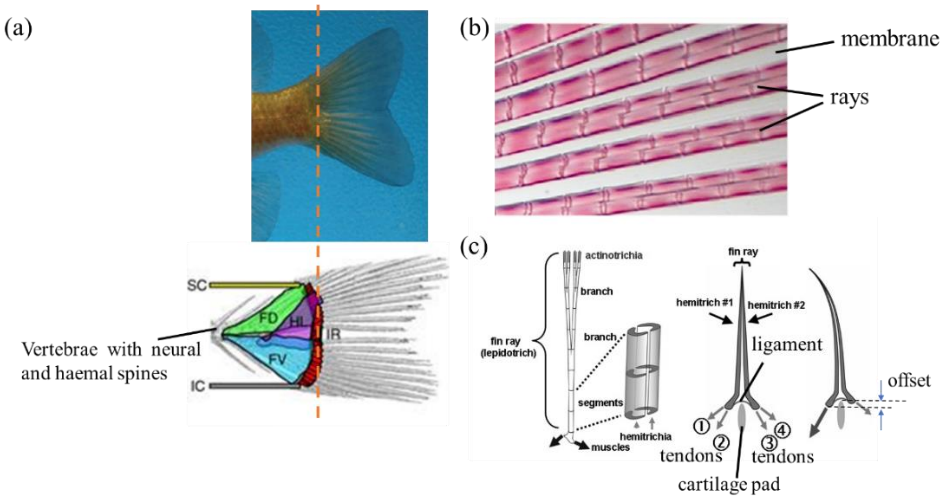

Fig. 2.1. The caudal fin skeleton of a bluegill sunfish demonstrating the supporting elements of the tail adapted from Lauder and Drucker (2004) and Flammang and Lauder (2009) (a), close-in view of fin rays adapted from Lauder et al. (2011a) (b), and schematic showing a fin ray with two hemitriches (Alben et al., 2007; Lauder, 2007) (c). The intrinsic caudal muscles presented in (a) are the flexor dorsalis (FD), flexor ventralis (FV), hypochordal longitudinalis (HL), infracarinalis (IC), interradialis (IR), and supracarinalis (SC).

Kinematics of sunfish tail

Attributed to the complex structures of fin rays, the fish can dynamically change the fin movement which has been observed in biological experimental of live fishes. A high-speed camera is a commonly used tool in recording fin kinematics. For example, Lauder (2000) conducted a three-dimensional kinematics analysis of caudal fin movement during steady swimming using two high-speed video cameras for the lateral and posterior view. It was revealed that the dorsal and ventral lobe of the bluegill tail does not function symmetrically as previously expected despite its homocercal morphology. Instead, the dorsal lobe undergoes around 50% larger lateral excursion with higher movement speed compared with the ventral lobe (Lauder, 2000). He also observed that a remarkable acute angle to the horizontal plane is presented by the dorsal lobe and thus, suggested that the caudal fin would generate lift force during steady swimming. Given that the dorsal and ventral flexor muscles are approximately symmetrical about the horizontal axis, he conjectured that this asymmetrical movement of the homocercal bluegill sunfish tail is caused by active intrinsic tail musculature. This is supported by the electromyographic recordings showing that hypochordal longitudinalis muscle (see Fig. 14 in that work), which may affect the ventral lobe movement, is the only active muscle when the asymmetry is presented. In addition, this muscle recruitment varies significantly with steady-swimming speeds (Flammang and Lauder, 2008). Another observation of the caudal fin of bluegill sunfish by Tytell (2006) revealed that the dorsal and ventral lobe may lead the tail beat during steady swimming which causes lagging of the central tail during lateral movement, forming a cup-like fin surface.

The above measurement of caudal fin movement is limited to steady swimming which seems to only involve the hypochordal longitudinalis muscular activity. A subsequent study revealed that the complex fin rays structures presented in Fig. 2.1 can produce more complex conformation changes of the fin during maneuverability (Flammang and Lauder, 2009). Specifically, kick-and-glide, braking, and backing maneuvers were considered in their experiment, and the corresponding conformations of the fin are shown in Fig. 2.2. They observed large and rapid excursion of the caudal fin, followed by the adduction of fin rays which causes the reduction of the surface area during the kick-and-glide maneuvers. During braking, the dorsal and ventral lobe of the tail moves in the opposite direction that forms an "S" shape of the caudal fin with strong activity in the interradialis muscles. In comparison, a bending wave initiated from the ventral lobe to the dorsal lobe was observed at the trailing edges of the fin during the backing maneuver (Flammang and Lauder, 2009). A subsequent study of backward swimming in live bluegill sunfish focused on this ventral-to-dorsal wave in the caudal fin surface conformation (Flammang and Lauder, 2016), which is seen in the reverse direction during forwarding swimming and would produce a force directing ventrally. It was hypothesized that this reverse lift would help control pitch and yaw instability encountered from pectoral-driven backward locomotion (Flammang and Lauder, 2016).

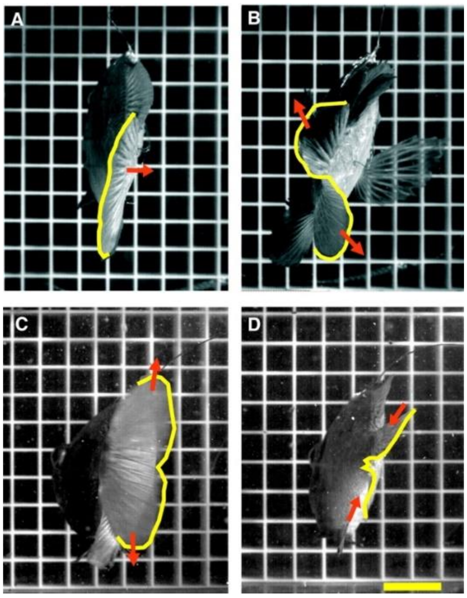

Fig. 2.2. Images of the bluegill sunfish tail in posterior view at steady swimming (A), braking (B) kicking (C), and gliding (D) maneuvers (Flammang and Lauder, 2009). The trailing edge of the fishtail is marked with yellow color, and the arrows indicate the movement direction of the dorsal and ventral lobe.

Hydrodynamics of sunfish tail

In addition to the above morphology and kinematics studies on live fishes, hydrodynamics analysis can also be conducted to understand swimming biomechanics in the laboratory environment. Digital particle image velocimetry (DPIV) techniques are effective tools to help visualize the fluid field around the swimming fish. An early application of DPIV to the measurement of the flow field around the pectoral fin of bluegill sunfish was reported by Drucker and Lauder (1999). The obtained thrust and lift force calculated from the measured vortex ring orientation and momentum matched well with that empirically determined counter force of the drag and weight, indicating the feasibility and accuracy to use DPIV to study the unsteady flows around swimming fish. A subsequent study focused on the wake of caudal fin using DPIV techniques (Lauder, 2000). Due to the aforementioned dorsal-ventral asymmetrical movement of the caudal fin, Lauder (2000) predicted that a lift force would be produced so that the vortices shed by the tail should have a ventral inclination to the horizontal. This was evidenced by the velocity vector and vorticity contour obtained by DPIV techniques, as shown in Fig. 2.3(a). He also hypothesized the tail can produce linked vortex rings based on the measurement as depicted in Fig. 2.3(b).

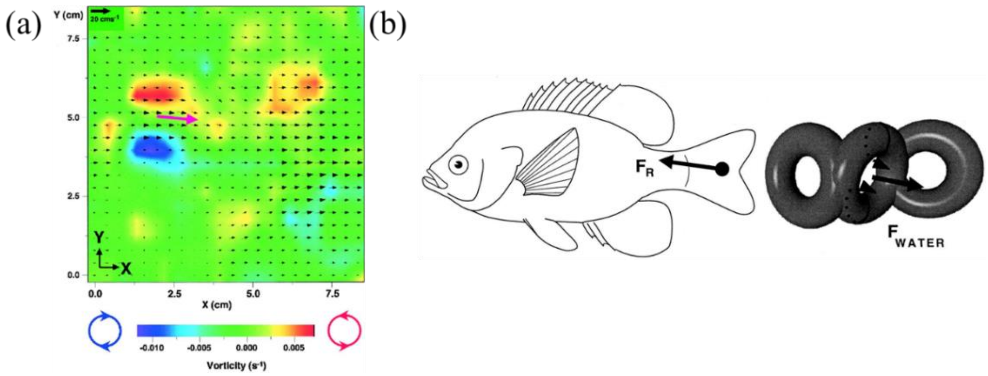

Fig. 2.3. Fluid velocity vector (arrow) and *Z*-vorticity (color contour) in the vertical plane (a) and schematic illustration of the vortex wake (b) behind a bluegill tail in steady swimming (Lauder, 2000).

Subsequently, PIV measurements were performed by Tytell (2006) to investigate more complex vortices interaction shed by dorsal, anal, and caudal fins. He found that circulations of the dorsal and anal fin vortices do not differ much from that of the caudal fin vortices, thus, argued that the generated forces by them are approximately equal. The contributions from different positions of the fish posterior were also analyzed according to vortices circulations. A more recent study examined the flow around bluegill sunfish in linear acceleration using PIV techniques (Wise et al., 2018). Wake vortices were found to have higher circulation during acceleration compared with steady swimming.

A new volumetric velocimetry imaging system was then utilized to provide three-dimensional views of wake structures of swimming fish (Flammang et al., 2011a; Flammang et al., 2011b). Volumetric wake patterns produced by the caudal fin of bluegill sunfish were first reported by Flammang et al. (2011b). They also visualized the three-dimensional vortex interaction between the dorsal and anal fins and the tail by using this volumetric velocimetry method, a significant improvement compared with Tytell (2006) where only planar vortex interaction was presented.

2.1.1.2 Taking tuna fish as the example

Structure of tuna fishtail

Compared with bluegill sunfish, tuna and other scombrids have more streamlined bodies with a tear-drop-shaped body and forked lunate tail behind the narrow peduncle. Anatomical studies revealed that neutral and haemal spines which overlap near the rear caudal vertebrae are depressed posteriorly (Fierstine and Walters, 1968), as shown in Fig. 2.4(a). Some caudal vertebrae have lateral flanges at both sides which form the peduncular keel composed of a thick layer of collagen fibers, reinforcing the bending rigidity of the caudal peduncle. The hypural and urostyle are fused into a single hypural plate at the ending of the peduncle. The ridges and grooves of this hypural plate often indicate the base of the caudal fin ray.

Fierstine and Walters (1968) suggested that the caudal muscles of scombroid fishes are reduced compared with other fishtails, e.g., a sunfish tail introduced in section 2.1.1.1. Therefore, the asymmetry of the dorsal and ventral lobes is minimized. Specifically, a great lateral tendon, as shown in Fig. 2.4(b), pasts the peduncle and reaches the hypural plate to insert upon the caudal fin rays. They form a flat fleet of collagen fibers that connect each fin ray. The caudal fin of tuna fish consists of collagens fibers and embedded fin rays, as depicted in Fig. 2.5. The number of principal rays is almost always 17 with nine above the posterior hypural notch and eight below it (Fierstine and Walters, 1968). Each fin ray is composed of spinous rays which extend from the leading edge to the middle of the fin and soft rays in the posterior part of the fin (Morikawa et al., 2008). In general, the caudal musculature of tuna fish is not as complex or developed as that of some other ray-finned fish, like sunfish, which may limit the fine control of each single fin ray. The stiffened fin rays, the hypural plate, and the collagen fibers together form the main structure of the caudal fin, which withstands the majority of resistance that fish experiences when it swims. Thanks to the utilization of advanced micro-computed tomography (μCT), more clear images of caudal fin morphology of yellowfin tuna were reported in recent studies (Delepine, 2013; Wainwright and Lauder, 2020).

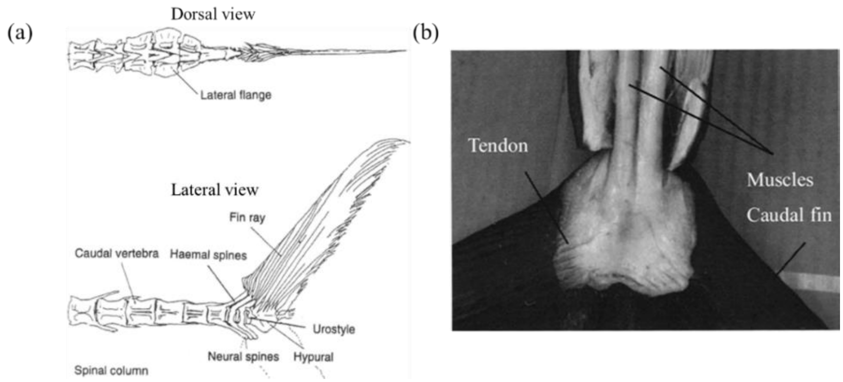

Fig. 2.4. The caudal skeleton (a), and muscles and tendons (b) of bluefin tuna (*Thunnus thynnus*) (Morikawa et al., 2008).

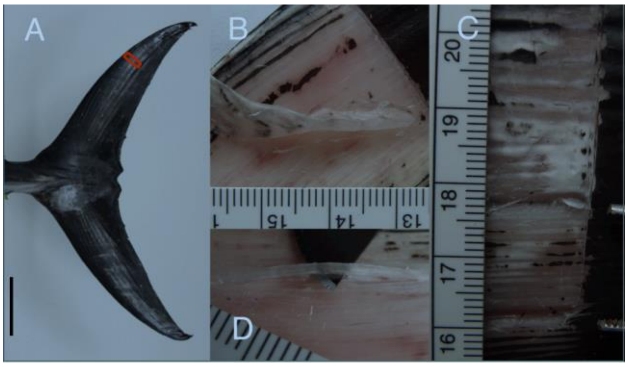

Fig. 2.5. The dissected area marked by a red rectangle of the caudal fin (A), collagenous filaments surrounding fin rays (B), measurement of the fifth fin ray indicated by tips of thumb forceps (C), and small rectangular beams fused together to form a fin ray (Delepine, 2013).

Kinematics of tuna fishtail

The detailed kinematics of tuna fish during swimming was well recorded in an early experimental study by Fierstine and Walters (1968). Their measurement indicated that the propulsive wave only traves at the last part of the body antero-posteriorly, a key feature for a thuniform swimmer. They also found that the dorsal and ventral tips of the caudal fin in swimming scombrids lag behind the middle hypural base during sweeping, forming a cupping shape. Nevertheless, their study relied on planar cine film recording, thus no more detailed three-dimensional data can be provided. A later water tunnel experiment of live yellowfin tuna conducted by Dewar and Graham (1994) revealed that the tail-beat frequency increases with the swimming speed as in most fishes. They also found that the propulsive wavelength of the tunas, ranging from 1.23−1.29 fork length in the experiments, is 30−60% longer than that of cruise-adapted teleosts like salmon fish. This long propulsive length associated with morphological and anatomical adaptations was thought to minimize the drag from the anterior body and maximum thrust by the tail. A similar study that provided a quantitative kinematic comparison of kawakawa tuna and chub mackerel was reported by Donley and Dickson

(2000). These studies concentrated on general swimming kinematics while the dynamic movement of the caudal fin was excluded.

As mentioned before, scombrid fishes like tuna have a dorsal-ventral symmetric tail with reduced intrinsic musculature. Thus, they have been often assumed to move in a dorsal-ventral symmetrical manner and produce no lift force as predicted by the homocercal tail model. However, three-dimensional tail kinematics analysis of swimming chub mackerel, Scomber japonicus, by placing motion makers on the fishtail (see Fig. 2.6(a)) suggested that the dorsal lobe of the tail undergoes a 15% larger lateral excursion than the ventral lobe does (Gibb et al., 1999). It was inferred that this asymmetrical movement of the caudal fin is caused by the axial musculature and transmitted to the tail, as the angles subtended by the peduncle and caudal fin in the front plane (*xz* plane shown in Fig. 2.6(b)) are almost the same. The previous study also reported this dorsal-ventral asymmetry at low speeds, but meanwhile, fish was seen to tip its body up into the flow during slow swimming (He and Wardle, 1986). Nevertheless, this asymmetric tail movement was observed at all swimming speeds in the experiment of Gibb et al. (1999). Thus, they tended to believe that this asymmetry of the tail produces lift force to keep the fish from sinking due to a negatively buoyant body and balance the anterior lift generated by the pectoral fins (Aleev, 1969).

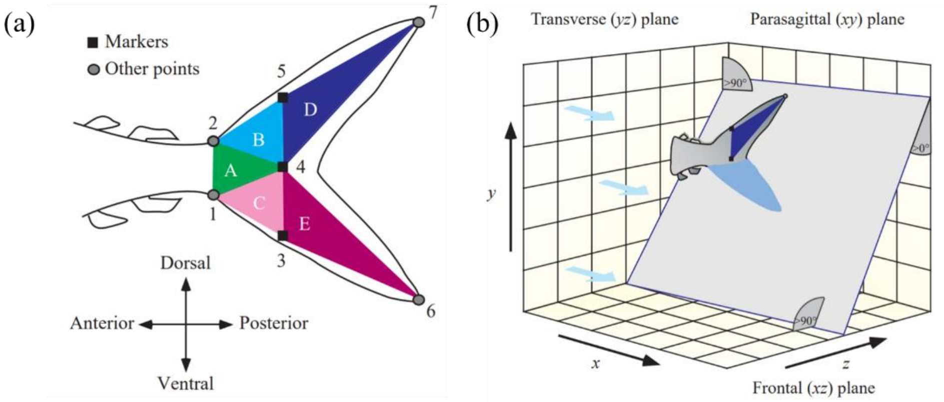

Fig. 2.6. The motion monitor makers (a) and illustration of the mackerel tail in threedimensional space (b) of the experiment of live chub mackerel by Gibb et al. (1999).

Hydrodynamics of scombroid fishtail

During the kinematics analysis of the finlets of the chub mackerel, Nauen and Lauder (2000) found that the finlets oscillated in the horizontal and vertical planes. Thus, they predicted that finlets could deflect the water longitudinally along the posterior body and then influence the flow around the caudal fin region. Following this discovery, Nauen and Lauder (2001) presented the flow visualization near the caudal peduncle and finlets of chub mackerel in steady swimming in a recirculating water tank using DPIV. It was found that the flow field in the vertical plane was not affected by the finlets. In comparison, the strong planar flow was measured in the horizontal plane as the peduncle decelerated, indicating that finlets can redirect cross-peduncular flow, and thus affecting local flow. Nevertheless, given the small height of caudal keels, they thought that keels, located within the boundary layer of flow, have little effect on surrounding flow (Nauen and Lauder, 2001). These studies did not present insights into the possible influence of caudal finlets or keels on the downstream tail flow field or hydrodynamics interaction between them.

A subsequent study by Nauen and Lauder (2002) focused on the hydrodynamics of the caudal fin of chub mackerel. The flow patterns obtained by DPIV techniques behind the tail consisted of a series of linked elliptical counter-rotating vortex rings with central jet flow, consistent with theoretical predictions. Based on the measured wake data, lift, thrust, and lateral forces were calculated. The calculated lift force was not zero but tended to rotate the fish to tip the head down. This supports the kinematics observations that the homocercal caudal fin of scombroid fish functions asymmetrically in the vertical plane (Gibb et al., 1999; Nauen and Lauder, 2002). Their calculation also suggested relatively large lateral forces due to propagated bending waves during swimming.

Concluding remarks

In this section 2.1.1, biological studies of sunfish and tuna fish, focusing on their tail structure, kinematics, and hydrodynamics during swimming, are reviewed. It is found that fishtails have complex morphological structures and can perform complex 3D movements. This motivates researchers to replicate these fishtail movements either by experimental device or numerical modeling in an attempt to understand the underlying mechanism in structural and fluid dynamics. It also motivates this thesis to investigate propulsion and hydrodynamic features utilizing non-uniform stiffness distributions of fish body and tail using FSI simulations.

2.1.2 Mechanism studies by robotic device

Although the above direct observation and measurement of live fishes have advanced our understanding of the fundamental mechanism of fish swimming, experiments on live fishes have limitations to control the animals and allow isolations of individual factors that may influence propulsive performance. Robotic models that hold similarities to real fishes are effective to enable more specific parameter control of factors in affecting fish swimming, e.g., the flexibility of fish fin, and easier measurement of force production and flow visualization (Lauder, 2010). In this section, the mechanism studies of fish swimming by robotic device inspired by sunfish and tuna fish are reviewed.

2.1.2.1 Taking sunfish as the prototype

An early mechanical model that mimics pumpkinseed sunfish as shown in Fig. 2.7(a) was reported by McHenry et al. (1995). This high-fidelity model was molded by a real sunfish. The focus was to investigate the role of flexural stiffness, driving frequency, and amplitude on swimming performance. A fish-like bending waveform was presented during forced oscillation by this mechanical fish model. Their experimental results showed that change of body stiffness and driving frequency can both control propulsive wavelength, Froude efficiency, and swimming speed. The mechanical control results of the sunfish model revealed that live sunfish may stiffen their bodies to increase swimming speed (McHenry et al., 1995).

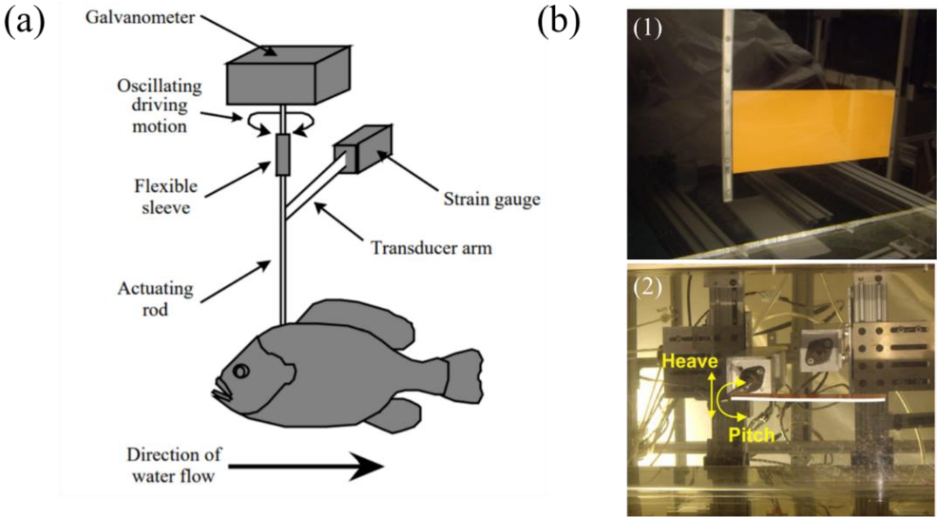

Fig. 2.7. The molding model of pumpkinseed sunfish in a flow tank (McHenry et al., 1995) (a), and the experimental setup of a flexible foil model (Lauder et al., 2011a) (b).

Following experimental studies using simple flexible foil models were also reported (Kancharala and Philen, 2014; Lauder et al., 2011a; Lauder et al., 2011b; Lauder and Madden, 2007; Wen and Lauder, 2013). These simplified foil models are aimed at replicating either fish body or fin. Under the simple forced movement such as heave, pitch, or coupled motion of these two, as shown in Fig. 2.7(b), similar bending patterns to the real fish deformation can be generated by these foil models. Some subsequent studies of flexible foil were made of biomimetic non-uniform materials rather than commonly used uniform ones to yield biological bending patterns (Lucas et al., 2014). It was reported that non-uniform stiffness of propulsors tends to result in performance improvement in terms of propulsive thrust production and flapping efficiency (Kancharala and Philen, 2016; Lucas et al., 2015; Reddy N et al., 2018; Riggs et al., 2010).

In addition to the above foil models, some more complex robotic devices capable of precise control of propulsive surfaces by fish-inspired fin rays were manufactured to study fin propulsion. For example, a high-fidelity robotic fin inspired by the anatomy of the pectoral fin of bluegill sunfish was developed by Tangorra et al. (2007) and Tangorra et al. (2010), as shown in Fig. 2.8(a). This robotic fin with five flexible fin rays that can be controlled individually produced three-dimensional movements such as sweep, curl, expansion, and cupping which have been observed in real fish pectoral fin motion. The quantitative measurements of the biorobotic pectoral fin with real biological fish fin kinematics and structural properties revealed that a slight variation of flexural rigidities or operating conditions would result in a significant impact on the propulsive forces (Tangorra et al., 2010). They also found that the generated thrust and lift force scaled with fin ray stiffness, and increased with a larger flapping speed or reduced flow velocity.

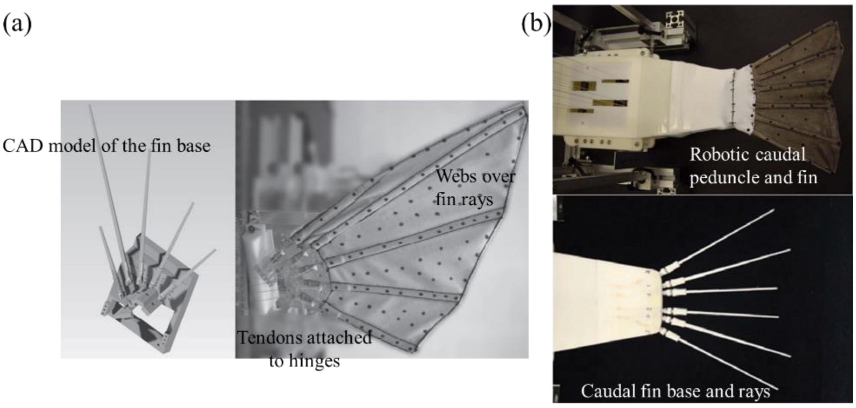

Fig. 2.8. Robotic pectoral fin (Tangorra et al., 2010) (a), and robotic caudal peduncle and fin (Esposito et al., 2012) (b).

Using similar materials and methods, Esposito et al. (2012) designed and made a robotic fish caudal fin with six individually moveable fin rays inspired by the tail of bluegill sunfish, as depicted in Fig. 2.8(b). This robotic caudal fin replicated complex tail conformations such as cupping motion, “W” shape motion, “S” shape motion, and rolling movement observed in biological sunfish tail (see Fig. 2.2). Force measurements during these different fin movements suggested that the cupping motion produced the most thrust in almost all cases of their experiments. Only the undulation motion of the robotic fin produced a lift force as large as the thrust force. Their experimental results of different motion programs generally agree with the expectations of force production during corresponding maneuvres, which enhances our understanding of these complex tail conformations in terms of hydrodynamics. Similar robotic devices inspired by the sunfish caudal fin were also reported in several following experimental studies (Hu et al., 2016; Ren et al., 2016b; Wen et al., 2018).

2.1.2.2 Taking tuna fish as the prototype

Similar to the sunfish-inspired experimental studies, foil models are also applied to the mechanism study of tuna fish swimming. These models often have a narrow peduncle and/or forked tailing edge like the tuna tail. For example, Lauder et al. (2011b) compared the self-propelled speeds of heave flexible foils with different tail shapes, as shown in Fig. 2.9, and found that the foil with a forked tail, similar to the tuna caudal fin, did not present fast speed as its biological prototype. This suggested that a lunate-shaped tail is not the single factor in determining its swimming performance. They conjectured that the reduced performance of the notched shape may be caused by the twisting dorsal and ventral lobes, which is absent during tuna swimming whose upper and lower lobes are substantially stiffened (Lauder et al., 2011b).

A subsequent study by Feilich and Lauder (2015) took the caudal peduncle depth and absence of the tuna-like forked caudal fin into consideration and systematically compared the swimming performance of four foil shapes, as shown in Fig. 2.10, made of plastics with three different flexural stiffnesses. The tuna-like foil model did not exhibit a remarkable advantage over other shapes. They did not find a single “optimal” foil producing the best performance in all metrics including swimming speed, forces production, and power consumption, indicating that foil shape and stiffness interact in complicated ways.

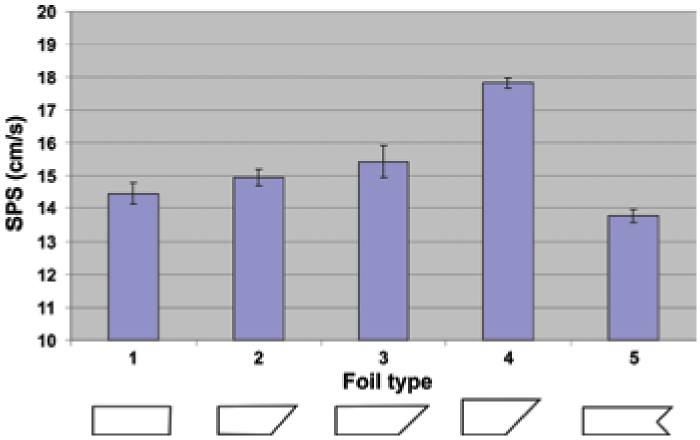

Fig. 2.9. The self-propulsion speed (SPS) of foils with the same flexural stiffness and heave actuation at the leading edge but with different shapes (Lauder et al., 2011b).

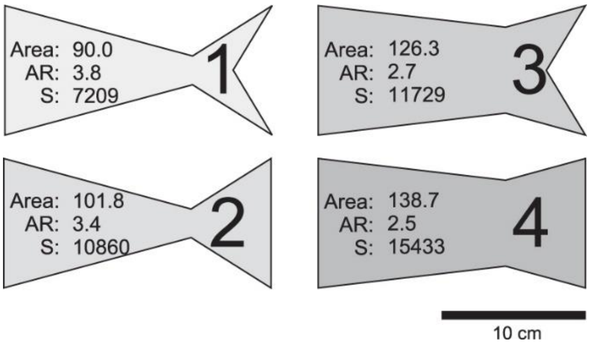

Fig. 2.10. Foil shapes with the area (cm^2), aspect ratio (AR), and second moment of area (S, cm^4) (Feilich and Lauder, 2015).

Following Feilich and Lauder (2015), Muñoz-Benavent et al. (2017) focused on the tuna-inspired foil, the no.1 foil in Fig. 2.10. They systematically analyzed the swimming performance of this tuna-tail-shaped foil of a wide range of stiffnesses, heave amplitudes, and frequencies. Although it was revealed that intermediate stiffness yielded the largest thrust in their experiment, it lacks reference for others since how large the stiffness can be regarded as intermediate or stiff is not clear practically. Their foil model has a tuna-like peduncle and tail shape but was made of materials with uniform stiffness, distinct from real tuna body and fin which have variable stiffness. Besides, the actuation mechanism may also be different with tuna swimming in which active muscular activity is involved. Thus, the kinematics of the foil during swimming was found to differ from the data obtained from a live tuna fish.

A more recent study included the keels and finlets, which have been ignored in much previous tuna-tail-inspired robotics, in the design of a tuna-like foil model by Wainwright and Lauder (2020). Their experimental results showed that both the tuna lateral keels and flexible finlets decrease the swimming energy consumption, likely by reducing the lateral forces and yaw torques. Nevertheless, the lateral keels and flexible finlets also lead to thrust reduction compared with models without these features or with stiff finlets, indicating a tradeoff between the power requirement and thrust generation.

Apart from the above relatively simple foil models, more tuna-like robotic devices were developed to help study the propulsion mechanism. For example, a high-fidelity robotic caudal fin inspired by the skipjack tuna tail was created by Ben-Zvi and Shadwick (2013). The motion parameters, fin size, shape, and material properties of this tail model were properly chosen to match with *in-vivo* measurements. Nevertheless, the propulsive efficiency of the bio-inspired tail was estimated below the evaluation predicted in the literature, indicating the significant challenge for a biomimetic model to present the high performance of the biological prototype.

A more advanced tuna-like robotics platform was developed to explore the performance space of swimming fishes (Thandiackal et al., 2021; White et al., 2021; Zhu et al., 2019). This tuna robot featured yellowfin tuna-inspired body and tail profiles. Their experimental tests highlighted the importance of body and tail flexibility in replicating fish-like kinematics and swimming performance. This platform enables simultaneous measurement of power consumption, kinematics, hydrodynamics, and mechanical power output during robotic fish propulsion which is not possible in real fish swimming. It is promising to become an effective tool to study fundamental tuna fish swimming mechanisms and provide insights into the design of high-performance engineering robotic systems.

2.1.3 Numerical studies

Although in the above experimental studies by robotic devices, biomimetic models can be constructed with different physical materials, they are still subjected to the availability of material diversity for conducting a systematic parametric study. Additionally, some key hydrodynamics parameters (e.g., surface force and structural stress of fish) remain less known in experimental work. To compensate for these weaknesses associated with experimental testing, numerical simulation plays a role in presenting holographic flow information, as it enables to answer ‘‘what if’’ type questions, which makes it also attractive in comparison with experimental studies. Especially thanks to the high-performance computation and high-fidelity numerical techniques, computational modeling becomes an indispensable approach along with experiments in biomimetic research.

In this section, two types of numerical studies of caudal fin propulsion will be reviewed. The first type excludes the material property of the swimmer, while the second one considers structural material and resultant fluid-structure interaction. In the former scenario, the deformation of the swimmer is prescribed mathematically according to the kinematics data obtained from the measurement of live fishes. Thus, only the hydrodynamic response to the designated model deformation is examined, whereas the effect of resultant fluid forces on the swimmer is neglected. In comparison, for the latter scenario, the FSI study considers the so-called “two-way” coupling between the flexible structure and surrounding fluid, which resolves the structural and fluid dynamics simultaneously. Although this thesis focuses on the FSI studies that take structural materials into consideration, the single-field computational fluid dynamics (CFD) research excluding FSI is still essential to reveal the hydrodynamics mechanism during fish swimming. Therefore, they are included in this literature review as well.

2.1.3.1 Numerical studies with prescribed kinematics

With the development of advanced CFD numerical techniques and accurate measurements of fish swimming kinematics, numerical simulations involving complex fish body and fin deformation are conducted by solving three-dimensional Navier-Stokes equations. Early works of numerical simulations were reported by Liu et al. (1996) and Liu et al. (1997) of 2D and 3D tadpole swimming, respectively. Subsequently, a Cartesian-grid-based immersed-boundary solver was used to simulate the pectoral fin hydrodynamics of a numerical bluegill sunfish model by Mittal et al. (2006). The computed wake structures and streamline distribution near the pectoral fins during a complete abduction-adduction cycle were visualized, which showed reasonable agreement with the PIV measurements of the flow field around live fish. Force evaluation by their computation revealed that positive thrust can be produced during all phases of the pectoral flapping cycle.

Following Mittal et al. (2006), more detailed computational modeling and analysis of hydrodynamics of bluegill sunfish pectoral fin were reported (Bozkurttas et al., 2009; Dong et al., 2010). Specifically, proper orthogonal decomposition (POD) analysis suggested that the complex pectoral fin kinematics is dominated by few main orthogonal modes, including "cupping" motion, "expansion" and a wave-like spanwise motion. Simulation results indicated that these three modes produce 92% thrust force of the pectoral fin (Bozkurttas et al., 2009). The effects of Reynolds number (Re) and Strouhal number (St), defined as St = fA/U with L being the fish length, U being the swimming speed, and A denoting the maximum lateral excursion of the tail, on the thrust production capability were also examined in this work. Another numerical study using the same immersed-boundary method-based solver focused on a further quantitative comparison with the experimental work of pectoral fin swimming of sunfish by Lauder et al. (2006). It was revealed that the produced strong and long-lasting, attached tip vortex during fin abduction is associated with most of the thrust generated during this phase (Dong et al., 2010).

Some other numerical studies concentrated on the role of the caudal fin and other median fins (dorsal and anal) of sunfish during swimming and maneuvers. For example, the caudal fin was found to contribute up to 70% of the instantaneous hydrodynamic force during stage 2 of the C-start when sunfish rapidly bends out of the C-shape by Borazjani (2013). The anal and dorsal fin under active control may relate to reducing the roll and pitch movement during the C-start. A recent study reported a systematical hydrodynamic analysis of a sunfish-like numerical model with median fins (Han et al., 2020). The prescribed movement of the body and fins were extracted from experimental data digitilized from video recordings to ensure a high-fidelity kinematics replication. Compared with the previous study (Zhu et al., 2002), the effect of posterior body vortices on tail-generated vortices was analyzed more specifically. It was revealed that both the thrust and efficiency of the caudal fin can be improved attributed to the collision between the upstream posterior body vortices and tail leading-edge vortices. The flapping phase of the dorsal/anal fin also affects the caudal fin performance (Han et al., 2020). It may improve caudal fin efficiency (phase-leading) or increase thrust production of the tail (phase-lag).

In addition, some numerical studies also took tuna and other Scombridae fishes as the biological prototype. For example, Borazjani and Sotiropoulos (2008) conducted a numerical investigation of the hydrodynamics of a mackerel-like swimmer in the transitional and inertial flow regimes. Their simulation results found that the Froude efficiency based on the thrust force at a given Strouhal number, increases with Reynolds number, suggesting that mackerel fish is more efficient in the inertial regime. This finding is consistent with the fact that carangiform kinematics is the preferred mode for fast swimmers (high Re) (Borazjani and Sotiropoulos, 2008). They also found that the wake structure behind the swimmer is primarily dependant on the St. Namely, a single row of vortices was presented at low St, while a more complex double row of vortices was observed at higher St at all the Re studied in their simulations. In a subsequent study by them, the effects of body shape and kinematics on hydrodynamics were investigated using the same numerical method (Borazjani and Sotiropoulos, 2010). It was found that the mackerel-like swimmer with carangiform kinematics achieved higher swimming speed than a lamprey-like anguilliform swimmer. Body form and kinematics were proven to have little effect on the 3D wake structure.

The numerical simulation of a mackerel-like swimmer also indicated that an attached leading-edge vortex (LEV) of the fishtail can dramatically alter the pressure distribution and thus, the force production of the caudal fin (Borazjani and Daghooghi, 2013). Besides, the finlets and caudal keels, unique features of tuna fish, have become the research focus in more recent numerical studies. High-fidelity simulations of a biologically realistic multiple-finlet model with reconstructed kinematics were conducted by Wang et al. (2020a) to examine the hydrodynamic performance and vortex dynamics. It was revealed that the interactions among finlets in pitch and heave motion reduce the total finlet drag force, and pitching motions of finlets decrease the overall power consumption. Another numerical study of a 3D yellowfin tuna-like model suggested that caudal keels would generate streamwise vortices which can enhance the thrust production of the caudal fin (Zhang et al., 2020b). This effect was found to be magnified with increased Reynolds number and Strouhal number.

2.1.3.2 Fluid-structure interaction studies

Foil and plate models

Flexible fish body and fin were simplified as two-dimensional compliant thin foils with uniform chordwise flexibility in many previous FSI numerical studies (Huang et al., 2007; Lin et al., 2019; Michelin and Llewellyn Smith, 2009; Wang and Tang, 2019; Zhang et al., 2017; Zhu et al., 2014a). A pitch or heave movement was imposed on the leading edge while the trailing edge was set free whose deformation is the result of the dynamic interaction of the structure and immersed fluid. For example, the influence of the bending stiffness of a flexible heaving fin was investigated by Michelin and Llewellyn Smith (2009). In their work, the flow was resolved based on potential flow theory and the structural motion was described using a 2D inextensible Euler-Bernoulli beam model. The flexibility was shown to enhance the propulsion efficiency as shown in many FSI studies. It was also revealed that maximum trailing-edge deformation is presented at certain rigidities at which a resonance between forcing frequency and the natural frequency of the structure system occurs. This resonance of frequencies resulted in maximum thrust and power input for flapping. Subsequent studies also reported that maximum free-swimming speed and swimming efficiency can be reached at specific bending stiffness and actuation frequency (Kim et al., 2016; Zhu et al., 2014b).

The stiffness distribution profile of the foil may also influence its propulsive capabilities. The propulsive thrust of a 2D filament at low Reynolds numbers was reported to be significantly enhanced by the variable flexibility distribution along the chordwise direction compared with a uniform stiffness profile (Peng et al., 2017). Nevertheless, this performance improvement is configuration-dependent: for a leading-edge clamped foil, increased flexibility towards the trailing edge enhances the thrust production, while decreased flexibility towards the tail-end is instead favorable. Propulsion performance enhancement due to the non-uniform flexibility of a filament was also reported by Liu et al. (2021).

In addition to the above two-dimensional simplified foil models, three-dimensional numerical flexible plate models were also utilized to mimic the motion and deformation of fish fins. For example, fully coupled FSI simulations of a 3D flapping plate with chordwise and spanwise flexibility were conducted to investigate the flapping motion (Zhu, 2007). This numerical model resolved the fluid dynamics using the boundary-element method and structural dynamics based on a nonlinear thin-plate model. Two fluid conditions were considered, i.e., a low-density fluid in which the deformation is primarily determined by the inertial of the foil, and a high-density fluid where the fluidic loading dominates the deformation. It was revealed that chordwise and spanwise stiffness distributions affect the thrust production and flapping energy requirement differently within the two different fluids.

Subsequent FSI studies of 3D flexible flapping plate models resolved N-S equations which took the fluid viscosity into account, which was excluded by Zhu (2007), for better accuracy.

The thrust performance of a flexible low-aspect-ratio pitching plate was examined using an FSI solver coupled by a viscous incompressible immersed-boundary-based flow solver and a nonlinear finite-element structural solver for thin-walled structures by Dai et al. (2012a). Their simulation results showed that wake transitions for the flexible plate are observed with a varied Strouhal number similar to that behind a 3D rigid plate. Specifically, the wake structure behind the flapping plate consists of a chain of interlocked horseshoe-shaped vortices at low Strouhal number (St < 0.28), while two rows of closed vortex rings with hairpin legs are presented at high Strouhal number beyond 0.28. This finding is consistent with a previous simulation result of a mackerel-like numerical swimmer (Borazjani and Sotiropoulos, 2008). Similar studies of the three-dimensional flexible flapping rectangular plate were reported in the literature (Hoover et al., 2018; Yeh and Alexeev, 2014, 2016b).

Given that the caudal fins of fishes vary in shape, the trailing-edge shape of the model was considered in few recent studies which do not limit to rectangle profiles in the above research. One example is the CFD-CSD coupled analysis of a biomimetic fin-and-joint system reported by Chung et al. (2018). The fin-joint models mimicked the caudal peduncle and fin of white bass and tuna fishtail, respectively, as presented in Fig. 2.11. A more detailed study of the trailing-edge shape of the bioinspired flapping fin was reported by Zhang et al. (2020a) and Li et al. (2021). Their simulations revealed complex variations of propulsive performance of the swimmer, such as free-swimming speed, thrust production, and efficiency, attributed to different trailing shapes, varied stiffness, and flapping frequencies, indicating complex interactions among these factors. Nevertheless, even though these models took the tail shape into account which presents more fish-like features, their stiffness profile is uniform and the deformation is mainly in the chordwise direction, distinct from a real fish fin deformation that dynamically changes chordwise and spanwise simultaneously.

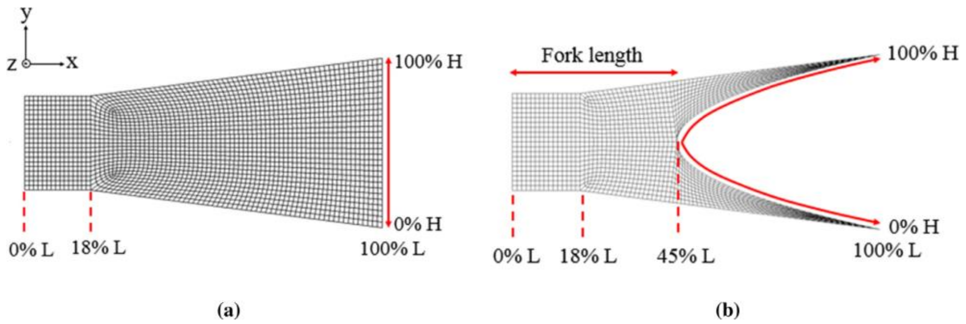

Fig. 2.11. Geometry and generated CFD mesh of the peduncle-fin system with a trapezoidal fin (a) and forked fin (b) (Chung et al., 2018).

Ray-strengthened fin models

Inspired by the ray and membrane structure of fish caudal fin, a skeleton-strengthened fin model depicted in Fig. 2.12 was developed by Zhu and Shoele (2008). The biomimetic fin rays, as shown in Fig. 2.12(c), were modeled as uniform Euler-Bernoulli beams with circular cross-sections that can sustain stretching, bending, and twisting loads in their work. The rest of the fin model was idealized as a membrane that can sustain stretching/compression but not bending by distributing spring-dampers between neighboring rays (Zhu and Shoele, 2008). In this way, their ray-strengthened fin model is closer to real fish fin geometry and structure compared with the above foil and plate model. This structural model was incorporated with a potential flow theory-based hydrodynamic model to yield an FSI numerical tool. Using the homocercal kinematics mode, their simulation results demonstrated that three-dimensional anisotropic deformability of the fin model leads to a significant enhancement of thrust generation compared to that with rigid rays.

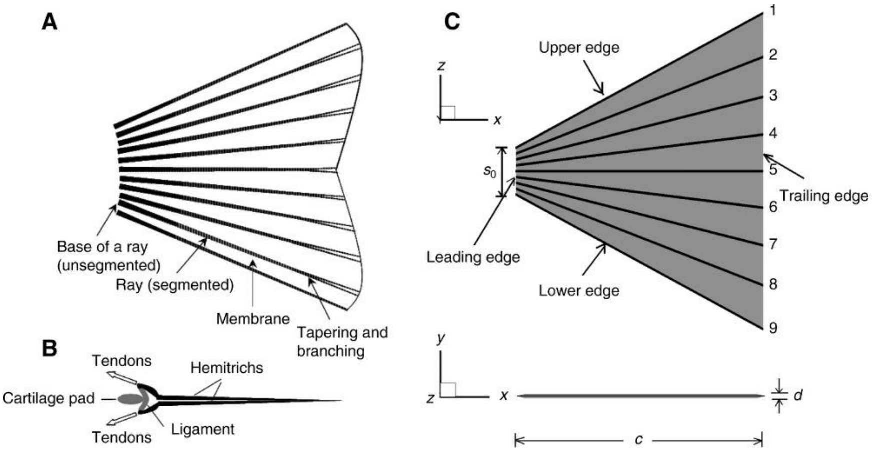

Fig. 2.12. schematic plot of a typical ray-strengthened caudal fin (a), the dorsal view of the internal structure of a ray (b), and the numerical model of the skeleton-strengthened fin (c) (Alben et al., 2007; Zhu and Shoele, 2008).

This skeleton-reinforced numerical fin model was then applied to the study of pectoral fins of bony fishes during labriform locomotion (Shoele and Zhu, 2009, 2010). It was revealed that the phase lag between neighboring rays is a primary factor in determining the propulsive performance of the fin through creating variations of the effective angle of attack at the leading edge and shape changes of the fin surface. Simulation results also indicated that strengthening the leading-edge ray is key to improving performance by reducing the effective angle of attack and power requirement during the recovery stroke (Shoele and Zhu, 2010). A subsequent paper by them focused on this effect of leading-edge strengthening by distributing variable stiffness of the rays of a two-dimensional fin model (Shoele and Zhu, 2012). By using a 2D immersed-boundary method, they found that a higher propulsion efficiency due to the leading-edge strengthening of rays was achieved by reducing the angle of attack at the leading and mitigating the leading-edge separation.

A more recent study of the effect of stiffness distributions of sunfish-like caudal fin rays on its spanwise deformation and propulsion capabilities was conducted by Zhu and Bi (2017). This work first showed that complex fin movements observed in fish swimming, such as cupping, heterocercal, and “W” shape, can be replicated by purely passive deformations attributed to non-uniform stiffness distributions. It was also found that this non-uniform flexibility profile may achieve an increase in propulsion efficiency and reduction in lateral force generation.

Recently, Shi et al. (2019) coupled this ray-strengthened structural model with a three-dimensional viscous Navier-Stoke fluid solver to develop a fully coupled FSI solver. Using this numerical FSI model, they investigated the propulsion performance of an actively and passively controlled skeleton-reinforced caudal fin (Shi et al., 2020). Significant improvement of fin’s performance by active control via added actuation force along the fin ray was reported when the mean phase lag between the sway motion and actuation force is below 90 deg. A recent paper also focused on its application to numerical research on a manta-ray-inspired medial pair fin (MPF) undulation locomotion (Shi and Xiao, 2021). However, their fin models were geometrically simplified as a rectangular plate composed of several flexural rays connected by linear springs. Thus, the deformation of their predicted flexible fin surface is not smooth, inconsistent with the smooth curvature fashion observed from real fish.

In summary, effective, accurate, and high-fidelity numerical FSI models that are capable of replicating the anisotropic material and complex three-dimensional deformations of fish fins are rare in the literature. The underlying numerical challenges include: firstly, the fluid solver must be able to allow for dynamic three-dimensional large-displacement deformations at the boundaries; secondly, the structural solver needs to model the nonlinear material behavior due to the non-uniform stiffness distributions of the swimmer; last but not least, the numerical instability during the coupling computation of fluid and structural solver attributed to the added-mass effect must be dealt with carefully. This thesis aims to develop an FSI solver which can cope with these numerical challenges.

2.2 Jet Propulsion

2.2.1 Biological studies of squid

Structure of squid

The main structure of the squid is shown in Fig. 2.13. They have a highly streamlined elongated body, large eyes, two tentacles, and eight arms. The mantle is the main structure of a squid. It is a conical, muscular envelope that surrounds the mantle cavity where the viscera are suspended (Ward and Wainwright, 1972). Squids are mostly soft-bodied, but they have a thin, non-calcified, chitinous skeleton element termed the pen in the dorsal mantle to serve as the supporting frame. The pen is rigid and mostly inextendible that can sustain the lateral bending to resist the length change of the mantle. Three small cartilaginous ridges are contained within the mantle around the collar. These ridges are employed to seal the mantle inhalant openings by locking onto the underlying cartilaginous grooves (Ward and Wainwright, 1972). A pair of fins are attached to the closed end of the mantle. Distinct from the fins of the above sunfish and tuna fish, the fins of the squid do not have a well-formed substantial fin ray base which means that they cannot withstand large hydrodynamic force, and in return would not produce much thrust. Therefore, squid fins mainly aid maneuvers and provide partial thrust in addition to jet propulsion at low and moderate swimming speed.

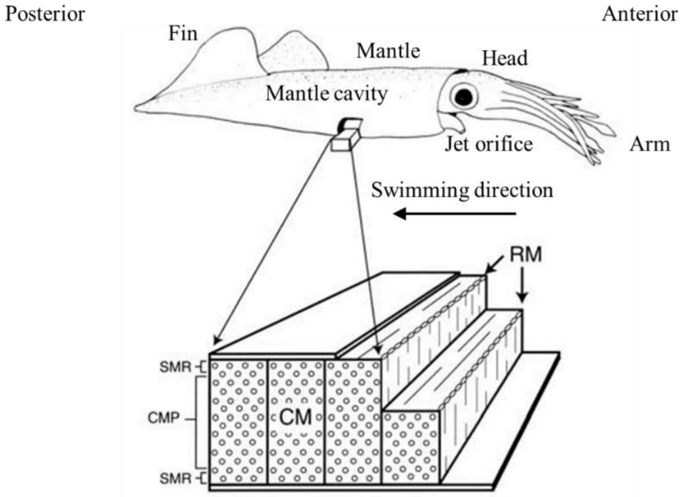

Fig. 2.13. Structure of a squid and diagram of the ventral portion of the mantle. CM, circular muscle fibers; RM, radial muscle fibers; CMP, central mitochondria-poor zone of circular muscle fibers; SMR, superficial mitochondria-rich zones of circular muscle fibers (Kier and Thompson, 2003).

Mechanically, the squid mantle can be viewed as a cylinder with a closed conical end posteriorly. The outer and inner surfaces of this cylinder are formed by tunics and suspended from one another by tensile connective fibers (Ward and Wainwright, 1972). Experiments indicated that the squid mantle contains two predominant muscle groups, i.e., circumferential muscle fibers or so-called circular muscles that constitute the bulk of the mantle wall, and radial muscles that extend from the inner to the outer surface of the mantle wall, as presented in Fig. 2.13 (Thompson and Kier, 2006). The circular muscle fibers can be differentiated into three zones: the outer zone near the external surface of the mantle, the inner zone near the inner surface of the mantle, and the middle zone between these two zones. The circular muscle fibers of the inner and outer zone of the mantle are termed superficial mitochondria-rich fibers (SMR), while the middle one is known as central mitochondria poor (CMP) fibers, as depicted in Fig. 2.13. These circular muscle fibers are divided into rectangular blocks by thin partitions of radial muscle fibers and electrically coupled to adjacent circular muscle fibers (Bone et al., 1981). These muscle fibers are not continuous around the mantle but only run a few millimeters. The circular and radial muscle fibers are both obliquely striated and uninucleate.

Kinematics of squid

As mentioned in section 2.1.1, bony fish fins like the sunfish fins are characterized by a soft collagenous membrane supported by embedded rays. Although multiple degrees of freedom motion can be achieved by these composite structures, they inevitably increase the complexity in the design and manufacture of bio-inspired underwater vehicles. In comparison, jet kinematics employed by squids and other cephalopods is more straightforward to duplicate. The jetting process starts with the inflation of the mantle, during which the internal volume of the cavity increases so that water fills the mantle cavity through the mantle aperture, as shown in Fig. 2.14. This inflation was termed an inhalant phase or recovery stroke by Ward (1972). Afterward, the squid contracts the mantle and the volume of the mantle cavity begins to decrease. Subsequently, water is ejected through the funnel tube as a fast jet during the exhalant or power stroke phase to propel the squid in the opposite direction.

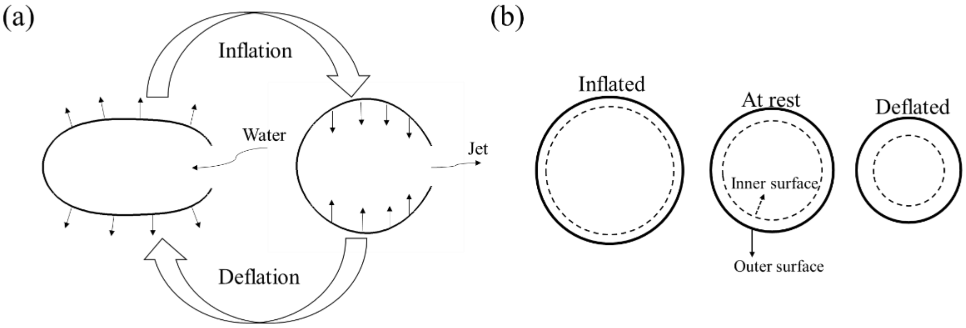

Fig. 2.14. Sketch of the deflation-inflation cycle (a), the crosssection change of a cylinder with an isovolumetric body wall (b) (modified from Kurth et al. (2014)).

These two activity patterns were reported in Gosline et al. (1983). According to electromyographic recordings, the hyperinflation of the mantle is powered by the radial muscles, the deflation is actuated by circular muscles, and the refilling is mainly powered by the radial muscles through the release of stored elastic energy in the structure. Through this propulsion mechanism, effective escape locomotion and high maneuverability can be achieved (O'Dor, 2013). Some small squids, e.g., the larvae of *Loligo vulgaris,* are capable of bursting as fast as 25 body lengths per second (Gosline and DeMont, 1985).

Packard (1969) reported that the mantle of freshly hatched squid does not change in length during jetting while the volume of the mantle and contained water is at least halved during the deflation phase based on measurement of live squids (*Loligo vulgaris*). He also found a reduction of 30% in body width from the inflated condition in adult squids during jetting in the air. More detailed kinematics data of squid jetting was provided by Ward (1972). It was revealed that only smooth and uniform changes in diameter (around 15% in moderate jetting) are presented in different parts of the mantle during inflation-deflation cycles and most of the changes in shape occur at the mid-ventral portion of the mantle. He suggested that the mantle cross-section may remain approximately circular through the cycle, as demonstrated in Fig. 2.14(b). Kinematics data of jet velocity, angle, and mantle cavity volume change during jetting of live squid was also reported by Anderson and DeMont (2000).

Since the volume of the mantle tissue and the length of the mantle remain essentially unchanged during the inflation-deflation process, the thickness must vary during jetting. This would lead to non-uniform circumferential strain across the mantle body, implying that fibers at the inner surface of the mantle (see Fig. 2.14(b)) must sustain greater circumferential strain than other zones (Kurth et al., 2014). Fibers near the inner surface of the mantle were found to be more folded than the others near the outer surface to accommodate this greater strain. It was also found that the extent, rate, and frequency of contraction of the circular muscles vary little with swimming speed (O'Dor, 1988). The roles of fins and aperture during squid jetting were investigated by Anderson and Demont (2005) and Staaf et al. (2014), respectively. A recent study also focused on the turning performance in squid in addition to the straight-line swimming commonly studied in the above work (Jastrebsky et al., 2016). Quantitative kinematic data of live squids including the length-specific radius of the turn, a measure of maneuverability, and angular velocity, a measure of agility, suggested squids are highly maneuverable and moderately agile compared with flexible fish of similar size by coordination between the jet and fins.

Hydrodynamics of squid

Based on the measured kinematics, body deformation, and mantle cavity volume of swimming squid (*Loligo pealei*) obtained by high-speed and high-resolution digital video, Anderson and DeMont (2000) evaluated the jet velocity, jet thrust, intramantle pressure, and propulsive efficiency with the unsteady effect being taken into account. The derived equation by them to calculate the efficiency showed a resemblance with the form of rocket motor propulsion efficiency. Similar quasi-steady and unsteady analyses of squid hydrodynamics based on observed kinematics data were reported by Anderson et al. (2001). Their findings offered new perspectives on the locomotory hydrodynamics of jetting process of squid and other jet propulsion based organisms, but the jet flow field information around squids was not provided.

Like the biological hydrodynamics studies of sunfish and tuna fish in section 2.1.1, DPIV techniques were also utilized to visualize the jet flow of squids. One pioneering application of DPIV to live squid swimming experiments was reported by Anderson and Grosenbaugh (2005). It was shown that squid jets were periodic, steady, and prolonged emissions of fluid with an elongated core of high speed (Anderson and Grosenbaugh, 2005). Continuous jets discharged from the squid were found to be unstable in the jet shear layer followed by the jet breakup into packets of vorticity. The squid jetting is accompanied by background swimming speed rather than still fluid, and the jetting speed is always greater than the swimming speed.

The wake structure and swimming hydrodynamics of squids through ontogeny were investigated in a subsequent work using DPIV techniques (Bartol et al., 2008). It was found that squid hatchings (paralarvae) that operate in low and intermediate Reynolds numbers primarily relied on a vertically directed, high-frequency, and low-velocity jet which mostly consisted of elongated vortex rings without clear pinch-off from the trailing tail component (Bartol et al., 2008). In comparison, the wake patterns of juvenile/adult squids that operate at high Reynolds numbers exhibited more diversities, and two principal jet modes were observed. In jet mode I during slow swimming, the ejected fluid rolled up into an isolated vortex ring with each jet pulse, as shown in Fig. 2.15(A). A leading vortex ring pinched off from a long trailing jet during each jet pulse was presented in jet mode II during fast swimming as depicted in Fig. 2.15(B). Two fin wake patterns were also observed during fast swimming of juvenile/adult squids. Their estimations about the propulsion efficiency suggested that jetting of paralarvae was much more efficient than that of juveniles/adults. The following work by them focused on the swimming hydrodynamics of squid paralarvae at intermediate Reynolds numbers (Bartol et al., 2009b) and juvenile/adult squid (Bartol et al., 2009a), respectively.

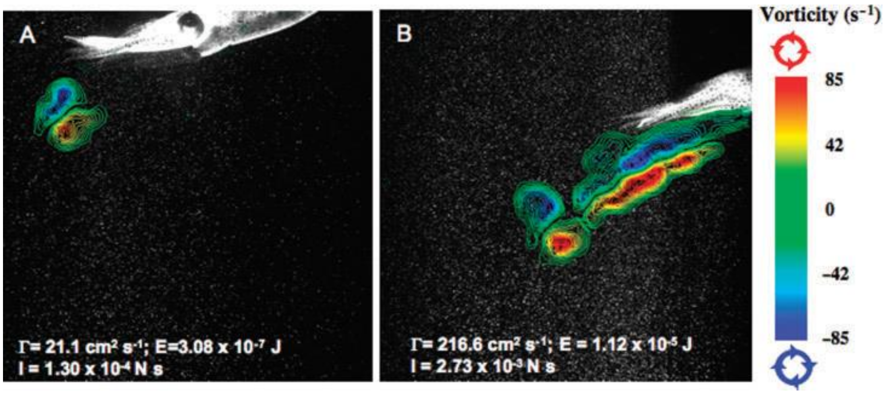

Fig. 2.15. Vorticity contours of the jet of a brief squid swimming at 6 cm/s (jet mode I) (A), and swimming at 10 cm/s (jet mode II) (B) (Bartol et al., 2008).

The aforementioned volumetric velocimetry technique, used in studies of the flow field around swimming sunfish and tuna fish, was also utilized to visualize the three-dimensional vortex ring structures behind the squid jet wake in recent papers (Bartol et al., 2016; York et al., 2020). For example, the flow structures during arms-first and tail-first swimming modes of brief squid were reported by Bartol et al. (2016), as shown in Fig. 2.16. They found that 3D vortex rings and their derivatives were dominant reoccurring features during the two modes despite the remarkable complexity in wakes of squid with multiple propulsor patterns simultaneously. 3D velocimetry techniques also revealed two escape jet patterns throughout the ontogeny of squids, i.e., “escape jet I” characterized by short rapid pulses resulting in the vortex ring formation, and “escape jet II” featured by long high-volume jets with leading-edge vortex ring (York et al., 2020).

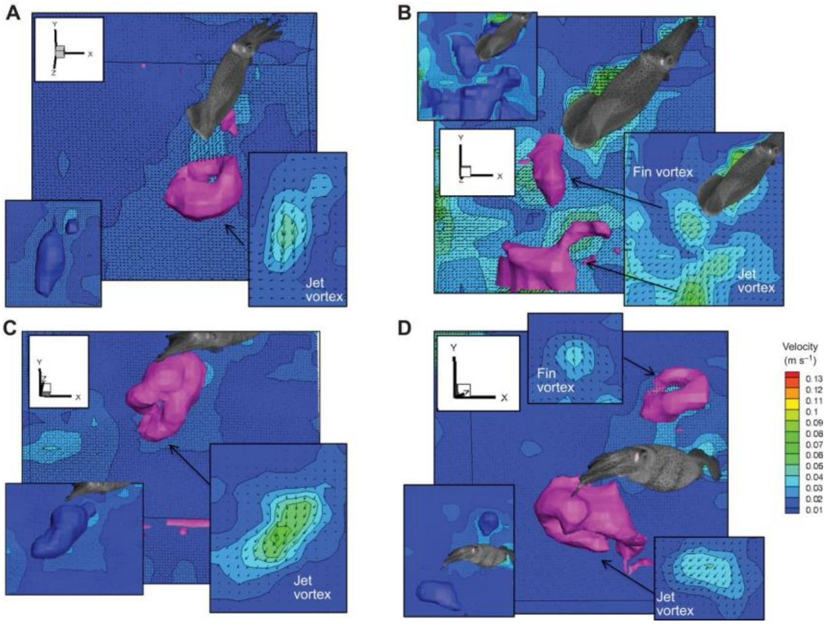

Fig. 2.16. The flow structures around brief squid swimming at low speeds (<1.5 dorsal mantle lengths per second) in the arms-first (A, B) and tail-first (C, D) orientations. Vorticity magnitude isosurfaces are pink, velocity magnitude isosurfaces are blue, and insets with arrows are velocity slices (Bartol et al., 2016).

2.2.2 Mechanism studies by robotic device

Jet flow containing vortex rings can be produced by piston/cylinder experimental setup in the laboratory environment in addition to discharging fluid from squid. Therefore, such piston/cylinder arrangement that focuses on vortex ring formation is also valuable in elucidating the underlying mechanism of jet propulsion. In this section, mechanism studies by less biologically relevant piston/cylinder arrangement, and by squid-inspired robotic devices are reviewed.

Piston/cylinder arrangement

One classical experimental work of using a piston/cylinder arrangement in a water tank to study vortex ring formation was conducted by Gharib et al. (1998). The velocity and vorticity fields of vortex rings using DPIV indicated that two flow patterns can be produced depending on the value of piston stroke to cylinder diameter (L/D) (stroke ratio), as shown in Fig. 2.17. Namely, the flow field generated by a small stroke ratio only shows a single vortex ring, while it consists of a leading vortex ring followed by a trailing edge at a large stroke ratio. These two patterns correspond to the two jet modes I and II observed from live squid, respectively (Bartol et al., 2009a). The transition between these two distinct states occurs at a stroke ratio around 4, which was termed “formation number” by them. The maximum circulation a vortex ring can attain is reached at this formation number. This may explain the observed jet mode II around squids in which continuous jetting consists of a leading vortex ring followed by trailing vortices during fast swimming.

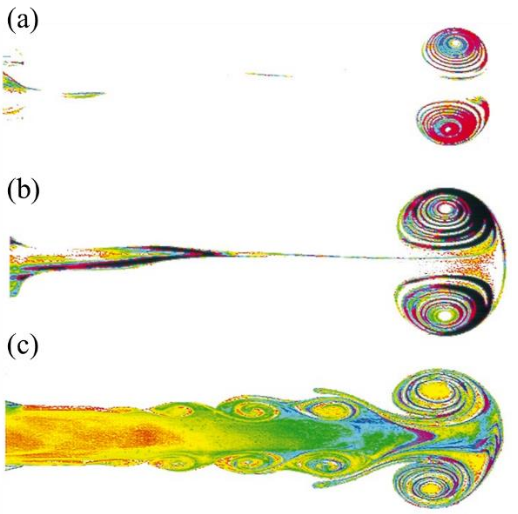

Fig. 2.17. Visualization of vortex rings and trailing vortices at maximum stroke ratio is 2 (a), 3.8 (b), and 14.56 (c) at formation time 8 (Gharib et al., 1998).

The discovery of the formation number, a universal time scale for vortex ring formation, suggested a possible maximization principle at starting jet for jet propulsion. To test this hypothesis and examine the relative contribution of the vortex ring and trailing jet for thrust production, Krueger and Gharib (2003) used a piston-cylinder mechanism to generate jets with stroke ratios ranging from 2 to 8. It was revealed that vortex ring formation contributes more thrust per unit L/D than a trailing jet, implying that vortex ring pinch-off represents an optimization principle in terms of thrust production. This is attributed to that over-pressure at the nozzle exit supplies additional impulse during vortex ring formation.

The jets emitted from a cylindrical piston in the presence of background flow were utilized by Anderson and Grosenbaugh (2005) to mimic the swimming squid jetting. The jet flow from a piston with background flow was found to develop differently compared with that ejected into still water. And under the scenarios with background flow, flow velocity may be more important than the stoke ratio to predict jet structure whose produced thrust and circulation are reduced compared to still water, assuming jet velocity to be the same. Eight different jet velocity programs of a piston jetting device were considered in a subsequent study reported by Querzoli et al. (2010). A criterion to calculate the time when the vortex ring is no longer influenced by the orifice flow was proposed based on the experimental measurements. This time, reached when the averaged ejection speed reaches the maximum, can be easily and univocally determined from the velocity profile. In addition, the piston-cylinder mechanism was also utilized to study the impulse and kinematic energy of jets with non-zero radial velocity (Krieg and Mohseni, 2013), vortex ring formation at low Reynolds numbers (Palacios-Morales and Zenit, 2013), and unsteady jet with flexible flaps at the channel exit (Das et al., 2018). Nevertheless, it is unclear whether these fundamental mechanism studies can apply to squid-like jet propulsion, which may need more experimental and biological validations.

Squid-like robotics

A squid-inspired underwater robot named “Robosquid” was developed by Moslemi and Krueger (2010) to investigate the effect of the jet velocity program and duty cycle on the propulsion performance of pulsed jet. They reported higher propulsive efficiency of the trapezoidal jet velocity profile than the triangular velocity pattern. It was also found that pulsed jets outperform steady jets at low jet slug length-to-diameter ratios and high duty cycles in terms of propulsion efficiency. Experimental tests based on Robosquid were also conducted to examine the effect of Reynolds number (Moslemi and Krueger, 2011) and robot configuration on propulsive capabilities (Nichols and Krueger, 2012). The considered Reynolds number based on average vehicle speed and diameter ranged from 37 and 60. It was found that pulsed-jet propulsion was efficient for millimeter-scale propulsion system under this low Re compared with large Re (1300~2700) as the ratio of pulsed-jet to steady jet efficiency increased with smaller Re. Tests based on Robosquid also revealed that sharp-edged orifices could increase vehicle swimming speed and propulsion efficiency compared to smooth nozzles due to stronger vortex rings produced by the former (Nichols and Krueger, 2012). A recent paper reported the development of a squid-like aquatic-aerial robot with soft morphing fins and arms (Hou et al., 2019). The novel soft pneumatic morphing design enabled it to shuttle between water and air.

Although the above bio-inspired robots utilize jetting propulsion, the jets are produced by pneumatic or piston actuation rather than inflation-deflation of the body, a key feature of squid jetting. Some squid-inspired soft robotic devices considered body deformation to produce pulsed jets. For example, a squid-like robot prototype composed of the soft mantle, outflow orifice, and ingestion valve was developed by Serchi et al. (2012), as presented in Fig. 2.18. It is the first soft robot that combines the concept of soft robotics with principles of vortex-enhanced pulsed jet propulsion. Experimental tests on this prototype suggested that propulsive performance heavily relies on the elastic response of the shell to the actuation cycle. Learning from these preliminary results, they then updated this squid-like robot in subsequent studies (Giorgio-Serchi et al., 2016; Renda et al., 2015a; Renda et al., 2015b). Besides, a coupled propulsion-elastodynamics model that combined structural dynamics and thrust production formula was derived for this biomimetic robot. This model was validated against experimental results performed with the robot prototype. A more recent work based on this squid-like soft robot suggested that fluid momentum loss in the deflected nozzle was the most significant factor influencing its turning performance (Wang et al., 2019a). In general, experimental tests of this squid-inspired robot prototype mainly provided insights into structural behavior during the inflation-deflation of used soft material, while jet hydrodynamics was not the main focus.

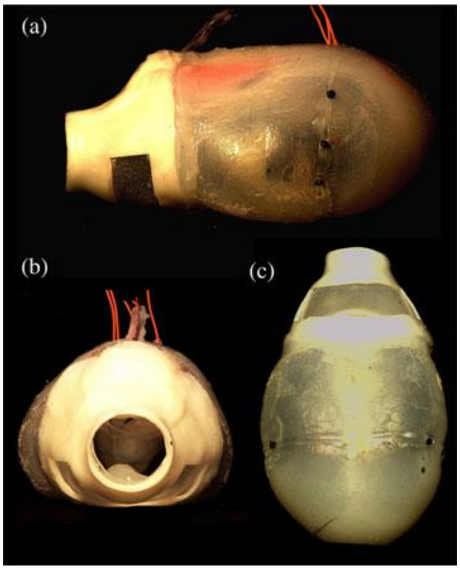

Fig. 2.18. Squid-inspired prototype with a soft mantle, orifice, and ingestion valve: side view (a), front view (b), and ventral view (c) (Serchi et al., 2012).

Using a simple squid-inspired flexible hull robot, as shown in Fig. 2.19(a), Weymouth et al. (2015) demonstrated that rapid-size change can recover fluid energy that can be utilized to improve jet propulsion performance. They also proposed a fundamental deflation scaling parameter to characterize the flow control mechanism by shape change based on the experimental data. A similar robotic device as depicted in Fig. 2.19(b) was utilized to study the effect of energy recovery in the fast jet escape maneuvers of squids by Steele et al. (2017). Their results highlighted the role of the shrinking speed and Reynolds number in determining the success of energy recovery during jetting. Nevertheless, the two simplified squid-like models can only perform one deflation cycle, making it impossible to study continuous inflation-deflation jets.

More recent robotic jet propulsors inspired by squids and other cephalopods were reported in Christianson et al. (2020) (see Fig. 2.19(c)) and Bujard et al. (2021) (see Fig. 2.19(d)). Repeatable jet propulsion was achieved by changing the internal volume and cross-sectional area to take advantage of jet flow and added mass effect (Christianson et al., 2020). It was also revealed that the resonance effect of a coupled mass-spring-mass oscillator based squid-like robot can significantly improve the pulsed jet swimming speed and efficiency (Bujard et al., 2021). This robot also showed a preferred Strouhal number for efficient swimming, which bridged the gap between jet propulsion and existing findings in efficient fish swimming.

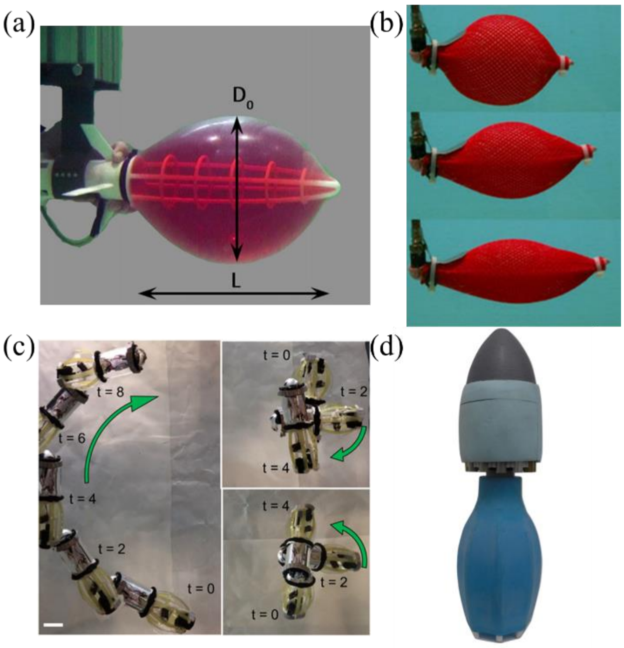

Fig. 2.19. A squid-like robot filled with pressurized water dyed in red (a) (Weymouth et al., 2015), a shape-changing body in Steele et al. (2017) (b), a cephalopod-inspired robot in turning maneuver developed by Bi and Zhu (2020) (c), and a flexible bio-inspired resonant robot prototype with blue membrane mounted (d) (Bujard et al., 2021).

2.2.3 Numerical studies

In the past decades, thrust production and hydrodynamic propulsion efficiency were analyzed based on two different numerical models. One is the vortex ring model that assumes the wake shed from the jet propulsor as a vortex street with a symmetrical group of vortices (Siekmann, 1963; Weihs, 1977). Each of these vortices pairs consists of two vortices with equal strength and opposite rotation direction. During the periodic thrust intervals, it is supposed that the exhaust has a uniform mean velocity over the cross-section of the discharge nozzle (Siekmann, 1963). This vortex ring model predicted that a larger average thrust can be generated compared to a continuous jet with an equivalent mass flux rate, on the condition that the jetting is sufficiently frequent so that the distance between ring centerlines is smaller than three ring radii (Weihs, 1977). The assumption of symmetrical vortices arrangement behind the nozzle showed similarity to the observed flow pattern I (Fig. 2.15(A)) behind swimming adult squids to some extent (Bartol et al., 2008).

In comparison, the prolonged jet model was more frequently applied to analyze the hydrodynamics of squid jet propulsion (Anderson and Demont, 2005; Anderson and DeMont, 2000; Johnson et al., 1972; Packard, 1969). Within this model, the squid jet is assumed as an elongated mass of fluid with high speed. The jets around real squids are then marked by a three-dimensional shear layer, through which the velocity of the fluid varies continuously from the jet core to surrounding fluids (Anderson and Grosenbaugh, 2005). The momentum theorem is usually applied to calculate thrust velocity based on the fluid velocity inside the swimming squids. The intramantle pressure is evaluated by solving the unsteady form of the Bernoulli equation without the large-reservoir approximation. Nevertheless, the exact form of the Bernoulli equation is dependent on whether the flow is laminar or turbulent (Anderson and Grosenbaugh, 2005). Besides, the effect of the acceleration of the fluid inside the mantle cavity is excluded, which may cause inaccuracy.

On the other hand, studies on the hydrodynamics of vortex ring formation which holds an inherent correlation to jet propulsion also provided insights into the propulsive performance of squids (Gharib et al., 1998; Linden and Turner, 2001; Mohseni and Gharib, 1998; Rosenfeld et al., 1998). For example, the existence of formation number proposed by Gharib et al. (1998) was confirmed by analytical modeling based on the slug model in Mohseni and Gharib (1998) and numerical simulations through the resolution of the axisymmetric compressible Navier-Stokes equations (Mohseni et al., 2001). The universality of the formation number was further confirmed by a numerical study reported by Rosenfeld et al. (1998). Beyond that, their numerical studies extended the experimental study (Gharib et al., 1998) to examine the effects of non-impulsive velocity profiles, different vortex generator configurations, and Reynolds number.

Furthermore, Linden and Turner (2001) performed a theoretical analysis to elucidate the underlying physics of the observed formation number. They compared the circulation, impulse, volume, and kinetic energy of the jet plug with the counterparts of a finite-core vortex ring. Their results showed that a single vortex ring cannot retain these properties after the critical equivalent stroke ratio is reached. Besides, they suggested the limiting vortex is "optimal" in achieving maximum impulse for given energy input, equivalent to the highest propulsive efficiency. However, experimental measurement of swimming squids suggested that adult squids do use continuous long jets with $L/D >> 4$, corresponding to the jet mode II as shown in Fig. 2.15(B), suggesting that live squids may not necessarily employ the "optimal" vortex ring formation to enhance efficiency.

In addition to the above analytical modeling and simplified numerical studies, computational fluid dynamics is also an effective tool to simulate the jet propulsion associated with vortex ring dynamics. For example, the vortex ring formation and the thrust production of a 2D axisymmetrical piston/cylinder arrangement in the presence of background flow were numerically studied using commercial software FLUENT by Jiang and Grosenbaugh (2006). Different vortex evolutions were presented with varied combinations of the ratio of background flow speed to the mean piston velocity, and stroke ratio of the piston in their work. It was found that the vortex structure would never pinch off from the trailing edge even at a large stroke ratio under the high-speed background flow condition due to the strong interaction between the vorticity layer of the jet and the opposite-signed vorticity layer from the initial wake (Jiang and Grosenbaugh, 2006). Comparison between the thrust production by long and continuous jets and short pulses with the same mass flux suggested that the former yielded larger thrust. Although their model considered the effect of existing background flow on vortex dynamics and jet hydrodynamics, consistent with the real squids jetting conditions (Anderson and Grosenbaugh, 2005), it was two-dimensional and based on a rigid body, distinct from cephalopod locomotion involving body deformation. Thus, the relevance to the actual aquatic jet swimmers is not clear.

Similar numerical studies of piston/cylinder vortex generators to examine the vortex ring dynamics and jet propulsion by solving N-S equations can be found in subsequent papers (Abdel-Raouf et al., 2017; Danaila et al., 2009; Gao et al., 2020; Olcay and Krueger, 2010; Zhang et al., 2020c). It was found that the jet velocity program and associated stroke ratio play significant roles in determining the added mass momentum (Olcay and Krueger, 2010). Simulations by Abdel-Raouf et al. (2017) also showed that increased pulsation frequency results in the propulsion efficiency of a fixed piston propulsor, and the sinusoidal pulsed inflow jets are more efficient than the unit pulsed jets. Recent simulations investigated the advantages of using vortex ring thrust as a novel propulsion device (Zhang et al., 2020c) and revealed the possibility to maximize the pressure impulse to enhance overall impulse production by augmenting the over-pressure effect and mitigating the negative-pressure effect (Gao et al., 2020). However, like the aforementioned paper by Jiang and Grosenbaugh (2006), these studies used a simplified two-dimensional rigid piston model as the vortex generator, distinct from the body-deformation induced jet generation process of squids. Besides, the fluid field evolution within the mantle body during jetting was mostly ignored which may lead to inaccuracy when calculating the thrust production.

Body shape change was considered in a handful of numerical studies to elucidate the underlying mechanism of jet propulsion. A simple shape-changing body was demonstrated to be able to hover or ascend in an oscillating background flow by Spagnolie and Shelley (2009), and the achieved velocity burst was thought to be related to the escape dynamics of aquatic invertebrates. Subsequent studies revealed the significance of added-mass energy recovery in the bursting motion of shape-changing bodies (Steele et al., 2017; Weymouth and Triantafyllou, 2013). It was illustrated that considerable thrust augmentation, almost comparable to the jet-generated thrust, can be obtained from the recovery of added-mass energy as the body deflates. Nevertheless, successful energy recovery depends highly on the body's shrinking speed and Reynolds number. In these studies, the body kinematics were prescribed, and the interaction between the flexible body and surrounding fluid was not considered. Additionally, the internal cavity flow was excluded.

Following these studies, a series of numerical simulations have been conducted by Bi and Zhu (2018, 2019a, 2019b, 2020) to understand the combined effect of jetting and body deformation. By using a three-dimensional boundary-element method, they investigated the burst-coast swimming of a cephalopod-like deformable body with a pressure chamber, as shown in Fig. 2.20(a). They focused on a single bursting cycle and found the optimal speed coincides with the critical stroke ratio. However, their numerical model was based on the potential-flow theory, where the viscosity effect was not included so that the accuracy of the results was compromised.

A two-dimensional fluid-structure interaction model based on the immersed-boundary framework was developed subsequently to study the fully-viscous response of the squid-like jet propulsion system activated by a sequence of springs, as shown in Fig. 2.20(b), in tethered (Bi and Zhu, 2019b) and free-swimming (Bi and Zhu, 2019a) modes under low Reynolds number conditions. Symmetry-breaking instability of the jet wake was found after continuous jet. It was revealed that added-mass-related force contributes significantly to thrust production. Three wake patterns were observed, nozzle-vortex dominated wake, transit wake, and asymmetrical wake during the acceleration, steady-state swimming, and off-track swimming phase, respectively (Bi and Zhu, 2019a). These FSI models were limited to laminar flow while real squids, especially adult squids, can operate at turbulent flow conditions. On the other hand, the inflation of their model was the result of the release of elastic energy of virtually linear springs rather than that of the mantle structure like a real squid.

A subsequent study in which the mantle deformation was prescribed to examine the effect of jet velocity profiles highlighted the role of jet acceleration and viscous dissipation during the vortex ring evolution (Bi and Zhu, 2020). Nevertheless, this study was characterized by an axisymmetric model. Moreover, like many other studies (e.g., (Advaith et al., 2017; Krueger et al., 2008; Nguyen et al., 2019)), this axisymmetric study was conducted in a still fluid environment, a scenario different from real squid locomotion in steady swimming (Anderson and Grosenbaugh, 2005).

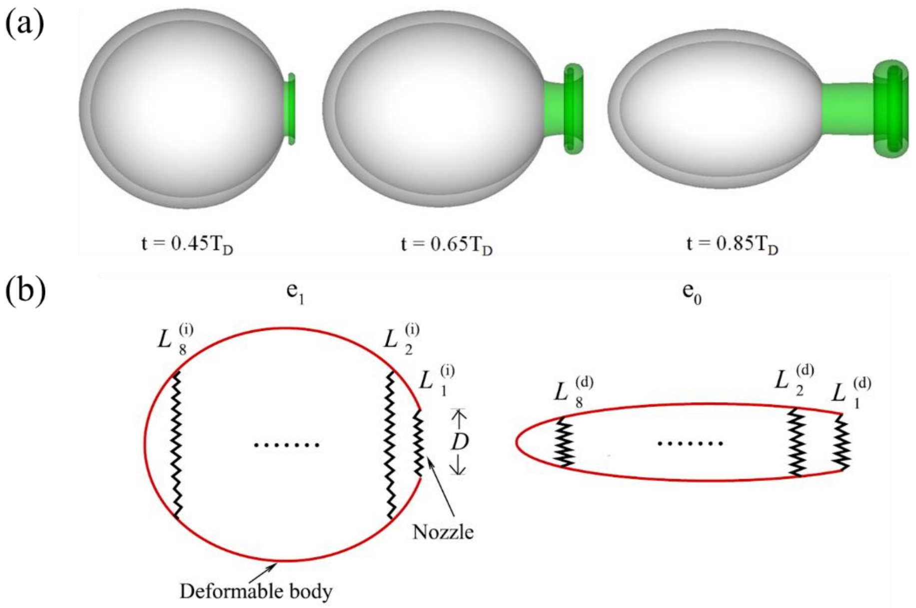

Fig. 2.20. Evolution of the wake elements during the deflation of a 3D squid-like swimmer (a) (Bi and Zhu, 2018), reference states during inflation (e_1) and deflation (e_0) phases with eight springs inside the mantle (Bi and Zhu, 2019a).

It can be found that most of the existing numerical studies of squid-inspired jet propulsion focus on laminar flow conditions. The real adult squids operate in turbulent flows which may affect the propulsion performance and vortices evolution differently from the laminar flow. Besides, there is no high-fidelity three-dimensional numerical model of jet propulsion that considers the body deformation and viscous effect in the literature. Therefore, this thesis aims at studying jet propulsion in turbulent flows by considering FSI between the deformable body and surrounding fluid. A high-fidelity 3D jet numerical model will be also proposed according to the real deformation patterns of squids. And based on this 3D model, some key factors such as background flow, jet velocity, and body deformation extent, affecting the jet propulsion and vortex ring dynamics will be studied systematically.

2.3 Fish Swimming in Altered Fluid Conditions, and Motion Control on Fish Locomotion Using PID Control

2.3.1 Fish swimming in altered fluid conditions

Most of our current understandings of fish locomotion are based on the studies conducted in still water or steady flow conditions. However, the majority of fishes commonly experience and operate in altered flows (Liao, 2007). The change from still or steady flows to altered flows can be caused by nearby external structure, e.g., accompanied cruising ship and static rocks in a river, or biologically mutual interaction of swimming fishes, e.g., fish schooling.

The present literature review is limited to the former scenario to explore the fish swimming change in response to environmental stimuli.

Biological studies of fish swimming in altered fluid

Early research of fish swimming behaviors in the altered fluid was mostly conducted in field studies (Fausch, 1993; Heggenes, 1988, 2002; McLaughlin and Noakes, 1998; Scholander, 1959; Shuler et al., 1994). Dolphins are often seen to surf in the wave created by cruising boats and ships, which is called bow-riding. It was suggested that dolphins can take advantage of the wave force to swim forward by proper body posture in the bow wave (Yuen, 1961). Fishes are also found to select locations in rivers to hold the position. For example, steelhead parr favors structures with the overhead cover more often than those without overhead cover for habitat selection (Fausch, 1993). They also tend to select structures adjacent to the swiftest fluid velocities available and closest to other natural overhead covers. A similar preference of swimming location was observed in brown trout fishes. Shuler et al. (1994) found that brown trout choose feeding sites primarily based on water velocity and cover, and boulder structures might provide the most energetically favorable locations for them. Besides, the current-velocity refuge was able to reduce the swimming cost of brook trout fish by 10% on average without affecting the frequency of foraging attempts made, as demonstrated in a field test by McLaughlin and Noakes (1998). Habitat selection behaviors of trout fishes were also reported in Heggenes (1988) and Heggenes (2002).

In addition to the above field studies, laboratory studies, in which the fluid conditions are subject to elaborated control, have also been conducted to explore fish swimming in altered flows. For example, the entrainment behavior of river chub and smallmouth bass on cylinders was investigated in a water tank by Webb (1998). It was found that fishes favor entraining on the cylinders at higher current speeds. The temperature of the fluid also affected the entrainment of the tested fishes. The turbulence of the surrounding flow was reported to increase the energetic cost of fish swimming (Enders et al., 2003; Lupandin, 2005; Smith et al., 2005).

Nevertheless, some unsteady flows, e.g., vortex flows, excluding the above turbulent flows, may be taken advantage of by fishes to reduce their swimming energy cost by tuning their kinematics according to the incoming flow. One classical experimental study of rainbow trout in vortex street behind a bow cylinder in a uniform flow by Liao et al. (2003) demonstrated the active adaption of swimming kinematics to altered flows. They compared the axial swimming kinematics in three different fluid conditions, i.e., in the free stream, in the bow wake, and behind the D-shaped cylinder, as shown in Fig. 2.21. It was revealed that trout fish behind the cylinders adopted a novel and distinctive pattern of movement to hold the station in the vortex street. During this gait, termed Kármán gait by them, body undulation amplitudes and curvatures were much larger than those fishes swimming at an equivalent flow velocity in the absence of a nearby cylinder. The tail-beat frequency was found to match the vortex shedding frequency of the cylinder. This suggested that trout fishes do not only seek refuge from the main current to take advantage of regions of reduced flow velocity behind a bluff body (“flow refuging”), demonstrated in the above studies (McLaughlin and Noakes, 1998; Shuler et al., 1994), they can also tune their body kinematics to synchronize with the incoming vortices to capture energy from these vortices by the environment. This behavior was remarkable when the cylinder diameter was large compared to fish length (Liao et al., 2003). Interestingly, when trout fish was placed in the bow wake, they tended to stay there and would return immediately to the front rather than behind the cylinder if displaced. Low tail-beat frequency, body wave speed and posterior body curvature during staying in the bow wake suggested this may be the most energy-saving region of all the three flow conditions in Fig. 2.21(A).

A subsequent electromyographic study of trout fish swimming behind a cylinder revealed that vortices determine the overall head motion using Kármán gait (Liao, 2004). The passive mechanism of thrust production by Kármán gait was supported by measurements of axial muscle activity. Following this study, Beal et al. (2006) found that even a dead fish can be propelled upstream when placed in the wake of a bluff cylinder, for which the energy harvest is purely passive due to the resonance oscillation of its flexible body under the action of incoming vortices.

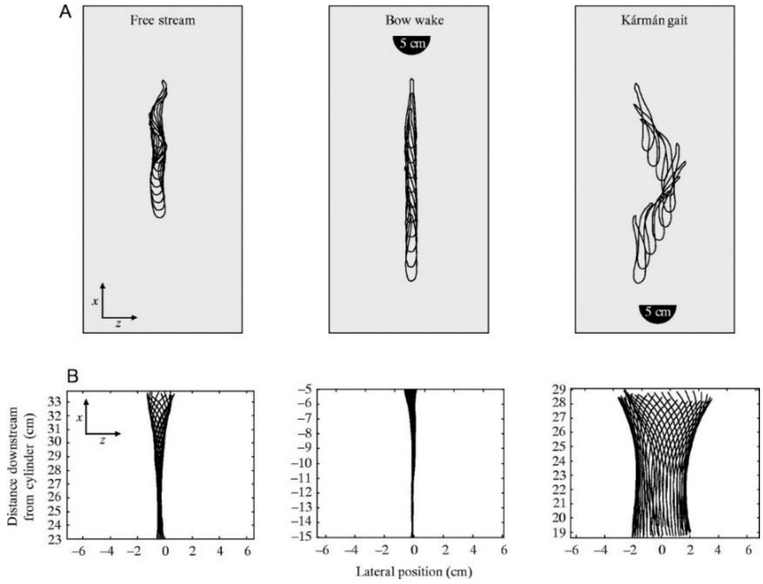

Fig. 2.21. The superimposed body outlines (A) and body midlines (B) of a trout fish swimming in the free stream (left), bow wake (middle), and behind a 5 cm D-cylinder (right) (Liao et al., 2003). The flow direction is along the positive *x*-axis direction.

Several following experimental studies have been conducted to further investigate the fish swimming behavior involving Kármán gait (Akanyeti and Liao, 2013a, b; Liao, 2006; Liao and Akanyeti, 2017; Stewart et al., 2016; Taguchi and Liao, 2011). It was found that the lateral line plays a more significant role in affecting the body kinematics during station-holding of trout fish than the vision ability that may determine the preference to associate with a turbulent vortex street (Liao, 2006). Measurements of consumption of oxygen when rainbow trout holds the station at different locations near a cylinder by Taguchi and Liao (2011) suggested fish entraining consumed the least energy at the swimming speed of 3.5 body length per second, followed by Kármán gait, bow waking, and free stream swimming. However, bow waking required the least oxygen when speed increased to 5.0 body length per second. Another study proposed a kinematics model of Kármán gait based on measurements of live fish holding station behind the cylinder (Akanyeti and Liao, 2013b). This kinematic model consists of four motion components including body bending, lateral translation, body rotation, and head motion. Comparison of actual and modeled midlines supported the accuracy of this model, which provided the kinematic basis for the robotic design and numerical simulation to study swimming behavior duing Kármán gait in vortex street.

Numerical studies of fish swimming in altered fluid

Most of the existing numerical studies of fish swimming in altered fluid took cylinder-generated vortices as background flow conditions. This may be explained by three reasons. Firstly, vortex flow behind the cylinder is unsteady with certain predictability but not necessarily turbulent, making the fluid variations more controllable so that examination of the effect of an isolated factor is possible (Liao, 2007). Secondly, there have been many previous experimental findings of fish swimming near cylinders in the literature, which facilitates the comparison of numerical results with them. Last but not least, flow conditions around the cylinder include regions of reduced flow velocity (ahead of the cylinder) and vortex street (behind the cylinder) so that the mechanisms of flow refuging and vortex capturing behaviors of fishes observed in the natural environment can be well replicated in a numerical setup.

For example, inspired by the above experimental studies of live fish, some numerical simulations were conducted in an attempt to elucidate the underlying hydrodynamic mechanism when fish swims near a rigid body, e.g., a cylinder. It started with the simplification that the swimmer kinematics was prescribed mathematically in many studies (Bao and Tao, 2013; Li et al., 2017a; Shao et al., 2010; Wu et al., 2014; Xiao et al., 2012b). The fish body was usually simplified as a 2D fishlike undulating foil behind a D-shaped or circular cylinder in a uniform flow. Depending on the distance from the cylinder, the wake areas can be divided into three domains: suction zone, thrust enhancing zone, and weak influence domain. The undulating foil significantly enlarges the suction zone compared to a case without a foil or a stationery foil case (Shao et al., 2010). The thrust generation of the foil is affected by the location (distance) relative to the upstream cylinder, undulation frequency, phase angle, and heaving motion. Foil thrust production can be maximized at a certain optimal distance relative to the cylinder at the given foil kinematics mode (Xiao et al., 2011). Meanwhile, the cylinder drag reduces due to the presence of the downstream undulating foil, suggesting a passive drag reduction mechanism. The effect of cylinder size was investigated by Xiao et al. (2012b) and Wu et al. (2014). It was revealed that drag force is reduced when an undulating plate is placed upstream of the cylinder compared to the case of a plate behind the cylinder. A more recent numerical study reported effective application of deep learning techniques to training a self-propelled anguilliform swimmer to adapt its motion to optimally achieve specific tasks near a cylinder (Zhu et al., 2021). This work demonstrated the possibility of combining deep learning with an immersed boundary-lattice Boltzmann method to investigate the hydrodynamics of fish swimming in both uniform flow and Kármán vortex street.

Nevertheless, the effect of structural flexibility and resultant dynamic interaction between the flexible deformation and the surrounding flow is excluded in the above studies, distinct from real biological scenarios where the fish body and fins are characterized as flexible structures. A few studies considered the fluid-structure interaction when the swimmer is swimming in the altered flow. For example, by assuming the fish body as a flexible filament, Tian et al. (2011) studied the hydrodynamic force and the deformation pattern of the filament in the Kármán gait region and the entrainment region termed by Liao et al. (2003). It was found that the presence of the flexible filament in the entrainment region tends to stabilize the flow around the cylinder, while the cylinder may destabilize the entraining filament instead. The drag force of a filament with a lower mass ratio and a longer length is reduced in the entraining region. In comparison, a lower mass ratio and short length result in decreased drag force of the filament in the Kármán gait region. In their modeling, the filament was fixed in the location and the deformation was purely passive without active acuation, distinct from the real fish free-swimming involving active tuning.

A subsequent study reported the swimming behavior of a self-propelled flexible fin in the wake of a circular cylinder (Park et al., 2016), as shown in Fig. 2.22(a). The leading edge of the flexible fin was prescribed to heave transversely while the trailing edge lateral amplitude was determined by the hydrodynamic interaction between the fin and the fluid. In a uniform flow, the heaving fin was not able to overcome the drag and always drifted downstream. Nevertheless, three behaviors were presented when it was placed behind the cylinder:

propulsion upstream, drift downstream and holding the station at an equilibrium position. The heaving frequency of the fin was observed to equal the vortex shedding frequency during position-holding, accompanied by a slaloming behavior between the incoming vortices. Besides, the equilibrium position was determined by the initial longitudinal position in the cylinder wake and the phase of the fin heaving motion regarding the phase of vortex shedding (Park et al., 2016). Energy expenditure to drive the heave motion was reduced during the slaloming behavior. A similar phenomenon was reported in a following study (Wang et al., 2019b), in which two tandem cylinders were considered to yield a more complex hydrodynamic environment, as demonstrated in Fig. 2.22(b). Two releasing styles of the flexible plate were considered: the plate heaves at its initial position before the flow comes (style I), and it starts to flap after the vortex shedding is fully developed (style II). It was revealed that the plate tends to hold stationary in style I despite that more energy is consumed.

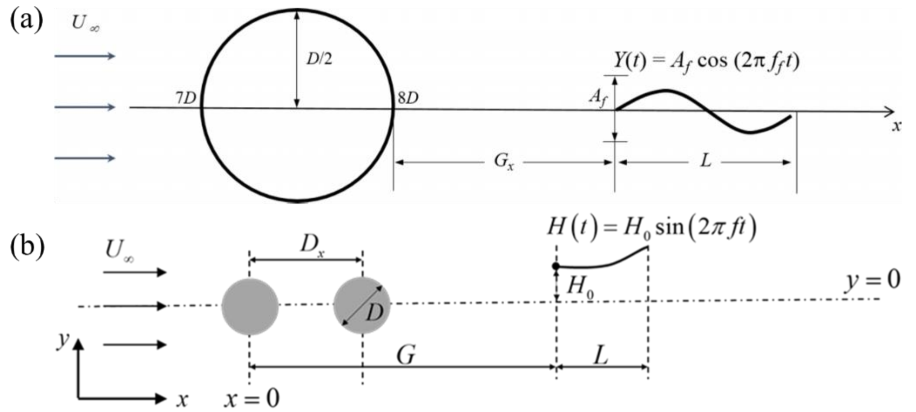

Fig. 2.22. Schematic diagram of a self-propelled flexible plate behind a cylinder (a) (Park et al., 2016), and two tandem cylinders (b) (Wang et al., 2019b).

Nevertheless, fishes were found to favor holding the station in the bow wake (Liao et al., 2003). Most of the existing research concentrated on the swimming behind the cylinder, few on the behavior in front of the cylinder. It is thus necessary to study the latter scenario which would help to elucidate the mechanism of station-holding or the so-called “flow refuging” behavior. One such example is an FSI simulation of the interaction between a flexible filament and a downstream rigid cylinder by Tian et al. (2010). It was found that the drag forces of the filament and the cylinder largely depend on the distance between them and the Reynolds number. The filament and the cylinder can both obtain drag reduction regardless of the change of the length and mass ratio of the filament under the parameters considered. This model was fixed at a location without self-propulsion, thus it is unclear how the interaction would influence free-swimming behavior. Carling et al. (1998) suggested that the force calculated in this tethered mode could differ remarkably from the force developed by a freely swimming model. Although their work demonstrated that drag reduction is possible as the fluid immediately upstream of a bluff body is being “pushed”, the deformation of the filament was purely passive, distinct to the fish swimming where both active actuation and passive deformation are involved to achieve the objectives of swimming forward or holding station.

In general, numerical studies that consider the FSI between the swimmer and surrounding altered flow are rare in the literature. It would be interesting to investigate how the flexible swimmer would respond to and interact with complex altered flows compared with uniform flows, and how this interaction could affect the free-swimming performance and energy expenditure.

2.3.2 Motion control on fish locomotion

Motion control on swimming locomotion is extensively considered in bio-inspired robotics, but mainly from the engineering application perspective. In practice, a mapping among environment state, current state, targets, and actions is required to specify the robot to execute specific tasks. Speed control and orientation control are two main respects in the locomotion of an underwater biomimetic robot. Proportional-integral-derivative (PID) control as a classical feedback control method, is commonly used in bio-inspired underwater robot studies to establish the mapping and achieve control objectives of speed and/or orientation (Coral et al., 2018; Kopman et al., 2014; Salumäe et al., 2017; Yu et al., 2004; Zhao et al., 2006). PID control aims at eliminating the error (tracking error) between the measured target and the desired target by applying correction based on proportional, integral, and derivative terms (Zhu, 2020). P term is proportional to the current value of tracking error, I term is proportional to the time integral of the tracking error, and D terms serve to estimate the future trend of the tracking error by calculating its time derivative. Despite that PID control is based on linear theory or approximate measurement, its effectiveness has been proved in previous studies. For example, high precision of the muscles’ position control of a bass-inspired robot fish was achieved with minor overshoots in water and air utilizing a simple PID controller by Coral et al. (2018). Even in a more complex fluid condition, such as Kármán vortex street, the application of the PID control method coupled with artificial lateral line sensing to flapping foil was effective (Free and Paley, 2018).

Within the implementation of motion control of bio-inspired robots, simplified analytical models are commonly used to evaluate the thrust production and drag force of the swimmers (Boyer et al., 2008; Porez et al., 2014; Shen et al., 2013; Wen et al., 2011; Yen et al., 2018). For example, an analytical model based on the large-amplitude elongated-body theory was developed by Wen et al. (2011) to evaluate the body thrust production of a mackerel-like swimmer under the inviscid conditions. The simplified dynamic model of the swimmer was then coupled with a PID controller and their results of speed control showed good convergence to the targets. These analytical modeling methods compromise the accuracy and cannot provide much flow information during fish swimming but are practical in engineering applications for online control.

Few studies of motion control of fish swimming based on numerical methods which resolve Navier-Stokes equations were reported. For example, a feedback PID controller was used to tune the oscillation amplitude of a fish-like NACA0012 airfoil to achieve self-propulsion when the average net drag of the foil is zero and maintain the heading of the fish by adjusting the camber by Maertens et al. (2017), enabling the calculation of quasi-propulsive efficiency. The control results were then taken as input for the gait optimization to find the minimum swimming power expenditure at a given speed and Reynolds number. It was demonstrated that swimming efficiency can be significantly improved by adding a deformation based on measured displacement for carangiform swimming. The energy savings of a pair of interacting swimmers attributed to vortices interactions were also reported. This PID controller was extended to control the motion of the fish body and tail by Gao and Triantafyllou (2018). Two controllers were implemented to adjust the thrust to zero by tuning the oscillation amplitude, and steer the fish to swim in a straight line by adjusting the tail pitch bias, respectively. Their results reported a significant improvement of swimming efficiency for a fish swimming in the wake of an upstream fish by using independent pitch control of its caudal fin compared with the cases without such independent control. The propulsive performance was found to be sensitive to small variations of tail movement, suggesting the importance of accurate flow sensing and feedback control (Gao and Triantafyllou, 2018).

Very few studies of motion control of fish swimming consider complex fluid-structure interaction of the swimmer and immersed fluid due to the significant challenge to establish this FSI modeling coupling with a feedback controller. A recent study reported the effective implementation of a feedback PID controller to manipulate a soft swimmer to follow specific target trajectories (Hess et al., 2020). The considered robotic fish was modeled as a 2D swimming flexible beam with a finite thickness, with contractive strains being imposed on two sides periodically, as shown in Fig. 2.23 (a) and (b). The undulation of the swimmer was tuned by changing the amplitude and frequency of the active strain to produce thrust. And turning motions were achieved by asymmetrical strain on the two sides of the beam. Besides, the relative angle between the swimmer and target and their distance were both taken into account to calculate the tracking error within the control scheme, as depicted in Fig. 2.23(c). Their fluid-structure interaction simulation results indicted that effective and accurate trajectory control to follow a moving target can be achieved using far fewer control parameters. However, similar studies are still very rare in the literature.

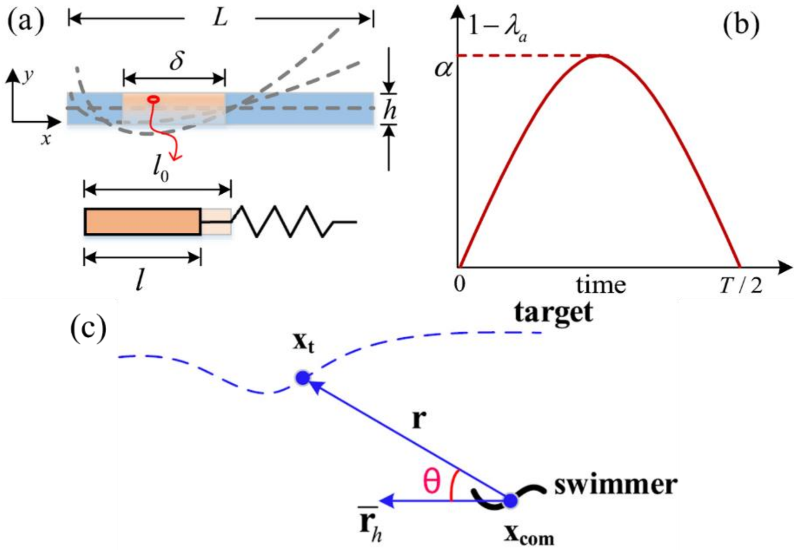

Fig. 2.23. The 2D beam under contractile actuation. The active segment length is δ (a). Contractile actuation is applied alternatively on the two sides of the beam, which exponentially decays in the y-direction (b). Demonstration of the control scheme based on the translational and rotational motion of a soft swimmer concerning the target x_t (c) (Hess et al., 2020).

It can be found that most of the studies on fish motion control focused on static or uniform flows. The classic control method, the PID method, has been proved to be effective in these flow conditions. It would be interesting to apply it to altered flow conditions to explore the effectiveness of motion control on a flexible self-propelled swimmer by combining it with an FSI solver. In this way, the energy consumption of swimming in altered flows can be evaluated to compare the energy savings during the “flow-refuging” of fish.

2.4. Summary of numerical techniques for biomimetics studies

As aforementioned, aquatic propulsion involves fluid dynamics, structural dynamics, and the dynamic interplay between these two. Therefore, it is a multi-physics problem. For example, the fish body and/or fin are featured as composite structures with anisotropic materials. The interaction of the body and fin with immersed fluid involves shear layer separation and vortex shedding which are directly related to fluid viscosity. However, it is challenging to resolve these fluid and structural features in a single numerical model. Therefore, researchers have to make some assumptions and simplifications within the fluid and structural modeling of real fish fin and jet propulsion. Recently, few high-fidelity fluid-structure interaction numerical models were reported which will be briefly summarized in this section. It is noted some work may have been mentioned in the above review, but they may be included in this section from the viewpoint of numerical techniques.

2.4.1. Fluid dynamics

In this subsection, the inviscid and viscous flow models used to study hydrodynamics around swimming fishes in the past decades are reviewed.

Potential flow modeling

In the potential flow theory, the flow around the swimmer is assumed as inviscid, incompressible, and irrotational. The velocity potential $\Phi(\boldsymbol{x},t)$, a function of space and time, can be decomposed into two parts, $\Phi_b(\boldsymbol{x},t)$ and $\Phi_w(\boldsymbol{x},t)$, where $\Phi_b(\boldsymbol{x},t)$ is related to body motion and $\Phi_w(\boldsymbol{x},t)$ is caused by wake vorticity, each satisfying Laplace's equation. On the surface of the swimmer, the non-flux conditions are imposed, and the Kutta condition is usually enforced at the trailing edge. The velocity distribution is obtained from the velocity potential, and from which the pressure distribution is calculated by resolving Bernoulli's equations. The computational cost of the potential flow model is inexpensive. Thus, it can usually provide rapid evaluation of fluidic force around the swimmer. Many previous fluid solvers in biomimetic studies are based on the potential flow model (Kagemoto et al., 2000; Shoele and Zhu, 2009; Wolfgang et al., 1999; Zhu, 2007; Zhu and Bi, 2017; Zhu et al., 2002). However, the inviscid flow models may bring in inaccuracy when simulating fish swimming where shear layer separations and complex vortices evaluations due to the viscous effect dominate the surrounding flows (Shi et al., 2019).

Viscous flow modeling

The flow around the swimmers considering the viscous effect is governed by unsteady 3D Navier-Stokes equations. With the inclusion of fluid viscosity, the turbulence effect should be considered in the numerical modeling. Direct Numerical Simulation (DNS) directly solves the Navier-Stokes equations without modeling assumption, and thus, it requires to solve a substantial range of temporal and spatial scales of turbulence, making it enormously computationally expensive. Various turbulence models are then proposed to reduce the computational cost but meanwhile obtain reliable solutions, such as solving Reynolds-averaged Navier–Stokes equations (RANS) and performing large-eddy simulation (LES). Compared with RANS, LES requires more computational cost as it still directly resolve the largest and most energy-containing scales of turbulence, while the former only models all the eddies without resolving them. Therefore, RANS is more popular in biomimetic simulations for its relatively less computational cost and acceptable accuracy (Li et al., 2017b; Yang and Su, 2011). It is noted that for most of the flow conditions considered here with the Reynolds number below or in the order of 10^3, the turbulence effect may play an insignificant role in the flow field, which was proved from some previous studies (Bozkurttas et al., 2009; Buchholz and Smits, 2006). Thus, laminar flow is accepted for these biomimetics studies in this thesis (see examples in Dong et al. (2010) and Liu et al. (2017)).

Biomimetic propulsion involves complex 3D body and/or fin deformations, and thus, it is required for the flow solver to handle the dynamic change of structural boundaries. The body-fitted grid method and fixed and non-body-conformal Cartesian grid method are two widely used techniques to accommodate the unsteady boundary shape. The body-fitted grid method can be implemented based on a structured (Nakata and Liu, 2012; Shi et al., 2019) and an unstructured grid (Chung et al., 2018; Li et al., 2017b). The body-fitted grid method is usually implemented using the arbitrary Lagrangian-Eulerian (ALE) formulation to handle the moving boundaries by mapping the deformations of the interface to the interior meshes. With this body-fitted grid method, it is straightforward to impose boundary conditions at the interface and refine the local fish to resolve the boundary layer. Nevertheless, it is not suitable for arbitrarily large deformations without remeshing the grid which would increase the computational expense (Gatzhammer, 2014).

In comparison, flow solvers based on the fixed and non-body-conformal grids, especially the immersed-boundary method (IBM), provide an attractive alternative. IBM resolves the Navier-Stokes equations on a stationary Cartesian grid without the need to contend with the body motion or deformation. The non-slip boundary conditions on the body surface are enforced by the modification in the form of source terms (or forcing functions) in the governing equations to reproduce the effect of a boundary in the IBM (Tu et al., 2018). Attributed to the advantages of simple grid generation and strong grid deformation adaptability, IBM based fluid solvers are widely used in biomimetic simulations (Borazjani and Sotiropoulos, 2008; Huang et al., 2007; Liu et al., 2015; Mittal et al., 2006; Shoele and Zhu, 2012). Nevertheless, an extremely fine grid around the body surface is needed to resolve the flow field within the boundary layer for high Reynolds number simulation, increasing the computational cost significantly for an IBM-based solver.

2.4.2. Structural dynamics

The inclusion of structural flexibility of fish body and/or fin is a significant improvement compared with simplified numerical studies with prescribed kinematics. It involves structural dynamics solutions during the interaction between the swimmer and the immersed fluid. In this regard, two most popular structural models are implemented in an FSI solver, i.e., the lumped-torsional flexibility and solid continuum models. Within the lumped-torsional flexibility model, the flexibility is assumed to be localized which leads to the dynamics dictated using an ordinary differential equation (Arora et al., 2018), such as a rotational momentum equation (Xiao et al., 2014). It has been applied to the studies of fish swimming

(Eldredge, 2008; Li et al., 2018; Wilson and Eldredge, 2011; Zhao et al., 2020) and flapping wings (Toomey and Eldredge, 2008; Vanella et al., 2009; Xiao et al., 2014; Zhang et al., 2010). This simplified structural model can only yield low-order flexibility and cannot model complex composite structures like real fish bodies and fins.

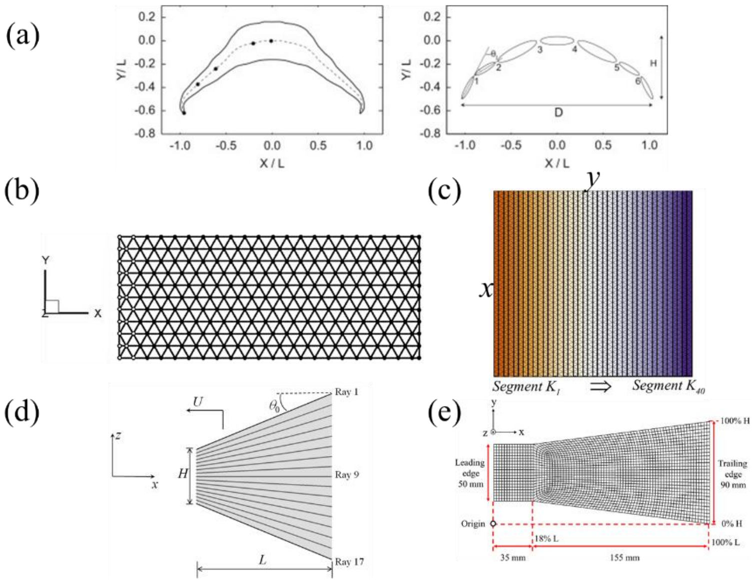

Fig. 2.24. A simplified jellyfish model and articulated system of linked rigid bodies and numbering system used for hinges (a lumped-torsional flexibility model) (Wilson and Eldredge, 2011) (a), a swimmer modeled as a triangular lattice within LSM (Yeh and Alexeev, 2016b) (b), the generated meshes for the thin-plate model (Wang et al., 2020b) (c), idealized model of a ray-supported caudal fin (Zhu and Bi, 2017) (d), the FEM model of a fin-and-joint system (Chung et al., 2018) (e).

The solid continuum models consider the fish body and fin to be entirely flexible along their length and thus can model more detailed material behaviors. Among them, the lattice spring model (LSM), beam or thin-plate model, and finite-element method are the most popular in biomimetic studies (see examples in Fig. 2.24). In the LSM, the flapping fin or wing is assumed as a continuous elastic plate which is usually discretized into a network of masses connected by harmonic springs arranged on a regular lattice (Yeh and Alexeev, 2016a). The solid mass nodes withstand forces from the springs and the fluidic force at the interface, and the deformation is then evaluated by integrating Newton's equations of motion at each mass node using the velocity Verlet algorithm (Yeh and Alexeev, 2014). The LSM was employed to model the thin flapping wings and fins in previous studies (Masoud and Alexeev, 2010; Yeh and Alexeev, 2014, 2016b; Yeh et al., 2019).

Since the thickness of the flapping fin and wing is small compared to other dimensions, they are usually modeled as a thin beam or plate in structural dynamics. Thus, their deformations are computed by directly resolving the unsteady Euler–Bernoulli beam equation (Dewey et al., 2013; Michelin and Llewellyn Smith, 2009; Olivier and Dumas, 2016; Paraz et al., 2016) or thin-plate equation (Fu et al., 2018; Wang et al., 2020b; Zhang et al., 2020a; Zhu, 2007). Inspired by the webs-like fin structure supported by bony spines of real fishes, Zhu and Shoele (2008) proposed a numerical skeleton-strengthened fin model in which the supporting rays are depicted as nonlinear Euler–Bernoulli beams and the deformations of the membrane between the neighboring rays is modeled by linear springs, as shown in Fig. 2.24(d).

FEM-based structural solvers have broader adaptability to model complex geometries and irregular shapes, such as the composite structure of fishes, and thus can provide high-fidelity structural solutions including deformations, stress distributions, etc. Applications of FEM to flapping wings (Luo et al., 2010; Nakata and Liu, 2012; Shahzad et al., 2018; Tian et al., 2014) and fish swimming (Chung et al., 2018; Hoover et al., 2017; Lin et al., 2019; Liu et al., 2019) have been reported in the literature.

2.4.3. Fluid-structure coupling

There are two fundamentally different classes of procedures to solve FSI numerical simulations, i.e., monolithic and partitioned approaches. The monolithic method establishes and deals with one single global system of equations containing the flow variables, structural variables, and the coupling between the two. In comparison, in the partitioned fashion, separate systems of governing equations of the fluid and structure are established, and the coupling is resolved externally. Most of the FSI solvers in biomimetics simulations are based on a partitioned coupling fashion as they can take advantage of existing simulation tools that are highly specialized to the specific single-field physical solution without the need to establish a new numerical tool using the monolithic approach. Thus, it is the focus of this summary. The partitioned coupling scheme can be categorized into two types, i.e., explicit (or weak) coupling and implicit (or strong) coupling.

Explicit coupling

Under the implementation of the explicit coupling fashion, the information at the interface between the fluid and structure only exchanges once within one iterative time step. Due to its simplicity of implementation, it was employed within many FSI solvers (Chung et al., 2018; Nakata and Liu, 2012; Shi et al., 2019; Wang et al., 2020b; Yeh and Alexeev, 2016a). Among the explicit coupling, the so-called conventional serial staggered (CSS) procedure is one of the widely used in FSI simulations. Within a CSS method, the fluid and structural solvers execute in an inter-field sequential way. While the fluid solver uses the structural solution at the last timestep n, the structural solver uses the updated solution of the fluid solver at the current timestep n+1 in an implicit fashion (Gatzhammer, 2014). It was shown that the CSS method has a first-order temporal accuracy, regardless of the temporal accuracy of the used fluid and structural solvers (Piperno et al., 1995). Because there is no additional treatment for the guarantee of dynamic equilibrium or energy balance between the common boundaries of the fluids and structures, the explicit coupling may become numerically unstable when dealing with strongly coupled FSI problems (Causin et al., 2005).

Implicit coupling

Within the implicit coupling scheme, the FSI simulations are performed in an iterative process, usually involving the repeated solution of partitioned flow and structural dynamics in one timestep, in an attempt to obtain solutions close to that of a monolithic system without numerical instability. Schwarz procedure and Newton-Raphson scheme are two popular implicit coupling methods in FSI simulations (Gatzhammer, 2014). Within the Schwarz procedure, the partitioned system of the fluid and structural governing equations is directly used to establish a fixed-point iteration. The residuals of the fluid and structural solution between iterations are used as a convergence criterion of the fixed-point iteration. Also, post-processing techniques are needed to stabilize the coupling iterations. One of the most straightforward methods is to use a constant under-relaxation in iterations and it has been implemented in some FSI solvers (Luo et al., 2010; Tian, 2014; Tian et al., 2014). Nevertheless, the constant under-relaxation method may lead to unmanageable computational cost for poor convergence behavior (Fernández, 2011; Gatzhammer, 2014). The Aitken relaxation technique was then used to accelerate the convergence by dynamically changing the relaxation factor, which has been applied in few biomimetic studies (Li et al., 2019; Liu et al., 2019; Radtke et al., 2018).

In comparison, the Newton-Raphson scheme tried to find the root of the defined residual equations of the fluid and structural solution. The residual equations can be solved with Newton-Raphson iterations where the key is to obtain the derivative information in the Jacobi matrices (Matthies and Steindorf, 2003). Nevertheless, we may not have direct access to calculate the Jacobian, and thus it can be approximated using reduced-order models, termed the quasi-Newton method. Vierendeels et al. (2007) proposed an interface block quasi-Newton method with least-squares approximation (IBQN-LS) for two black-box solvers. This method uses reduced-order models of the fluid and structural problems built up during the coupling iterations in the timestep or from previous timesteps to approximate the interface Jacobians directly. Subsequently, Degroote et al. (2009) developed another interface-quasi-Newton coupling technique based on the IBQN-LS, called interface quasi-Newton with inverse Jacobian from a least-squares model (IQN-ILS). The key difference between these two is that the IQN-ILS algorithm aims to approximate the inverse of the Jacobian that appears in the Newton linearization rather than the Jacobian itself. A comparison of the IQN-

ILS method with other popular implicit coupling algorithms was reported in Degroote et al. (2010). A 2D flexible beam and 3D flexible tube were considered to compare their performance. It was found that the IQN-ILS and IBQN-LS methods performed the best in both cases, followed by Interface-GMRES and trailed by Aitken acceleration in terms of the number of solver evaluations per timestep and relative duration for the simulation. Nevertheless, few FSI solvers in biomimetic simulations have taken advantages of these advanced interface quasi-Newton (IQN) methods for efficient coupling.

2.5. Summary of the literature review

In this chapter, a broad literature review has been made to revisit the previous studies of caudal fin locomotion, jet propulsion, fish swimming in altered flow conditions, and locomotion control of fish swimming by PID control. The numerical techniques including fluid dynamics, structural dynamics, and the FSI coupling used in biomimetic simulations have also been summarized. From the critical review of these previous research relevant to this thesis, the following gaps in the literature have been identified.

1. The majority of existing studies of underwater bio-inspired propulsion are experiments based on live fish or robotic devices. In comparison, numerical studies, especially high-fidelity numerical modeling, have received relatively less attention.

2. In the past numerical studies, the complex three-dimensional fish body and fin movements were mathematically pre-defined by reconstructing the kinematics observed/recorded from the live fish experiment. Therefore, only the hydrodynamic response to the designated structure deformation was examined, whereas the effect of resultant fluid forces on the flexible fins was neglected.

3. Most of the existing numerical FSI models are based on a simplified Euler-Bernoulli beam or thin plate model, which is not able to resolve fish-like structures which involve complex material behaviors along with large displacement and complex deformation. Also, the applications of some advanced coupling schemes, e.g., IQN-ILS, to biomimetic simulations for numerical stability and efficient computation are still rare in the literature.

4. Fish bodies and tails are featured as composite structures with non-uniform stiffness distributions. Very few studies consider the effect of chordwise and spanwise flexibility profiles of the fish body and tail on the propulsive performance. Thus, some observed complex body and tail comformations from live fishes cannot be well replicated or explained by these studies of a rectangular flexible plate with uniform stiffness patterns.

5. Most of the existing numerical studies of jet propulsion focused on the laminar fluid conditions, which only cover the flows that squid hatchlings operate. The jet vortices evolution and propulsion performance at high Reynolds numbers remain poorly understood.

6. Previous numerical models of squid-like jet propulsion are mostly limited to the two-dimensional rigid bodies in the still fluid environment. Three-dimensional jet swimmer models involving body deflation to produce jets in the presence of background flow as real squids do are needed.

7. Very limited research considered dynamically changing the swimming gait or actuation scheme in the altered flow, as real fishes do. A real fish can constantly and actively tune its body and/or fish oscillation in response to environmental hydrodynamic stimuli for acceleration/deceleration to swim towards a specific target, as well as holding a position in an unsteady fluid environment. And high-fidelity FSI model coupled with feedback control capable of simulating real fish swimming is very rare in the literature.

Therefore, the main chapters of this thesis aim at filling the gaps listed above using computational models of caudal fin propulsor and squid-like jet propulsor that consider the main features of their biological prototypes.

Chapter 3 Mathematical Formulations, Numerical Methods, and Validations

As aforementioned, a high-fidelity FSI solver that is capable of resolving complicated fish structures characterized by nonlinear materials along with three-dimensional complex deformation is rare in the literature. This motivates the present thesis to develop such an FSI solver by coupling the existing in-house fluid solver and open-source finite element method-based structural solver. Both of them are capable of individual single-field simulation, and thus, a partitioned coupling scheme is used to preserve their advanced features. The coupling of these two solvers by adapting the fluid solver is one of the main contributions of this thesis, which contributes to the advanced numerical toolkit to study bio-inspired propulsion involving fluid-structure interaction in the literature.

In this chapter, the mathematical models and numerical schemes of the fluid and structural dynamics are presented. Specifically, the fluid and structural governing equations and numerical techniques are described in Section 3.1 and 3.2 respectively. The coupling between the fluid and structural solver is introduced in Section 3.3. Section 3.4 provides the validations of the FSI solver via the coupling of the fluid and structural solvers. The fluid and structural domains are represented by Ω_f with the boundary Γ_f and Ω_s with Γ_s, respectively. The fluid-structure interface $\Gamma_i = \Gamma_f \cap \Gamma_s$ between the fluids and structures is the common boundary of the two domains. The information at the interface is exchanged between the fluid and the structural solver.

3.1 Fluid Dynamics

It is noted that the present study is based on an in-house compressible flow solver. There are two reasons here to use this compressible flow solver to study incompressible flows involving bio-inspired propulsion under certain conditions. Firstly, we have plenty of experience in using this flow solver and it has been proved to be accurate enough to simulate various incompressible flows. Secondly, the present flow solver is quite handy to use and allows us to tailor it to modeling specific problems proposed in this thesis.

3.1.1 Governing equations

The in-house fluid solver resolves viscous compressible flow using a cell-centered finite volume method based on a multi-block grid system. The flow is governed by the laws of the conservation of mass and momentum. The fluid body forces such as gravity are not considered in the present work, and then the governing equations can be expressed in the integral form as

$$\frac{\partial}{\partial t}\iiint_{\Omega_f} \mathbf{W} d\Omega_f + \oiint_{\Gamma_f} \left(\mathbf{F}_c - \mathbf{F}_d\right) \bullet \mathbf{n} d\Gamma_f = 0, \tag{3.1}$$

where **n** is the unit normal vector in the outward direction. The conservative variable vector **W** in Eq.(3.1) is defined as

$$\mathbf{W} = \left\{\rho, \rho u, \rho v, \rho w, \rho E_f\right\}^T, \tag{3.2}$$

where ρ is the density of the fluid, u, v, w represent the three velocity components in the Cartesian coordinates system and E_f denotes the total energy of the flow, given by

$$E_f = e_f + \frac{1}{2}\left(u^2 + v^2 + w^2\right), \tag{3.3}$$

where e_f is the internal energy. The tensor $\mathbf{F}_c$ in Eq.(3.1) is the convective flux which is given by

$$\mathbf{F}_c = \begin{bmatrix} \rho u_r & \rho v_r & \rho w_r \\ \rho u u_r + p & \rho u v_r & \rho u w_r \\ \rho v u_r & \rho v v_r + p & \rho v w_r \\ \rho w u_r & \rho w v_r & \rho w w_r + p \\ \rho E_f u_r + p u & \rho E_f v_r + p v & \rho E_f w_r + p w \end{bmatrix}, \tag{3.4}$$

where p is the pressure. To allow for the movement and deformation of the domain boundary, the ALE formulation is the most commonly used to handle the flow equations on a deformable mesh. It is achieved here by defining fluxes relative to the motion of the surfaces of the control volume, which are expressed by the relative velocity u_r, v_r, and w_r given as

$$\begin{aligned} u_r &= u - u_g \\ v_r &= v - v_g \\ w_r &= w - w_g, \end{aligned} \tag{3.5}$$

where the flow velocity $\{u,v,w\}^T$ and the grid velocity $\left\{u_g,v_g,w_g\right\}^T$ are described in a stationary Cartesian coordinate system.

The diffusion flux arising from the viscous shear stresses is denoted by $\mathbf{F}_d$ and can be formulated as

$$\mathbf{F}_d = \begin{bmatrix} 0 & 0 & 0 \\ \tau_{xx} & \tau_{xy} & \tau_{xz} \\ \tau_{yx} & \tau_{yy} & \tau_{yz} \\ \tau_{zx} & \tau_{zy} & \tau_{zz} \\ u\tau_{xx} + v\tau_{xy} + w\tau_{xz} - q_x & u\tau_{yx} + v\tau_{yy} + w\tau_{yz} - q_y & u\tau_{zx} + v\tau_{zy} + w\tau_{zz} - q_z \end{bmatrix}, \quad (3.6)$$

where, for a Newton-Fourier fluid considered here, the shear stresses $\tau_{\alpha\beta}$ are defined as

$$\tau_{\alpha\beta} = \mu\left[\left\{\frac{\partial u_\alpha}{\partial x_\beta} + \frac{\partial u_\beta}{\partial x_\alpha}\right\} - \frac{2}{3}(\nabla \bullet \mathbf{u})\delta_{\alpha\beta}\right], \text{ with } \alpha, \beta \in (x, y, z), \quad (3.7)$$

where μ is the dynamic viscosity, **u** denotes velocity vector and $\delta_{\alpha\beta}$ is the Kronecker function. The heat fluxes $\boldsymbol{q}$ are defined as

$$\boldsymbol{q} = -\kappa \nabla T_t, \quad (3.8)$$

where κ is the thermal conductivity and T_t represents the temperature.

As aforementioned, this fluid solver resolves compressible fluid. For a perfect gas considered here, the pressure in the computational domain can be evaluated following the relations

$$l = c_v T,\ R_f = c_p - c_v,\ \gamma_h = \frac{c_p}{c_v}, \quad (3.9)$$

and ideal gas law

$$\frac{p}{\rho} = R_f T, \quad (3.10)$$

then we have

$$p = (\gamma_h - 1)\rho\left[E_f - \frac{1}{2}\left(u^2 + v^2 + w^2\right)\right], \quad (3.11)$$

where l is the internal energy, c_p and c_v are the specific heats at constant pressure and volume, respectively, γ_h is the ratio of specific heats, and R_f is the gas constant. The force and moment from the calculation of the above pressure are normalized using the fluid density, the fluid speed, and considered characteristic length. In such a way, the dimensionless results of this compressible solver can be compared with that of an incompressible solver when studying incompressible flow problems.

The coefficient of laminar viscosity is obtained by Sutherland's formula (Sadeghi, 2004):

$$\frac{\mu}{\mu_0} = \left(\frac{T_t}{T_{t0}} \right)^{1.5} \frac{T_{t0} + 110.3K}{T_t + 110.3K}, \tag{3.12}$$

where μ_0 and T_{t0} are reference viscosity and temperature respectively.

The speed of sound for a perfect gas is given by

$$a_s = \sqrt{\frac{\gamma_h p}{\rho}}, \tag{3.13}$$

and the Mach number is then defined as

$$Ma = \frac{\sqrt{u^2 + v^2 + w^2}}{a_s}. \tag{3.14}$$

3.1.2 Spatial discretization

In this study, the governing equations of flow, i.e., Eq.(3.1), are discretized using a cell-centered finite volume method based on a multi-block structured grid system. Using a structured methodology, the fluid domain Ω_f is divided into an array of hexahedral cells. For each cell indexed by (*i,j,k*) Eq.(3.1) holds and can be reformulated in the semi-discrete form given by

$$\frac{\partial}{\partial t}\left(\mathbf{W}_{i,j,k} \Delta\Omega_f \right)_{i,j,k} - \mathbf{R}_{i,j,k} = 0, \tag{3.15}$$

where $\mathbf{W}_{i,j,k}$ are the average flow variables of the cell, $\Delta\Omega_{f_{i,j,k}}$ denotes the cell volume, and $\mathbf{R}_{i,j,k}$ is the residual, which measures the net fluxes entering the hexahedral cell through all six cell faces $\Delta\Gamma^l_{f_{i,j,k}}$:

$$\mathbf{R}_{i,j,k} = \sum_{l=1}^{6} \mathbf{Q}^{l}_{i,j,k} \Delta\Gamma^l_{f_{i,j,k}} + \mathbf{D}_{i,j,k}, \tag{3.16}$$

where $\mathbf{Q}^l_{i,j,k}$ is the flux tensor on the cell face *l* of the cell (*i,j,k*) and calculated by averaging the fluxes at the centers of two adjacent cells:

$$\begin{array}{ll} \mathbf{Q}^1 = \frac{1}{2}\left(\mathbf{Q}_{i,j,k} + \mathbf{Q}_{i-1,j,k} \right) & \mathbf{Q}^2 = \frac{1}{2}\left(\mathbf{Q}_{i,j,k} + \mathbf{Q}_{i+1,j,k} \right) \\ \mathbf{Q}^3 = \frac{1}{2}\left(\mathbf{Q}_{i,j,k} + \mathbf{Q}_{i,j-1,k} \right) & \mathbf{Q}^4 = \frac{1}{2}\left(\mathbf{Q}_{i,j,k} + \mathbf{Q}_{i,j+1,k} \right). \\ \mathbf{Q}^5 = \frac{1}{2}\left(\mathbf{Q}_{i,j,k} + \mathbf{Q}_{i,j,k-1} \right) & \mathbf{Q}^6 = \frac{1}{2}\left(\mathbf{Q}_{i,j,k} + \mathbf{Q}_{i,j,k+1} \right) \end{array} \tag{3.17}$$

This central Jameson-Schmidt-Turkel (JST) scheme proposed by Jameson et al. (1981) assumes the same influence from both sides of the cell face, and it causes nonphysical oscillations and odd-even decoupled problems which can be alleviated by adding artificial dissipation term $\mathbf{D}_{i,j,k}$ in Eq.(3.16). Green's theorem is applied to obtain the first-order derivatives when calculating the viscous flux tensors for an auxiliary cell around the vertex, e.g.,

$$
\begin{aligned}
\frac{\partial u}{\partial x} &\approx \frac{1}{\Delta\Omega_f}\sum_{n=1}^{6}\left(u n_x \Delta\Gamma_f\right)_n \\
\frac{\partial u}{\partial y} &\approx \frac{1}{\Delta\Omega_f}\sum_{n=1}^{6}\left(u n_y \Delta\Gamma_f\right)_n , \\
\frac{\partial u}{\partial z} &\approx \frac{1}{\Delta\Omega_f}\sum_{n=1}^{6}\left(u n_z \Delta\Gamma_f\right)_n
\end{aligned}
\tag{3.18}
$$

where $\Delta\Omega_f$ is the auxiliary cell volume, and n_x, n_y and n_z are the Cartesian components of the unit normal vector on the cell surface which point outward.

3.1.3 Temporal integration

The time derivative in Eq.(3.15) is discretized with an implicit backward-difference scheme of second-order accuracy

$$
\frac{3\left(\mathbf{W}\Delta\Omega_f\right)^{(n+1)} - 4\left(\mathbf{W}\Delta\Omega_f\right)^{(n)} + \left(\mathbf{W}\Delta\Omega_f\right)^{(n-1)}}{2\Delta t} = \mathbf{R}\left(\mathbf{W}^{(n+1)}\right),
\tag{3.19}
$$

where the solution vectors of two previous time levels are used here which are denoted by a superscript (n) and ($n-1$).

An iterative method is applied to obtain the solution of the above nonlinear and implicit equations system for the flow variables vector $\mathbf{W}_{n+1}$. Through the application of the dual-time stepping scheme (Jameson, 1991), Eq.(3.15) can be reformulated at each time step as the following steady-state flow problem in a pseudo-time t^*

$$
\frac{\partial}{\partial t^*}\mathbf{W}^{(n+1)} = \frac{1}{\Delta\Omega_f}\mathbf{R}^*\left(\mathbf{W}^{(n+1)}\right),
\tag{3.20}
$$

where

$$
\mathbf{R}^*\left(\mathbf{W}^{(n+1)}\right) = \mathbf{R}\left(\mathbf{W}^{(n+1)}\right) - \frac{3\left(\mathbf{W}\Delta\Omega_f\right)^{(n+1)} - 4\left(\mathbf{W}\Delta\Omega_f\right)^{(n)} + \left(\mathbf{W}\Delta\Omega_f\right)^{(n-1)}}{2\Delta t}.
\tag{3.21}
$$

The semi-discrete Eq.(3.20) can be integrated using a multistage Runge-Kutta scheme to march to convergence in pseudo time t^*. For m stages, the integration is carried out as

$$
\begin{aligned}
&\mathbf{W}_{i,j,k}^{(0)} = \mathbf{W}_{i,j,k}^{(n)} \\
&\mathbf{W}_{i,j,k}^{(1)} = \mathbf{W}_{i,j,k}^{(0)} + \alpha_1 \frac{\Delta t_{i,j,k}^{*}}{\Delta\Omega_{f_{i,j,k}}^{(n+1)}} \mathbf{R}^{*}\left(\mathbf{W}_{i,j,k}^{(0)}\right) \\
&\ldots \\
&\mathbf{W}_{i,j,k}^{(m)} = \mathbf{W}_{i,j,k}^{(0)} + \alpha_m \frac{\Delta t_{i,j,k}^{*}}{\Delta\Omega_{f_{i,j,k}}^{(n+1)}} \mathbf{R}^{*}\left(\mathbf{W}_{i,j,k}^{(m-1)}\right) \\
&\mathbf{W}_{i,j,k}^{(n+1)} = \mathbf{W}_{i,j,k}^{(m)},
\end{aligned}
\tag{3.22}
$$

where α_m are the stage coefficients and $\Delta t_{i,j,k}^{*}$ is the local time step of the cell (i,j,k). For a five-stage time-stepping, the used coefficients are

$$
\alpha_1 = \frac{1}{4}, \alpha_2 = \frac{1}{6}, \alpha_3 = \frac{3}{8}, \alpha_4 = \frac{1}{2}, \alpha_5 = 1. \tag{3.23}
$$

The reformulated discretized Eq.(3.20) has the form of an equivalent steady-state problem. Thus, the local time-stepping and multigrid methods, which are originally developed for steady-state simulations, are directly applied to the present unsteady computation involving pseudo-time iteration without affecting the real-time accuracy (Jameson, 1991). Parallelization is enabled by domain decomposition via the message passing interface (MPI) to achieve large-scale computation. Meanwhile, implicit residual smoothing is applied to increase the stability of the solution. More details about the fluid solver can be found in previous studies (Liu and Ji, 1996; Liu and Zheng, 1994; Liu and Zheng, 1996; Sadeghi, 2004; Sadeghi et al., 2003).

3.1.4 Boundary conditions

The boundary conditions setup is imposed by specifying the respective values of flow variables of the introduced two layers of additional virtual ghost cells around the physical grid cell, as shown in Fig. 3.1. The flux and derivatives at the flow field boundaries can be calculated in the same way as that of the interior cells, which would not require special treatment. The first layer of the ghost cell, adjacent to the boundary, is indexed by 1, and the second layer is denoted by 2, as demonstrated in Fig. 3.1. The specific treatment of used boundary conditions in this thesis, i.e., adiabatic solid wall and far-field, are introduced as follows.

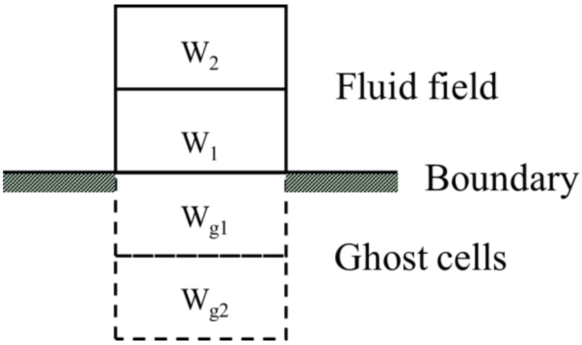

Fig. 3.1. Ghost-cell notation (Sadeghi, 2004).

The fluxes through an adiabatic solid wall surface should be zero. For a viscous flow without slip on the wall surface considered in this work, it requires that the velocity is zero at the surface. This can be accomplished by specifying a negative velocity value of the interior cell to the ghost cell so that their average to be zero:

$$\boldsymbol{V}_{g1} = -\boldsymbol{V}_1. \tag{3.24}$$

Besides, the temperature gradient in the wall-normal direction is required to be zero for the adiabatic solid wall condition. This can be achieved by specifying the density, energy, and pressure in the first ghost cell to equal that in the first interior cell:

$$\begin{aligned} &\rho_{g1} = \rho_1, \\ &E_{f,g1} = E_{f,1}, \\ &p_{g1} = p_1. \end{aligned} \tag{3.25}$$

For the external flows considered in this thesis, the far-field boundary condition must be quasi nonreflective. The Riemann invariants are used with taking approximate account of the characteristic wave propagation, where a quasi-one-dimensional method is applied along the normal direction of each cell (Gatzhammer, 2008). The 1D Riemann invariants in the normal direction are given by

$$\begin{aligned} r_+ &= \boldsymbol{V}_+ \cdot \boldsymbol{n} + \frac{2a_{s+}}{\gamma_h - 1}, \\ r_- &= \boldsymbol{V}_- \cdot \boldsymbol{n} + \frac{2a_{s-}}{\gamma_h - 1}, \end{aligned} \tag{3.26}$$

where a_{s+} and a_{s-} are the speed of sound corresponding to the Riemann invariants r_+ and r_-. Depending on the wave propagation direction, the flow variables at the boundary can be extrapolated by that from freestream (denoted by ∞) and interior cells (with subscript 1) in different directions. Specifically, for subsonic inflows where the boundary normal velocity $V_{b,n} \leq 0$ and $V_{b,n} + a_{s,b} > 0$, it is given by

$$\begin{aligned} \boldsymbol{V}_{+} &= \boldsymbol{V}_{1},\ a_{s+} = a_{s1}, \\ \boldsymbol{V}_{-} &= \boldsymbol{V}_{\infty},\ a_{s-} = a_{\infty}. \end{aligned} \tag{3.27}$$

For supersonic inflow where $V_{b,n} < 0$ and $V_{b,n} + a_{s,b} < 0$

$$\begin{aligned} \boldsymbol{V}_{+} &= \boldsymbol{V}_{\infty},\ a_{s+} = a_{\infty}, \\ \boldsymbol{V}_{-} &= \boldsymbol{V}_{\infty},\ a_{s-} = a_{\infty}. \end{aligned} \tag{3.28}$$

For subsonic outflows where $V_{b,n} \geq 0$ and $V_{b,n} - a_{s,b} \leq 0$

$$\begin{aligned} \boldsymbol{V}_{+} &= \boldsymbol{V}_{1},\ a_{s+} = a_{s1}, \\ \boldsymbol{V}_{-} &= \boldsymbol{V}_{\infty},\ a_{s-} = a_{\infty}. \end{aligned} \tag{3.29}$$

For supersonic outflows where $V_{b,n} > 0$ and $V_{b,n} - a_{s,b} > 0$

$$\begin{aligned} \boldsymbol{V}_{+} &= \boldsymbol{V}_{1},\ a_{s+} = a_{s1}, \\ \boldsymbol{V}_{-} &= \boldsymbol{V}_{1},\ a_{s-} = a_{s1}. \end{aligned} \tag{3.30}$$

The normal velocity $V_{b,n}$, and speed of sound $a_{s,b}$ at the boundary are then obtained as

$$\begin{aligned} V_{b,n} &= \frac{1}{2}\left(r_{+} + r_{-}\right), \\ a_{s,b} &= \frac{\gamma_h - 1}{4}\left(r_{+} + r_{-}\right). \end{aligned} \tag{3.31}$$

Considering that the tangential velocity component is invariant in the quasi-one-dimensional method, the velocity vector at the boundary is given by

$$\boldsymbol{V}_{b} = \begin{cases} \boldsymbol{V}_{\infty} + \left(V_{b,n} - \boldsymbol{V}_{\infty} \cdot \boldsymbol{n}\right)\boldsymbol{n}, \text{ if } V_{b,n} \leq 0 \text{ (inflow);} \\ \boldsymbol{V}_{1} + \left(V_{b,n} - \boldsymbol{V}_{1} \cdot \boldsymbol{n}\right)\boldsymbol{n} \text{ if } V_{b,n} > 0 \text{ (outflow).} \end{cases} \tag{3.32}$$

The density at the boundary is obtained by

$$\rho_b = \left(\frac{a_{s,b}^2}{\gamma_h \dfrac{p_b}{\rho_b^{\gamma_h}}} \right)^{\frac{1}{\gamma_h - 1}}, \tag{3.33}$$

where $\frac{p_b}{\rho_b^{\gamma_h}}$ is the entropy at the boundary computed from the freestream values for inflow and the first interior cell for outflow (Shi, 2020). The pressure and the total energy can be calculated with the known velocity, density, and speed of sound at the boundary.

The flow variables in the ghost cells are defined as

$$\mathbf{W}_{g1} = 2\mathbf{W}_b - \mathbf{W}_1, \tag{3.34}$$

where $\mathbf{W}_b$ denotes the flow variables vector obtained using the flow variables with the subscript b described above, and $\mathbf{W}_1$ represents the flow variables at the first layer of the interior cells.

3.1.5 Mesh deformation scheme

In FSI simulation, the structure is subject to deformation under the surface normal force applied to it. The configuration of the interface Γ_i changes with time and the flow grid has to be updated to accommodate the unsteady boundary. It is too time-consuming to regenerate a new mesh at each time step during the whole process of structural deformation. Instead, an efficient algebraic method is applied to interpolate the displacements of the meshes at the interface Γ_i to yield displacements of the inner grid points of the fluid domain Ω_f by iteratively solving the equations of static equilibrium with a predictor-corrector process (Tsai et al., 2001). Hereby, all the block corner points of the fluid domain are assumed to be connected with each other by springs whose rigidities are inversely proportional to the length of the connecting edge. The displacement of a grid vertex at the boundary of the fluid domain is defined as $\Delta\mathbf{x}$ here, and it can be obtained by the difference of its current position $\mathbf{x}$ between the initial position $\mathbf{x_0}$ at $t = 0$: $\Delta\mathbf{x} = \mathbf{x} - \mathbf{x_0}$.

It is noted that the positions of the vertices at the interface are obtained by the solution of structural deformation. After they are determined, the displacements of inner points are obtained in the following four steps:

1) Given the displacement of the grid-block corner at the boundary of the fluid domain, the corners inside the domain are updated using a spring analogy method (Batina, 1990);

2) The corner displacements are interpolated along internal block edges based on the one-dimensional arc-length-based Trans-Finite Interpolation (TFI) method (Sadeghi et al., 2003);

3) The edge displacements are interpolated along the internal block faces using the two-dimensional TFI algorithm;

4) All the displacements of the internal grid points are obtained by the three-dimensional TFI method.

These interpolated displacements are then added to the original undisplaced grid coordinates. To retain the original grid quality after deformation, Hermite polynomials are used to maintain the grid angles of the original grid near the wall.

It is worth noting that when simulating the incompressible flow problems considered here using the present compressible flow solver, it is necessary to ensure that the compressibility is negligibly small. As did in the previous applications to other relevant incompressible flow simulations (Liu et al., 2016; Shi et al., 2020; Shi et al., 2019; Xiao and Liao, 2010; Xiao et al., 2012a), the freestream Mach number, defined as $Ma_\infty = U_0/a_\infty$ with U_0 denoting the freestream flow velocity and a_∞ being the speed of sound, is chosen as 0.06−0.1 for all the simulations in this work. This value is chosen because it is far below the critical value of 0.3, where the compressibility effect becomes pronounced, to simulate incompressible flow problems considered there, but still sufficiently large to ensure numerical stability. Given that when the boundary is moving during the deformation of the body, the actual Mach number may become larger than Ma_∞ around the swimmer. Therefore, the Mach number distribution in the whole computational domain for each simulation is monitored during computation to ensure that they are always below the critical value for computational accuracy. Besides, our numerical results of the free-swimming of a flexible plate show that the variation of pressure from density change attributed to resolving compressible flow is negligible at this Mach number range (less than 2%).

3.2 Structural Dynamics

3.2.1 Governing equations

For the present biomimetics propulsion applications in which the temperature is assumed to be known, the basic equation of the finite element method is the weak form of the balance of momentum which can be written in the differential form as

$$\rho_s \frac{D^2\mathbf{U}}{Dt^2} = \nabla \bullet \mathbf{P} + \rho_s \mathbf{f}, \tag{3.35}$$

where the acceleration of the material point is obtained by the second derivatives of displacement vector **U** of the structure, surface forces are modeled by the second Piola-Kirchoff stress tensor **P**, and body forces of per unit mass such as gravity are represented by **f**. The solid density is denoted by ρ_s.

A constitutive equation describing the relation between the stress and the strain is used to close up Eq.(3.35). For a Saint Venant–Kirchhoff material, the second Piola-Kirchoff stress tensor **P** is obtained by

$$\mathbf{P} = \mathbf{C} : \mathbf{E}, \quad \mathbf{E} = \frac{1}{2}\left(\mathbf{F}_g{}^{\mathbf{T}}\mathbf{F}_g - \boldsymbol{\delta}\right), \tag{3.36}$$

where **C** is the elasticity tensor, **E** represents the Green–Lagrange strain tensor, the deformation gradient is characterized by $\mathbf{F}_g$ and $\boldsymbol{\delta}$ is the unit tensor.

3.2.2 Spatial discretization

The general governing equation of the solid dynamics, i.e. Eq.(3.35), is discretized using the finite element method. Within the present work, the solid domain Ω_s is divided into a number of three-dimensional small volumes called finite elements:

$$\Omega_s = \sum_e \Omega_{se}, \tag{3.37}$$

where Ω_{se} is the volume of a finite element before deformation. The displacement field within each of these finite elements is assumed to be a continuous function of the displacement at a discrete point *i* which can be taken as “nodes”:

$$\mathbf{U}(\mathbf{X}) = \sum_{i=1}^{N} \varphi_i(\mathbf{X})\mathbf{U}_i, \tag{3.38}$$

where **X** is the position vector in material coordinates, φ_i denotes the shape function and $\mathbf{U}_i$ represents the node displacement vector.

Using the standard virtual work method (Dhondt, 2004), a linear algebraic equation system can be obtained by discretizing Eq.(3.35) in the whole solid domain as

$$[\mathbf{K}_s]\{\mathbf{U}\} + [\mathbf{M}_s]\frac{D^2}{Dt^2}\{\mathbf{U}\} = \{\mathbf{F}_s\}, \tag{3.39}$$

where $[\mathbf{K}_s]$ is the global stiffness matrix, $[\mathbf{M}_s]$ is the global mass matrix, and $[\mathbf{F}_s]$ is the global force vector respectively. The three assembled terms are given by

$$\begin{aligned} [\mathbf{K}_s] &:= \sum_e [\mathbf{L}]_e^T [\mathbf{K}_s]_e [\mathbf{L}]_e, \\ [\mathbf{M}_s] &:= \sum_e [\mathbf{L}]_e^T [\mathbf{M}_s]_e [\mathbf{L}]_e, \\ [\mathbf{F}_s] &:= \sum_e [\mathbf{L}]_e^T \{\mathbf{F}_s\}_e, \end{aligned} \tag{3.40}$$

where $[\mathbf{K}_s]_e$ denotes the element stiffness matrix, $[\mathbf{M}_s]_e$ is the element mass matrix, and $[\mathbf{F}_s]_e$ is the element force vector. The element localization matrix $[\mathbf{L}]_e$ is defined here to localize the degrees of freedom of element *e* in $\{\mathbf{U}\}$:

$$\{\mathbf{U}\}_e = [\mathbf{L}]_e \{\mathbf{U}\}, \tag{3.41}$$

where $\{\mathbf{U}\}_e$ is the displacement vector of element *e*.

3.2.3 Temporal integration – the α-method

As aforementioned, the space domain of Eq.(3.39) is discretized with finite elements. In this section, the time domain is discretized using the *α*-method here. Denoting the velocity vector $\{\mathbf{V}\} := \{\dot{\mathbf{U}}\}$ and acceleration vector $\{\mathbf{A}\} := \{\ddot{\mathbf{U}}\}$, the solution at time level *n*+1 can be obtained by

$$\{\mathbf{V}\}_{n+1} = \{\tilde{\mathbf{V}}\}_{n+1} + \gamma \Delta t \{\mathbf{A}\}_{n+1}, \tag{3.42}$$

$$\{\mathbf{U}\}_{n+1} = \{\tilde{\mathbf{U}}\}_{n+1} + \beta (\Delta t)^2 \{\mathbf{A}\}_{n+1}, \tag{3.43}$$

where $\{\tilde{\mathbf{V}}\}_{n+1}$ and $\{\tilde{\mathbf{U}}\}_{n+1}$ can be considered as the predictor at time level *n*+1 which are only dependent on the values at time level *n*, given by

$$\{\tilde{\mathbf{V}}\}_{n+1} = \{\mathbf{V}\}_n + (1-\gamma)\Delta t \{\mathbf{A}\}_n, \tag{3.44}$$

$$\{\tilde{\mathbf{U}}\}_{n+1} = \{\mathbf{U}\}_n + \Delta t \{\mathbf{V}\}_n + \frac{1}{2}(\Delta t)^2 (1-2\beta)\{\mathbf{A}\}_n. \tag{3.45}$$

By applying Newton's Second Law of Motion, the acceleration vector $\{\mathbf{A}\}_{n+1}$ in Eq.(3.42) and Eq.(3.43) can be obtained by solving the following equation

$$\left[\mathbf{M}_s^*\right]\{\mathbf{A}\}_{n+1} = \left\{\mathbf{F}_s^*\right\}, \tag{3.46}$$

where

$$\left[\mathbf{M}_s^*\right] = [\mathbf{M}_s] + (1+\alpha) K \beta (\Delta t)^2, \tag{3.47}$$

$$\left\{\mathbf{F}_s^*\right\} = (1+\alpha)\{\mathbf{F}_s\}_{n+1} - \alpha\{\mathbf{F}_s\}_n - (1+\alpha)\mathbf{K}_s\tilde{\mathbf{U}}_{n+1} + \alpha\mathbf{U}_n. \tag{3.48}$$

The values of the constants *β* and *γ* are dependent on the chosen constant value *α*, and it is proved that if *β* and *γ* satisfy

$$\beta = \frac{1}{4}(1-\alpha)^2, \ \gamma = \frac{1}{2} - \alpha, \tag{3.49}$$

the *α*-method considered here yields a second-order accuracy and is unconditionally stable for $\alpha \in [-1/3, 0]$ (Dhondt, 2004).

In this work, the implementation of finite element method solver is based on CalculiX written by Dhondt (2004), in which a variety of element types including the brick element, the tetrahedral element, and the wedge element are used to discretize the solid domain and define the shape functions. The details of this structural solver are described in Dhondt (2003, 2004).

3.3 Fluid-structure Interaction Coupling

Since this in-house fluid code (Liu et al., 2016) and CalculiX (Dhondt, 2004) are both highly specialized in its specific single-field physical solution, i.e., fluid and structure respectively, and provide some advanced features, a partitioned or segregated coupling scheme, as shown in Fig. 3.2, is used to reduce the effort for the minimum adaption of original computation code. In this way, the coupling scheme, data mapping, and communication between the two solvers are needed to combine them for an FSI solver, which is introduced in this section.

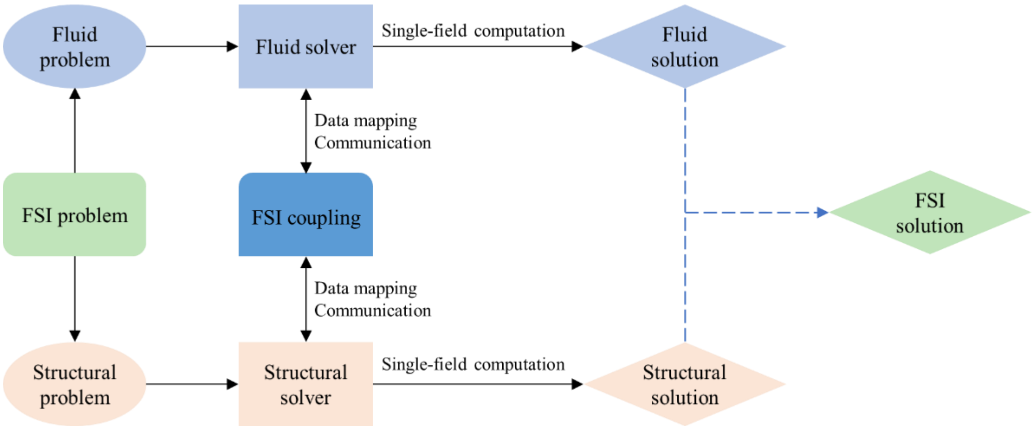

Fig. 3.2. Demonstration of a partitioned FSI coupling approach.

3.3.1 Coupling scheme

A partitioned method does not mean a loose coupling, in which numerical instability poses challenges to convergence (Förster et al., 2007; Küttler and Wall, 2008). It is commonly known that the added-mass effect of the fluid around the surface of structures may give rise to numerical difficulties. In the current FSI application for a bio-inspired fish fin and jet propulsion, the densities of fluid and solid are comparable, and thus the numerical instabilities must be carefully dealt with (Causin et al., 2005).

Within the present framework of partitioned coupling, to ensure the aforementioned numerical stability during FSI simulation, an implicit scheme is designed here, as shown in Fig. 3.3. Specifically, sub-iterations are introduced to implement multiple data exchanges per physical time step in the implicit methods. In this way, some convergence criterion is used to monitor the convergence of the underlying coupling system at the interfaces. If the specified criterion is not met, another sub-iteration will be implemented within the same time step. Therefore, it can handle strong interactions when an explicit scheme fails to reach convergence, although it often requires much more computational cost compared with the explicit one.

The coupling of the in-house fluid flow solver with the structural solver Calculix is achieved via an open-source coupling library for partitioned multi-physics simulations, preCICE (Bungartz et al., 2016), which is demonstrated in Fig. 3.4. Through adaption, i.e., adapter of fluid code, the fluid solver can establish communication with CalculiX as well as data mapping. The internal run mechanism of the fluid solver is redesigned to cooperate with the coupling algorithm implemented in preCICE. The adapter of CalculiX used to connect it with preCICE is implemented by Uekermann et al. (2017). The basic method for an implicit coupling used here is to allow for sub-iterations within one timestep. The adaption of the fluids solver which enables it to connect to preCICE is described as follows.

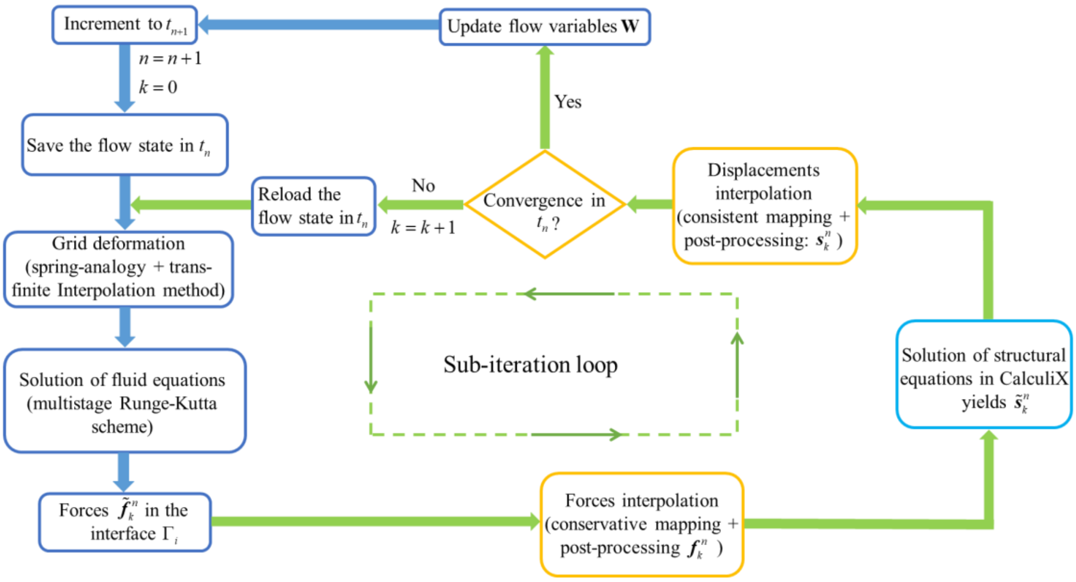

Fig. 3.3. Flow chart of the serial implicit FSI coupling in a partitioned approach.

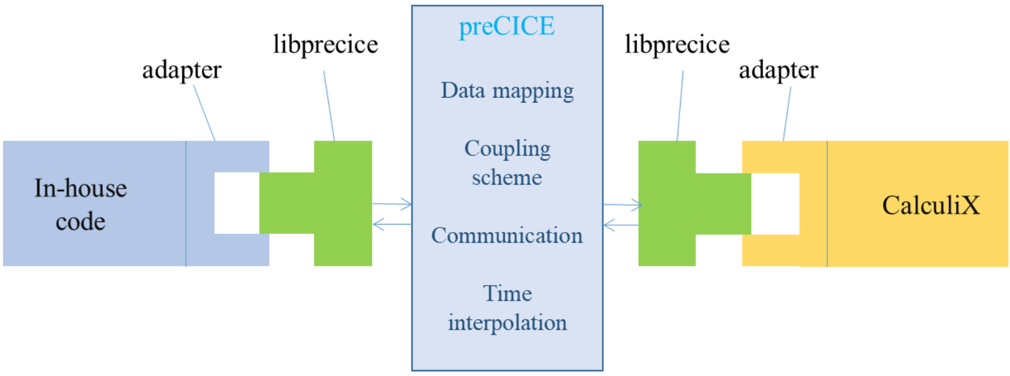

Fig. 3.4. Coupling of the in-house fluid code with FEM code CalculiX via preCICE (Uekermann et al., 2017).

The framework of the in-house fluid solver before adaption can be abstracted in Algorithm 3.1. To enable preCICE subroutines to be called by the in-house code, the preCICE coupling library (see Fig. 3.4) needs to be linked while compilation. This can be achieved by a highly flexible application program interface (API) provided by preCICE to implement the desired functionality. The main principle of the adaption is that the adapter should be minimally invasive to the existing code and avoid contaminating its original functions. The adapter is compiled with the in-house code together and its related configuration will be achieved as regular input settings with only several parameters being added. Therefore, the input setup of FSI analysis via preCICE is almost the same as single-physics simulations without recompilation. The extended code for coupling with preCICE is outlined in Algorithm 3.2.

In this pseudo-code shown in Algorithm 3.2, a flag of "*preciceuse*" is introduced to control the usage of preCICE. All preCICE relevant subroutines will be activated only if it is "TRUE". If preCICE is used, the subroutine "*precice_prepare*" will be called firstly to prepare for the coupling by preCICE including establishing data structures of IDs for forces and displacements, etc. After that, the subroutine "*preciceWetvertex*" will be executed to allocate necessary data structures for interface coupling, e.g., collect grid vertex information at the interface and transfer them to preCICE. While the simulation is ongoing, i.e., external iteration is smaller than the specified maximum number of external iterations, the preCICE loop is executed within each time step or so-called internal iteration. At the very beginning of a time step, the "internal state" or the "*checkpoint*" will be saved, which includes flow coordinates, each cell volume and area, and state variables at the previous time step in the in-house code. In case the current sub-iteration does not converge to the criterion, these parameters will be reloaded, and as a result, the simulation returns to the original state at the beginning of the current step. Saving the "*checkpoint*" correctly is of extreme significance for an implicit fixed-point iteration. Only it is handled in the right way, it is possible for the implicit algorithm to converge (Gatzhammer, 2014).

```
call MPI_INITIALIZE
call input
if (IHC_usage) then
  call IHC_initialize
  call IHC_implementation
end if
call geometry_preprocessing
call boundaryConditionSetup
if external_iteration < max_external_iteration then
  if (mesh_deformation) then
    call move_grid
  end if
  if (IHC_usage) then
    call IHC_initialize
    call IHC_implementation
  end if
  call driver_run
  call convergence_monitor
  if (convergence) then
    update_flow_and_coordinates
  end if
  if (need_write_output) then
    call output
  end if
  external_iteration++
end if
call MPI_FINALIZE
```

Algorithm 3.1. Typical in-house solver run in pseudo-code, reduced to core subroutines. IHC means implicit hole cutting technique for overset grid utilization which is part of the fluid solver.

N-S equations are solved in "*driver_run*", followed by the subroutine "*preciceCalculateForces*" which is invoked to calculate forces at interface nodes and transfer them to preCICE. Afterward, the subroutine "*preciceAdvance*" is called which triggers the coupling scheme in preCICE as well as receiving and remapping displacements at the FSI interface computed by the structural solver. During this procedure, the convergence judgment is conducted to determine either to stay in the current time step or proceed to the next one. Then subroutine "*preciceGetDisplacement*" is triggered to receive the displacements of vertices at the interface and distribute them to respective processors. According to the result of the convergence test, the next move will be "*reloadOldState*" which means the current sub-iteration fails to meet the convergence criterion and a new one is required, or to jump out the current loop and update flow variables and grid positions and advance to next time step. When each time step converges and overall time steps are all fulfilled, the FSI simulation is over. The command "*precice_finalize*" is responsible for closing up the preCICE related communication channel and deallocating used memory.

To facilitate the description of the partitioned coupling scheme, the fluid and solid solvers are denoted as operators $\boldsymbol{F}_o$ and $\boldsymbol{S}_o$. They yield the dynamic solution vector and kinematic solution vector at the interface Γ_i, which is represented by $\boldsymbol{f}_i$ and $\boldsymbol{s}_i$ respectively. Here, $\boldsymbol{f}_i$ consists of the fluid forces acting on the interface, and $\boldsymbol{s}_i$ comprises the displacements of grid vertices at Γ_i. By applying the Dirichlet-Neumann decomposition (Bungartz et al., 2016), the correlation of input-output between the solution of the fluid and solid can be obtained as

$$\boldsymbol{F}_o\left(\boldsymbol{s}_i\right)=\boldsymbol{f}_i,\ \boldsymbol{S}_o\left(\boldsymbol{f}_i\right)=\boldsymbol{s}_i. \tag{3.50}$$

Two implicit coupling fashions, i.e., parallel and serial, are implemented in preCICE (Mehl et al., 2016). Here, to take serial as an example, the simplified flow chart illustrating the serial implicit coupling is presented in Fig. 3.3. As shown, a sub-iteration loop is introduced during each time step *n*. Within the current coupling framework, an improved IQN-ILS method (Degroote et al., 2009) implemented in preCICE, is applied to stabilize and accelerate the coupling iterations. The input and output data of previous iterations are used to approximate the inverse Jacobian of the residual operator of a fixed-point iteration equation and perform a Newton-like solver step (Mehl et al., 2016). In addition, to avoid the potential singularity of the approximated inverse Jacobian, a QR-based filtering technique is employed to filter out data that is linearly dependent (Haelterman et al., 2016).

```
call MPI_INITIALIZE
call input
if (preciceuse) then
  call precice_prepare
end if
call geometry_preprocessing
if (preciceuse) then
  call preciceWetvertex
end if
call boundaryConditionSetup
if external_iteration < max_external_iteration then
  do while (preciceuse)
    if (need_writeCheckpoint)  then
      call writeCheckpoint
    endif
    call move_grid
    if (IHC_usage) then
      call IHC_Initialize
      call IHC_Implementation
    end if
    call driver_run
    call preciceCalculateForces
    call preciceAdvance
    call preciceGetDisplacement
    if (need_reloadCheckpoint)  then
      call reloadOldState
    else
      exit
    endif
  enddo
  call convergence_monitor
  if (convergence) then
    update_flow_and_coordinates
  end if
  if (need_write_output) then
    call output
  end if
  external_iteration++
endif
if (preciceuse) then
  call precice_finalize
end if
call MPI_FINALIZE
```

Algorithm 3.2. In-house solver run extended for implicit coupling with preCICE in pseudo-code, reduced to core subroutines.

Following the flow chart of Fig. 3.3, at the very beginning of the time step n, the internal state of the current time step, i.e., the flow variables $\mathbf{W}$ and grid coordinates $\mathbf{x}$, are saved (corresponding to "*writeCheckpoint*" in Algorithm 3.2), which will be reloaded if the current sub-iteration fails to converge ("*reloadOldState*" in Algorithm 3.2). This serves to retain the same residual equation in every sub-iteration to approximate the aforementioned inverse Jacobian (Mehl et al., 2016). Within one time step, the structural solution s_k^n at the interface, i.e., the displacements of the vertices at the boundaries in coupling iteration k, which has been post-processed using the aforementioned IQN-ILS scheme, is transformed to the fluid solver in a consistent mapping approach (whose counterpart is conservative mapping which will be described later). With the displacements, the spring-analogy and trans-finite interpolation (TFI) method-based grid deformation technique is performed to update the inner fluid grid (Sadeghi, 2004). After the solution of the flow governing equations in the current sub-iteration, the fluid forces $\tilde{\boldsymbol{f}}_k^n$ are derived from the pressure and the viscous shear stress of the interface. They are post-processed as $\boldsymbol{f}_k^n$ and then transformed to the structural solver in a conservative mapping approach. Here, the fluid forces are calculated based on each cell surface on the coupling boundaries but represented by a node fashion.

For a parallel implicit coupling, the fluid and solid solver execute at the same time and both the output data including displacements and forces undergo post-processing. In the present work, a parallel coupling is mainly employed for better efficiency, despite that both lead to the same physical results which have been demonstrated in Mehl et al. (2016).

Through the above fixed-point iteration of the solution at the interface, the implicit coupling ensures the dynamic equilibrium and attempts to regain the solution of a monolithic system.

3.3.2 Data mapping and communication

As aforementioned, the fluid and solid spatial domains are discretized through finite volume and finite element method, respectively. The fluid and structural meshes may not share a coincident node-to-node distribution at the coupling interface; even if they have different geometries at the mesh interface, as demonstrated in Fig. 3.5(a) and (b), respectively. The so-called non-matching and non-conforming meshes make it impossible to copy the data values from one side to another directly. Therefore, an interpolation method is necessary to map data between two solvers at the interface.

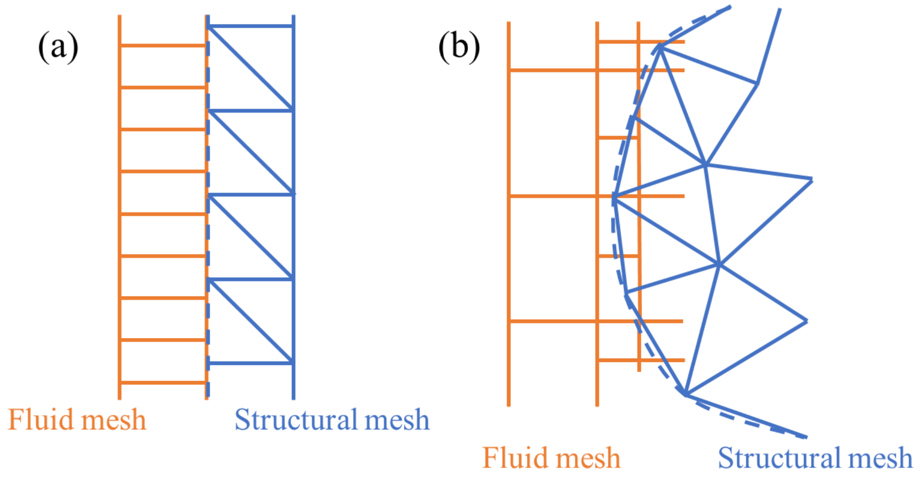

Fig. 3.5. The coupling interface in solid line between the fluid and structural solvers. (a) shows the two meshes have consistent geometry but different node positions, which is called non-conforming. (b) presents a non-matching mesh interface where the fluid mesh has adaptive Cartesian nodes (left)while the structural mesh is composed of triangle elements (right). Adapted from Fig. 2.12 in Gatzhammer (2014).

In this work, the radial basis functions (RBF) based interpolation as described in Lindner et al. (2017), is applied to transfer node forces from the fluid to the solid and vertices displacements oppositely. An RBF interpolation works only on scattered data and no mesh topology information is needed. As the main ingredient of the RBF mapping approach, the basis function has a significant impact on its performance. Here, a globally supported thin-plate splines basis function is chosen as the kernel of the RBF. Both the conservative and consistent mappings are implemented in the RBF interpolation. We apply a consistent mapping during the transformation of displacements, and a conservative mapping for forces which makes the sum of the data values on both sides is equal to ensure the energy balance over the interface (de Boer et al., 2008), which can be demonstrated in Fig. 3.6.

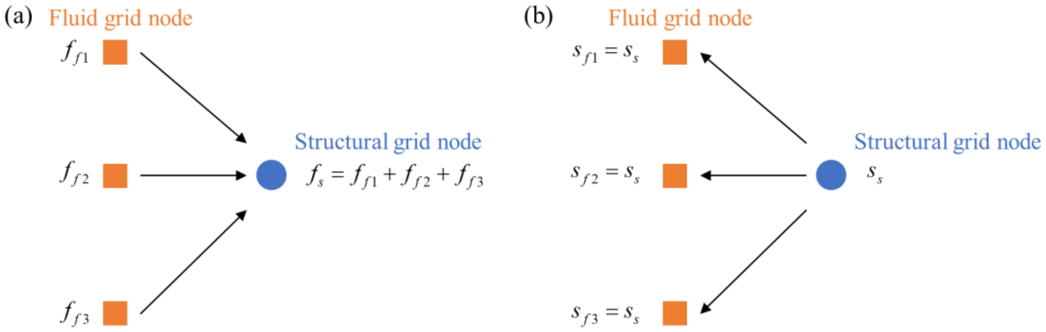

Fig. 3.6. Conservative mapping of force from the fluid grid nodes to its corresponding structural grid node during which the sum of the force values does not change (a). Consistent mapping of displacement from the structural grid node to its corresponding fluid grid nodes during which the displacement values at respective fluid grid nodes are consistent with that of its dependant structural grid node (b).

The communication between the fluid and structural solver is a fully parallel point-to-point fashion. In this study, it means that the communication channels are only constructed between those processors that have been assigned with blocks with boundaries interface which are marked after the distribution of grid blocks.

3.3.3 Convergence criterion

A crucial ingredient of the partitioned coupling is the measurement of its convergence towards the monolithic solution in each time step. The residuals at the current sub-iterations $\boldsymbol{r}_{k+1}$ of displacement and forces are used as a convergence criterion, given as

$$\begin{aligned} \boldsymbol{r}_{s,k+1} &= \boldsymbol{S}_o\left(\boldsymbol{f}_k\right) - \boldsymbol{s}_k, \\ \boldsymbol{r}_{f,k+1} &= \boldsymbol{F}_o\left(\boldsymbol{s}_k\right) - \boldsymbol{f}_k. \end{aligned} \tag{3.51}$$

By applying the discrete l_2 norm of the difference of displacements between the current and last iteration, a scalar representative of the residual vector can be obtained as

$$\left\|\boldsymbol{r}_{k+1}\right\|_2 = \left(\sum_i \left(r_{k+1,i}\right)^2\right)^{1/2}. \tag{3.52}$$

Therefore, a relative convergence measure yields as

$$\frac{\left\|\boldsymbol{r}_{s,k+1}\right\|_2}{\left\|\boldsymbol{s}_k\right\|_2} < \varepsilon \wedge \frac{\left\|\boldsymbol{r}_{f,k+1}\right\|_2}{\left\|\boldsymbol{f}_k\right\|_2} < \varepsilon, \tag{3.53}$$

where ε is predefined. With the proceeding of iterations, the relative residual is expected to drop. If it is not below ε, another sub-iteration will be performed again until the relative residual is small enough to satisfy the criterion. It is noted that the value of chosen ε should not be too small which may increase the computational cost to reach the strict convergence criterion, and even cause failure to convergence. But meanwhile, a too-large value may lead to inaccuracy. In this thesis, the value of ε is chosen as 0.003, so that the required sub-iterations, thus computational cost, would be not too many, and also the accuracy can be ensured.

3.4 Numerical Validations

The fluid solver has been extensively validated in previous studies (Liu, 2015; Sadeghi, 2004; Shi, 2020; Shi et al., 2019). Meanwhile, as a widely used open-source structural solver, CalculiX has been validated and applied to many structural resolutions in the literature (e.g., (Cinquegrana and Vitagliano, 2021; Lolis et al., 2016; Nguyen and Gatzhammer, 2015)). Here, only one validation test is provided to demonstrate its effectiveness and accuracy.

Besides, one fluid-only case is provided for the validation of the turbulence model. Therefore, in this section, the benchmark cases are mainly aimed at the validation of the coupled FSI solver. The validation cases are summarized in Table 3.1, whose problem diagrams are illustrated in Table 3.2.

Table 3.1. Summary of validation cases.

Validation case number	Validation case	Validation type	Validation purpose
1	Deformation of a thick plate under uniform pressure	Structural solver	CalculiX validation
2	Flow over a 2D NACA airfoil at high Re	Fluid solver	Turbulence model validation
3	Flexible deformation of a 2D cantilever behind a square cylinder	FSI solver	FSI coupling for 2D problem
4	Flow over a 3D flexible bending plate	FSI solver	FSI coupling for 3D problem
5	Response of a 2D flexible heave plate	FSI solver	FSI coupling involving active movement and passive deformation
6	Self-propulsion of a 2D flexible swimmer behind a cylinder	FSI solver	FSI coupling involving self-propulsion

Table 3.2. Demonstration diagrams of the validation cases.

Validation case number	Problem diagram	Reference source
1	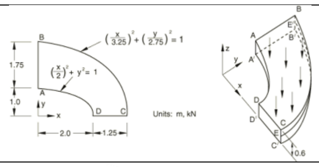	Systèmes (2010)
2		Abbott and Von Doenhoff (1959); Eleni et al. (2012)
3	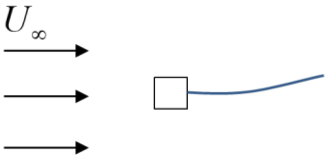	Dettmer and Perić (2006); Habchi et al. (2013); Wood et al. (2010)
4	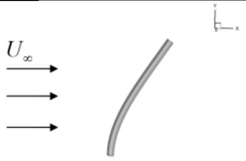	Tian et al. (2014)
5	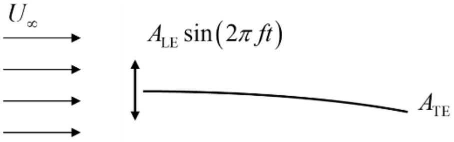	Paraz et al. (2014)
6	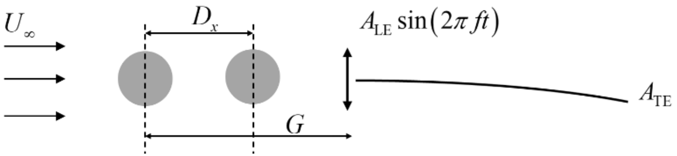	Wang et al. (2019b)

3.4.1 Deformation of a thick plate under uniform pressure

This case serves as the validation of the structural solver CalculiX. It involves the deformation of a three-dimensional thick plate under uniform pressure. The model schematic is presented in Fig. 3.7. The details are given as follows:

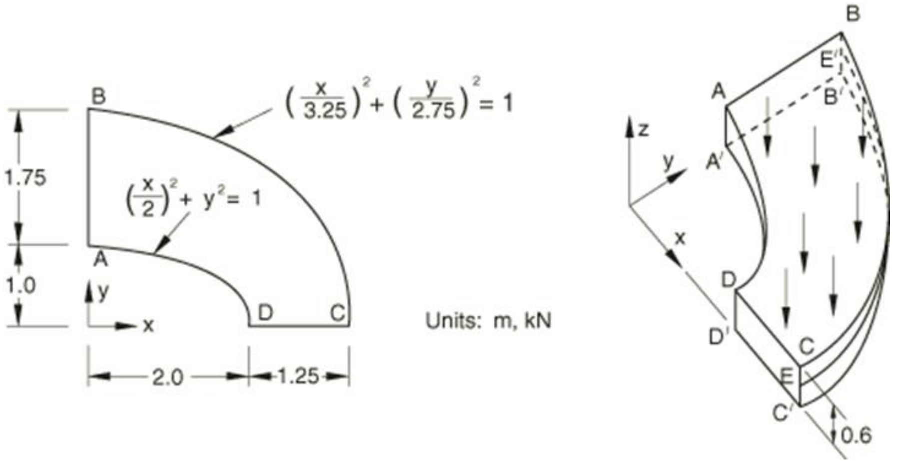

Fig. 3.7. Model description of a thick plate under uniform pressure (Systèmes, 2010).

Model: A thick plate under uniform pressure whose geometry is shown in Fig. 3.7.

Mesh: A coarse and a fine mesh with C3D20 and C3D20R elements (Dhondt, 2003, 2004) are tested. The C3D20 element is a quadratic brick element with 3×3×3 integration points and 20 nodes located at the vertices and middle of the edges. The C3D20R element is also a quadratic brick element but with reduced integration (2×2×2 integration points). The generated fine C3D20 finite mesh is depicted in Fig. 3.8.

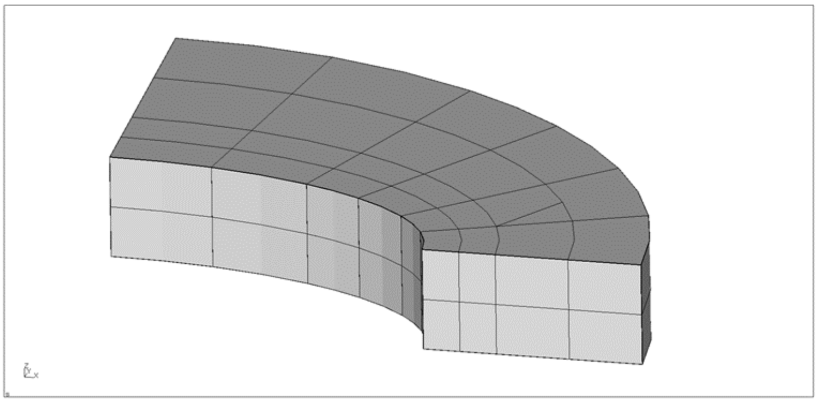

Fig. 3.8. Generated fine C3D20 mesh.

Material: Linear elastic, Young's modulus E = 210 GPa, Poisson's ratio ν = 0.3, density ρ_s = 7800 kg/m^3.

Boundary conditions: the y-displacement u_y = 0 on the face $\mathrm{DCD'C'}$. The x-displacement u_x = 0 on the face $\mathrm{ABA'B'}$. u_x = u_y on the face $\mathrm{BCB'C'}$. The z-displacement u_z = 0 on the line $\mathrm{EE'}$ (E is the midpoint of edge $\mathrm{CC'}$; $\mathrm{E'}$ is the midpoint of edge $\mathrm{BB'}$).

Loading: Uniform normal pressure of 1.0 MPa in the negative *z*-direction on the upper surface of the plate.

The results of the *yy* component of stress s_{yy} at corner D (see in Fig. 3.7) are shown in Table 3.3. The simulation errors are obtained by comparing with a solution $s_{yy} = 5.38$ MPa provided by the National Agency for Finite Element Methods and Standards (NAFEMS) for a standard benchmark considered here (National Agency for Finite Element and Standards, 1990). It is can be found from Table 3.3 that the results of the current simulation have good agreement with that of commercial results and the reference value.

Table 3.3. Results of the yy component of stress at corner D.

Solver	Element types	Coarse mesh			Fine mesh		
		Element number	s_{yy} (MPa)	error	Element number	s_{yy} (MPa)	error
Abaqus	C3D20R	12	-7.93	47.40%	48	-5.53	2.79%
CalculiX	C3D20R	12	-5.34	-0.07%	48	-5.68	5.5%
Abaqus	C3D20	12	-6.72	24.91%	48	-5.64	4.83%
CalculiX	C3D20	12	-5.18	-3.7%	48	-5.44	1.1%

3.4.2 Flow over a 2D airfoil at a high Reynolds number

This case serves as a validation of the *k*-*ω* turbulence model in the in-house fluid solver by simulating the two-dimensional flow over a NACA0012 airfoil. The Reynolds number for this simulation is $\mathrm{Re} = U_\infty c/\nu = 3\times10^6$, where *c* is the chord length of the airfoil, which is identical to the experimental data in Abbott and Von Doenhoff (1959). The height of the first cell is $1.0\times10^{-5}\ c$, corresponding to the value of y^+ approximately 0.2, which is smaller than 1 to sufficiently resolve the flow in the inner boundary layer. The uniform flow over the airfoil with the angle of 0°, 3°, 5°, 9°, and 12° when $\mathrm{Re} = 3\times10^6$ is simulated. The results are compared with the previous numerical (Eleni et al., 2012) and experimental (Abbott and Von Doenhoff, 1959) data in Fig. 3.9. The lift coefficients by the present simulations are slightly higher than the others as the angle of attack increases, but the discrepancy is still acceptable. The drag coefficients by numerical simulations are all slightly higher than the experimental results in Abbott and Von Doenhoff (1959). In general, the present results have a good agreement with those in previous studies.

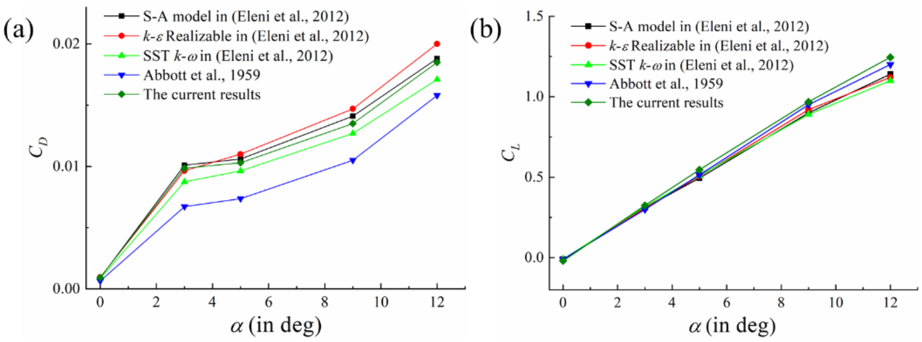

Fig. 3.9. Comparisons between experimental data from Abbott and Von Doenhoff (1959) and three different turbulent models simulation results in Eleni et al. (2012) of the drag C_D (a) and lift C_L (b) coefficient.

3.4.3 Flexible deformation of a 2D cantilever behind a square cylinder

This case consists of a fixed square bluff body with an elastic cantilever attaching in its wake (Nakata and Liu, 2012; Olivier et al., 2009; Wood et al., 2010). Previous studies indicated that the flow separated from the leading edge of the square cylinder would induce a periodic oscillation of the flexible cantilever.

The layout of the computational domain is presented in Fig. 3.10. In the present simulation, the fluid domain contains 153428 cells in the form of a multi-block grid whose height of the first layer of the grid is 0.002 *d*. The structural mesh comprises 123 quadratic wedge elements with standard shape functions (Dhondt, 2004).

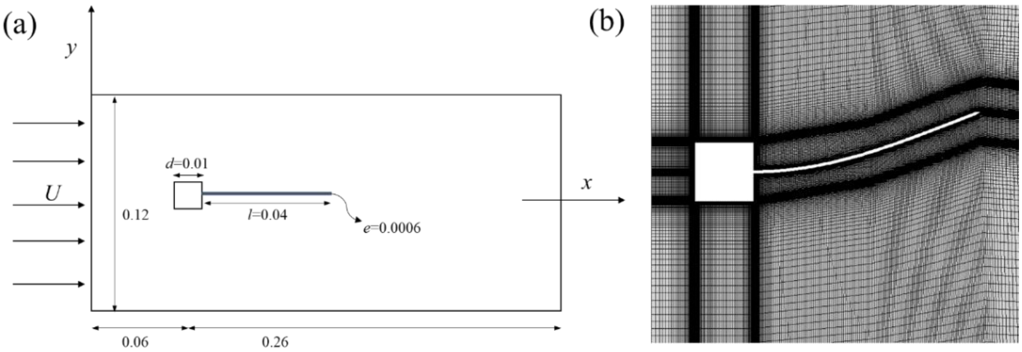

Fig. 3.10. The computational domain layout (a), and the generated fluid mesh around the cantilever after the deformation (b).

In this simulation, Re = $U_\infty d/\nu$ = 330 where U_∞ is the flow velocity, *d* is the diameter of the square cylinder, and ν denotes the fluid viscosity. Therefore, the laminar flow is solved. The chosen physical properties are as follows: the mass ratio $m^* = \rho_s e/\rho_f l$ = 1.27 with ρ_s and ρ_f being the density of the structure and fluid, respectively, and *e* and *l* denoting the thickness and the length of the cantilever; non-dimensional bending stiffness $K = EI/(\rho_f U_\infty^2 l^3)$ = 0.23 where *E* is Young's modulus and $I = e^3/12$ is the area moment of inertia of the cross-section, and Poisson's ratio ν_s =0.35. These physical properties are chosen to make the frequency of shedding vortex approximate the first Eigen-frequency of the cantilever so that a remarkable oscillation can be observed. In the structural part, the left end of the cantilever is set as fixed, and the movement of the whole cantilever is limited only in x and y-direction.

Fig. 3.11 depicts the displacement of the free end of the flexible beam in the y-direction with the dimensionless timestep size, defined as $\overline{\Delta t} = \Delta t U_\infty / d =$ 0.208. As seen, the displacement lies in a range of 0.95~1.20 cm, and the non-dimensional oscillation period $\overline{T} = TU_\infty / d$ varies around 17.0. Observed from previously published literature (Dettmer and Perić, 2006; Habchi et al., 2013; Matthies and Steindorf, 2003; Olivier et al., 2009; Wood et al., 2010), the displacement amplitude lies between 0.8~1.4 cm and $\overline{T}$ ranges between 15.80 and 17.44. Therefore, the current simulation results have a good agreement with the previous numerical solution.

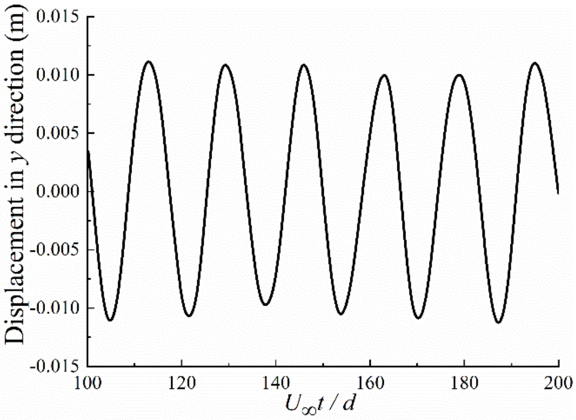

Fig. 3.11. Vertical tip displacement of the cantilever beam.

The generated mesh after deformation is depicted in Fig. 3.10(b). The vorticity contour in the z-direction within one oscillation period is presented in Fig. 3.12. During one oscillation period, two clock-wise vortices form at the upper region while another two counterparts form at the lower region. Besides, the Von Kármán vortex street behind the square bluff is dispersed due to the existence of the oscillating elastic cantilever. Then it seems to be stretched along the downstream direction but evolves to an independent round-similar shape away from the appendix.

The velocity and pressure contours around the square cylinder and the cantilever at this moment are shown in Fig. 3.13. The velocity distribution presents the unsteady behavior of the flow, especially around the cylinder and cantilever. Small velocity magnitudes are observed near the cantilever and cylinder surfaces which is consistent with the results in Habchi et al. (2013). It is also observed that the pressure difference between the upper and lower surface of the cantilever is pronounced, which may contribute to the unsteady oscillation of the cantilever directly.

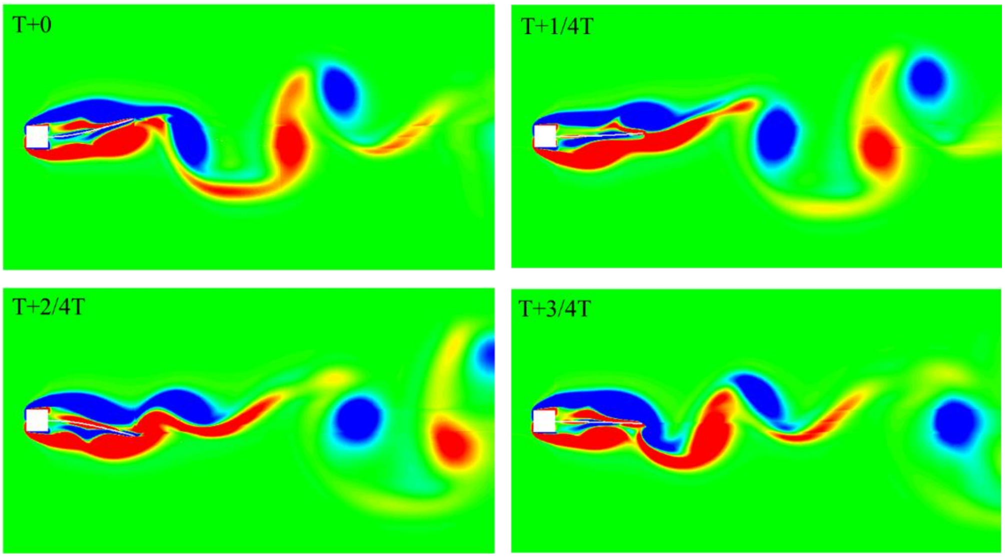

Fig. 3.12. Evolution of vorticity in *z*-direction around the cantilever within one oscillation period T.

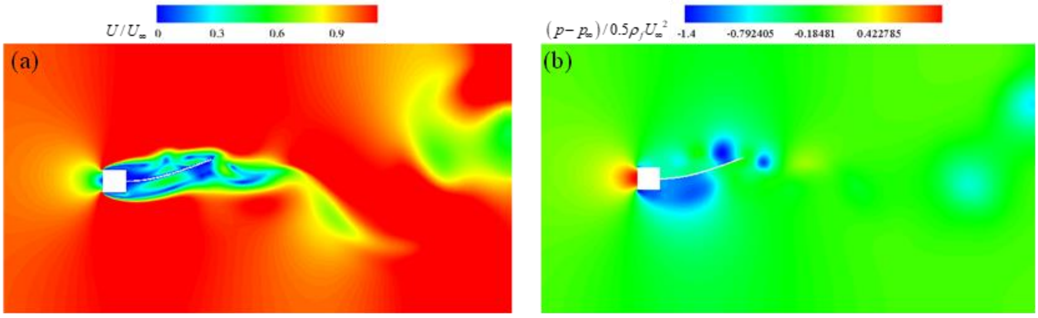

Fig. 3.13. The velocity magnitude contour (a) and pressure contour (b) around the cantilever when the tip displacement reaches the maximum.

3.4.4 Flow over a 3D flexible bending plate

This validation test involves a flexible plate that is bent while placed in crossflow. The original case derives from an experimental study on the flow-induced reconfiguration of flexible aquatic vegetation conducted by Luhar and Nepf (2011). One of their experiment cases was then numerically simulated as an FSI validation by Tian et al. (2014). In their work, they quantitatively compared the results with experimental data in the presence of gravity and buoyancy and performed a series of simulations in the absence of them for benchmark studies. Here, the simulation cases by Tian et al. (2014) without considering the gravity and buoyancy are chosen to validate our proposed multi-physics numerical suite.

The computational domain of the flow over the elastic plate is depicted in Fig. 3.14(a). The plate is placed vertically in the crossflow with its bottom end clamp-mounted while the free end can deform under the action of fluid forces. The parameters are all dimensionless: the length $h = 5\ b$, the thickness $t = 0.2\ b$, where b is the width, the flow is laminar and Re = $U_\infty h/v = 100$, mass ratio $m^* = \rho_s b/\rho_f t = 0.14$, $K = EI/(\rho_f U_\infty^2 b^3) = 2.39$ and $v_s = 0.4$. The fluid computational domains contain three meshes including a coarse grid with 2793362 cells, a medium one with 3916111 grid cells, and a fine mesh with 5585602 cells. The first grid height of the three meshes is 0.002 b. Three dimensionless time step sizes, which are defined as $\overline{\Delta t} = \Delta t U_\infty / b$, i.e., $\overline{\Delta t} = 0.0292$, $\overline{\Delta t} = 0.0208$ and $\overline{\Delta t} = 0.0148$ are used for the computation respectively. The structural mesh contains 1400 quadratic brick elements.

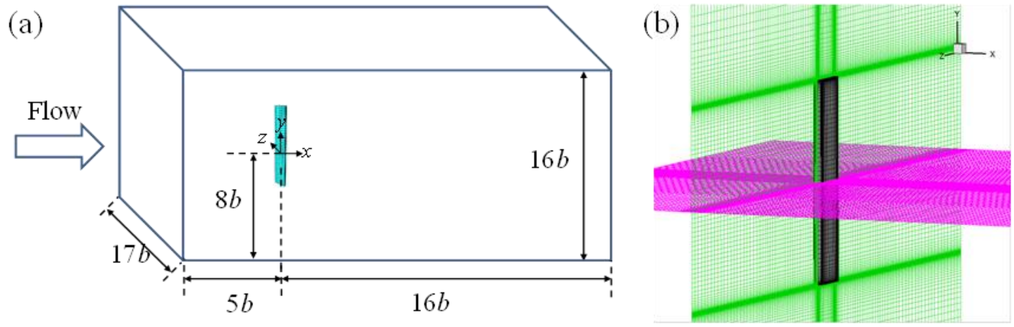

Fig. 3.14. The computational domain of flow over an elastic plate (a) and the generated medium-mesh around the plate (b).

The displacement of the plate center and the drag coefficient, which is defined as $C_d = F_x/(0.5\rho_f U_0^2 bh)$, in the absence of gravity and buoyancy when Re = 100 are compared in Table 3.4. Based on the results shown in Table 3.4, we also simulated the deformation of the plate at Re = 400 using the medium mesh with $\overline{\Delta t} = 0.0208$ and the results are shown in Table 3.5. It indicates that the present FSI simulation results match well with the counterparts in Tian et al. (2014).

During the simulation, the flexible plate eventually reaches a stable configuration, as shown in Fig. 3.15. As seen, the flow incident surface of the plate near the bottom end bears the largest fluid pressure, while approaching the top side, its hydrodynamic pressure experiences a continuous decrease, as well as the pressure difference between the two surfaces in the flow direction. This is consistent with the experimental data that in comparison with a rigid aquatic vegetation model, a flexible one tends to bend to a steady configuration to reduce the flow-induced drag (Luhar and Nepf, 2011; Tian et al., 2014).

Table 3.4. Comparison of drag coefficient and deformation in the absence of gravity and buoyancy when Re = 100.

	C_d	D_x/b	D_y/b
Tian et al. (2014)	1.02	2.34	0.67
Mesh_fine	1.05	2.31	0.675
Mesh_medium	1.06	2.31	0.678
Mesh_coarse	1.10	2.24	0.611

Table 3.5. The drag coefficient and deformation in the absence of gravity and buoyancy when Re = 400.

	C_d	D_x/b	D_y/b
Tian et al. (2014)	0.94	2.34	0.68
The present study	0.99	2.28	0.647

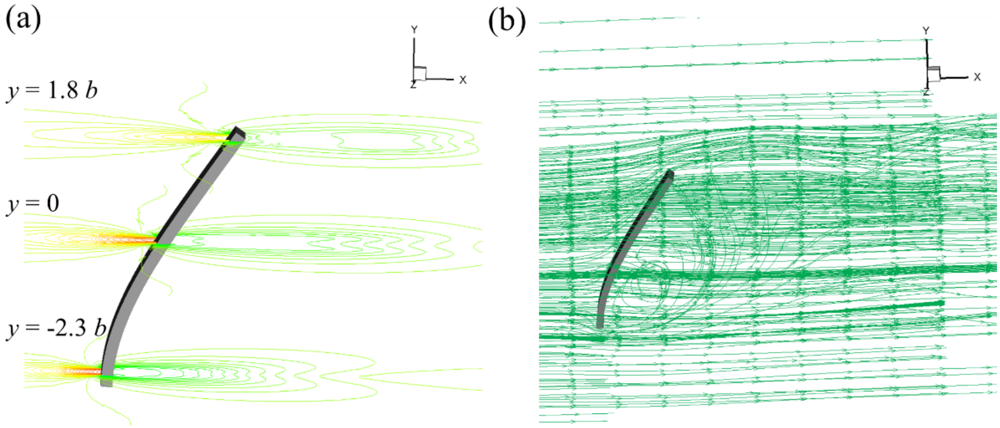

Fig. 3.15. The deformed plate with three representative horizontal slices colored with pressure distribution (a) and the streamline around the plate (b).

3.4.5 The response of a flexible plate in a forced harmonic heave motion

This numerical validation case involves an experimental study conducted by Paraz et al. (2014); Paraz et al. (2016). It consists of a horizontal flexible plate that is made of polysiloxane. The plate has a rounded leading edge and a tapered trailing edge. The thickness of the plate *e* is 0.004 m, chord length *c* is 0.12 m and span *L* is 0.12 m, giving an aspect ratio of 1. In their experiment, the leading edge was forced into a harmonic heave motion while the trailing edge was set free, as shown in Fig. 3.16(a). The elastic plate deforms under the hydrodynamic forces. More details about the experimental setup can be found in Paraz et al. (2014).

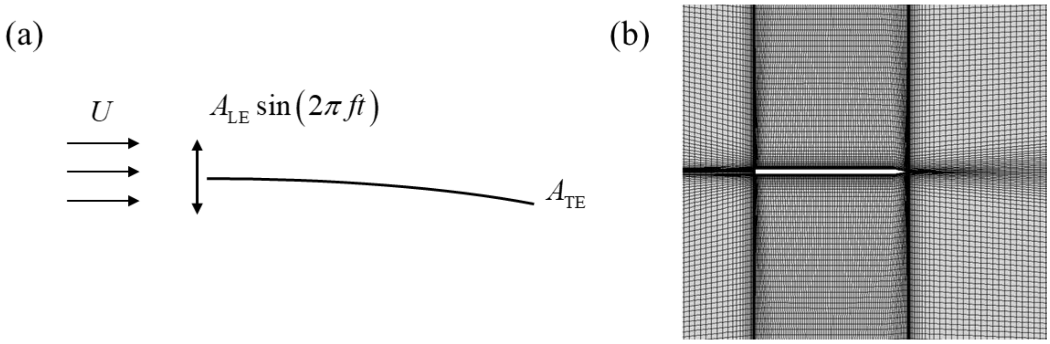

Fig. 3.16. Sketch of the experimental set-up of the flexible plate in a forced heave motion (Paraz et al., 2014) (a) and the generated fine mesh around the plate (b).

Three grids are generated: a coarse mesh with 40626 cells, a medium-size mesh with 57424 cells, and a fine mesh with 79514 cells. The first grid height of the three meshes is 0.0017 *c*. With these fluid meshes, we perform the grid and time-step size tests for the case when the normalized frequency $f/f_0 = 1$ where f_0 is the natural frequency of the plate and time-step corresponding to the coarse mesh is $\overline{\Delta t} = f\Delta t$=0.00694, the medium grid is $\overline{\Delta t} = 0.00501$ and for the fine grid is $\overline{\Delta t} = 0.00357$. The flow is assumed as laminar and the simulation is carried out with a structural grid with 105 quadratic brick elements (Dhondt, 2004). The response of the plate is characterized by the change of the relative displacement of the trailing edge concerning that of the leading edge A_{TE}/A_{LE} and the phase difference φ between them. The comparison of A_{TE}/A_{LE} under different resolutions is shown in Fig. 3.17. To reduce the computational cost and meanwhile, obtain accurate results, we chose the medium size mesh for the other simulations. Based on the medium-size mesh, the results of tip displacement A_{TE}/A_{LE} and phase shift φ are shown in Fig. 3.18.

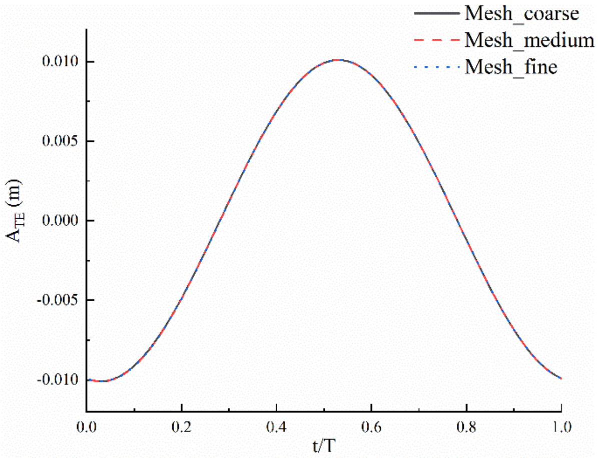

Fig. 3.17. Results of the relative displacement of the trailing edge with three different meshes when f/f_0=1, Re =6000, A_{LE} = 0.004 m, and rigidity B = 0.018 N·m.

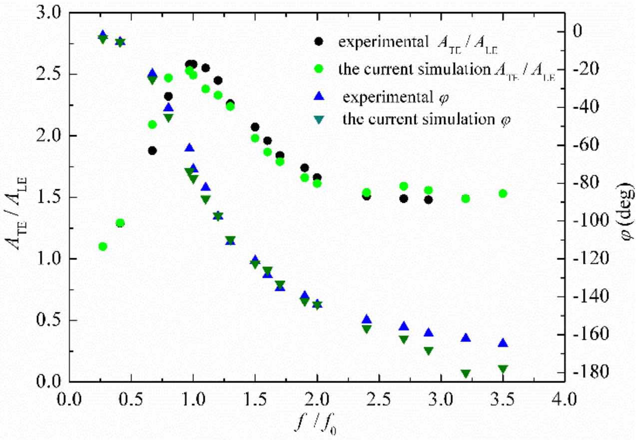

Fig. 3.18. The relative displacement of the trailing edge concerning that of the leading edge of the flexible plate, A_{TE}/A_{LE}, and the corresponding phase shift as a function of the normalized frequency f/f_0 for Re = 6000, A_{LE} = 0.004 m and rigidity B = 0.018 N·m.

It can be found from Fig. 3.18 that the current emulation results agree well with the counterparts in the experiment. A sharp peak is observed in the displacement curves of the trailing edge when the forcing frequency approximates the natural frequency f_0 in both experimental and numerical simulation, where the A_{TE} is 2.5 times larger than the A_{LE}. This is the first resonance peak according to the analysis by Paraz et al. (2014). With the increase of forcing frequency, the phase shift φ witnesses a continuous increase, which indicates stronger interactions between fluid and structure with a larger forcing frequency.

In Fig. 3.19, the deformation of the plate at the resonance frequency is illustrated by the superposition of the centerlines of the plate within one forcing cycle. According to the definition of Dai et al. (2012a), the current deformation pattern of the plate corresponds to the first mode. It is noted that a weak asymmetry in the up-and-down of the shape mode is observed in Fig. 3.19(a) from the experimental results, but not from that of the numerical simulation results. This may be explained by the fact that in the experiment, the density of the plate is slightly larger than that of water and the gravity effect plays a role in the response of the plate, while in the present simulation the gravity influence is ignored. Even so, since the two densities approximate each other, the neglect of gravity does not lead to a big difference.

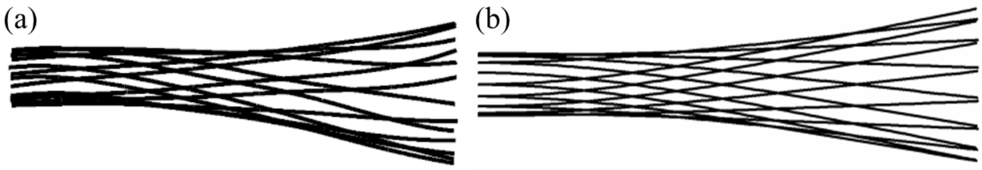

Fig. 3.19. Mode shape of the plate when f/f_0 = 1 obtained from the experiment (a) (Paraz et al., 2014) and current numerical simulation (b).

3.4.6 Self-propulsion of a 2D flexible swimmer behind a cylinder

This validation involves a self-propelled flexible plate in the wake of two tandem cylinders described in Wang et al. (2019b), as depicted in Fig. 3.20. In this simulation, the imposed motion on the leading edge of the plate is the heave motion, $H(t) = H_0\sin(2\pi ft)$ with H_0 being the maximum heave amplitude and f denoting the heave frequency, while the trailing edge of the plate is set free. The distance between the two cylinders D_x is 4.5 D with D being the diameter of the two cylinders. According to Wang et al. (2019b), if the plate can hold stationary in the wake, the flapping frequency needs to be identical to that of the vortex shedding. Therefore, we firstly perform a fluid-only simulation, i.e., the flow over the two tandem cylinders without the flexible plate in the wake of them, and obtain the Strouhal number, $St = f_vL/U_0 = 0.176$ (with f_v being the vortex shedding frequency, L being the length of the plate and U_0 denoting the incoming flow velocity), which is close to the value 0.185 reported by Wang et al. (2019b). Then the dimensionless heave motion frequency is defined as $f^* = fL/U_0 = 0.176$. In this validation, the governing parameters matching with the counterparts in Wang et al. (2019b) are as follows: the Reynolds number $\mathrm{Re} = U_0L/\nu = 200$, the mass ratio $\sigma = \rho_sh/\rho_fL = 1$, the bending rigidity $K = EI/(\rho_fU_0^2D^3) = 0.5$.

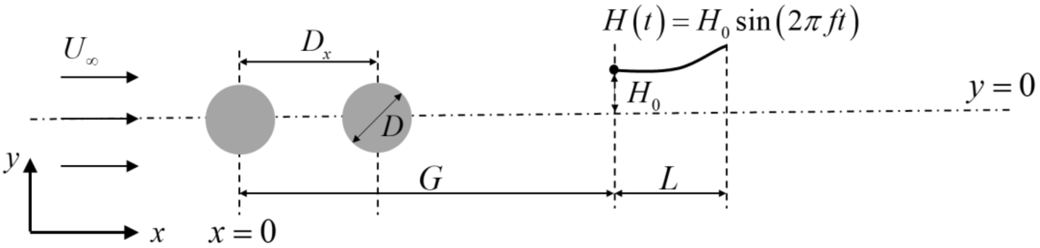

Fig. 3.20. Schematic diagram of a self-propelled flexible plate behind two tandem cylinders (Wang et al., 2019b).

There are three typical modes of the plate in the wake of the cylinders, i.e., drift upstream (DU), drift downstream (DD), and holding stationary (HS) when the flapping amplitudes H_0 and initial horizontal positions of the plate G_0 are varied, which are summarized by Wang et al. (2019b) as shown in Fig. 3.21. For the HS mode, we simulate the cases at $H_0 = 0.3\ L$, and the horizontal positions of the leading edge of the plate when it is holding station are listed in Table 3.6. The typical trajectories of the three motion modes in our simulations are shown in Fig. 3.22. Therefore, it can be seen that the yielded results by our numerical simulations present good agreement with the counterparts in Wang et al. (2019b).

Table 3.6. The horizontal station-holding positions of the leading edge of the plate when $H_0 = 0.3\,L$.

G_0/L	The present range of G/L	The range of G/L in Wang et al. (2019b)
15	17.15-17.25	16.0-16.1
17	19.89-20.01	18.9-19.0

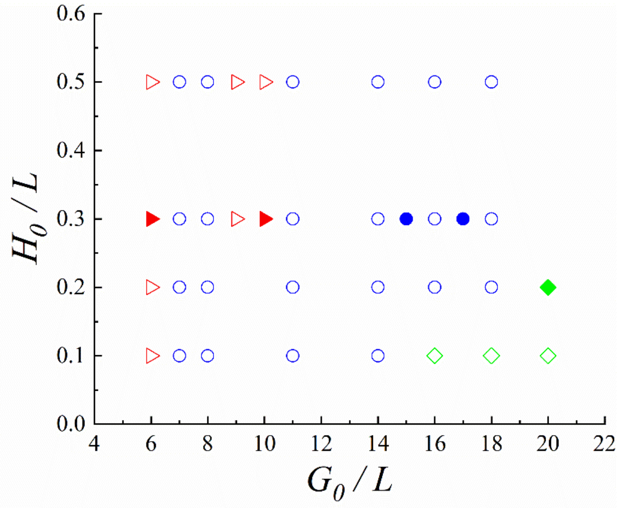

Fig. 3.21. Phase diagram for the three motion modes adapted from Wang et al. (2019b). The circles represent HS, the triangles denote DU and rhombuses represent DD modes. The solid points represent the cases we have simulated.

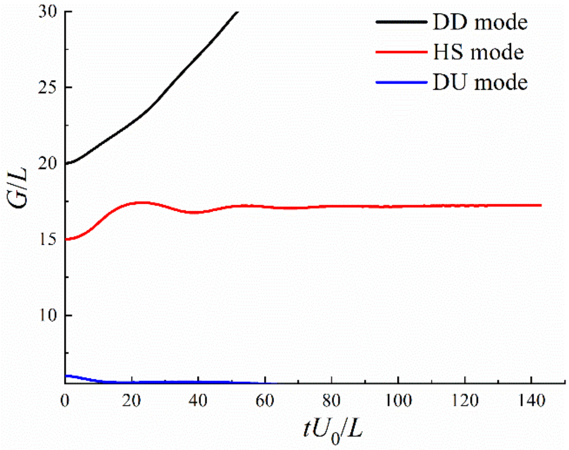

Fig. 3.22. The streamwise trajectory of the leading edge for the three-movement modes when $G_0/L = 6$ with $H_0/L = 0.3$ for DU mode, $G_0/L = 15$ with $H_0/L = 0.3$ for HS mode, and $G_0/L = 20$ with $H_0/L = 0.2$ for DD mode.

3.5 Summary

In this chapter, the governing equations of the fluid and structural dynamics are described, followed by the used numerical techniques to resolve these equations. Specifically, the fluid dynamics is resolved by solving compressible Navier-Stokes equations based on a cell-centered finite volume method. The structural dynamic response is obtained by solving the equations of the balance of momentum through a finite element method. The coupling between the two solvers to yield an FSI solver is also described. The main ingredients for this FSI coupling including coupling scheme, data mapping and communication, and convergence criteria are introduced.

One of the main contributions of the present work is the coupling between the in-house fluid code and a powerful structural solver CalculiX by adapting the fluid code which enables it to connect with CalculiX to form an FSI solver through preCICE. Therefore, the validations focus on the FSI coupling through properly selected classic benchmarks by comparing simulation results with the counterparts from previous numerical and/or experimental studies. The results demonstrate the effectiveness and accuracy of the solvers, which path the way for the following applications to studies of underwater bio-inspired propulsion involving complex fluid-structure interaction.

Chapter 4 Effects of Non-uniform Stiffness Distribution on Propulsion Performance of Flexible Body and Fin

This chapter applies the proposed FSI solver introduced in Chapter 3 to study bio-inspired flexible fish body and fin with non-uniform stiffness distribution which is a biological feature of real fishes (Zhu and Bi, 2017). Specifically, a tail model inspired by bluegill sunfish, and a tuna-like swimmer model are considered. These two biological prototypes are chosen because they represent two typical caudal fin types of ray-finned fish, i.e., one (bluegill sunfish) has a tail with a low aspect-ratio shape (defined as the ratio of the square of the span to the surface area) of an Acanthopterygii fish, and the other (tuna fish) has a high aspect-ratio of a Teleostei fish (Lauder, 2015). Besides, their morphology and kinematics information was well reported in the literature, which enables the comparison of our numerical simulations with the biological and experimental studies. Through the following simulations of a flexible fish body and fin, we aim at revealing the effect of non-uniform stiffness distribution on the propulsion performance. Meanwhile, this may also demonstrate the capability of the developed FSI to solve complex fluid-structure interaction problems.

4.1 Performance of a Bluegill Sunfish Inspired Fish Fin with Non-uniformly Distributed Spanwise Stiffness

4.1.1 Problem statement

The current peduncle and caudal fin model is inspired by the experiment test conducted by Esposito et al. (2012), where a robotic fishtail mimicking the locomotion of the Bluegill Sunfish (*Lepomis macrochrus*) has been experimentally examined. In their experiment, the robot consists of a rigid peduncle and a flexible caudal fin, as shown in Fig. 4.1, and more details for the experimental setup can be found in Esposito et al. (2012).

However, it is worthwhile to note that the current study does not attempt to duplicate the real fish in terms of its lifelike geometry or material features *in-vivo*. Instead, like the studies by Esposito et al. (2012) and Zhu and Bi (2017), we focus on some main characteristics, e.g., anisotropic flexibility and associated fluid-structure interplay, extracted from a real fish fin. Fig. 4.2 illustrates the geometry and dimensions of the peduncle and caudal fin model. The thickness h of the model is 0.02 c, where c is the chord length of the fin at the midline. All the edges are chamfered to ease our CFD mesh generation.

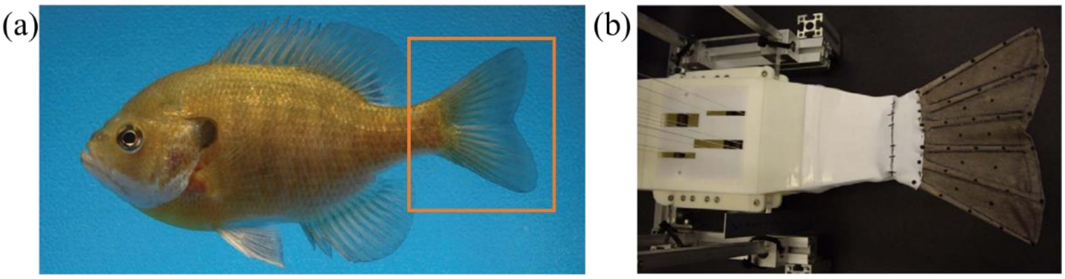

Fig. 4.1. Bluegill sunfish, *Lepomis macrochirus*, the biological model (a) for the robotic device (b) designed by Esposito et al. (2012).

The kinematics of the present model is described as follows. The peduncle combined with the caudal fin rotates harmonically around the z-axis with the reference point $\boldsymbol{O}$ in a uniform flow in the positive x-direction with a velocity of U_∞. The time-dependent pitch motion of the model is described by $\theta(t) = \theta_m \sin(2\pi f t)$, where θ_m is the peak amplitude and f denotes the oscillating frequency.

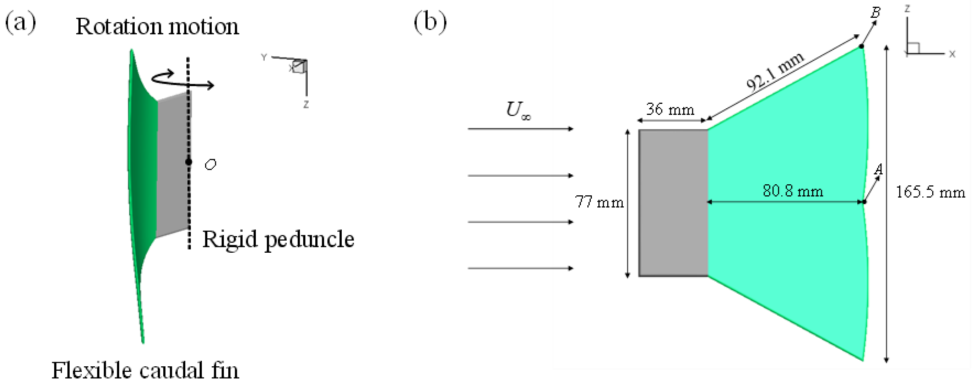

Fig. 4.2. Illustration of the fish peduncle-caudal model (a) and *xz* view of the model and dimensions (b).

The dimensionless parameters are defined as: the Reynolds number $\mathrm{Re} = U_\infty c/\nu$; mass ratio $m^* = \rho_s h/\rho_f c$; the reduced frequency $f^* = fc/U_\infty$; the Poisson ratio the ν_s; dimensionless stiffness $K = EI/(\rho_f U_\infty^2 c^3)$, where E denotes Young's modulus, $I = h^3/12$ is the area moment of inertia of the cross-section.

Structurally, this fin is composed of 19 segments (typically, the number of rays of a real fish fin ranges from 10 to 20, (Westneat et al., 2004)), as shown in Fig. 4.3(a). To replicate various fin deformation patterns observed in Esposito et al. (2012) and Zhu and Bi (2017), each segment is assigned with a unique K, i.e., for ith segment, the normalized flexural rigidity is $K_i = E_i I/(\rho_f U_\infty^2 c^3)$ ($i = 1, \ldots, N$), where $N = 19$. Five variation patterns of K corresponding to different deformation fashions are considered in this work:

1. Uniform distribution: $K_i = K_c$.

2. Cupping distribution: $K_i = K_c R_i / R$, where $R_i = 1 + \gamma \left[1 - \sin \frac{\pi(i-1)}{N-1} \right]$.

3. Reverse cupping distribution: $K_i = K_c R_i / R$, where $R_i = 1 + \gamma \sin \frac{\pi(i-1)}{N-1}$.

4. W-shape distribution: $K_i = K_c R_i / R$, where $R_i = 1 + \gamma \left[1 - \left| \sin \frac{2\pi(i-1)}{N-1} \right| \right]$.

5. Heterocercal distribution: $K_i = K_c R_i / R$, where $R_i = 1 + \gamma \left[1 - \sin \left(\frac{\pi |i-N|}{2(N-1)} \right) \right]$.

Here, $R = \frac{1}{N} \sum_{i=1}^{N} R_i$, and K_c is a constant which is used to quantify the mean flexibility of all the fin segments. The ratio of the stiffness between the least flexible segment and the most flexible one is determined by the parameter γ. In this simulation, $\gamma = 10$ is selected. The variations pattern of flexural rigidity is demonstrated in Fig. 4.3(b).

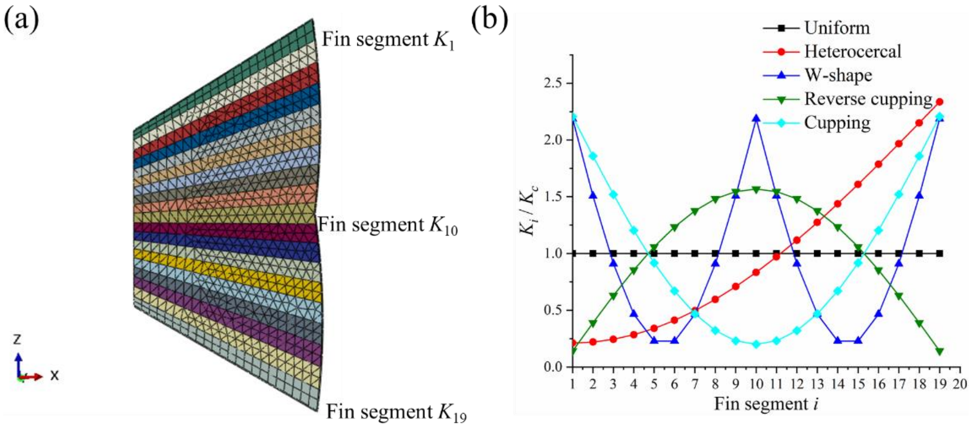

Fig. 4.3. The generated structural meshes of the fin with 19 segments in different colors (a) and the distribution patterns of stiffness (b).

To evaluate the propulsion performance of the caudal fin, the instantaneous thrust and power expenditure coefficients are defined as

$$C_T = -\frac{F_x}{\frac{1}{2}\rho_f U_\infty^2 S}, \quad C_P = -\frac{M_O \dot{\theta}}{\frac{1}{2}\rho_f U_\infty^3 S}, \tag{4.1}$$

where F_x is the total hydrodynamic forces on the caudal fin in the x-direction, S is the reference area, i.e., the area of the fin in xz plane, M_O represents the z-component of the reaction moment at point ***O***. Meanwhile, the lateral force is defined as the hydrodynamic forces in the y-direction, as well as lift force in the z-direction

$$C_y = \frac{F_y}{\frac{1}{2}\rho_f U^2 S}, C_z = \frac{F_z}{\frac{1}{2}\rho_f U^2 S}. \tag{4.2}$$

The propulsion efficiency η is given by

$$\eta = \frac{\overline{C_T}}{\overline{C_P}}, \tag{4.3}$$

where $\overline{C_T}$ and $\overline{C_p}$ are the time-averaged values of C_T and C_P within one oscillating period. It is noted that Froude efficiency proposed by Tytell and Lauder (2004) was defined to evaluate the swimming efficiency by many studies (Borazjani and Sotiropoulos, 2008; Liu et al., 2017). But it can only be applied when the mean value of net force acting on the swimmer's body is zero which does not apply to this work when the tethered mode is considered (Borazjani and Sotiropoulos, 2008), therefore, it is not defined in this study.

4.1.2 Mesh independence study

The mesh independence study is performed to assess the appropriate mesh and time-step resolution for Re = $U_\infty c/\nu$ = 2500, m^* = 0.02, v_s = 0.25, f^* =1, θ_m = 10 degree, and the fin is uniformly distributed with a dimensionless stiffness of K_c = 1. The computational domain and fluid mesh around the caudal peduncle-in model are shown in Fig. 4.4. On the peduncle-fin surface, the no-slip condition is applied, while for the other boundaries, the non-reflective far-field boundary condition is imposed. Three grids are generated: a coarse grid with 2294292 nodes and minimum spacing of 1.48×10^{-3} c in each direction, a medium grid with 4032768 nodes and minimum spacing of 9.9×10^{-4} c, and a fine grid with 5791680 nodes and minimum spacing of 6.19×10^{-4} c. The structural mesh contains 1461 quadratic wedge elements. Furthermore, the non-dimensional time-step corresponding to the coarse grid is $\overline{\Delta t} = \Delta t/T =$ 0.00909, where T is the oscillation period, the medium grid is $\overline{\Delta t} =$ 0.00694 and the time step size for the fine one is $\overline{\Delta t} =$ 0.00556. The results of C_T when three different grids and time step sizes are used are shown in Fig. 4.5, and the mean coefficients $\overline{C_T}$, $\overline{C_P}$ as well as efficiency, are compared in Table 4.1. Observed from the comparison, we find that the medium resolution setup is sufficient to simulate the flow field around the caudal fin. Therefore, the medium grid with a time-step $\overline{\Delta t} =$ 0.00694 is used for the following simulations.

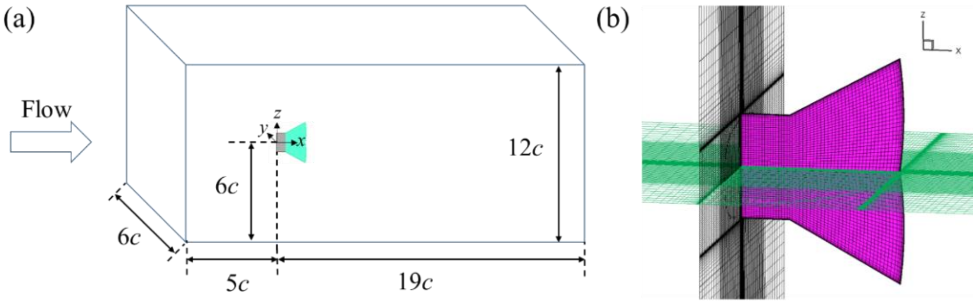

Fig. 4.4. Sketch of the computational domain (a) and the generated fluid mesh around the caudal peduncle-fin model (b).

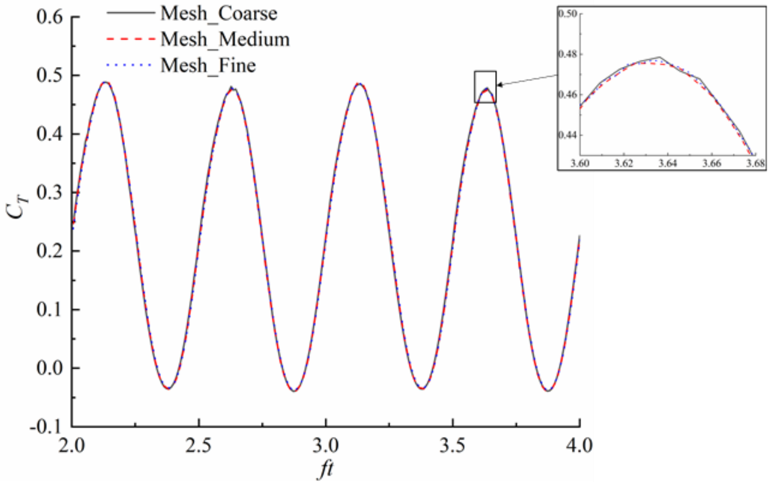

Fig. 4.5. Comparison of thrust coefficients C_T with three different resolutions for the simulations of a bluegill sunfish-inspired tail model.

Table 4.1. CFD mesh and time-step sensitivity test results.

Categories	$\overline{C_T}$	$\overline{C_P}$	η
Mesh_Coarse, $\overline{\Delta t} = 0.00909$	0.221	1.045	0.211
Mesh_Medium, $\overline{\Delta t} = 0.00694$	0.220	1.036	0.212
Mesh_Fine, $\overline{\Delta t} = 0.00556$	0.220	1.033	0.213

4.1.3 Results and discussions

With the above code verifications and resolution study, we apply the developed FSI solver to the flexible fins study aforementioned. The Reynolds number under consideration is Re = 2500, the mass ratio is $m^* = 0.02$, the rotation angle θ_m is 10 degrees, the Poisson ratio ν_s is 0.25, and the reduced frequency is $f^* = 1$. Most of these parameters are chosen to match with that in the experimental study by Ren et al. (2016a) at similar scales. It is worth noting that under such a relatively low Reynolds number, no turbulence model is employed in our study, i.e., the flow is assumed as laminar, which is adopted in many previous biomimetic studies (Liu et al., 2017; Mittal et al., 2006; Shoele and Zhu, 2012). For all the simulations, the relative coupling convergence criteria $\varepsilon_{relative}$ of displacement and fluid forces within each time step are set as 3×10^{-3} to ensure the energy balance at the interface.

The predicted time-averaged thrust, lateral forces, lift forces, power input coefficients, and efficiency, as well as the tail excursion at point A of the caudal fin under various flexural stiffnesses, are summarized in Fig. 4.6, in which the values of a rigid fin are also included for comparison. As seen from the figure, the flexibility and its distribution have a significant effect on the propulsive performance and the deformation of the caudal fin. Overall, for all the cases considered here, the tail excursion increases monotonically as K_c is raised, except that of the fin with a heterocercal profile when K_c is larger than 10. Meanwhile, the $\overline{C_T}$, $\overline{C_y}$, $\overline{C_z}$, $\overline{C_P}$ and η vary remarkably when the caudal fin is assigned with different stiffness distributions along the surface of fins. In addition, even with the same K_c, fins with different stiffness distributions present diverse propulsive capabilities. In particular, the heterocercal profile, the only asymmetrical distribution, shows distinct features as compared to others in terms of the curve variation patterns, which is consistent with the observations from the experiment work by Esposito et al. (2012).

Compared with a rigid fin, flexible fins yield larger thrust unless when the stiffness is very small, i.e., the fin is too compliant, and under this condition, the excursion of the flexible fin is also smaller than that of a rigid one. Under the parameters studied, the thrusts generated by flexible fins firstly witness a sharp increase, and most of them reach the peaks when $K_c = 5$, with an exception for heterocercal distribution, where it crests at $K_c = 10$. This is consistent with the findings by Esposito et al. (2012), where the mean fluid forces generated by both asymmetric and symmetric motions peak at different fin stiffness. After the crest, all the $\overline{C_T}$ decease with the increase of stiffness. This variation pattern can be found in many previous FSI studies involving bio-inspired propulsion (Dai et al., 2012b; Olivier and Dumas, 2016; Shi et al., 2017). Generally, among these five variations, $\overline{C_T}$ produced by a fin with heterocercal stiffness distribution differs most from others, and apart from when the fin is highly flexible, its magnitude is much smaller than the others. Meanwhile, the fin with cupping stiffness profile generates the largest thrust and these with uniform and W-shape distribution produce quite close thrust values, which is consistent with the results in Esposito et al. (2012).

With a closer inspection of Fig. 4.6(b), we can find that when $K_c < 5$, as the stiffness is increased, the differences of thrust generation due to the various flexibility distributions become more pronounced, which is consistent with the conclusion drawn by Esposito et al. (2012). In addition, for much stiffer fins, i.e., $K_c > 10$, the differences appear less distinct. This may be attributed to the fact that with the fins become stiffer, the deformations are more limited, and thus diminishing the differences caused by various stiffness profiles. This has been reflected by other research on flexible swimmer studies (Dai et al., 2012a; Olivier and Dumas, 2016). However, previous numerical studies (Shi et al., 2019; Zhu and Bi, 2017) concluded that the differences become more remarkable as the fins are more flexible, which seems contradictory with the present results and the experimental study. Nevertheless, it is noted that a fundamental difference exists in terms of kinematics and numerical model to calculate the deformation of fins. In their studies, the locomotion is accomplished by the sway motion of rays embedded in the fin membrane instead of the rotation in the experiment (Esposito et al., 2012) and this work. On the other hand, in their fin models, the various stiffness profiles are assigned on each fin ray, i.e., nonlinear Euler-Bernoulli beam, and the deformation of the fin is mainly determined by simplified linear spring models between rays. In this study, the fin is composed of segments with different rigidities, and the flexing is determined both by the fluid forces and assigned stiffness.

In terms of propulsion efficiency η, clear peaks are observed for all the variation patterns of stiffness with the increase of flexural rigidities K_c. The highest efficiency is achieved by the fin with cupping inflexibility distribution at K_c =1.5. Similar to the variation patterns of $\overline{C_T}$, η of the fin with a cupping stiffness profile performs best, and those of the fins with uniform and W-shape distribution show no evident difference. Again, the fin with a heterocercal stiffness fashion yields the lowest efficiency like the smallest thrust shown in Fig. 4.6(b) among these five variation patterns when K_c remains the same. In general, the efficiency is more sensitive to the variation of K_c when its values are small, which can be observed that when the K_c is small, e.g., when it is less than 1, the η curves drop sharply, and even a slight decrease of K_c results in a significant loss in propulsion efficiency. Instead, as the fin is much less flexible, the variation of η appears more gentle, which is consistent with previous results in Shi et al. (2019) and Zhu and Bi (2017).

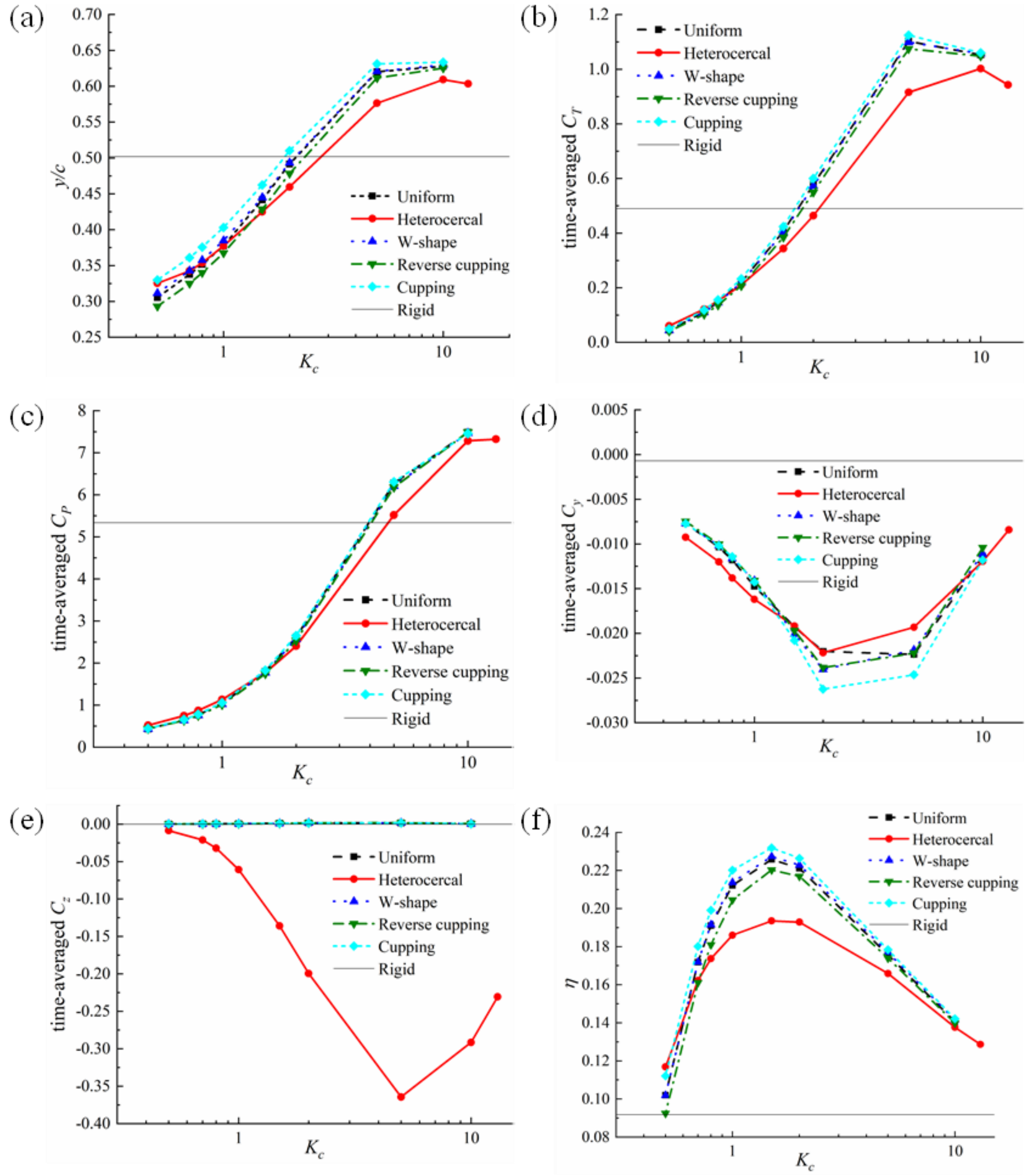

Fig. 4.6. Summary of the tail excursion at point *A* (a), time-mean thrust (b), power input coefficients (b), lateral forces (d), lift forces (e), and propulsion efficiency (f) when flexural rigidities are varied for uniform (black dash), heterocercal (red solid), W-shape (blue dot), reverse cupping (olive dash dot) and cupping (cyan short dash) stiffness distribution.

The propulsion efficiency is determined both by $\overline{C_T}$ and $\overline{C_P}$, therefore, the curves of time-averaged energy expenditure coefficients may explain the above-observed variation fashions. As seen from Fig. 4.6(c), apart from the $\overline{C_P}$ of the fin with a heterocercal stiffness profile when K_c is larger than 2, the five curves present no pronounced difference in magnitude. This may manifest the reason for the similarity of variations in $\overline{C_T}$ and η, i.e., when $\overline{C_P}$ approach with each other, the variation of η is mainly determined by $\overline{C_T}$. On the other hand, by comparison of Fig. 4.6(b) and (c), we may find that difference in the propulsion efficiency among the fin with heterocercal and other stiffness distributions mainly results from its less thrust production.

Regarding the time-averaged lateral forces coefficients, more complex variations are observed compared with the discussion above for $\overline{C_T}$ and $\overline{C_P}$ indicated by Fig. 4.6(b) and (c). Under the parameters studies, much larger lateral forces are produced by flexible fins in comparison with that by a rigid fin, and the $\overline{C_y}$ curves present a clear groove-similar profile. Large lateral force may not be beneficial to a straight-line cruising for a fish, but it can provide better maneuvering via providing a turning moment. It can be observed in Fig. 4.6(e) that, unsurprisingly, the heterocercal distribution, as the only asymmetrical stiffness fashion, yields the largest mean lift forces with the same magnitude as thrust, while $\overline{C_z}$ of fins with the other distribution patterns are negligible, which is in accordance with the experimental observation from Esposito et al. (2012).

The $\overline{C_z}$ of the fin with a heterocercal profile are all negative, indicating their contribution to the downwards maneuvering, and it witnesses a significant increase and then declines as the increase of stiffness. This may seem contradictory to the results of Zhu and Bi (2017), where they concluded that the lift forces which were all positive experienced a continuous drop when the fin is stiffer. However, it should be noted that in this study, the heterocercal profile differs from that in Zhu and Bi (2017), i.e., the flexural rigidity increases from ventral to dorsal as shown in Fig. 4.3(b), which is inverse to their counterparts. This may explain the resultant opposite lift direction. On the other hand, different variation patterns are likely to be attributed to the aforementioned differences such as kinematics and different numerical model and solution of deformation, combined with an inviscid fluid model which neglects the viscous effect and vortices effect shed from the leading dorsal and ventral edge.

To evaluate the swimming performance of aquatic animals, a dimensionless parameter, the Strouhal number, is widely used in biomimetic studies to quantify the propulsion of a pitch locomotor (Eloy, 2012; Sfakiotakis et al., 1999; Triantafyllou et al., 1993). Here we define it as $St = fa/U_\infty$, with a being the maximum peak-to-peak excursion of the tail. In Fig. 4.7, we re-plot the $\overline{C_T}$, $\overline{C_P}$ and η against the St. As depicted in Fig. 4.7, under the parameters studied, the St number ranges between 0.3 and 0.8. In most cases, with the increase of the St, $\overline{C_T}$ and $\overline{C_P}$ witness continuous rise for all the five stiffness variation patterns. It can be also observed that the peak efficiency typically occurs within a range of 0.4 to 0.6, which is in accordance with the results in Dai et al. (2012a) of a flexible pitching plate.

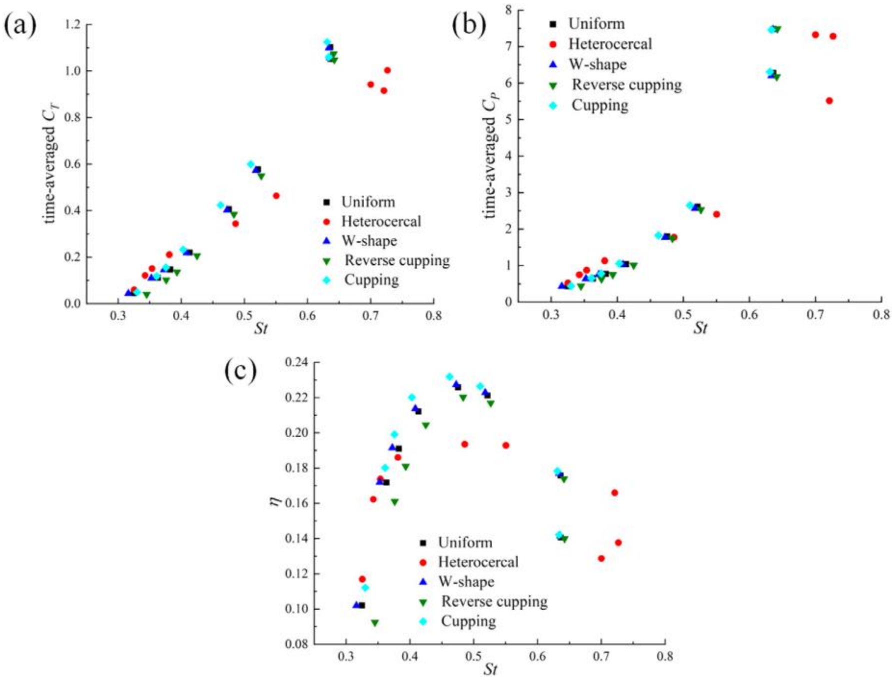

Fig. 4.7. The time-mean thrust (a), power input coefficients (b) and propulsion efficiency (c) re-plotted against the Strouhal number St defined using the tail excursion.

The instantaneous thrust, lateral forces, and power expenditure coefficients at $K_c = 5$ are depicted in Fig. 4.8. The other symmetric stiffness profiles present similar fashions as cupping which is shown in this figure. In accordance with the results in Esposito et al. (2012), the magnitude of the thrust of flexible fins increases as the fin accelerates from its extreme lateral position to the midline, and then reaches the largest approximately at the mid-stroke. Thrust gradually decreases after the fins pass the midline and then turns into a net drag, which is consistent with previous results (Akhtar et al., 2007; Zhu and Shoele, 2008). In terms of C_y, with a comparison of Fig. 4.6(d) and Fig. 4.8(b), even though the mean lateral force is smaller for a rigid fin, however, the curves of flexible fins are flatter, which means less disturbance from lateral forces, benefiting a steady straight line swimming for locomotors. Compared with a rigid fin, flexible fins require less power input, which may be explained by the fact that the flexibility reduces the work done to the surrounding fluid significantly.

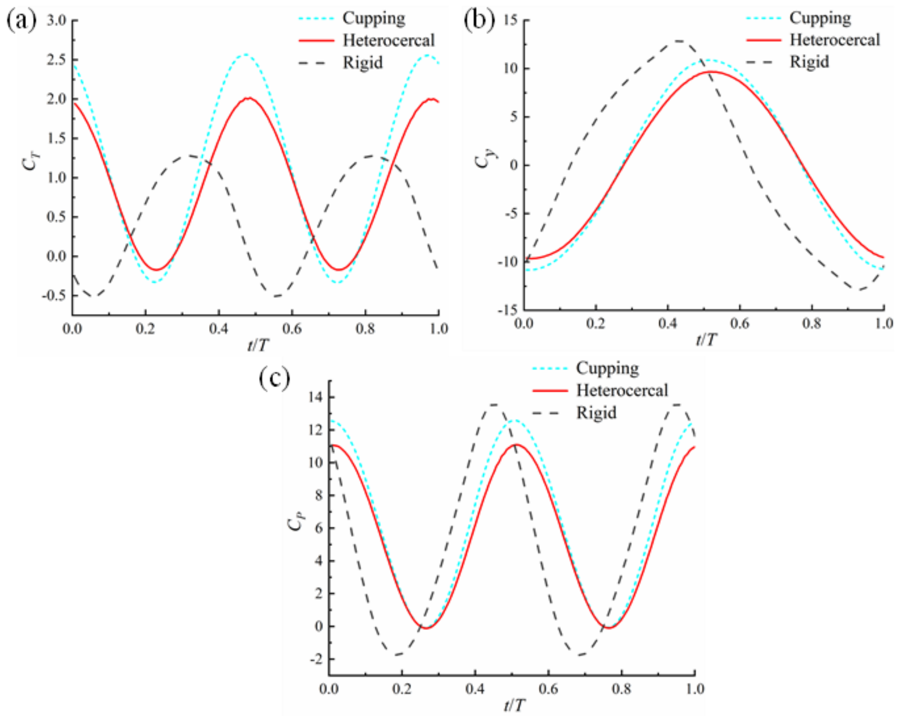

Fig. 4.8. Time history of C_T, C_y, and C_P within one oscillation period of a fin with cupping (cyan short dash), heterocercal stiffness distribution (red solid), and a rigid fin (grey dark dash) when K_c = 5.

The typical deformation patterns of fins with various stiffness fashions are presented in Fig. 4.9. For better visualization of the curvatures in the spanwise direction, Fig. 4.10 depicts the surface patterns of the trailing edge in the *y*-*z* plane during one flapping period. To facilitate the comparison, the posterior views of the real fish *in*-*vivo* obtained in the experimental studies using high-speed digital video cameras (Flammang and Lauder, 2008; Flammang and Lauder, 2009) are also presented. In their experiment, the fish was placed in a flow tank and induced to swim freely within the center region of the flow tank. By comparison of Fig. 4.9 with Fig. 4.10, it can be observed that the pure passive deformations of our models by assigning non-uniform stiffness distributions cannot exactly replicate as pronounced spanwise deformations as observed from a real fish fin. This difference may be explained by the fact that fish can actively control the propulsive surface conformation by complex muscle activities at the bases of the fish ray halves (hemitrichs) as suggested by Lauder and Madden (2006), and this active control may play a dominant role in the fin deformation. With a closer inspection of Fig. 4.10, it can be found that one common feature of the deformation styles of our models is that the deflection around the center of the fin is smaller than those away from the central segment regardless of how the stiffness distributes. This deformation pattern was also observed by Zhu and Shoele (2008) in a ray-strengthened caudal fin study. This is because the deflection of a cantilever, the flexible segment herein which composes the fin surface, is entirely determined by the external fluid load, its structural stiffness, and the segment length.

The displacements of the point *A* and *B* at the trailing edge of the caudal fin are shown in Fig. 4.11. In general, it can be observed that point *A* always leads the excursion. Like the propulsive performance presented in Fig. 4.6, the displacements of *A* and *B* of the fin with uniform and W-shape stiffness style show no evident distinction. The excursions of *A* and *B* for a heterocercal distribution present significant differences with each other, which is caused by the large deflection of the dorsal fin segment. It can also be observed that for a highly flexible fin, the deflection in the *y*-direction is rather small, which is directly associated with the actual pitching angle of the peduncle-fin model with respect to the *x*-axis. With the increase of inflexibility, the actual pitching angle increases accordingly. This may explain the thrust enhancement depicted in Fig. 4.6(b) when K_c = 5 compared with that of fins that are more compliant.

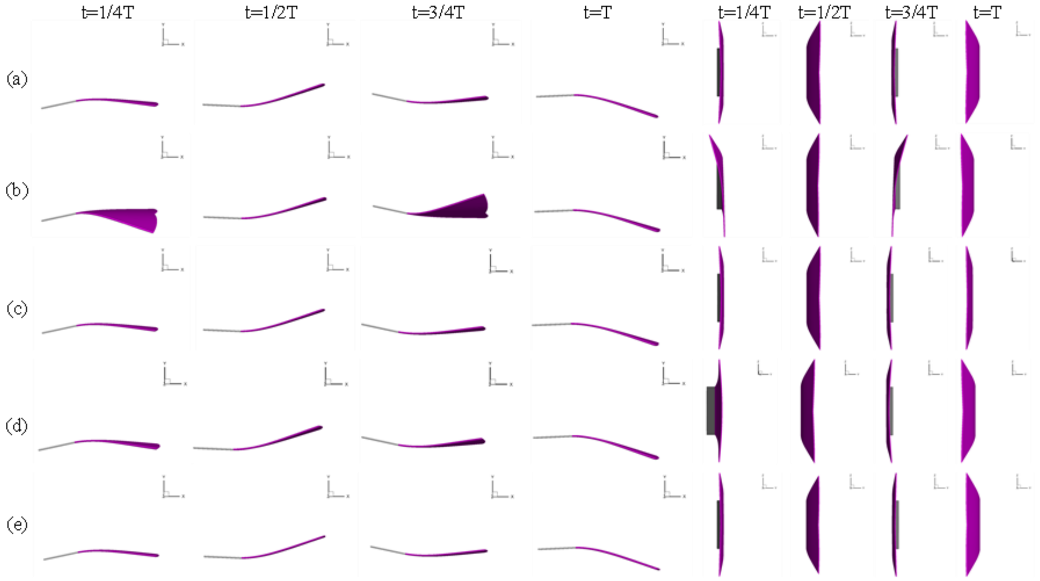

Fig. 4.9. Typical fin deformation in *xy* (left column) and *yz* view of fins with uniform (a), heterocercal (b), W-shape (c), reverse cupping (d), and cupping (e) stiffness profile. The fin is dyed in pink color for recognition.

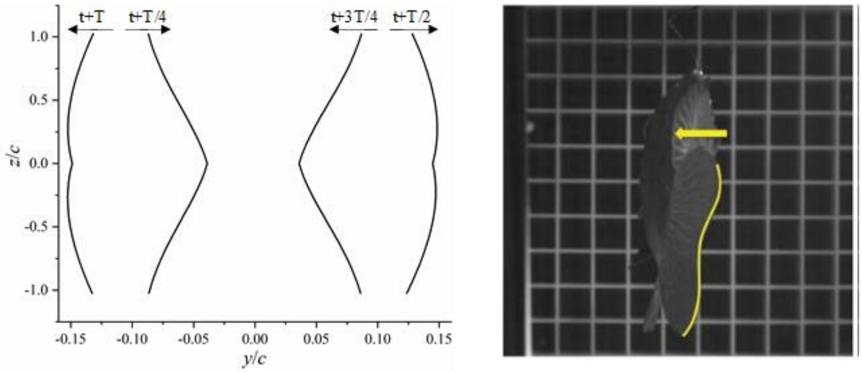

Uniform profile Flat motion

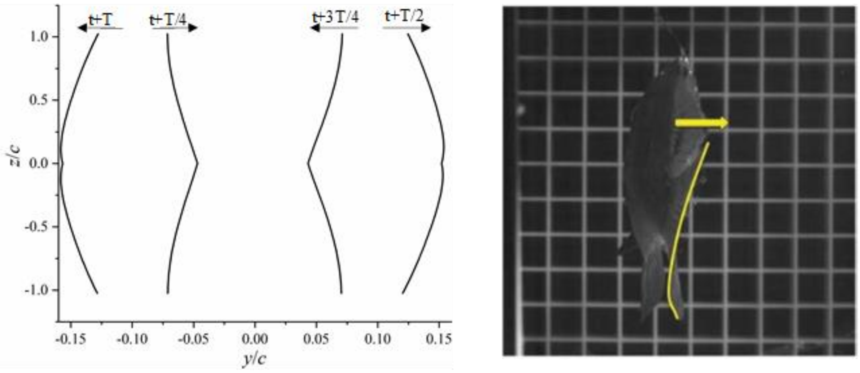

Cupping profile Cupping motion

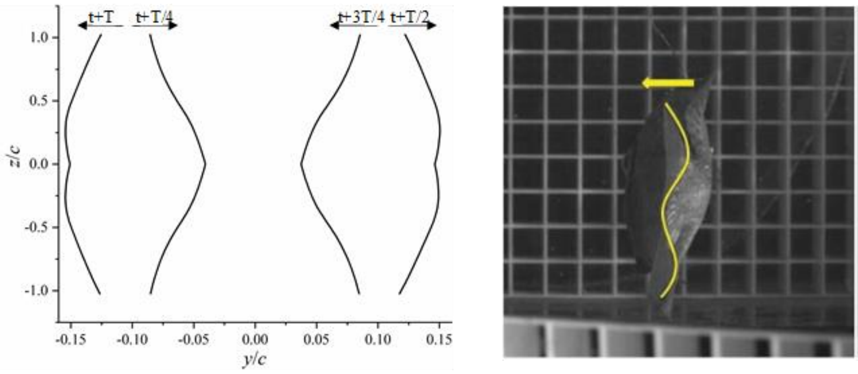

W-shape profile W motion

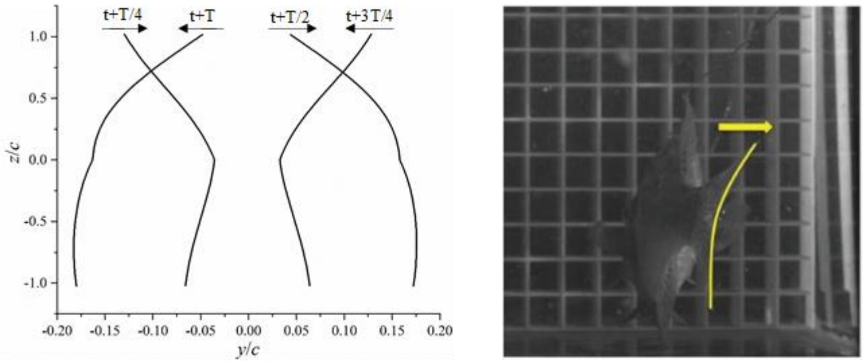

Heterocercal profile Rolling motion

Fig. 4.10. The deformation patterns of the trailing edge of the fin when $K_c = 0.5$ (a), and posterior view of a bluegill fish adopted from Esposito et al. (2012) (b).

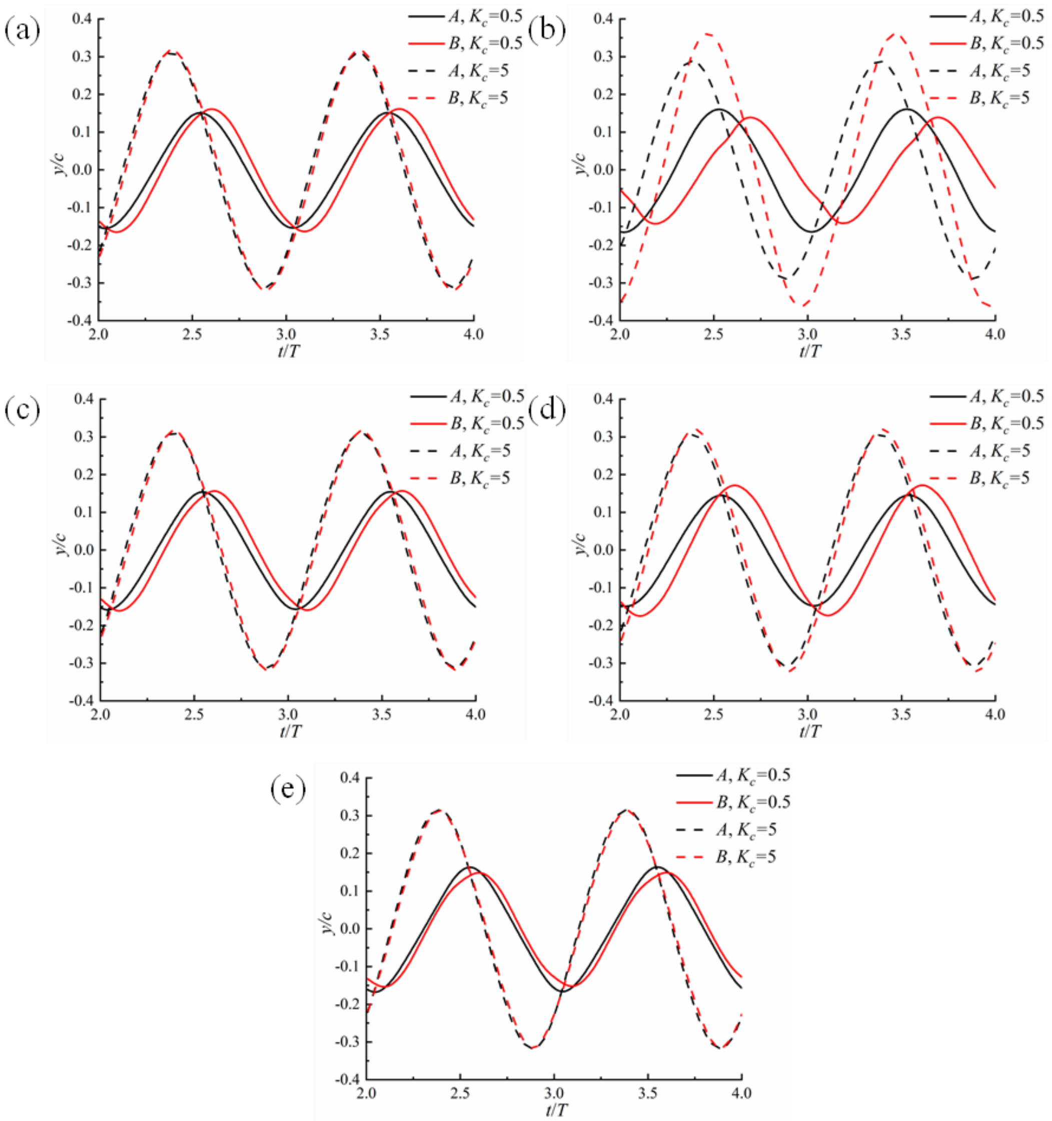

Fig. 4.11. The displacements of the point A and B when K_c = 0.5 and K_c = 5 for the fin with uniform (a), heterocercal (b), W-shape (c), reverse cupping (d), and cupping (e) stiffness distribution.

Fig. 4.12 presents the wake flows of the caudal peduncle-fin in *Y* vorticity contour. Two main tip vortices shed from the dorsal- and ventral-most trailing edge of the fin are formed parallel and alternatively. They have opposite rotation directions with one counterclockwise and the other clockwise, and for symmetrical stiffness profiles, their vortices are approximately equal. These results match those obtained in Esposito et al. (2012) and Ren et al. (2016a) using digital particle image velocimetry (DPIV) techniques and previous numerical simulations (Shi et al., 2019). A closer inspection of Fig. 4.12(e) reveals that another two observable pairs of small vortices are also attached right behind the trailing edge of the fin with cupping stiffness style, and away from that, the farther wake vortices are funneled inward towards the midline. As observed by Esposito et al. (2012), this funneling causes an accelerated jet of fluid between the vortices. These additional small vortices and remarkable funneling effect may contribute to the best propulsive performance of cupping distribution among the five profiles.

However, in comparison, the asymmetrical distribution of vortices breaks the funneling as well as the increase of fluid velocity in the wake of the fin with heterocercal stiffness distribution, which deteriorates its thrust generation.

The wake structures of the flexible fins with the cupping and heterocercal stiffness distribution when $K_c = 2$ are depicted in Fig. 4.13. It can be observed that the wake of the fins is composed of a sequence of vortex rings that induce a jet flow in the forward thrust generation direction. The cow-horn-shaped vortex rings associated with a cupping stiffness profile present a perfect symmetry relative to the midline in the z-direction. Similar wake patterns are generated by the fins with a symmetric stiffness distribution, i.e., uniform, W-shape and reverse cupping style, therefore, they are not presented here. For a heterocercal stiffness style, as the Y vorticity shown in Fig. 4.12(b), the vortex rings show a distinctive asymmetry about the midline, which induces the flow to point slightly downwards (or upwards). Therefore, prominent lift forces are produced as depicted in Fig. 4.6(e).

The pressure distribution along the fin surface is depicted in Fig. 4.14. With an exception of the fin with a heterocercal stiffness profile, which is asymmetric in both the left and right sides, the others are all symmetric in the z-direction. The right side, as the incident flow surface, is covered by negative pressure, which applies to symmetric stiffness variation patterns. However, the pressure distribution on the left side shows that a cupping profile fin has the largest high-pressure zone thus yielding the largest pressure difference. This prominent pressure difference along the negative x-direction contributes to the thrust generation as indicated by the largest thrust shown in Fig. 4.6(b). Due to that the power input is almost identical for four symmetric stiffness profiles as displayed in Fig. 4.6(c), a maximum efficiency is achieved with a cupping fin.

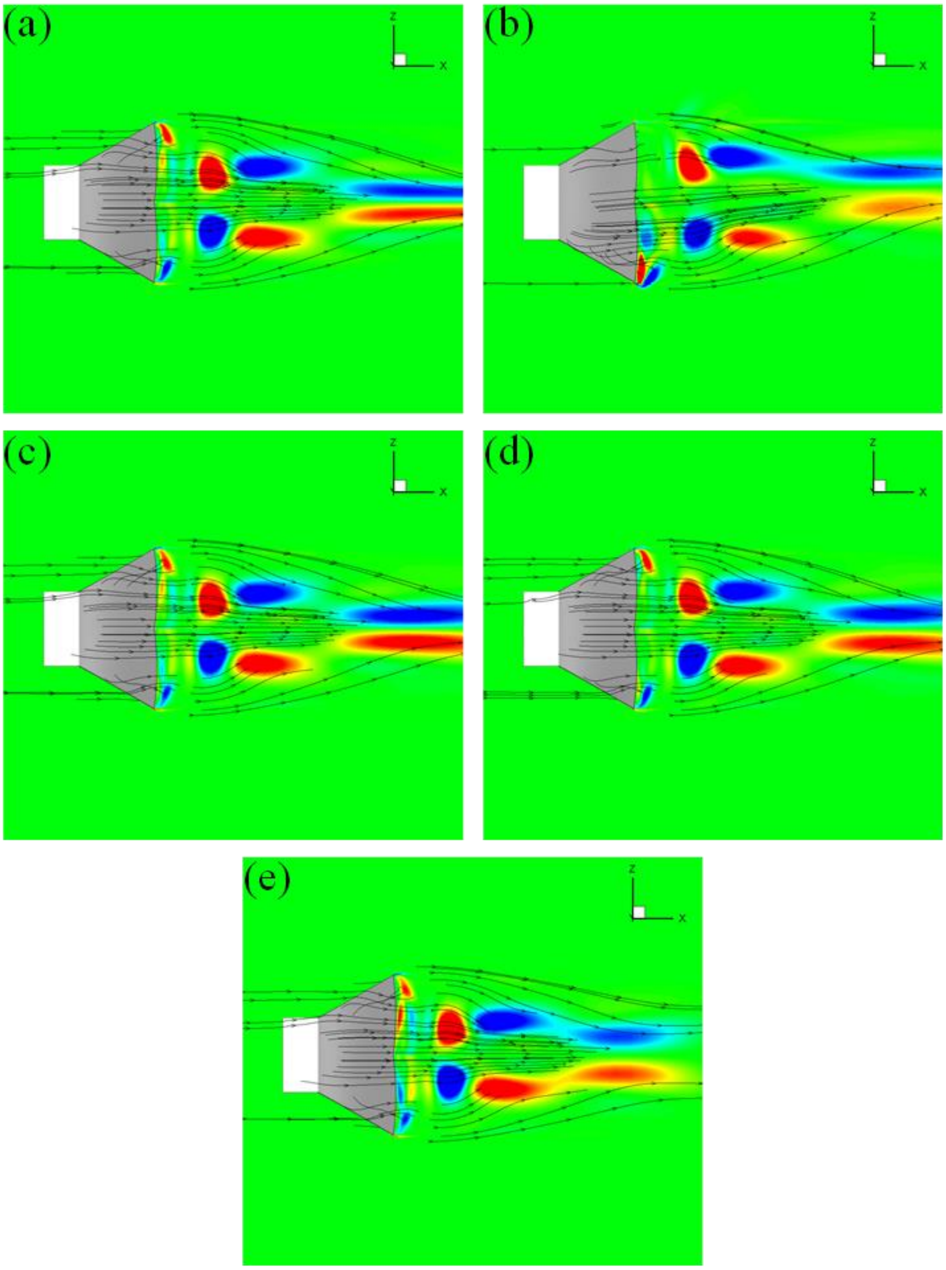

Fig. 4.12. The wake flow contoured in *Y* vorticity along with streamlines at plane $y = 0.3\ c$ when $K_c = 2$ at $t = T$ of the flexible fin with uniform (a), heterocercal (b), W-shape (c), reverse cupping (d) and cupping (e) stiffness distribution.

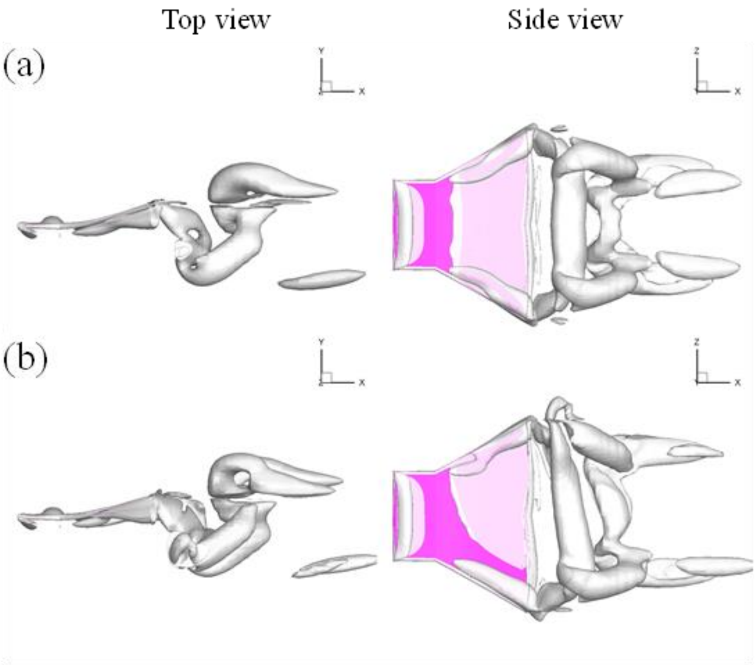

Fig. 4.13. Iso-surface of vorticity field (Q criterion) when $K_c = 2$ at $t = T$ in the wake of the flexible fins with cupping (a) and heterocercal (b) stiffness distribution. The peduncle-fin is dyed in pink color for recognition.

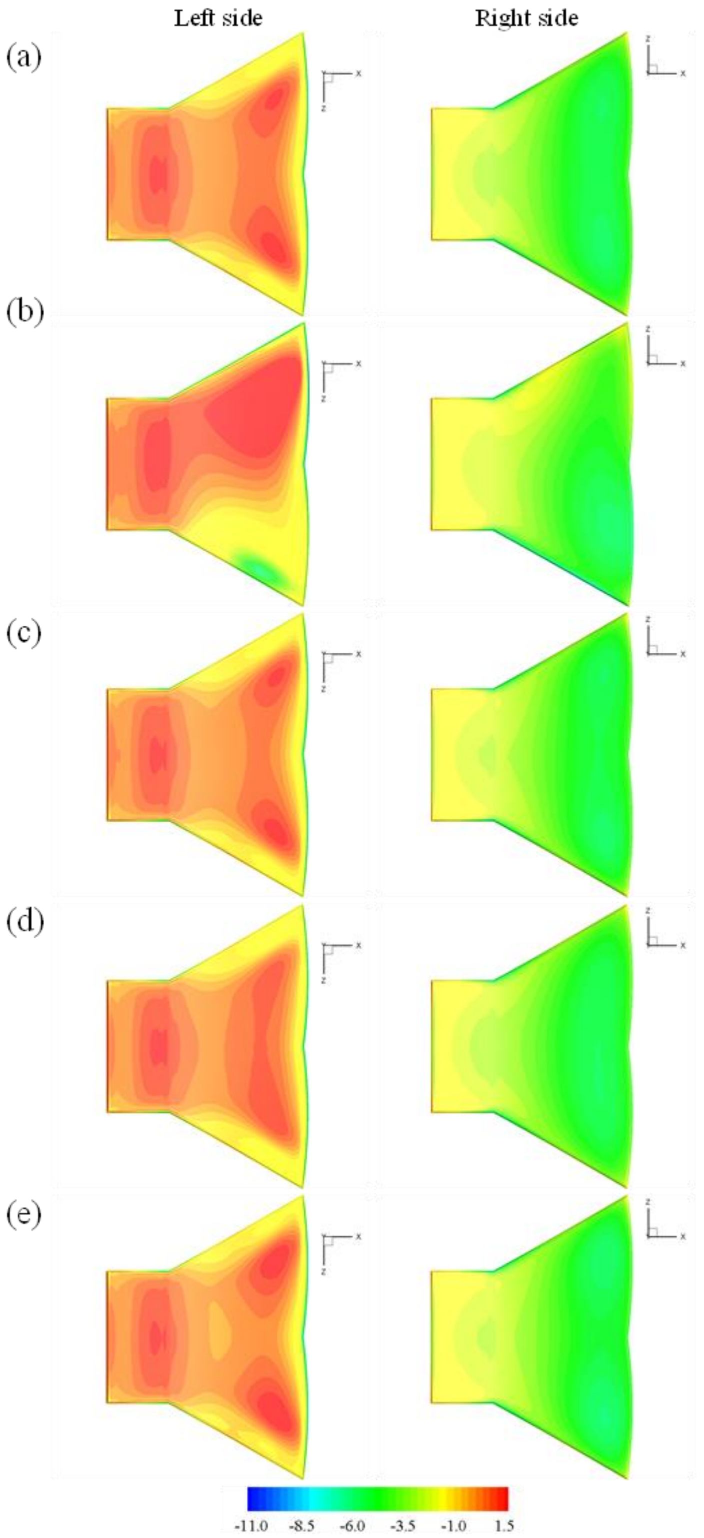

Fig. 4.14. The distribution of the pressure coefficient $C_{pressure} = p/0.5\rho_f U_\infty^2$ on the left and right side of the surface of the caudal peduncle-fin when $K_c = 2$ at $t = T$ of the flexible fin with uniform (a), heterocercal (b), W-shape (c), reverse cupping (d) and cupping (e) stiffness distribution. The left and right are defined from the viewpoint at the posterior.

4.1.4 Concluding remarks

In this section, we employ the developed multi-physics solver to simulate a rotational passively deformed caudal fin model inspired by the bluegill sunfish tail with the non-uniform flexibility distribution along the fin surface. The fin consists of nineteen segments with variable stiffness. In an attempt to test whether the numerical modeling is possible to replicate the real fin deformation, five stiffness distribution patterns are considered, e.g., uniform, heterocercal, W-shape, reverse cupping, and cupping.

The obtained numerical simulation results are consistent with the experimental data from Esposito et al. (2012) in two aspects. Firstly, we illustrate that the fin deformation, particularly the trailing edge curvature resembles the experimental observation. Secondly, the fin with cupping deformation yields the best overall performance, whereas the fin with a heterocercal profile, representing the rolling motion of fish, produces the least thrust but with considerable lift forces for maneuvering purposes. This is different from the results of Zhu and Bi (2017) where the uniform and W-shape style was reported to produce the largest thrust using a boundary element method-based fluid solver. We also showed more detailed flow structures around the swimmers with a wider range of stiffness and further explained the lift force generation mechanism by the heterocercal stiffness profile from the hydrodynamics viewpoint compared with the experiment (Esposito et al., 2012). The excellent performance brought by fin with cupping stiffness is due to the aforementioned remarkable funneling effect and the attached small vortices around trailing edges. However, this does not occur with a heterocercal pattern. We also find that with the increase of flexural rigidities, the difference in terms of thrust generation becomes more pronounced before the flexibility reaches a threshold.

4.2 The Effect of Variable Stiffness of Tuna-like Fish Body and Fin on Propulsion Performance

4.2.1 Problem statement

The present tuna-like model in Fig. 4.15(b) is inspired by the experimental studies of Feilich and Lauder (2015) and Rosic et al. (2017) and has the same dimension and size as that in the experiments. In this study, we consider the stiffness variations of the body (from the leading edge to the peduncle, as shown in Fig. 4.15(b)) and the caudal fin separately, with an attempt to shed light upon their respective effect on propulsive performance and kinematics.

However, it is worthwhile to note that the present study does not attempt to reproduce the real fish in terms of its lifelike geometry or material features *in-vivo*. Instead, like the above study in section 4.1, we focus on some key characteristics, e.g., anisotropic flexural rigidities and associated fluid-structure interaction extracted from a real fish.

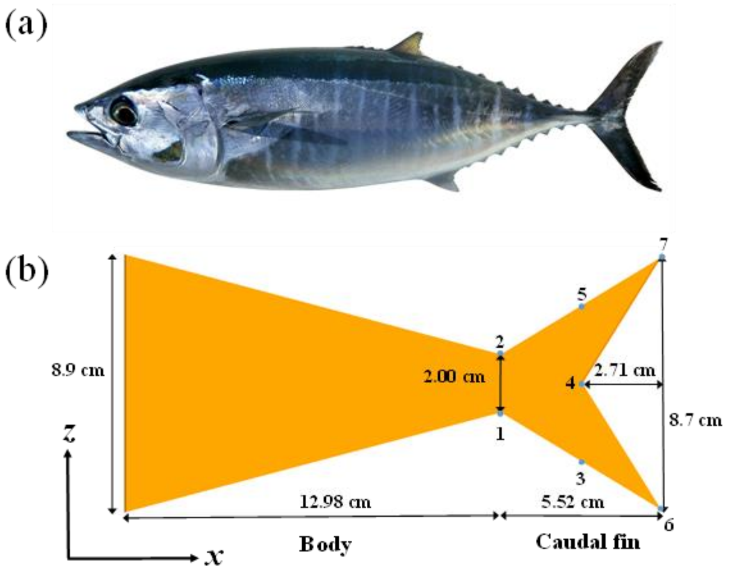

Fig. 4.15. Image of a bluefin tuna (a) (Reproduced with permission from [lunamarina / https://stock.adobe.com]) and the geometry and dimensions of the tuna-inspired swimmer (b). The leading edge of the swimmer corresponds to the point at which the body length and caudal fin height are approximately equal (Rosic et al., 2017).

The length of the model L is defined as the characteristic length in this problem, and its thickness h is 0.139 cm. The leading edge of this model matches 30% total body length point on a real live fish (Rosic et al., 2017). All the edges of the model are chamfered to ease our fluid solver mesh generation. Following the experimental studies in Feilich and Lauder (2015) and Rosic et al. (2017), the swimmer performs heave motion in the y-direction, i.e., the leading edge moves laterally in heave without the pitch motion, in a uniform flow along the positive x-direction with a velocity of U_∞. The time-dependent heave motion of the model is described by $y(t) = y_0\sin(2\pi ft)$, where y_0 is the maximum heave amplitude and f denotes the oscillation frequency.

The dimensionless parameters are defined in this study as the Reynolds number Re = $U_\infty L/\nu$ with ν being the kinematic viscosity of the fluid; the mass ratio $m^* = \rho_s h/\rho_f L$, with ρ_s and ρ_f representing the density of the solid and fluid respectively; the reduced frequency $f^* = fL/U_\infty$; the non-dimensional stiffness $K = EI'/(\rho_f U_\infty^2 b'L^3)$, where E denotes Young's modulus and $I' = b'h^3/12$ is the area moment of inertia of the cross-section per unit height. It is worth noting that the height of the model b' is variable along the body length. We take the unit height b' as a reference here for simplification (Dai et al., 2012a).

As aforementioned, the stiffness distributions of the body and caudal fin are considered separately to avoid the interactive effect. Specifically, two scenarios are considered here, i.e., one is varying stiffness along the body while the other has different spanwise stiffness distributions in the tail.

Firstly, the stiffness variation along the body length is described. The body of this model which is considered as 70% total length of a real fish is chosen to be composed of 21 segments in our study (the vertebral number for various scombrid fishes ranges from 22 to 66 (Fierstine and Walters, 1968)), as shown in Fig. 4.16. Each body segment is assigned with a unique K, i.e., for the ith segment, the normalized flexural rigidity is $K_{bi} = E_{bi}I'/(\rho_f U_\infty^2 b' L^3)$ ($i = 1,\ldots, N_b$, where $N_b = 21$). To our knowledge, there are no direct stiffness measurements of tuna bodies in the literature. Instead, inspired by the stiffness distributions measured by McHenry et al. (1995) of a Pumpkinseed Sunfish, the variation pattern of K_{bi} is written in the form of part of an elliptic equation as

$$K_{bi} = K_c \left\{ 1.1 - \sqrt{1.002 \times \left[1 - \frac{\left(i - N_b - 1\right)^2}{445.444} \right]} \right\}, \tag{4.4}$$

where K_c is a constant and denotes the normalized flexural rigidity of the first segment. Meanwhile, a uniform profile $K_{bi} = K_c$ is also used for comparison. These two variation patterns are denoted by NU (**n**on-**u**niform) and UB (**u**niform along the **b**ody length) modes for simplification. The variation patterns of the flexural rigidities of the body segments are depicted in Fig. 4.16(b). In all these cases, the stiffness of the first segment is 10 times that of the segment near the peduncle, which is within the range of stiffness variation naturally observed in live fishes (McHenry et al., 1995). When the stiffness of the body segments is varied, the caudal fin has a uniform stiffness with a value of 0.04 K_c which is derived from the estimation from the measurement in McHenry et al. (1995).

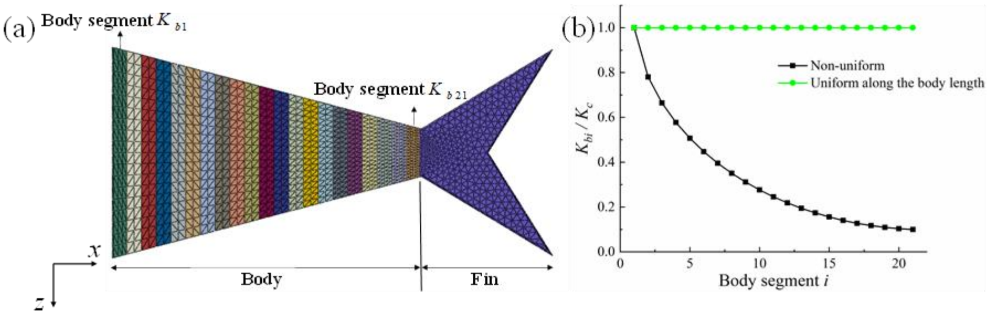

Fig. 4.16. The structural mesh with different segments of the body (the different color represents a unique stiffness) (a), and the distribution patterns of the body segment stiffness (b).

Regarding the flexural rigidities variation of the fin surface, inspired by the studies by Zhu and Bi (2017), the following stiffness profiles are used in an attempt to replicate some deformation patterns of the caudal fin observed from scombrid fishes in Fierstine and Walters (1968) and Gibb et al. (1999), i.e., a cupping and heterocercal fashion. The total number of principal caudal-fin rays of a tuna fish is almost always 17 according to Fierstine and Walters (1968), and therefore, there are 17 segments in the fin part of our model ($N_f = 17$), as shown in Fig. 4.17(a). Following the study by Zhu and Bi (2017) and Shi et al. (2019), the variation styles of K_{fi} corresponding to different deformation fashions can be described as:

1. Cupping distribution: $K_{fi} = K_m R_{fi}/R$, where $R_{fi} = 1 + \gamma\left[1 - \sin\frac{\pi(i-1)}{N_f - 1}\right]$;

2. Heterocercal distribution: $K_{fi} = K_m R_{fi}/R$, where $R_{fi} = 1 + \gamma\left[1 - \sin\frac{\pi(i-1)}{2(N_f - 1)}\right]$;

3. Uniform distribution: $K_{fi} = K_m$.

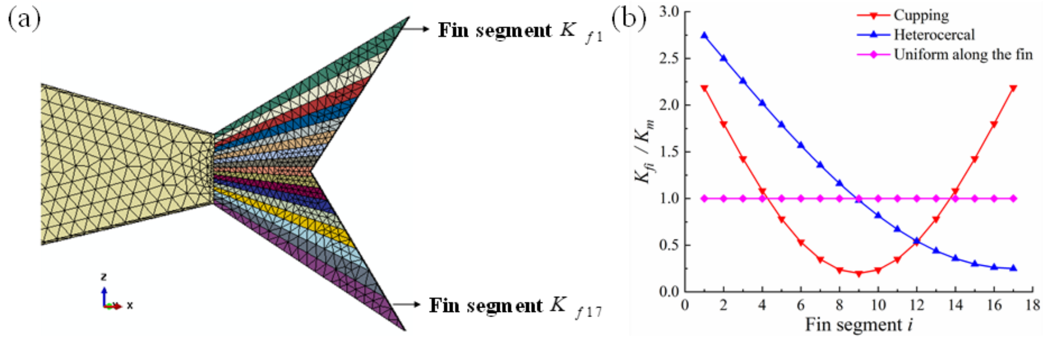

Fig. 4.17. The structural mesh with different segments of the fin (the different color represents a unique stiffness) (a), and the distribution patterns of the fin segment stiffness (b).

Here, $R = \frac{1}{N_f}\sum_{fi=1}^{N} R_{fi}$, and K_m is the mean value of the stiffness of all the fin segments. The parameter γ is used to determine the ratio of the stiffness between the least flexible segment and the most flexible one. Like the study of a bluegill sunfish-inspired tail in section 4.1, γ = 10 is selected in this work. The uniform distribution is also introduced here for a comparison. The three stiffness fashions are notated by CF (**c**upping style **f**in segments), HF (**h**eterocercal style **f**in segments), and UF (**u**niform style **f**in segments), and their corresponding stiffness profiles of the fin segments are presented in Fig. 4.17(b). Like the above practice, when the stiffness of the fin segments is varied, the stiffness of the body is uniform and has a value of 25 K_m. Following an experimental measurement of the kinematics of Sombrid fishes by Gibb et al. (1999), we also placed seven maker points, as shown in Fig. 4.15(b), on the fin surface to monitor the fin deformation during the locomotion.

The propulsion performance of the tuna-like swimmer is characterized by the mean thrust coefficient $\overline{C_T}$, the mean energy expenditure coefficient $\overline{C_P}$, the mean lateral force coefficient $\overline{C_y}$ in the *y*-direction, and the mean vertical force coefficient $\overline{C_z}$ in the *z*-direction. These mean values can be obtained by averaging the instantaneous values over one locomotion period *T*. The instantaneous thrust generated by the model is defined as

$$C_T = -\frac{F_x}{1/2\rho_f U_\infty^2 S}, \tag{4.5}$$

where *S* is the reference area, i.e., the area of the model in *xz* plane, and F_x is the component of total hydrodynamic force in the *x*-direction. Similarly, the lateral and vertical force coefficients are written as

$$C_y = \frac{F_y}{1/2\rho_f U_\infty^2 S}, \tag{4.6}$$

$$C_z = \frac{F_z}{1/2\rho_f U_\infty^2 S}, \tag{4.7}$$

where F_y and F_z are the components of hydrodynamic force in the *y*- and *z*-direction respectively. For the present tethered model in the flow, the power expenditure coefficient can be evaluated as (Olivier and Dumas, 2016)

$$C_P = \frac{F_y \dot{y}}{1/2\rho_f U_\infty^3 S}. \tag{4.8}$$

With the mean value of C_T and C_P over one period, the propulsion efficiency is given by

$$\eta = \frac{\overline{C_T}}{\overline{C_P}}. \tag{4.9}$$

4.2.2 Mesh independence study

A mesh independence study is performed to assess the appropriate mesh and time-step resolution for $f^* = 2.5$ when the stiffness of the body segments is varied in the UB pattern with $K_c = 0.1$. Three grids are generated: a coarse grid with 2628096 cells of which the minimum grid spacing is 1.48×10^{-3} *L*, a medium grid with 4056000 cells of which the minimum grid spacing is 9.73×10^{-4} *L*, and a fine grid with the cell number is 5679360 of which the minimum grid spacing is 5.95×10^{-4} *L*. The computational domain and the medium fluid mesh around the tuna-like locomotor are shown in Fig. 4.18. On the model surface, the no-slip condition is applied, while for the other boundaries, the non-reflective far-field boundary condition is imposed. The structural mesh contains 4937 quadratic tetrahedral elements. For the three fluid meshes, different non-dimensional time-step sizes, defined as $\overline{\Delta t} = \Delta t / T$ are used, i.e., $\overline{\Delta t} = 0.0087$ corresponding to the coarse mesh, $\overline{\Delta t} = 0.0069$ corresponding to the medium mesh, and $\overline{\Delta t} = 0.0056$ for the fine mesh. The time variation of C_T within one locomotion period, when three meshes with different time-step sizes are used, are compared in Fig. 4.19. As seen, the results yielded by the medium and fine mesh are quite close. Therefore, the medium mesh and $\overline{\Delta t} = 0.0069$ are used for our following simulations to reduce computational cost while retaining sufficient accuracy.

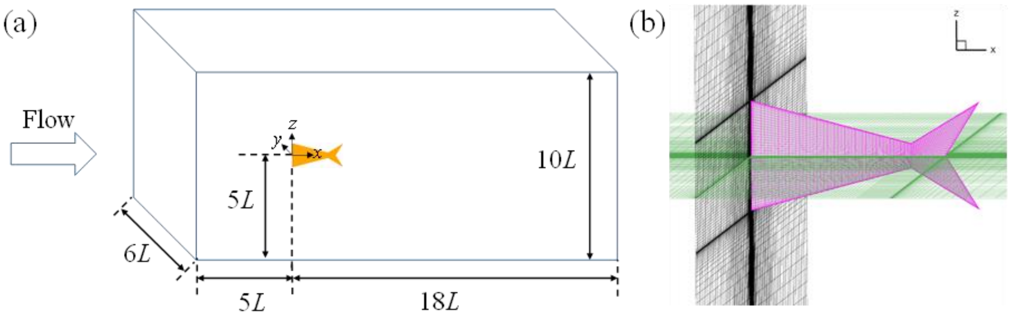

Fig. 4.18. Sketch of the computational domain (a) and the generated medium fluid mesh around the tuna-like model (b).

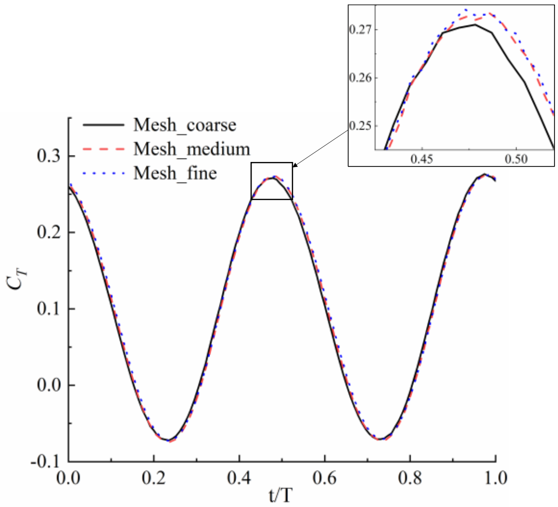

Fig. 4.19. Comparison of thrust coefficient C_T with three different meh resolutions for the simulations of a tuna-like swimmer.

4.2.3 Results and discussions

For all the simulations in this section including the above mesh independence study, the Reynolds number Re = 8000, mass ratio m^* = 0.0089, the heaving amplitude y_0 =1 cm, the Poison ratio v_s = 0.25. Most of the parameters are chosen to match that in the experiment by Rosic et al. (2017). It is worth noting that the flow in our study is assumed to be laminar. At this Reynolds number regime (below or in the order of 10^3), the turbulence effect may play an insignificant role on the flow field, which was proved in some previous studies (Bozkurttas et al., 2009; Buchholz and Smits, 2006). Thus, laminar flow is accepted for biomimetic studies (see (Dong et al., 2010; Li et al., 2018; Liu et al., 2017)).

4.2.3.1 Results when stiffness distribution of the body is varied

The midline kinematics envelopes of the tuna-like models with uniform and non-uniform stiffness variations along the body length at f^* = 2.5 are depicted in Fig. 4.20. The variation pattern of the model at K_c = 2 corresponds to the first mode defined by Michelin and Llewellyn Smith (2009). They characterized the vibration modes of the flexible wings according to the number of necks in the enclosing envelope. Therefore, other patterns correspond to a second mode. We also find that material flexural rigidity governs the number of waves and an increase of wavelengths along the model with increasing inflexibility is observed here which was also demonstrated in previous studies (Dai et al., 2012b; Feilich and Lauder, 2015; Rosic et al., 2017).

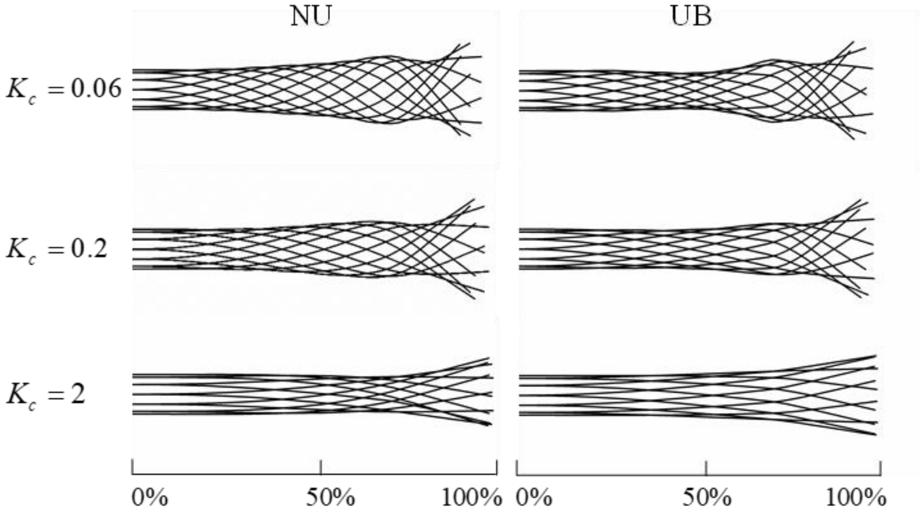

Fig. 4.20. Midline kinematics of the tuna-like models with non-uniform and uniform stiffness distributions along the body when f^* = 2.5, K_c = 0.06, 0.2 and 2.

With a closer inspection of the quantitative results of the lateral displacements, as shown in Fig. 4.21, the difference in the excursion in the lateral direction between the two stiffness distributions is mainly seen between 40−80% of the model length. The maximum tail tip displacement is experienced by the intermediate-stiffness model when K_c = 0.2 of the model with NU stiffness variation pattern, followed by that of the model with UB profiles when K_c = 0.2 and 0.06.

The total lateral displacements presented by live tuna kinematics measured by Donley and Dickson (2000), the S3 foil model in the experimental study (Rosic et al., 2017), and the current FSI tuna-like swimmer model are compared in Fig. 4.22. It can be found that the latter two show different kinematics variation patterns compared with that observed from a real kawakawa fish. The most evident difference between the tuna-like models and tuna is that the minimum lateral displacement of the tuna fish is located at around 20−40% of its “thrust producing” body length which corresponds to 44−58% of its total length, while for most of the other models they are observed around 50−80% of the models’ length, as shown in Fig. 4.21 and Fig. 4.22.

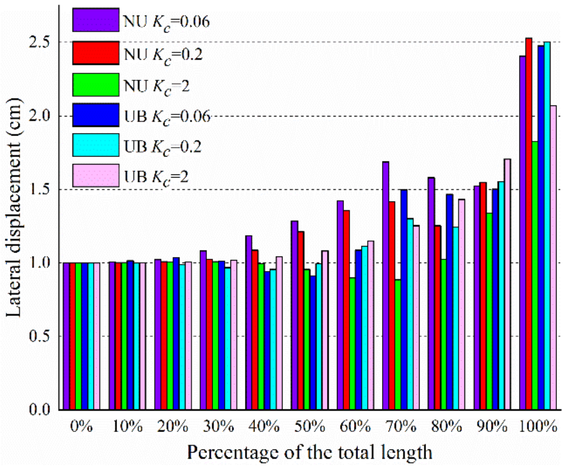

Fig. 4.21. The lateral displacement as the percentage of the model length when the stiffness along the body length is varied at f^* = 2.5.

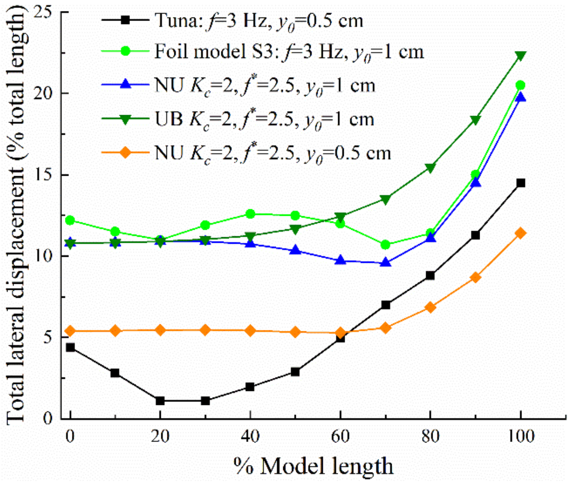

Fig. 4.22. The lateral displacement as the percentage of the length posterior of the point of the maximum body depth of a tuna (square) (Donley and Dickson, 2000), percentage of the length of the foil S3 (circle) (Rosic et al., 2017), and the percentage of the length by the present model (triangles). The heave amplitude of the tuna means the lateral displacement at the position of the tuna's body corresponding to the leading edge of S3 foil in (Rosic et al., 2017) and the present models.

The results of $\overline{C_T}$, $\overline{C_P}$ and η when K_c is varied under different heave frequencies are depicted in Fig. 4.23. As can be observed from Fig. 4.23(a), the generated thrusts generally increase with a larger locomotion frequency. The effects of body stiffness distribution patterns on thrust production are not monotonous. Under the parameters studied here, the NU mode generally creates a larger thrust than the UB mode by a small majority (15 out of the total 26 cases). Nevertheless, the advantages of the NU mode are only presented in low frequencies, i.e., f^* = 2 and f^* = 2.5, where larger thrust force is yielded by the NU style in more than 70% of the cases (13 out of 18 cases). In contrast, for a higher frequency when f^* = 3.7, the UB mode produces a larger thrust for most cases (6 out of the 8 cases). Based on an experimental study of flexible rectangular foils in Shelton et al. (2014), one would expect the maximum thrust occurs at K_c = 8 which has the largest stiffness when the frequency is fixed. However, our results indicate that at this point, thrust is not the largest when f^* = 3.7 even there is no thrust generated under a small frequency. This finding corroborates a similar conclusion by Rosic et al. (2017) that the stiffer models do not always produce more massive thrust.

The kinematic patterns are not reliable indicators in predicting swimming performance, as suggested by Rosic et al. (2017). For example, the models with the NU stiffness variation have the most "fish-like" kinematic curvatures at K_c = 0.2 (see Fig. 4.20), and therefore they are expected to present high performance. However, their thrust production is poor in some circumstances, e.g., at f^* = 2.5 and K_c = 0.2, compared with that of the cases at K_c = 0.06 and K_c = 0.5 at the same frequency. On the other hand, based on the experimental results of rectangular foils by Lucas et al. (2015), they suggested that a larger lateral displacement, especially the tail tip displacement, leads to a larger thrust. By the comparison between Fig.

4.21 and Fig. 4.23(a), we find that for the UB mode when K_c = 0.06 and f^* = 2.5, the tip displacement is 2.48 cm and $\overline{C_T}$ = 0.12. Nevertheless, for the NU mode, it yields a tip displacement of 2.41 cm and a larger thrust coefficient $\overline{C_T}$ = 0.16 at the same stiffness and frequency. Consistent with the experimental results in Rosic et al. (2017), this indicates that the tail tip displacement does not necessarily predicate the propulsion performance in isolation.

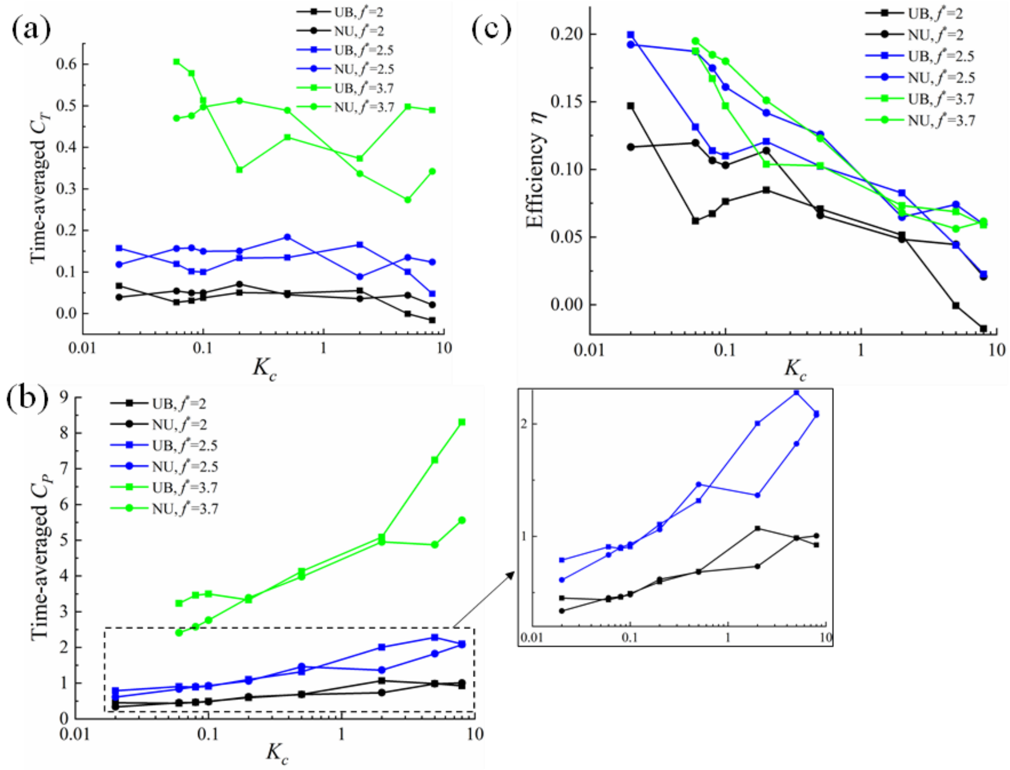

Fig. 4.23. The time-averaged coefficient of thrust C_T, power input C_P, and efficiency η when the stiffness along the model length is varied under different locomotion frequencies.

In Fig. 4.23(b), significant distinctions in $\overline{C_P}$ between the two modes are observed for very flexible and stiff cases when f^* = 3.7, and at this frequency, the NU mode is more energy-saving (7 out of the 8 cases) compared with the UB mode. When the frequency is smaller, i.e., f^* = 2 and 2.5, the difference of $\overline{C_P}$ between the two stiffness styles is less noticeable, except for a few stiffness values, e.g., K_c = 2. A quantitative comparison between these two modes revealed that a smaller $\overline{C_P}$ is seen for the NU mode in a majority of the total cases (18 out of the total 26), although some of the differences are marginal, e.g., when K_c is near 0.2.

Regarding the variations of propulsion efficiency, the effect of frequency on η is not so dominant as that on thrust and power expenditure. Namely, a high frequency does not always yield high efficiency, especially at f^* = 3.7. Generally, the more flexible models are almost always more efficient, which is in line with the experimental results in Rosic et al. (2017). This may not be applicable when the flexibility is sufficiently high, as indicated by FSI studies in Dai et al. (2012a). Given the same locomotion frequency, the NU mode performs more efficiently than the UB mode in most cases (19 out of 26 cases).

It is interesting to compare the present numerical results with that of flexible flapping wings. For example, in the numerical study of a 2D flexible flapping wing in forwarding flight, Tian et al. (2013) found that the thrust value always peaked at certain wing flexibility as the flexibility was varied (see Fig. 3(a) and Fig. 4(a) in their paper). However, in this work, global and several local thrust peaks are reached as the bending stiffness is varied at a fixed frequency, as shown in Fig. 4.23(a). The difference in variation patterns of power expenditure coefficient and efficiency between the current tuna-like model and the flapping wing can be also found in contrast with the results in Tian et al. (2013). This may be attributed to the different model shapes and kinematics imposed on the models. The present model comprises a 3D body and a forked tail while a 2D flexible plate model was used in the study of Tian et al. (2013). Besides, in Tian et al. (2013), the flapping wing performed asymmetrical combined translational and rotational locomotion, while only a heave motion is applied to the tuna-like swimmer here. When pure heave locomotion is applied to the models, the occurrence of several local thrust peaks as the variation of stiffness was also reported previously (Dai et al., 2016; Ryu et al., 2019; Zhu et al., 2014b).

As shown in Fig. 4.23(a) and (b), the data plotted using conventional dimensionless parameters defined in section 4.2.1 is not organized concisely. Thus, it may be interesting to investigate a new scaling parameter to present the data. Inspired by the scaling parameter study by Kang et al. (2011), two non-dimensional parameters are defined here, i.e., the effective stiffness $\prod_1 = E\bar{h}^3 / \left\{12\left(1-{\nu_s}^2\right)\rho_f U_\infty^2\right\}$ with $\bar{h} = h/L$ is the thickness ratio, and the relative tip deformation $\lambda = (w_{tip} - w_{root})/y_0$ where w_{tip} and w_{root} are the displacement of the tail tip and the root of the model. The resulting scaling plotted in the log-scale for the UB and NU stiffness styles is presented in Fig. 4.24. Two linear fits are used to approximate the correlation between $\log_{10}(C_T/\Pi_1)$ and λ when the value of $\log_{10}(C_T/\Pi_1)$ is positive and negative, respectively. When the frequency is small, i.e., $f^* = 2$, the values of $\log_{10}(C_T/\Pi_1)$ are all smaller than zero, and their relation to λ is well represented by the linear fit with a coefficient of determination (R^2) as 0.93. Under higher frequency, especially when $f^* = 3.7$, the variation of $\log_{10}(C_T/\Pi_1)$ with λ is less regular, indicating a more complex interaction between the structure and the fluid. With an inspection of Fig. 4.24(b), we find that more than half of the points with high frequency, i.e., $f^* = 3.7$, lie above the linear fitted line. In contrast, other smaller frequencies are more likely to be seen below this line, which indicates that frequency has a significant effect on power expenditure.

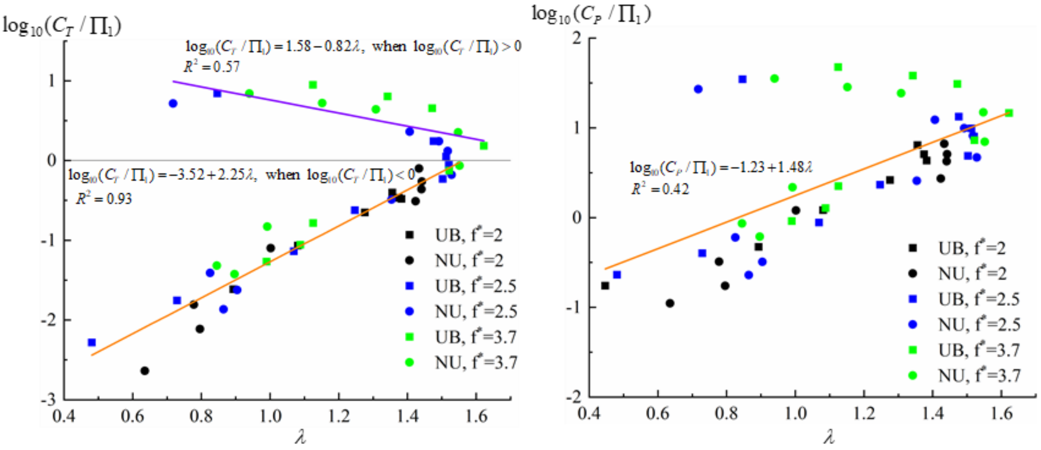

(a) (b)

Fig. 4.24. The scaled thrust coefficient (a) and power expenditure coefficient (b) as a function of λ.

The time histories of the thrust and power input within one locomotion period of the two stiffness distribution modes along the body length are depicted in Fig. 4.25. As can be observed, the non-uniform stiffness profile only slightly changes the phase positions of the peak and valley values of C_T and C_P compared with uniform distribution. Meanwhile, it significantly increases the amplitude of the instantaneous thrust, e.g., a 23% increase of the peak thrust from the UB to the NU mode. Moreover, the case with non-uniform stiffness distribution generates no drag throughout the entire motion period, which is reminiscent of a previous study on a flexible pectoral fin that fish can avoid the creation of drag force by complex 3D conformations (Mittal et al., 2006). In contrast, the power expenditure only shows a minor difference, thus leading to a significant increase of propulsion efficiency (45 % from the UB mode) at $K_c = 0.2$ and $f^* = 3.7$, as observed in Fig. 4.23(c).

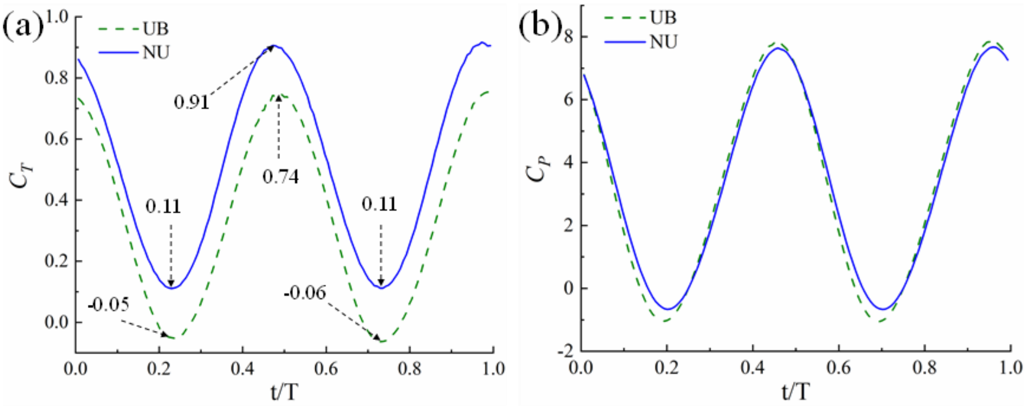

Fig. 4.25. Time histories of the thrust coefficient C_T (a) and power expenditure C_P (b) over one flapping period of the body part stiffness distribution UB and NU when K_c = 0.2 and f^* = 3.7.

The wake structure around the tuna-inspired models when body stiffness is varied is visualized in Fig. 4.26. Remarkable cow-horn-shaped posterior body vortices (PBVs) are generated near the dorsal edge (PBV(D)) and the ventral edge (PBV(V)) in the wake of swimmers with the UB and NU mode. Similar PBVs were also reported in the numerical simulations of the swimming Crevalle Jackfish by Liu et al. (2017) and a bluegill sunfish by Han et al. (2020). The dorsal and ventral PBVs are compressed towards the root of the caudal fin, as shown in Fig. 4.26(e) and (f), which has also been presented in Zhu et al. (2002) (see Figure. 8 in their paper) and Liu et al. (2017) (see Figure. 11 in their paper). This vortex compression is due to the narrowing peduncle at the posterior fish body. Leading-edge vortices (LEVs) and trailing-edge vortices (TEVs) are seen near the caudal fin whose strength is weaker than the PBVs. In comparison, the previous shed TEVs of the swimmer with the NU stiffness profile is stronger than that of the UB mode (see Fig. 4.26(e) and (f)). Additionally, the tooth-shaped vortices are seen near the first quarter model length which is covered by high pressure when the swimmer flaps at the right-most position and is about to stroke reversal.

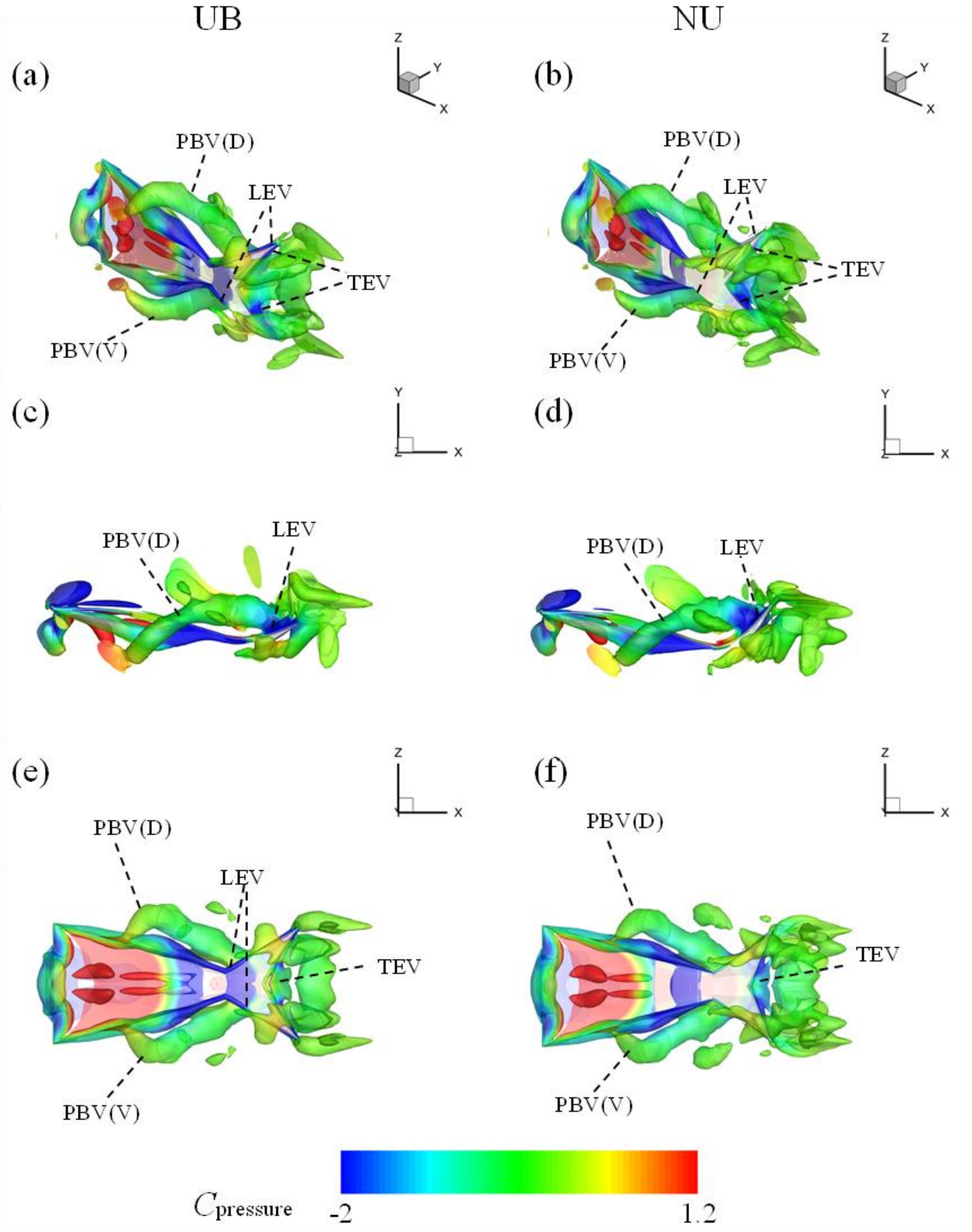

Fig. 4.26. Iso-surface of vorticity field (Q criterion) superimposed with the pressure coefficient near the tuna-like models with the UB (a,c,e) and NU (b,d,f) stiffness mode at t = 0.25 T when K_c = 0.2 and f^* = 3.7, where $C_{\text{pressure}} = (p-p_\infty)/0.5\rho_f U_\infty^2$. The 3D view, top view in the xy plane and side view in the xz plane are shown.

The Z-vorticity formulation within the *xy* plane around the locomotors with the NU and UB stiffness fashion is presented in Fig. 4.27. As can be seen, the vorticity of the two cases is qualitatively similar. At this instant, a pair of leading-edge vortices of the body and trailing-edge vortices of the tail can be observed clearly. With the illustration of the streamline, we can observe remarkable vortex flow, especially for the NU mode, near the left surface of the leading edge part of the propulsor. By comparison, the clockwise vortices near the trailing edge of the tail with the NU mode are slightly larger than that of the UB mode. The dense distribution of the streamline near the wake of the trailing edge also indicates the suction effect on the flow velocity, which may contribute to the thrust production.

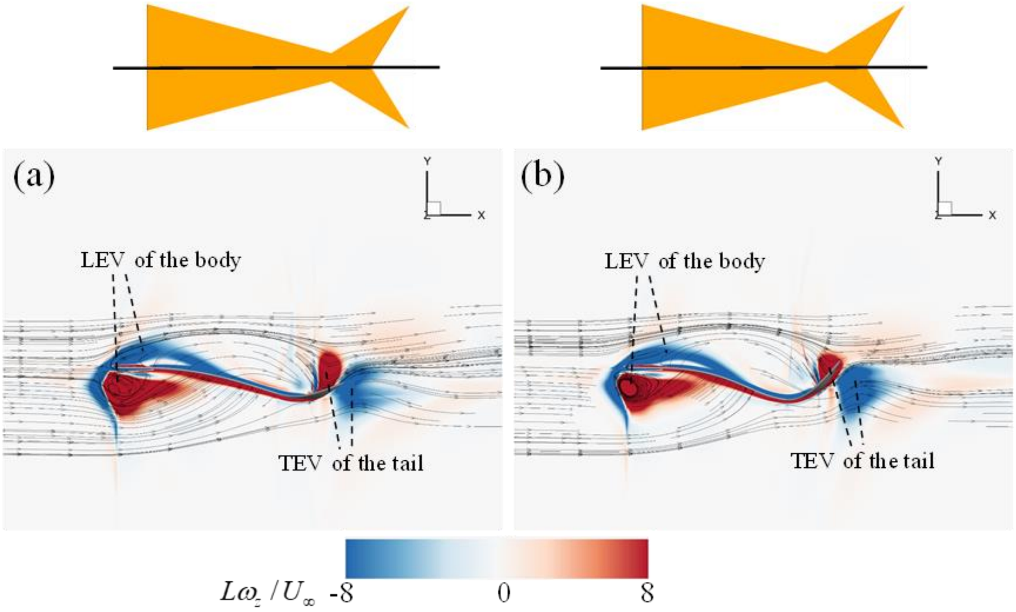

Fig. 4.27. The instantaneous *Z*-vorticity field along with the streamline condition at the plane $z = 0$, whose position is shown by the black line on the top of the figure, near the tuna-like models with the UB (a) and NU (b) stiffness mode at $t = 0.25\ T$ when $K_c = 0.2$ and $f^* = 3.7$.

To visualize the pressure distribution along the model surface, we depict the pressure coefficient contours on both sides of the model in the *xz* plane in Fig. 4.28. The area and magnitude of the high (left side surface, Fig. 4.28(a)) and low (right side surface, Fig. 4.28(b)) pressure regions of the UB mode are larger than that of the NU mode (Fig. 4.28 (d) and Fig. 4.28(e)). These high and low-pressure regions may correspond to the counterclockwise and clockwise leading-edge vortices of the body, respectively, as shown in Fig. 4.27. For instance, the counterclockwise LEVs dominate at the left side surface of the body. Likewise, high-pressure distribution is observed near the anterior body part on the same side surface as shown in Fig. 4.28(a) and (d). This is reminiscent of a numerical simulation of the mackerel-like swimmers by Borazjani and Daghooghi (2013) which suggested that the LEVs could alter the pressure distribution on the tail. By comparison, the pressure difference in the anterior part of the UB mode is more pronounced than that of the NU through direct observation. However, it appears hard to apply this method to evaluate the pressure difference in the posterior part. Despite this, the configurations of the propulsors in the *xy* plane present very different bending patterns, i.e., the tail of the model with the NU mode as shown in Fig. 4.28(f) flexes to a more considerable extent and thus showing a much larger pitch angle. This leads to a better orientation of the hydrodynamic forces along the negative *x*-axis direction, which benefits the thrust generation directly.

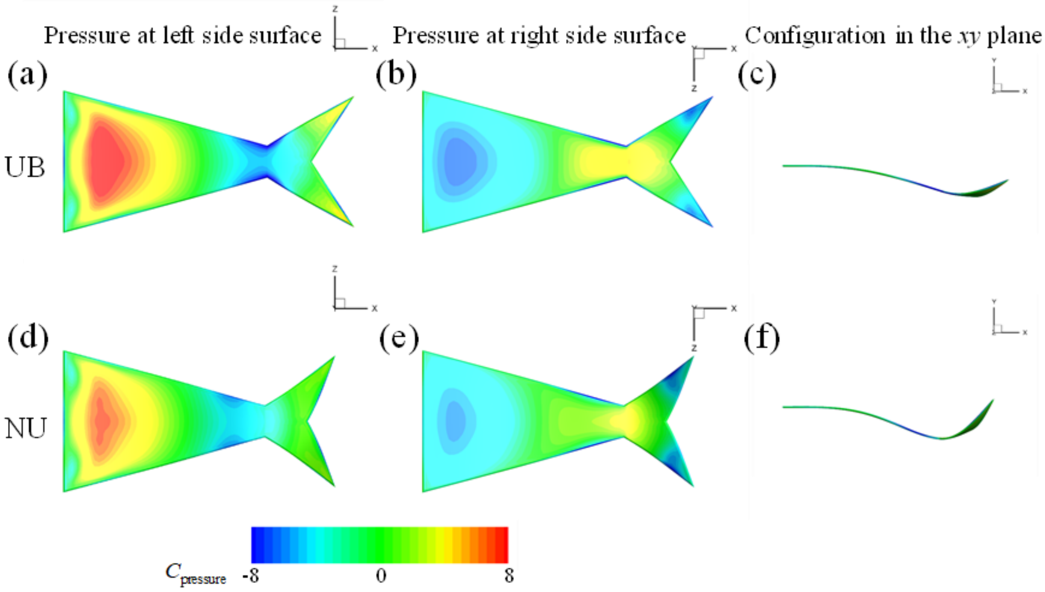

Fig. 4.28. The pressure distribution on the propulsor surface at the left and right side (defined from the posterior viewpoint), and the configurations in the *xy* plane at t = 0.25 T when K_c = 0.2 and f^* = 3.7.

The force vector, the magnitudes of C_T and C_y for the two stiffness distribution fashions within one motion period are presented in Fig. 4.29. An inspection of Fig. 4.29(a) reveals that the force generated by the model with the NU mode is almost always better oriented in the thrust direction, although in some cases the magnitude of the force is smaller than that of the UB mode. This leads the NU mode to have a larger thrust than the UB mode in the entire motion cycle, as demonstrated in Fig. 4.29(b). As shown in Fig. 4.23(c), the values of $\overline{C_P}$ for the two stiffness styles are quite close at K_c = 0.2 and f^* = 3.7, which indicates that this orientation of forces attributed to the flexing patterns of the tail does not require additional power expenditure. As a result, higher propulsion efficiency is obtained by the NU mode. The larger pressure difference at the anterior part of the model with the UB mode as shown in Fig. 4.28, however, only leads to a greater lateral force in the *y*-direction as depicted in Fig. 4.29(a) and (c), which may be adverse for the straight cruising of swimmers.

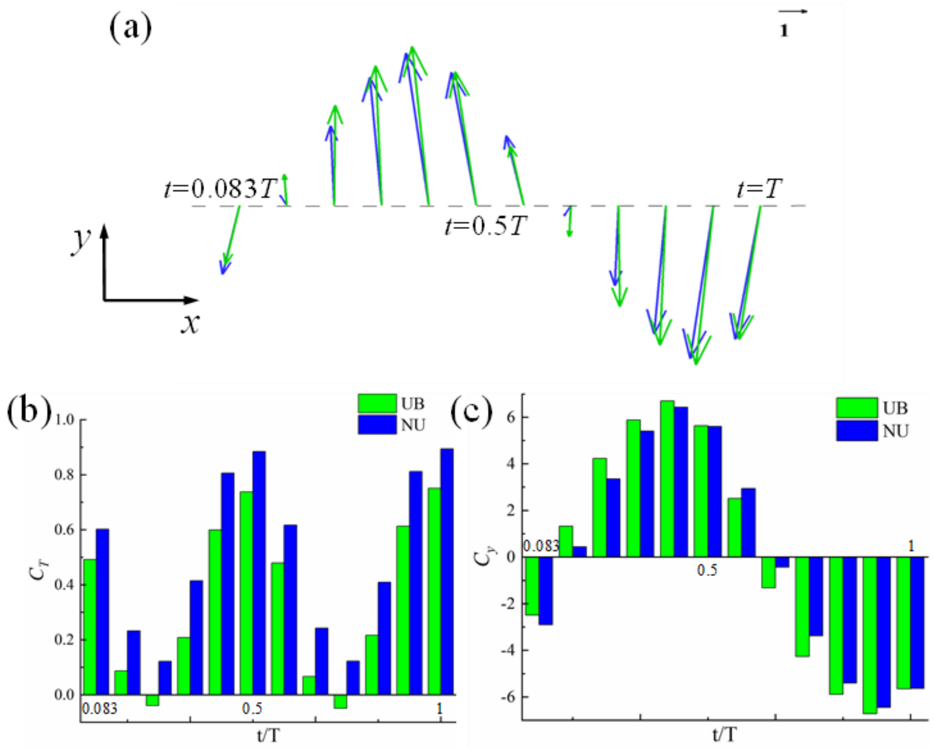

Fig. 4.29. Force vectors (a), thrust coefficient (b), and lateral force coefficient (c) of the models with the UB (green) and NU (blue) stiffness profiles over one locomotion period when K_c = 0.2 and f^* = 3.7.

4.2.3.2 Results when stiffness distribution of the tail is varied

The instantaneous deformation patterns of the swimmers with two different stiffness profiles assigned on the fin segments are presented in Fig. 4.30. The dorsal and ventral lobes of the tail with the CF mode are symmetrical concerning the middle horizontal plane, and similar conformation is observed from the UF mode and thus not shown. The tail with the HF stiffness profile yields an asymmetry of movement, i.e., the dorsal lobe leads the ventral lobe during the flapping. To quantitatively analyze the tail kinematics, the movement of the dorsal tail tip, i.e., point 7 in Fig. 4.15(b), in *x*, *y* and *z*-direction is plotted in Fig. 4.31. As can be seen, the present numerical tuna-like propulsors present relatively little tail movement in the vertical (*z*) and horizontal (*x*) dimensions but the majority of the locomotion occurs in the lateral (*y*) direction during one tail-beat cycle, which aligns with the experimental measurement of scombrid fishes by Gibb et al. (1999).

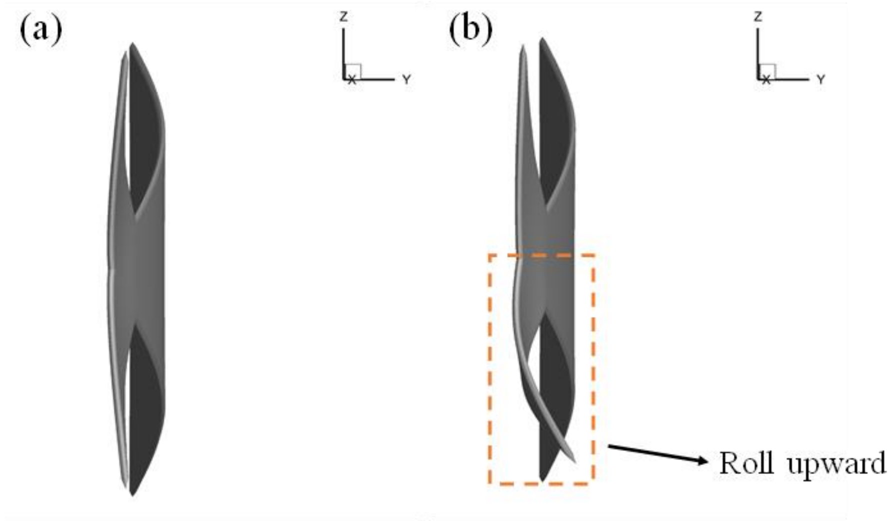

Fig. 4.30. The conformations of the tail with the CF (a) and HF (b) stiffness pattern at t = 0.25 T when K_m = 0.005 and f^* = 2.5.

By observing the time histories of the dorsal tail-tip lateral displacement and tail height in Fig. 4.32, we find that the amplitude of the tip displacement which is around 2.6 cm is close to that range around 3 cm observed from live *Scomber japonicus* fishes with a similar total body length (around 25 cm) (Gibb et al., 1999). Besides, the variation range of the tail height is about 0.5 cm and its variation period is around half of that of the varied tail-tip displacement, which is in line with the measurements by Gibb et al. (1999).

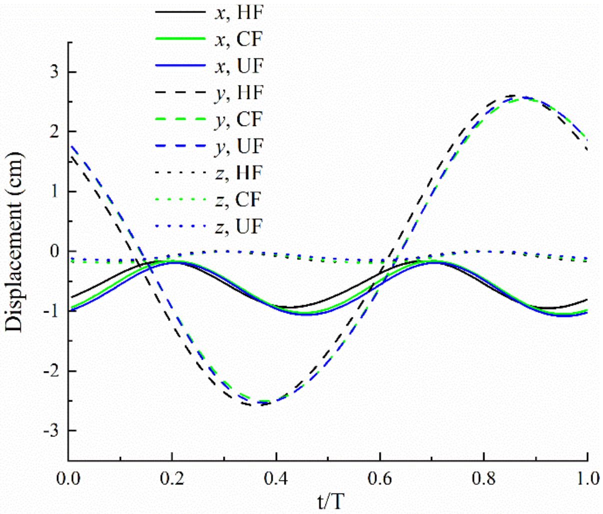

Fig. 4.31. The movement of the dorsal tail-tip of the fin in three dimensions, i.e, x (horizontal) displacement (solid line), y (lateral) displacement (dash line) and z (vertical) displacement (dot line), of the three fin segments stiffness profiles when K_m = 0.005 and f^* = 2.5.

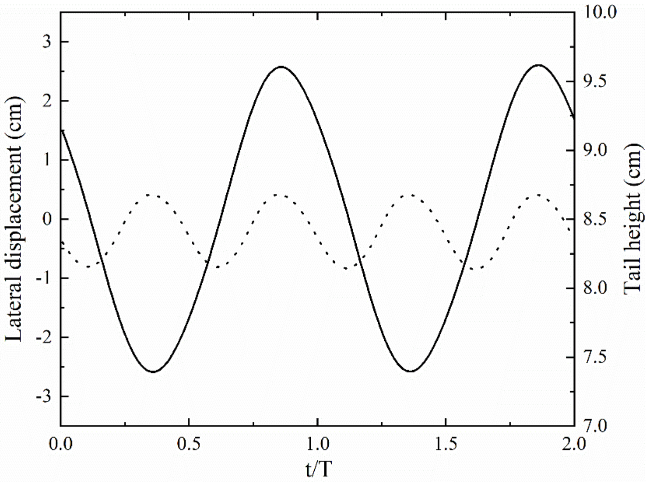

Fig. 4.32. The dorsal tail-tip lateral displacement (solid line) and the height of the tail (dash line) measured by the vertical distance of the dorsal and ventral tail-tip, when $K_m = 0.005$ and $f^* = 2.5$ for the HF mode. The UF and CF mode shows similar patterns and is not shown here. Note that the left and right vertical axis are shown at different scales.

The maximum displacements in x, y, and z-direction of the seven points 1−7 on the fin are shown in Fig. 4.33. The amplitude of the tail excursions tends to be smallest on the peduncle and mid-tail regions and larger at the tail-tips in all three dimensions, which agrees with the measurements of live *Scomber japonicus* fishes by Gibb et al. (1999). The excursions in x (horizontal) and z (vertical) direction are quite small compared with that in y (lateral) dimension whose magnitude is almost an order larger than the former.

The wave of the lateral displacement is propagated posteriorly as shown in Fig. 4.34. For instance, the ventral and dorsal peduncle points reach the maximum excursions in the lateral dimension around 10% of the flapping period time ahead of the tail tip. However, the ventral tail-tip reaches its maximum displacement of approximately 7% of the cycle time behind the dorsal tail-tip.

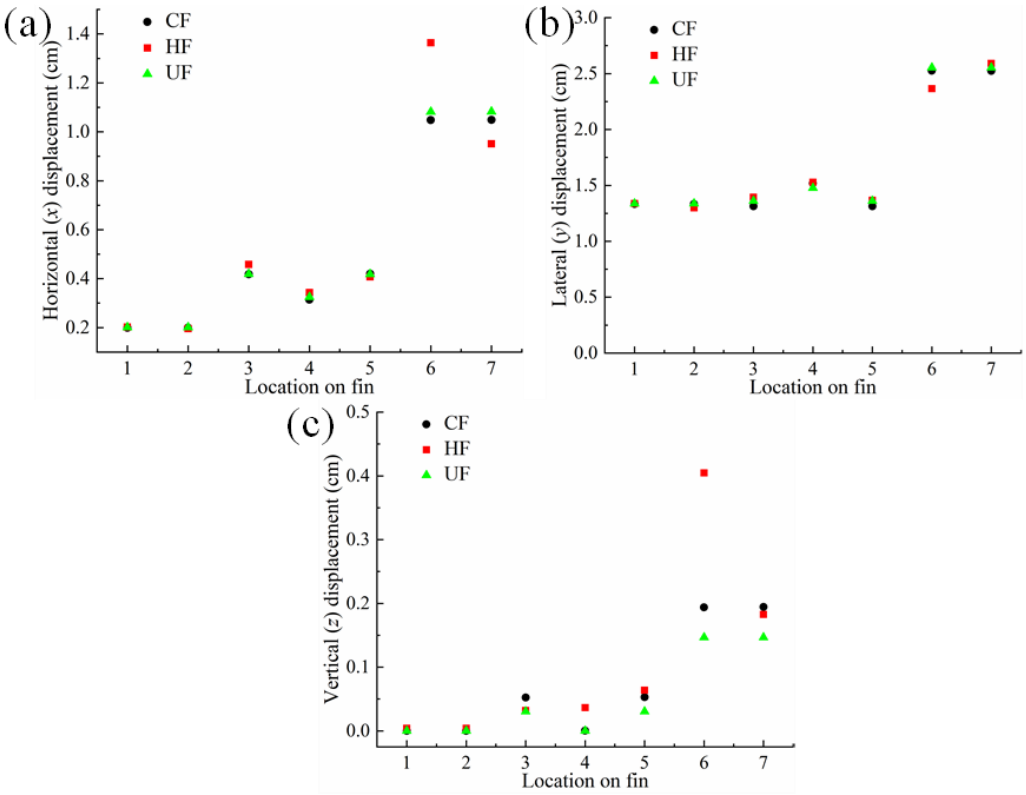

Fig. 4.33. The maximum excursion values in the three dimensions when K_m = 0.005 and f^* = 2.5. The location points marked on the fin as shown in Fig. 4.15 are: 1, ventral peduncle; 2, dorsal peduncle; 3, ventral mid-tail; 4, central mid-tail; 5, dorsal mid-tail; 6, ventral tail-tip; and 7, dorsal tail-tip.

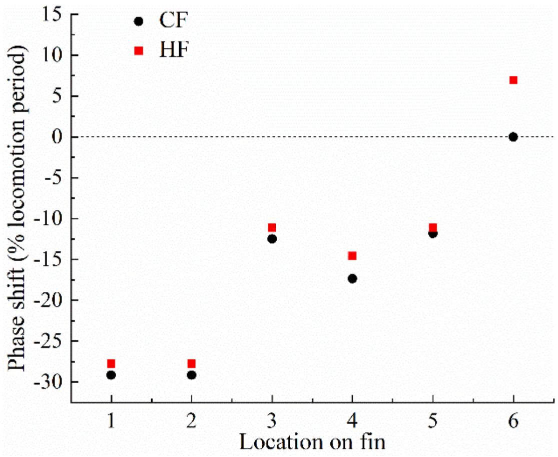

Fig. 4.34. Phase lag measured as the percentage of tail-beat cycle period illustrating the effect of location on the fin on the timing of lateral (y) locomotion of the fin. The dorsal tail-tip is defined as the reference location and therefore, has a zero phase shift. A negative value indicates that the point reaches its maximum lateral displacement before the dorsal tail-tip.

The results of $\overline{C_T}$, $\overline{C_y}$, $\overline{C_z}$, $\overline{C_P}$ and η when the stiffness is varied for the three different stiffness profiles are presented in Fig. 4.35. In general, the effects of different flexural rigidity distribution patterns on propulsive performance are mainly noticeable in the vertical-forces generation when the stiffness is the same, while others present close results. It also applies to the scenarios when the locomotion frequency is varied, and therefore they are not shown in this study.

With an inspection of the curves of thrust coefficient, we find that the tuna-like swimmers generate quite close thrusts unless at the very flexible and moderate stiff cases. At intermediate stiffness, models with the HF stiffness profile produce larger thrust compared with the others. For example, at K_m = 0.005 and 0.02, the thrust generated by the swimmer with the HF stiffness patterns increases by 4.8% and 4.0%, respectively, from that of the CF mode. Regarding the lateral (y) force production, the magnitudes of $\overline{C_y}$ for both the CF and UF fashions firstly decrease as stiffness is increased under highly flexible cases, and then experience a general increase with a larger K_m. In comparison, the lateral force by the HF mode almost always increases as the models become stiffer under the parameters studied. Only the swimmer with the HF stiffness profile yields non-negligible vertical forces, as presented in Fig. 4.35(c). The values of lift force ($\overline{C_z}$) by the HF stiffness model are generally smaller by an order of the magnitude of the thrust forces, which is in line with the experimental measurements of the forces produced by chub mackerel fishes (Nauen and Lauder, 2002). In terms of power expenditure, they all experience a continuous increase with larger inflexibility. On the contrary, the propulsion efficiency monotonously decreases as the swimmers become stiffer after the peak at K_m = 0.001. The performance drop presented in Fig. 4.35(a) and (e) at very flexible cases, i.e., K_m = 0.0008, may be attributed to the declining ability of a highly flexible swimmer to communicate momentum to the flow to induce thrust production, which has been demonstrated in Michelin and Llewellyn Smith (2009) and Olivier and Dumas (2016).

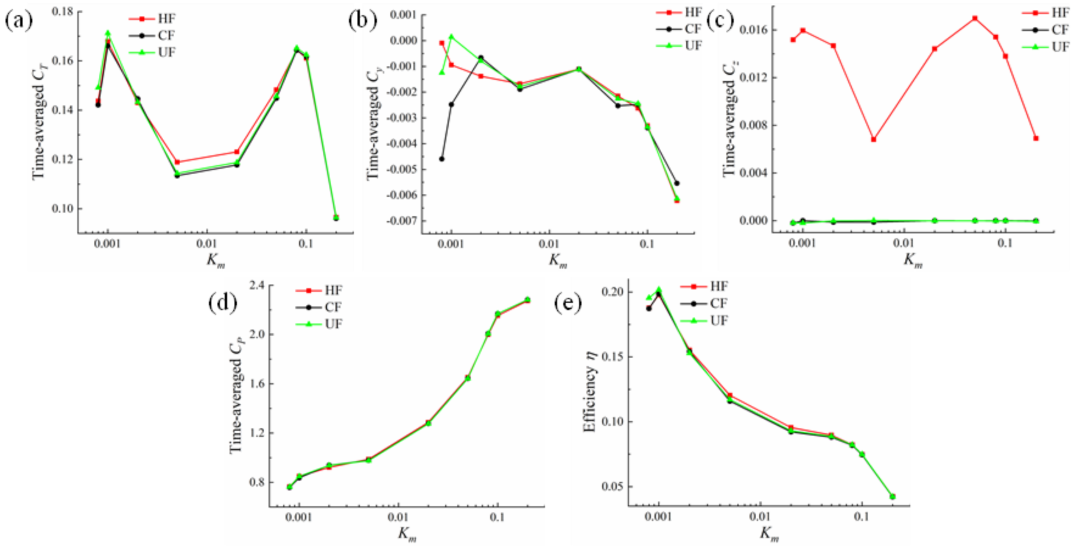

Fig. 4.35. The time-averaged coefficient of thrust C_T, lateral forces C_y, vertical forces C_z, power input C_P, and efficiency η when the stiffness along the fin surface is varied when f^* = 2.5.

To accurately distinguish the effects of body and fin on the thrust production, we split the total thrust of the swimmer into two parts as shown in Fig. 4.36. The cases when the body is rigid are also considered for comparison. As can be been, the difference in thrust among different stiffness distributions is indeed derived from the tail. Especially when the body is rigid, the thrust of the HF stiffness profile doubles compared with the others, which indicates a remarkable interaction between the body and tail during flapping.

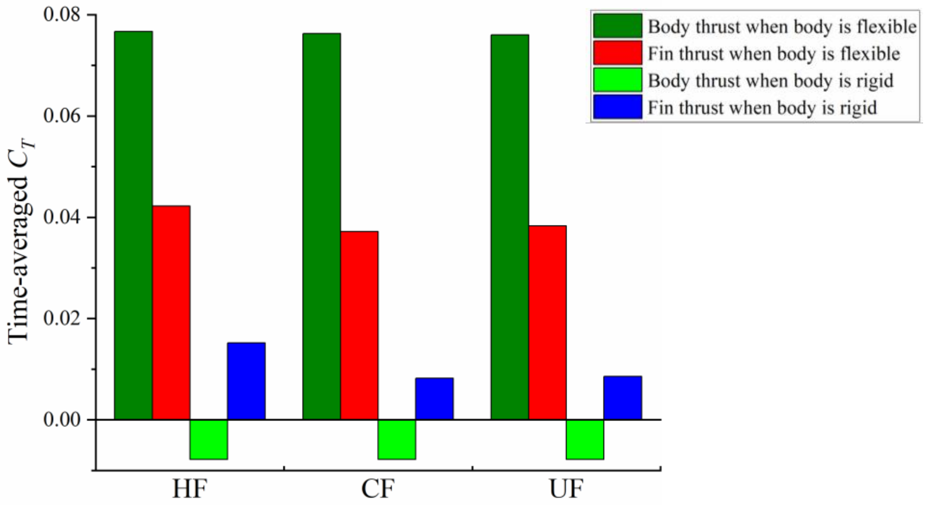

Fig. 4.36. Thrust generation of the body and caudal fin part when $K_m = 0.005$ and $f^* = 2.5$. The flexible body means the stiffness magnitude of the body part is 25 K_m as defined in section 4.2.1. The fin part is flexible in both cases.

The instantaneous variations of thrust and power expenditure over one locomotion cycle are depicted in Fig. 4.37. The total value of the model including the body and fin part and the partial value of the fin alone are both presented for comparison. With a closer inspection of Fig. 4.37(b), we find that the stiffness distribution along the fin surface appears to have little effect on the variations of C_P both of the entire model and the tail alone. Nevertheless, it has a more significant impact on the thrust production of the fin part, although this difference is almost entirely eliminated when combined into the overall consideration.

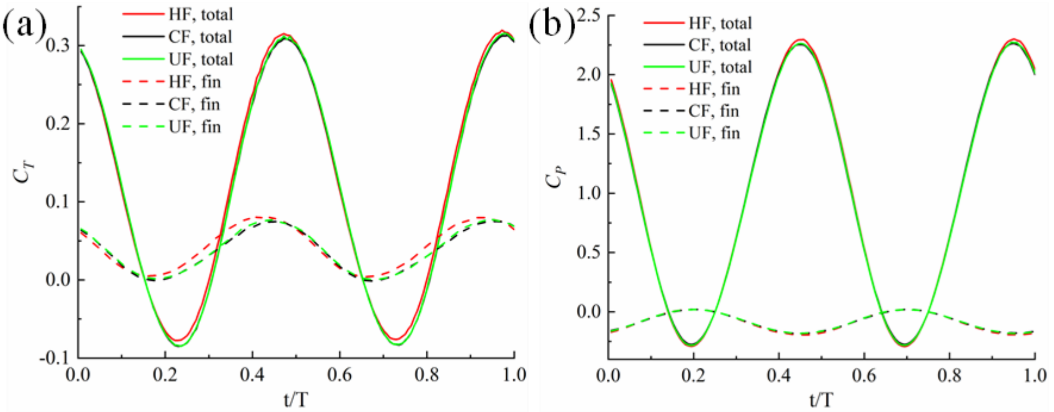

Fig. 4.37. Time histories of the thrust coefficient C_T (a) and power expenditure C_P (b) over one flapping period of the three fin segments stiffness distributions when $K_m = 0.005$ and $f^* = 2.5$.

Fig. 4.38 demonstrates the wake structure near the tail of the tuna-like swimmers with the CF and HF inflexibility patterns. The wake structures near the body are similar to those when the body stiffness is varied, as shown in Fig. 4.26. Therefore, only the vortex formation near the caudal fin is presented here. With an inspection of Fig. 4.38, we can find that the TEV of the CF mode generally presents a good symmetry relative to the middle line in the *z*-direction. A closed vortex ring is observed at the wake of the trailing edge of the swimmer with CF mode. In contrast, the counterpart near the tail of the swimmer with the HF stiffness style has an opening at the dorsal lobe, which indicates the symmetry is broken here.

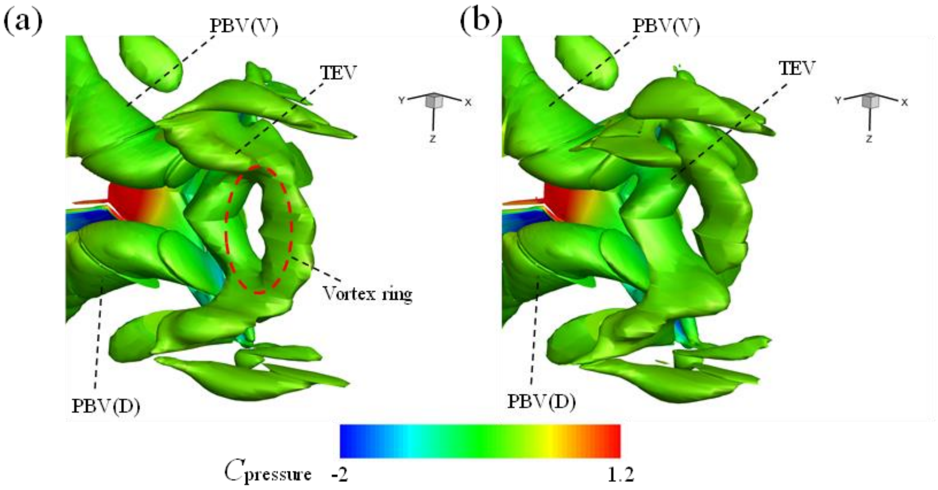

Fig. 4.38. Iso-surface of vorticity field (Q criterion) superimposed with the pressure coefficient near the tail with the CF (a) and HF (b) stiffness distributions on the fin at $t = 0.25\ T$ when $K_m = 0.005$ and $f^* = 2.5$.

The *Y*-vorticity contour and near-body streamline by the locomotor with the CF and HF profile are depicted in Fig. 4.39. As seen, the height of the vortices near the tail tip, i.e., the secondary trailing-edge vortices (STEVs), is approximately equal to the caudal fin height, which is consistent with the wake structure of chub mackerel fish obtained by using digital particle image velocimetry (DPIV) techniques (Nauen and Lauder, 2002). Their results also showed that the vortex jet was oriented at a slightly negative angle around -3 degrees relative to the horizontal x-axis. This is also presented in Fig. 4.39(b) where the perpendicular line to the streamline tilts from the vertical direction, indicating that the flow is slightly pushed downward along the negative *z*-direction as pointed by the black line.

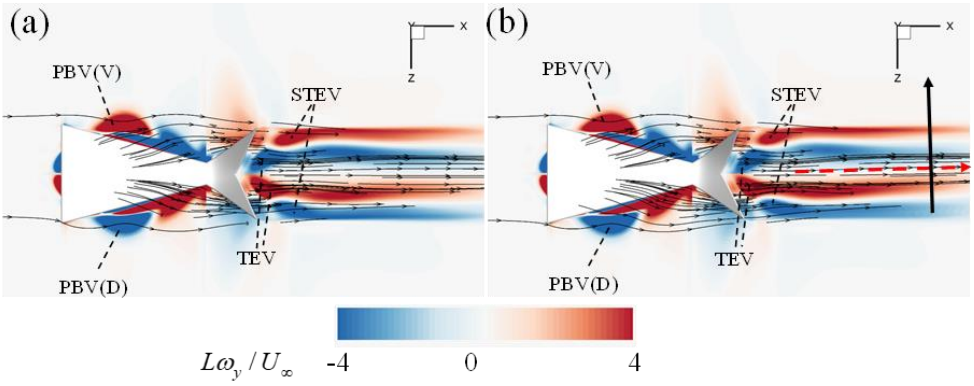

Fig. 4.39. The instantaneous *Y*-vorticity field along with the streamline condition at y = -0.012 m near the tuna-like swimmers with the CF (a) and HF (b) stiffness mode at $t = T$ when K_m = 0.005 and f^* = 2.5. The black line is perpendicular to the streamline in red color.

The pressure distribution along the swimmer surface is presented in Fig. 4.40. The main difference between the CF and HF mode is that much lower pressure (marked by a black circle in Fig. 4.40(d)) is located at the ventral lobe of the tail at the right side surface for the HF stiffness fashion. Therefore, a more considerable pressure difference between the left (high pressure) and the right (low pressure) is generated by the ventral lobe of the swimmer with the HF stiffness pattern. With an observation of the tail conformation at this instant in Fig. 4.30, one may find that the ventral half of the tail rolls upward. This orientation of the tail gives rise to a positive vertical component of forces resulted from the pressure difference, and it cannot be balanced by the dorsal lobe which is almost upright in vertical. This may explain the production of lift by the HF stiffness profile. In contrast, although there is also pressure difference generated both on ventral and dorsal lobes of the tail of the swimmer with the CF mode, these two forces are counteracted by the symmetrical distribution dorsally and ventrally.

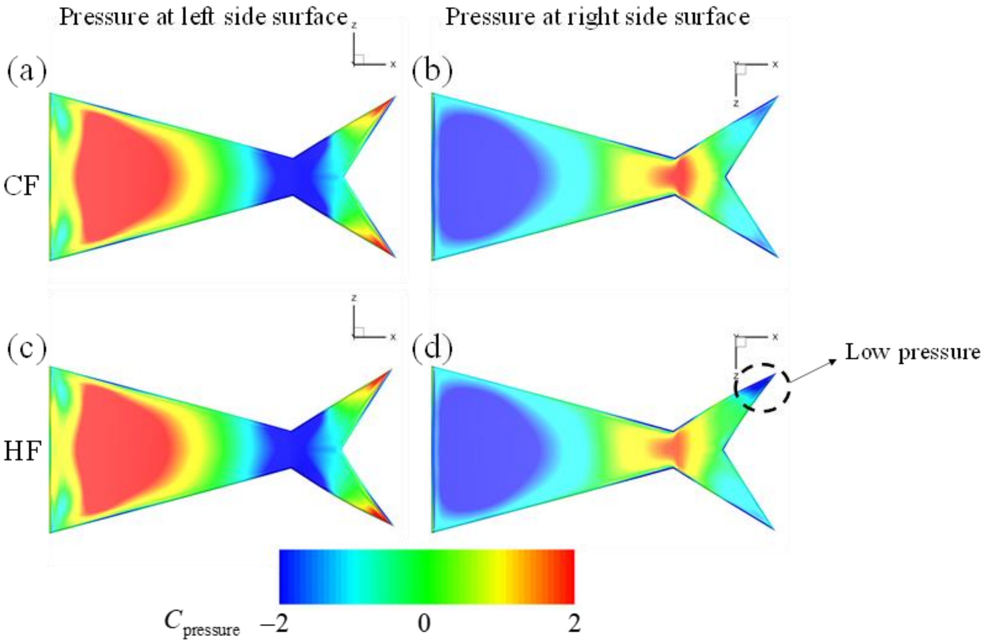

Fig. 4.40. The pressure distribution on the propulsor surface at the left and right side (defined from the posterior viewpoint) at t = 0.25 T when K_m = 0.005 and f^* = 2.5.

4.2.3.3 Discussion on passive control via non-uniform stiffness distribution

A few previous studies have indicated that it is possible to imitate some morphological features of fish using passive control via imposing appropriate stiffness distribution (McHenry et al., 1995). A study by Videler (1993) revealed that the rigidities of the pectoral fish fin are enhanced near leading-edge as rays are bonded together. This phenomenon was reinforced with numerical modeling of a flexible fin ray by Shoele and Zhu (2012). The mechanism behind this was the lessening of the effective angle of attack in the vicinity of the leading edge, which was reflected by the mitigation of leading-edge vortices separation (Shoele and Zhu, 2012). The experimental work from Lucas et al. (2015) also provided evidence that the model with a biologically relevant stiffness, i.e., the stiffer anterior, presented more fish-like kinematics than uniform foils.

Similar fish kinematic features are also revealed in the present study when attention is paid to fishtails. For example, the symmetrical and asymmetrical rigidity styles lead to rather different tail conformations, as shown in Fig. 4.30. Generally, the HF profile causes similar features of the scombrid fishtail previously observed in the experiment of Gibb et al. (1999). It is noted that such asymmetry only presents by HF profile, where the lateral excursion of the dorsal tail-tip is 9.6% larger than that of the ventral tail-tip as depicted in Fig. 4.33. The time-dependent dorsal-ventral asymmetry tail movements are also noticeable for the HF stiffness fashion (see Fig. 4.34). Although previous studies by Fierstine and Walters (1968) and Gibb et al. (1999) observed similar trends with a caudal fin of Skipjack tuna fish and a chub mackerel fish, to our knowledge, for the first time, such asymmetry trends in lateral displacement magnitude and phase shift of the tail-tip is well-replicated in this numerical FSI study covering a variety of flow and structure parameters.

However, it is challenging to replicate true-to-nature fish kinematics entirely relying on pure passive control via non-uniform stiffness. For instance, the location where the valley value of the lateral displacement occurs by the NU stiffness profile does not match that of a live tuna fish (Fig. 4.22). Additionally, the variation pattern of the lateral displacement of the numerical swimmer differs much from that of the real fish data at the first 60% model length. This may suggest that the fish body's active muscle contractions/extractions play a dominant role in the formulation of body waveform. Regarding the tail kinematics, the present models show a difference in the phase shift of the curves of tail-tip displacement and tail height with the experimental observations (Gibb et al., 1999), as depicted in Fig. 4.32. Particularly, their results suggested that the tail is maximally compressed at the maximum lateral displacement of the tail tip. Instead, in our results, the maximum lateral displacement almost appears at the same instant as the maximum abduction of the tail. Such difference is much likely the consequence of the sophisticated caudal fin muscle active control, which is hard to be achieved by purely passive deformations. This finding is also reminiscent of the speculation that the cyclical vertical compression of the Scombrid fishtail is a result of the action by interradialis muscle which is positioned such that contraction of this muscle could draw the dorsal and ventral rays towards one another by Gibb et al. (1999). Our numerical results corroborate this opinion.

In addition to the above locomotion kinematics, passive control on the flow field can also be achieved indirectly by the non-uniform stiffness distributions as presented in Shoele and Zhu (2012), where the strengthening leading-edge caused the mitigation of leading-edge vortices separation. In the present study, the bio-inspired non-uniform body stiffness profiles yield slightly stronger trailing edge vortices (Fig. 4.27) and alter the pressure distribution, reflected by reduced pressure at the anterior body surface and near the peduncle as shown in Fig. 4.28. Collectively, the non-uniform stiffness causes reorientation of the fluid force so that it points more towards the swimming direction and thus increases thrust as presented in Fig. 4.29. This applies to the thrust augmentation by the heterocercal stiffness profile along the fin surface. HF profile does not change the pressure magnitude very much but results in the rolling motion of the ventral lobe of the caudal fin, yielding a resultant force along the vertical direction (see Fig. 4.40 and Fig. 4.30). As a consequence of that, a lift force is also generated (Fig. 4.35(c)).

4.2.3.4 Discussion on the function of heterocercal conformation of mackerel fishtail

Scombrid fish has a homocercal tail with dorsal-ventrally symmetrical external and internal morphology. Due to this symmetric feature, it has usually been thought to function as a homocercal model (Gibb et al., 1999). Kinematics measurement suggested that its tail flaps asymmetrically to provide lift force during steady swimming (Gibb et al., 1999), which is presented by the heterocercal stiffness profile in our numerical models. Indeed, previous research has indicated that the fish body is negatively buoyant, tending to push fish moving towards the substratum (Magnuson, 1973). To prevent this sinking trend, the body is tipped up to deliver additional upward lift near the anterior part of the fish which is balanced by the vertical lift produced posteriorly by the tail (Aleev, 1969). This theory leads to a general prediction that the neutrally buoyant fish do not show asymmetrical tail conformation during swimming.

Interestingly, biological observations have suggested that significant dorsal-ventral asymmetry and tilting may also appear in some teleost fishes with near-neutral buoyancy (Gibb et al., 1999; Lauder, 1989; Lauder, 2000; Webb, 1993). Subsequent research revealed that this dorsal-ventrally asymmetrical tail deformation of bluegill sunfish is closely related to their maneuvering behaviors (Flammang and Lauder, 2009). Inspired by this finding, a biomimetic bluegill sunfish tail whose shape is plump without a sharp fork was numerically studied in section 4.1. Our results suggest that the asymmetrical heterocercal tail conformation continuously yields the smallest thrust and lowest efficiency during steady swimming among all the deformation patterns, including cupping and uniform styles. Similar conclusions have been drawn from the experiment on a robotic fish caudal fin with imposed tail motion derived from biological observation of the bluegill sunfish (Esposito et al., 2012). However, in the present study on the swimmer with a tuna-like tail, a heterocercal stiffness profile and its resultant asymmetrical deformation do not cause the deterioration of propulsion performance. Instead, in some instances, when the stiffness is at an intermediate level, the locomotors with the HF pattern even outperform the others in terms of thrust generation and propulsion efficiency (see Fig. 4.35(a) and (e)).

By comparing the present results with the other studies, we may propose one additional explanation/hypothesis to the asymmetric scombrid fishtail conformation: the role of it may play is not only to contribute to the lift force balance but also the thrust generation and propulsion efficiency. This is suggested at all speeds during the steady swimming of mackerel fish. However, this does not apply to bluegill sunfish with a different tail shape. Most of the bluegill fish are neutrally buoyant, and thus there is no need to balance the gravity and buoyancy force when they are swimming. In this situation, they adopt the asymmetric tail movement to offer additional lift force along with the thrust reduction during maneuvering.

It is also found that the stiffness profiles adopted in this study do not yield as remarkable an impact on the propulsion performance as that in the results from Zhu and Bi (2017) and the above study in section 4.1 where a bluegill sunfish inspired tail model was used. For example, the largest relative thrust difference is 29.3% seen between the models with cupping and heterocercal stiffness profile in Fig. 4.6 for a bluegill sunfish-inspired fin model. In contrast, the largest thrust distinction is seen between the HF and CF stiffness styles with a difference of 4.8% for a tuna-like tail as shown in Fig. 4.35. This may be related to the different tail shapes tested and the different intrinsic musculature conformations of the tails of their biological prototypes. Morphologically, the scombrid fishtail has a larger aspect ratio with a highly forked trailing edge while the bluegill sunfish has an unforked tail with a smaller aspect ratio. Hydrodynamically, the different tail deformations due to variable stiffness are more likely to induce different force production for the bluegill sunfish thanks to their large control surface. On the other hand, biologically, the intrinsic tail myology also determines the role the tail plays in swimming behavior. Anatomical studies revealed that there is an extensive complement of the intrinsic musculature of bluegill sunfish (Lauder, 2015). It is believed that complex conformations can control the adduction and abduction of individual fin rays, the movement of fin rays, and the relative motion of the upper and lower tail lobes. The utilization of these intrinsic muscle activities enables excellent control of the tail surface during different locomotor behaviors (Flammang and Lauder, 2009). In comparison, the intrinsic caudal fin musculature significantly reduces for scombrid fishes (Nursall, 1963), and there is even no intrinsic tail musculature as to black skipjack tuna fish (Fierstine and Walters, 1968).

In summary of the above discussions, the tuna-like tail may not be a favorable prototype when the maneuverability purpose is the focus. This is suggested from the results that the change of tail shape has little influence on the force generation, although their semilunate conformation is believed to offer high propulsion efficiency during high speed (Nauen and Lauder, 2002).

4.2.4 Concluding remarks

By the utilization of a fully coupled three-dimensional FSI solver described in Chapter 3, we have numerically studied a tuna-inspired swimmer in this section. Specifically, we investigate the effects of variable stiffness distributions along the body and tail on the kinematics and dynamics of a tuna-like swimmer separately. Firstly, a bio-inspired non-uniform rigidity profile of the body is compared with a uniform mode through systematic simulations. The numerical results indicate that given the parameters studied in this work, the larger thrust produced by the model with the bionic stiffness fashion was mainly seen under low frequencies. Instead, when the frequency is high, the swimmer with uniform stiffness produces a larger thrust in most cases. The enhanced performance by the non-uniform stiffness mode is more noticeable in terms of propulsion efficiency where more than 73% of the total cases see increased efficiency, and this improvement is seen for all three frequencies. Secondly, among the three different distributions of tail stiffness, i.e., heterocercal, cupping and uniform, the swimmer with a heterocercal pattern shows resemblance to that of real scombrid fishes in terms of tail kinematics. Additionally, those with the heterocercal stiffness profile also outperform those with other inflexibility distributions at an intermediate stiffness. The lift force produced by them is absent for the other two stiffness patterns. These findings suggest that the asymmetrical tail conformation does not only provides additional lift to balance the swimming body but may also contribute to efficient propulsion during steady swimming of scombrid fish. This heterocercal tail deformation has distinctive functions compared to that of a bluegill sunfish whose caudal fin has superior abilities in maneuvering.

Throughout our results, we also find that it is impossible to achieve entirely real fish-like kinematics if only the passive control, via the variable body and fin stiffness proposed here, is adopted. These are reflected by the comparison between our results with the experiments by Donley and Dickson (2000) and Gibb et al. (1999) as we discussed in section 4.2.3.3.

4.3 Summary

In this chapter, the developed FSI solver is applied to the simulations of a bluegill sunfish tail model and a tuna-like swimmer model, and both of which consist of non-uniform stiffness distribution structurally. The observed effect of the stiffness profile of the tail on the propulsion performance by our simulation results shows consistency with the counterparts from biological observations and measurements. Specifically, for the bluegill sunfish inspired tail model, the cupping spanwise stiffness profile shows the best propulsion performance while the heterocercal fashion always yields the least thrust but most remarkable lift force under the parameters studied, which is in line with the experimental study of a robotic fish caudal fin (Esposito et al., 2012).

In comparison, the heterocercal spanwise stiffness profile of a tuna-like tail model (thus a heterocercal tail spanwise deformation) produces the largest thrust at intermediate stiffness among other profiles including cupping and uniform patterns. This leads to a new explanation of the observed heterocercal deformation of a real tuna fish during steady swimming, i.e., this heterocercal deformation does not only provide additional lift force as explained by previous studies but also benefits the thrust production and efficiency. Therefore, by comparing the results in sections 4.1 and 4.2, we find that the effect of the spanwise stiffness profile of the tail is affected by the tail shape. Additionally, the shape of the caudal fin affects how much the variation of spanwise stiffness can affect the propulsion performance. A highly forked tail with a larger aspect ratio, like a tuna-inspired fin, would have a less significant effect on the propulsion compared with that with a smaller aspect ratio, e.g., a bluegill sunfish-inspired tail. This may be because that a tail with a smaller aspect ratio has a larger control surface which has a stronger capability to influence the surrounding fluid field.

The present numerical studies may also have implications for the design of bio-inspired underwater robots. For example, if the robots are supposed to have good maneuverability then a sunfish-tail-like biomimetic fin with a small aspect ratio may be considered. Provided swimming speed is the priority, a tuna fish-inspired forked tail may be more suitable for fast swimming. Besides, the material of the caudal fin should be flexible rather than commonly used rigid ones. A ray-reinforced bio-inspired fin structure with individual control of fish rays to form different spanwise deformations can aid maneuverability along with the rudder of the vehicles.

Chapter 5 Pulsed-jet Propulsion of a Squid-inspired Swimmer via Body Deformation

In this chapter, jet propulsion, distinct from the above fin propulsion is considered. Jet propulsion is more straightforward to implement in mechanics compared with fin propulsion which involves complex actuation mechanisms of composite structures. Two scenarios are considered here, one is a 2D squid-like jet swimmer at the high Reynolds number, and the other is a 3D squid-inspired swimmer in the presence of background flow. The first scenario aims at studying the jet performance involving the dynamic interplay between the surrounding flow and flexible swimmer structure. Therefore, it is resolved using the developed FSI solver. The objective of the 3D squid-like jet swimmer model is to investigate the effect of equivalent stroke ratio (a measurement of discharged fluid volume relative to the nozzle size) on jet flow and pulsed thrust production under the given jet velocity profiles. As a result, the deformation is prescribed at a given jet velocity profile and maximum equivalent stroke ratio, and only the fluid solver is used.

5.1 Pulsed-jet Propulsion of a 2D Squid-inspired Swimmer at High Reynolds Number

5.1.1 Problem statement

A two-dimensional swimmer inspired by the jet propulsion mechanism of squid is considered. It is modeled as an elliptical shell whose right end is removed to form the nozzle. The simplification of the squid-like swimmer as a hemi-ellipsoid has been found in previous studies (e.g., (Bi and Zhu, 2019b; Hoover and Miller, 2015)). The initial geometry of the body before deformations, as shown in Fig. 5.1, is given by

$$\frac{x^2}{a^2}+\frac{y^2}{b^2}=1,\ \text{for } x\le c, \tag{5.1}$$

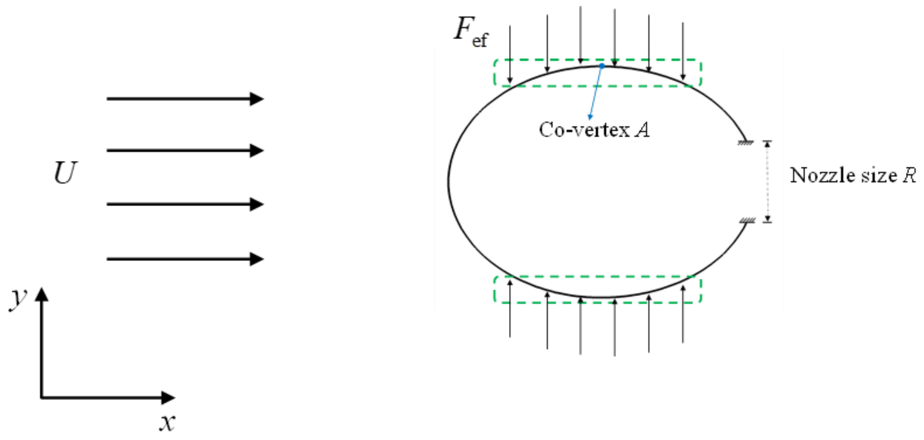

Fig. 5.1. The external force is evenly distributed on the mesh nodes in the green rectangular zone with the left boundary at $x = -0.78\ a$ and the right boundary at $x = 0.78\ a$ with a denoting the width of the ellipse of the initial geometry of the body. U is the free stream velocity and F_{ef} denotes the applied external force.

The body undergoes deflation and inflation during one jet cycle, similar to that observed in squid swimming. The jet propulsion of the squid involves two groups of muscles, radial and circular, as well as the mantle wall. The radial muscles are usually active during the escape or predation maneuver for hyperinflation of the mantle cavity. The contraction of the circular muscles actuates the deflation for the jetting. During regular swimming, the expansion is mostly powered by the elastic recoil of the mantle wall. Inspired by this mechanism, in this study the deformation of the mantle consists of two phases, active deflation which is actuated by the applied external force mimicking the function of the circular muscles, and the passive inflation resulting from the release of the elastic energy in the mantle structure. During the inflation phase, the enclosed area increases so that fluid enters through the nozzle (the opening of the ellipse with size R). Afterwards, the fluid is expelled via the nozzle when the internal area is decreased during the deflation. To drive the motion of the body, an external forcing term, F_{ef}, is applied to the body surface in the transverse direction, as presented in Fig. 5.1, which is given by

$$F_{\mathrm{ef}}(t) = \begin{cases} F_{\mathrm{ef0}} \sin(2\pi f_{\mathrm{ef}} t),\ t <= nT_{\mathrm{i}} + 1/2T_{\mathrm{ef}} \\ 0,\ t > nT_{\mathrm{i}} + 1/2T_{\mathrm{ef}} \end{cases}, \tag{5.2}$$

where n is a non-negative integer (n = 0, 1, 2, 3, …), $T_{\mathrm{ef}} = 1/f_{\mathrm{ef}}$ is the period of the external forcing term with f_{ef} being the actuation frequency, t is time, and T_i is the time it takes for the passive inflation of the body obtained from the free vibration study (which will be introduced later). The amplitude of the external force is $F_{\mathrm{ef0}} = 0.5\rho_f U^2 L \cdot C_{\mathrm{ef0}}$, where ρ_f is the density of the fluid, U is the free stream velocity, L is the contour length of the body with medium nozzle size ($R = 0.1\ L$), and C_{ef0} is the external force coefficient. The complete locomotion period, including inflation and deflation, is $T = 0.5\ T_{\mathrm{ef}} + T_i$.

The dimensionless parameters governing the problems are defined as: the Reynolds number Re = UL/v with v denoting the kinematic viscosity of the fluid; the dimensionless frequency (the Strouhal number) of the external force $St = f_{\mathrm{ef}}L/U$; the mass ratio $m^* = \rho_s h/\rho_f L$ with h denoting the thickness of the mantle and ρ_s the density of the structure; the non-dimensional stiffness $K = EI/(\rho_f U^2 L^3)$, where E is Young's modulus and $I = h^3/12$ represents the area moment of inertia of the cross-section; and the Poisson ratio v_s.

By integrating the distributed fluidic stress along the swimmer body, we obtain the instantaneous thrust coefficient as

$$C_T = -\frac{F_x}{\frac{1}{2}\rho_f U^2 L}, \tag{5.3}$$

where F_x is the component of the hydrodynamic force in the x-direction.

The instantaneous power expenditure coefficient is computed by

$$C_P = \frac{P_{\mathrm{ef}}}{\frac{1}{2}\rho_f U^3 L}, \tag{5.4}$$

where P_{ef} is the total power output of the external force, which is calculated as $P_{\mathrm{ef}} = \int \boldsymbol{F}_{\mathrm{ef}} \cdot \boldsymbol{u}(s)ds$ with $\boldsymbol{u}$ being the velocity of the grid node s where the external force is applied.

In the tethered case with a constant incoming fluid velocity, the propulsive efficiency is defined as the ratio between the mean thrust coefficient and the mean power expenditure coefficient so that we have

$$\eta = \frac{\overline{C_T}}{\overline{C_P}}. \tag{5.5}$$

5.1.2 Free vibration study

To find the free vibration frequency of the structure, we performed a numerical relaxation study where a constant external force with $C_{\mathrm{ef0}} = 0.64$, i.e., $F_{\mathrm{ef}}(t) = 0.5\rho_f U^2 L \cdot 0.64$, is applied on the mantle surface and then unloaded to let the body oscillate freely in the fluid. The response of the co-vertex A of the elliptical body shown in Fig. 5.1 is recorded and presented in Fig. 5.2, at $K = 0.05$ under different Reynolds numbers, and at Re = 1×10^5 as stiffness is varied, respectively. It can be found from Fig. 5.2(a) that the vibration amplitude of the body decays faster as the fluid viscosity is larger (smaller Re). The damping effect is pronounced at Re = 50 where the vibration fades out much quicker than the others, which have also been demonstrated in Hoover and Miller (2015). Nevertheless, the varied Reynolds number does not change the vibration frequency much, as the difference among them is within 2% with the value at Re = 1×10^5 as a reference, i.e., $St_v = f_{vibration}L/U = 6.3$. Another significant factor affecting the vibration response of the mantle cavity is structural stiffness, as shown in Fig. 5.2(b). As expected, the stiffer structure results in a higher-frequency oscillation. It can be found that deflation and inflation last for almost an equal period within one vibration cycle. Therefore, the passive inflation period T_i is chosen as half of the free vibration period in this study.

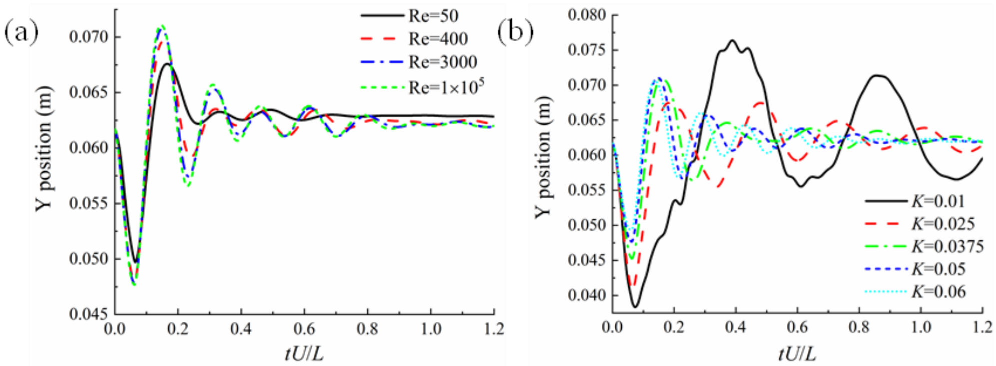

Fig. 5.2. The oscillation of the Y position of the co-vertex A as a function of non-dimensional time when $K = 0.05$ at different Reynolds number (a), and when Re = 1×10^5 at different stiffnesses (b).

5.1.3 Mesh independence study

The computational domain is shown in Fig. 5.3(a). On the squid-like swimmer surface, the no-slip/no-flux condition is applied, while for the upper and lower domain boundaries, the non-reflective far-field boundary condition is imposed. Velocity inlet and pressure outlet boundary conditions are imposed on the left and right domain boundaries, respectively.

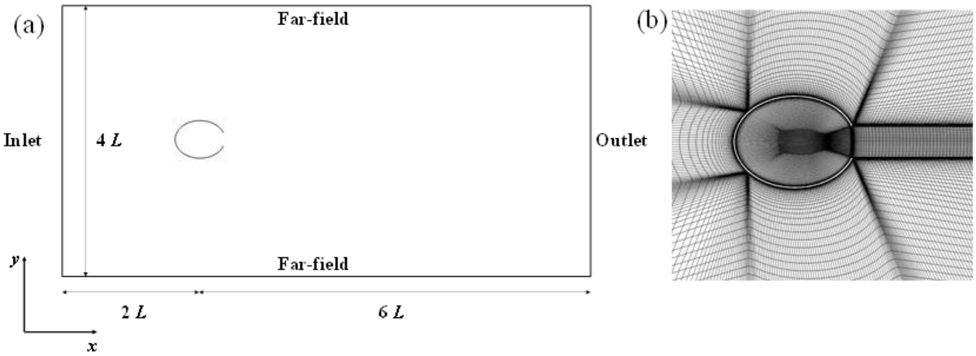

Fig. 5.3. The computational domain layout (a) and the generated medium size mesh around the swimmer (b) when the nozzle size $R = 0.1\ L$.

A mesh independence study is performed to assess the appropriate mesh and time-step resolution by solving the turbulent flow for $\mathrm{Re} = UL/\nu = 1\times10^5$, $m^*=0.05$, $K = 0.05$, $C_{\mathrm{ef0}} = 0.64$, $St = 4.4$, and $R = 0.1\ L$. Three fluid meshes are generated: a coarse mesh with 60290 cells, a medium mesh with 78758 cells, and a fine mesh with 105220 cells. The height of the first cell is $1.98\times10^{-4}\ L$ to yield a y^+ value of 1 for the three grids. The structural mesh contains 198 quadratic brick elements. Firstly, the mesh convergence test is performed in which three fluid meshes are used along with the dimensionless time step size, defined as $\overline{\Delta t} = \Delta tU/L$, $\overline{\Delta t} = 0.00113$. The discrepancy in C_T among results obtained with the three meshes is shown in Fig. 5.4(a) in terms of relative error with the result of the fine mesh as reference. It can be seen that the medium mesh yields result very close to that of the fine mesh with the maximum difference between them less than 2%. Thereafter, the effect of time step size when the medium mesh is used is also studied, as shown in Fig. 5.4(b). These tests show that the results are not sensitive to the mesh size and time step size if they are small enough. Therefore, to ensure the computation accuracy and meanwhile, reduce the computational cost, the medium mesh is used for the following simulations.

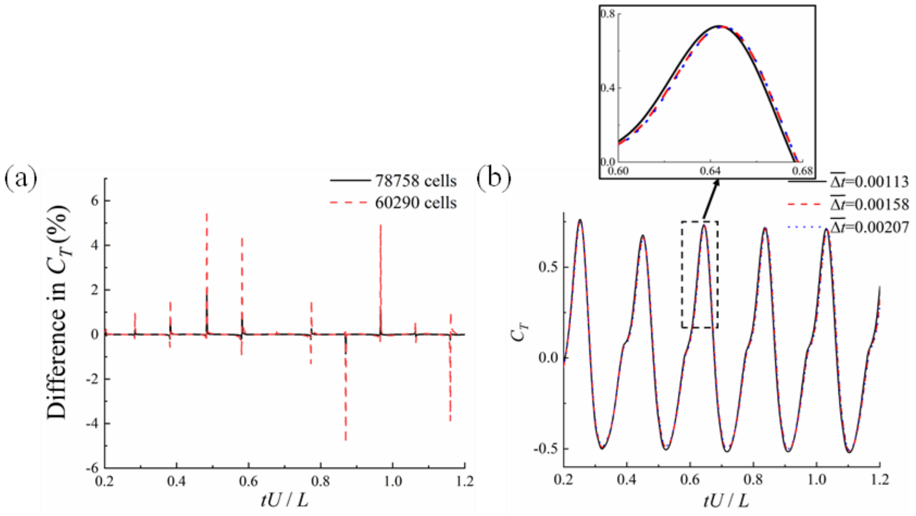

Fig. 5.4. The discrepancy in C_T among results obtained with the three different fluid meshes when $\overline{\Delta t} = 0.00113$ with the results of the fine mesh with 105220 cells as reference (a), and comparison of C_T for the medium size mesh when three different time step sizes are used (b).

5.1.4 Results

Numerical tests have been performed to determine the appropriate stiffness and external force amplitude after the mesh independence study. Our results indicate that under the combination of $K = 0.05$ and $C_{\mathrm{ef0}} = 0.64$, regular and periodic inflation-deflation locomotion is achievable and lasts sufficiently long to reach a steady state. Meanwhile, the deformation is not too large to induce instability of the locomotion system, or too small to produce thrust. Therefore, they are used in the following simulations in this study.

5.1.4.1 Steady-state response

The steady-state response of a typical case is presented to demonstrate the deflation-inflation cycle of the body and the resultant propulsive performance. In this simulation, the dimensionless parameters are listed in Table 5.1. It is noted that when $\mathrm{Re} = 1\times10^5$ and $K = 0.05$, the free vibration frequency of the body is $St_\mathrm{v} = 6.3$ obtained from the free vibration study in section 5.1.2. The passive inflation period T_i is half of the free vibration period, i.e., $T_\mathrm{i} = 0.5\ \mathrm{L}/(USt_\mathrm{v})$, as shown in Fig. 5.2. Therefore, the complete locomotion period is $T = 0.5\ L(1/St + 1/St_\mathrm{v})/U$.

Table 5.1. List of the parameters used in the simulation of a 2D squid-like jet swimmer.

Re	K	C_ef0	St	m^*	a	b	R
1×10^5	0.05	0.64	3.6	0.05	0.2 L	0.15 L	0.1 L

The change of body shape within one period is plotted in Fig. 5.5 to demonstrate the body deformation during the jet propulsion cycle. As can be seen, the deformation at this stiffness and external force frequency is not as noticeable as that in Bi and Zhu (2019b) (see Fig. 8 in their work) where the actuation mechanism is different from the current study. In that study, the inflation and deflation of the mantle wall were the results of the stretch and contraction of virtual lateral springs inside the cavity. By specifying the longitudinal position and stiffness of a single spring, they were able to control the deformation of the body along the longitudinal direction. However, the current deformation of the body is the response of the entire mantle structure to the external force, fluidic force, and structural inertial force. Mathematically, it is the solution of the fully coupled fluid and structure equations in Eq.(3.1) and Eq.(3.35). This may explain the difference in body deformation between the present study and that in Bi and Zhu (2019b). Specifically, the deformation is smooth along the circumferential direction, as shown in Fig. 5.5 in this work, which is reminiscent of the deformation of a jellyfish-like swimmer model in Hoover and Miller (2015) where a similar actuation mechanism was employed. In contrast, the deformation is more complicated in the circumferential direction in Bi and Zhu (2019b) (as shown in Fig. 9 in their study).

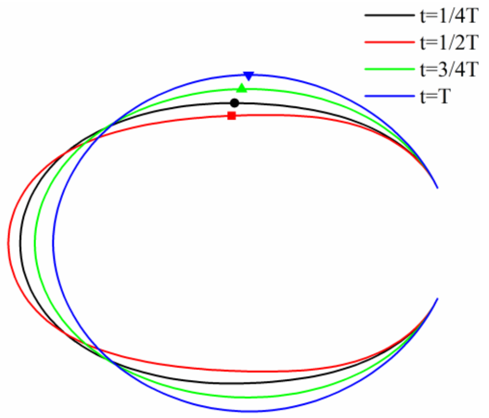

Fig. 5.5. The evolution of the body shape within one period. The co-vertex *A* is marked by a circle (*t* = 1/4 *T*), a square (*t* = 1/2 *T*), an up triangle (*t* = 3/4 *T*), and a down triangle (*t* = *T*).

To quantitatively record the locomotion of the mantle wall, we also depict the variation of the Y position of the co-vertex *A* shown in Fig. 5.1 in Fig. 5.6(a). As aforementioned, one locomotion period consists of the active deflation under external force and the passive inflation from structural recoil. It can be seen that even though the external forcing term is still in place, the body starts to swell ahead of the middle of the period, indicating that the external force is not large enough to counter the rebound force at this instant. The maximum Y position is seen slightly ahead of the beginning of the next cycle of exerting the actuation force, which implies that the maximum inflation is reached under the free vibration condition.

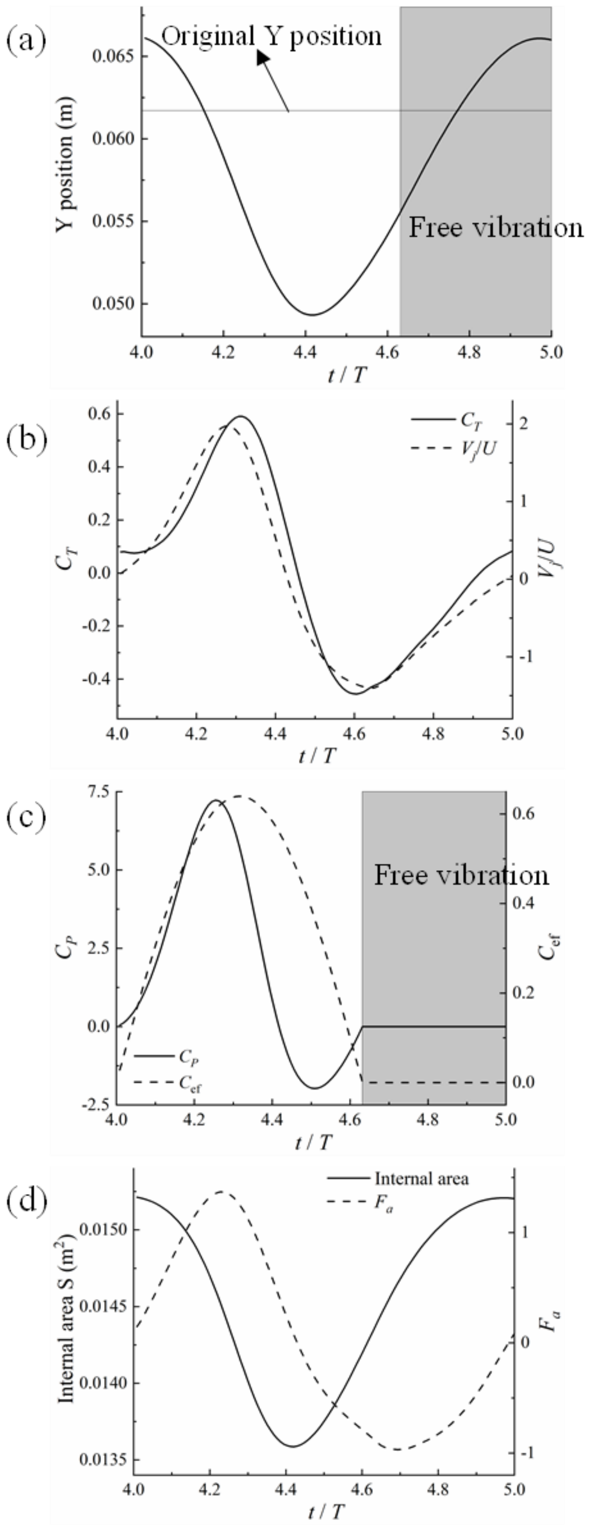

Fig. 5.6. Time history of the Y position of the co-vertex (a), the instantaneous thrust coefficient C_T and jet speed (b), the instantaneous power expenditure coefficient C_P and applied external force coefficient C_{ef} (c), and the internal surface area and dimensionless added-mass-related thrust coefficient (d) within one period. The duration of free vibration is filled with grey background in (a) and (c).

The variation of the thrust and jet speed is plotted in Fig. 5.6(b). A comparison of Fig. 5.6(a) and Fig. 5.6(b) reveals that most of the thrust is generated during the deflation phase, and the peak thrust occurs before the fully deflated status of the body. Although nearly half of a locomotion period is characterized by drag production, especially during the inflation phase, the mean thrust is still positive mainly due to a larger magnitude of maximum thrust than that of the maximum drag force. This feature is different from the fin-based propulsion mode, where a fish can almost avoid the creation of drag force by complex 3D conformations of the flexible fin (Han et al., 2020). Following Bi and Zhu (2019b), the average jet speed here is defined as $V_j = -\frac{1}{R}\frac{dS}{dt}$, where S is the internal area whose variation is depicted in Fig. 5.6(d). Similar to the finding by Bi and Zhu (2019b), there is a phase lag between the thrust production and jet speed, as shown in Fig. 5.6(b). This may be due to the influence of drag force on the mantle body, the jet acceleration effect (Bi and Zhu, 2020), and the added-mass-related thrust (Bi and Zhu, 2019b).

The power expenditure coefficient C_P and applied instantaneous external force coefficient C_{ef} are shown in Fig. 5.6(c). It can be observed that most of the actuated force does positive work unless near the end of the force-exerting phase when the structure recoils. The jet flow is directly associated with the internal area of the chamber, and the change of this body shape would induce added-mass-related thrust. Fig. 5.6(d) presents the variation of internal area and the added-mass-related thrust within one locomotion period. The dimensionless added-mass-related thrust is determined by $F_a = -\dot{m}_a U / 0.5 \rho_f U^2 L$ where m_a is the added mass. The instantaneous shape of the body is simplified as an ellipse with a semi-minor axis $\hat{b}$ to calculate the added mass which can be written as $m_a = \rho_f \pi \hat{b}^2$. Although the magnitude of F_a is larger than that of C_T, the time-averaged value of F_a is so marginal that it contributes little to the mean thrust, which was confirmed in Bi and Zhu (2019b) where a tethered swimming assumption was adopted as well. Under the tethered mode, the positive input of thrust sourced from added mass variation during the deflation phase is neutralized by the negative contribution during the inflation. In a subsequent study of the free-swimming scenario by Bi and Zhu (2019a), the added-mass-related thrust was proven to account for a considerable portion of the mean thrust production.

The evolution of the Z-vorticity around the swimmer is presented in Fig. 5.7. It can be found that a pair of vortices, i.e., jet-induced vortices with clockwise and counterclockwise rotational directions, is shed from the mantle cavity. This is somewhat similar to the vorticity pattern observed from the flow around the live squid (*Lolliguncula brevis*) obtained by DPIV techniques reported in Bartol et al. (2008), especially the mode I pattern according to Bartol et al. (2009a). Interestingly, strong internal body vortices are also observed in this study, while they are much weaker in a previous study (Bi and Zhu, 2019b) where the Reynolds number is much smaller (Re = 400). It is reasonable to conjecture that the Reynolds number affects the flow patterns around the system significantly, which will be discussed in the following section. A closer inspection of Fig. 5.7 reveals that the internal vortices and jet vortices are shed almost simultaneously at t = 2/3 T. As demonstrated by their rotational directions, the internal vortices originate from the outer body surface, while the jet vortices originate from the inner body surface. Generally, the jet vortices, internal vortices, and the wake external vortices attached on the outer surface are all symmetric concerning the horizontal midline within this period, although with opposite rotational directions above and below the axis of symmetry.

In addition to the vorticity pattern, the propulsive thrust is also closely linked to the pressure distribution around the swimmer. Fig. 5.8 shows the evolution of the pressure distribution around the swimmer during one period. A comparison between Fig. 5.8 and Fig. 5.6(a) and (b) illustrates that the peak thrust at around 1/3 T is directly related to the massive pressure difference around the body when it approaches the fully deflated state. Following the deflation, as the body is inflating, the upstream pressure starts to increase. Meanwhile, the downstream pressure decreases until t = 2/3 T. As a result, during this process, the thrust diminishes continuously until the body experiences the maximum drag force near the instant at t = 2/3 T.

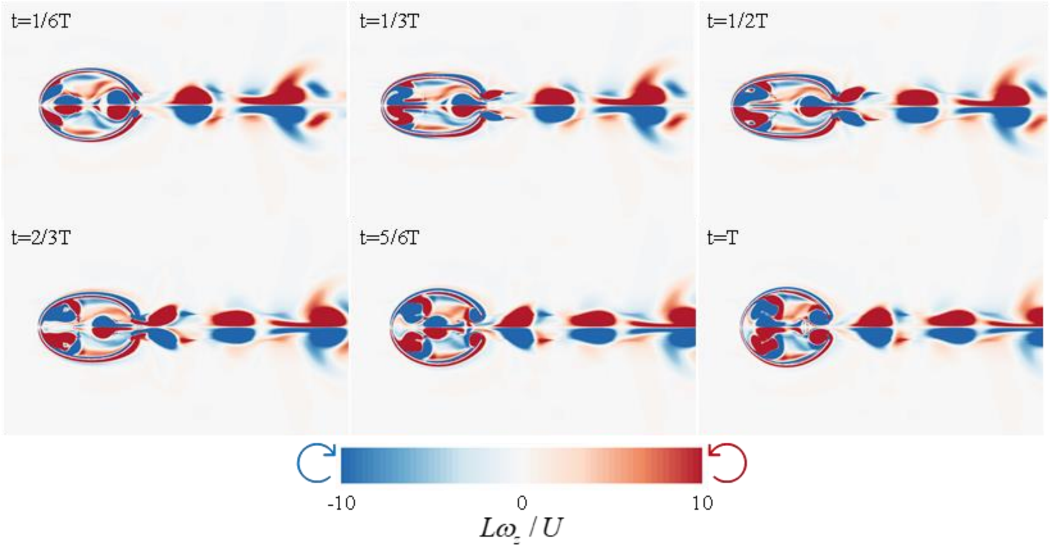

Fig. 5.7. The evolution of the Z-vorticity during one period.

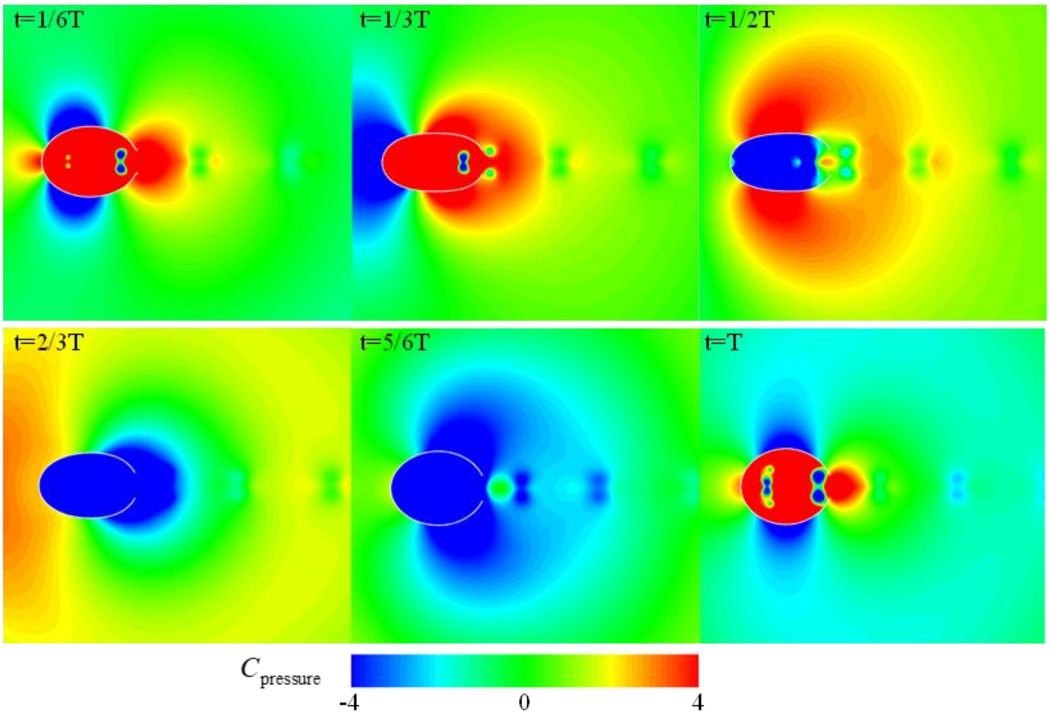

Fig. 5.8. The pressure contour during one period where $C_{pressure} = (p-p_\infty)/0.5\rho_f U^2$.

5.1.4.2 Propulsion performance

As can be observed in section 5.1.4.1, the vorticity pattern at Re = 1×10^5 is considerably different from the one at lower Reynolds numbers (Bi and Zhu, 2019b). It is thus evident that fluid viscosity has a significant impact on the flow evolution around the system, and, consequently, the propulsive performance. Parametric studies are conducted here to explore the flow regimes when Re = 50, 400, 3000, and 1×10^5, which are within the range of Reynolds number squids experience throughout ontogeny (Bartol et al., 2008). Apart from the Reynolds number, the effects of *St* are also studied. Most of the non-dimensional parameters are kept the same as listed in Table 5.1.

The time-averaged thrust coefficient $\overline{C_T}$, power expenditure coefficient $\overline{C_P}$, propulsion efficiency η, and the peak-to-peak displacement ratio of the co-vertex *A* (see Fig. 5.1) are shown in Fig. 5.9. In general, similar variation patterns of the four variables can be observed at Re = 400, 3000, and 1×10^5, while distinctive variation fashions are seen at Re = 50 where the viscous effect dominates.

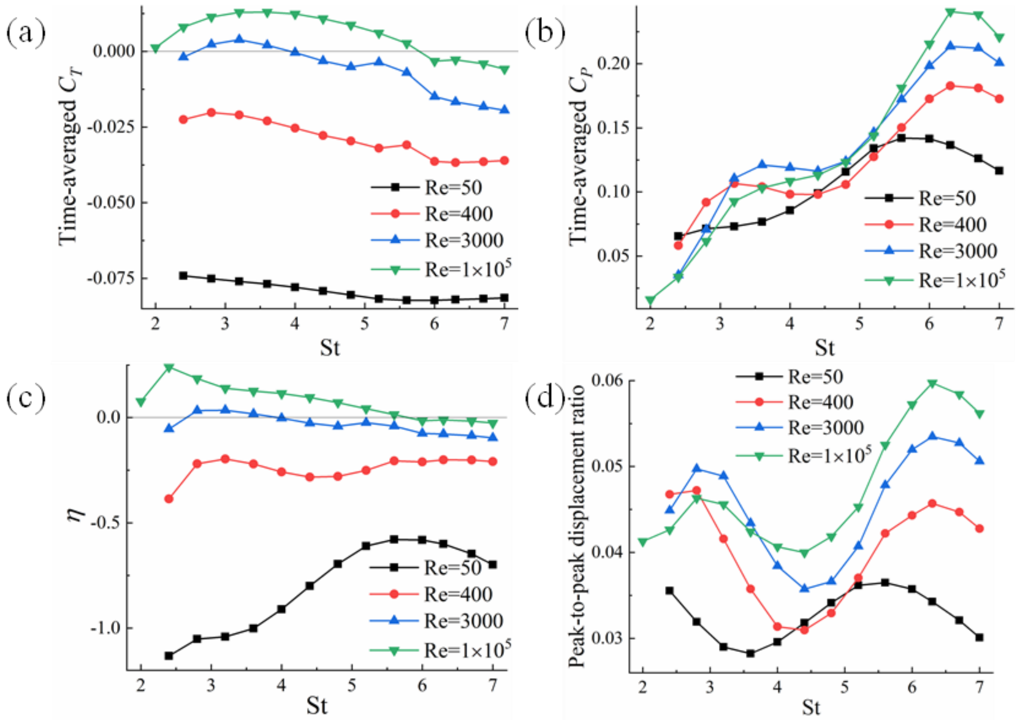

Fig. 5.9. The mean thrust (a), power expenditure coefficient (b), efficiency (c), and peak-to-peak displacement ratio of the co-vertex *A* (d) as functions of *St* for different Reynolds numbers.

With the increase of the Reynolds number, the mean thrust increases at fixed actuation frequency *St* as shown in Fig. 5.9(a). When the flow is laminar, the swimmer does not produce mean thrust in most cases. Instead, it only experiences drag force, although this drag decreases at a higher Reynolds number. The time-averaged thrust peaks at *St* = 3.2 with a value of 0.0039 when Re = 3000, and at *St* = 3.6 with $\overline{C_T}$ = 0.013 when Re = 1×10^5, yielding an increase by 200%. Drag force is seen at low or high actuation frequencies in both cases. Similar variation patterns are seen in the efficiency plot in Fig. 5.9(c), where maximum efficiencies are observed at *St* = 3.2 and *St* = 2.4 for Re = 3000 and 1×10^5, respectively. Specifically, the maximum efficiency at Re = 1×10^5 is 24.0%, a significant increase by 586% from the maximum efficiency at Re = 3000 (around 3.5%). As seen in Eq.(5.4), the power expenditure is directly associated with mantle displacement. As a result, their curves show some similarity, as depicted in Fig. 5.9(b) and (d). The maximum displacement of the co-vertex *A* and maximum power expenditure are seen near the free vibration frequency St_{v} = 6.3, except for cases of Re = 50 where the maximum is seen at a smaller *St*. With a closer inspection of Fig. 5.9(c) and (d), we also find a locally maximum displacement near *St* = 2.8 when Re is larger than 50. This second peak may correspond to another natural mode of the structure system, which has not been excited in our relaxation test in section 5.1.2.

The effect of the locomotion frequency has also been studied in Bi and Zhu (2019b) (see Fig. 11 in their work) at Re = 400. It would be interesting to compare it with the current results.

The time-averaged thrust coefficients they predicted were in general larger than those in the present work by one order of magnitude. This is attributed to the fact that the deformation of the mantle body in their model was much more significant than what we achieve with the current activation mechanism. As a consequence, their model produced stronger jet flow, as mentioned in section 5.1.4.1. Nevertheless, when higher Reynolds numbers are considered, the improvement in efficiency is dramatic according to our results. Namely, the maximum efficiency was below 15% in Bi and Zhu (2019b) at Re = 400, while our swimmer achieves an maximum efficiency of 25% at Re = 1×10^5.

Resonant deformation of the mantle body may not be the best choice for the squid-like swimmer. For instance, while the globally maximum displacement is reached at the free vibration frequency ($St_v = 6.3$) when the Reynolds number is higher than 50, no time-mean thrust is generated there. Taking Re = 1×10^5 as an example, the instantaneous thrust within one period at *St* = 2, 3.6, and 6.3 are depicted in Fig. 5.10. At the free vibration frequency *St* = 6.3, the largest deformation of the mantle indeed yields a much larger peak thrust. However, the thrust production does not last long (less than 2/5 of the whole period). Although the magnitude of the maximum drag is smaller than that of the thrust, the resultant time-averaged thrust is still negative. In comparison, thrust production lasts more than half of the period at *St* = 3.6. As a result, the largest mean thrust is obtained at this actuation frequency.

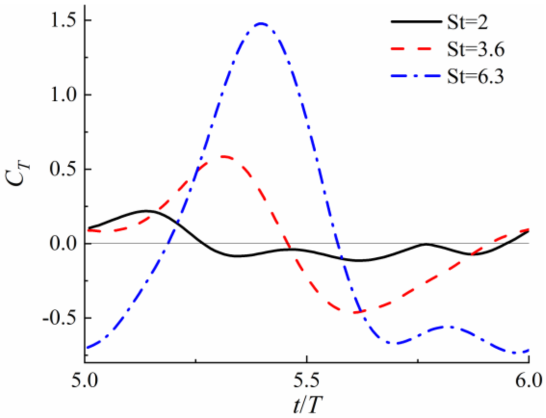

Fig. 5.10. The instantaneous thrust coefficient during one period at Re = 1×10^5 for three *St*.

The instantaneous thrust for different Reynolds numbers at *St* = 3.2 is compared against each other in Fig. 5.11. It can be found that in the laminar flow regime, the peak values of C_T all increase with a higher Reynolds number. The maximum instantaneous peak values of C_T among the four Reynolds numbers are seen at Re = 3000. Generally, a higher Reynolds number always results in an earlier occurrence of these maximum values. The variations of V_j

and F_a at these four Reynolds numbers are similar to that of C_T as shown in Fig. 5.11. Therefore, they are not shown here.

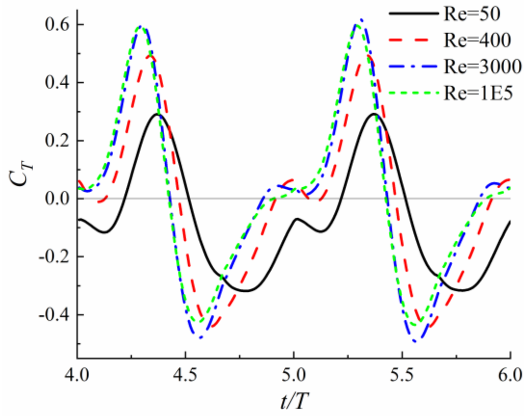

Fig. 5.11. The instantaneous thrust coefficient at *St* = 3.2 for different Re.

5.1.4.3 Flow patterns and symmetry-breaking instability

For interpretation of the propulsive performance under different parameters, visualization of the flow patterns is presented here. The Z-vorticity contours at the fully deflated state of the mantle at *St* = 3.2 for the four Reynolds numbers are presented in Fig. 5.12. With the increase of Re, the external body-generated vortices are weaker, while the jet vortices become more dominant. At very low Re, i.e., Re = 50 and 400, the jet vortices ejected from the intramantle and the internal body vortices dissipate quickly. Therefore, there are no noticeable vortex pairs in the wake or inside the mantle. Instead, the external body vortices, which are reminiscent of the vortices seen at the front surface of a circular cylinder in the laminar flow (Peppa and Triantafyllou, 2016), are the strongest, implying the drag force is dominating. This may explain that no thrust is produced for these two values of Re, as shown in Fig. 5.9(a). At Re = 1×10^5, the jet vortices in the wake are the strongest, and the drag-force-related external body vortices along the wall surface are highly suppressed, which contribute to the thrust generation directly.

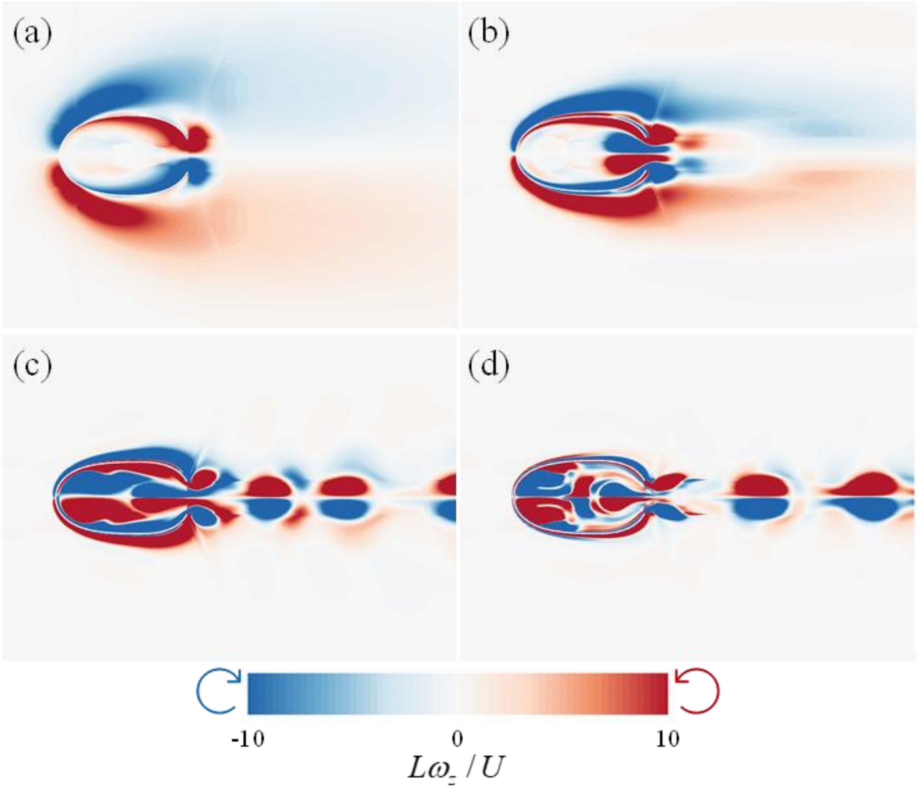

Fig. 5.12. The Z-vorticity contour at fully deflated state at *St* = 3.2 for different Re = 50 (a), 400 (b), 3000 (c) and 1×10^5 (d).

In addition to fluid viscosity, the actuation frequency of the external force also plays a significant role in the flow pattern around the swimmer, as shown in Fig. 5.13. There are three vorticity patterns observed at different ranges of *St*. At low frequency, e.g., *St* = 2, pattern I is presented where the external body and jet vortices are comparable in strength while internal body vortices are weak. This vorticity mode is associated with low thrust production. At pattern II, with *St* between 2.4 and 4.8, the jet vortices become dominant over the body-generated ones. Meanwhile, the internal body vortices grow stronger. Considerable thrust generation is seen within this pattern, e.g., at *St* = 3.6 and 4.8, as shown in Fig. 5.9(a). High efficiencies are reached near the transition from pattern I to the jet vortices-dominated pattern, i.e., at *St* = 2.4 and 2.8, as presented in Fig. 5.9(c). This is consistent with the findings in Bi and Zhu (2019b). In pattern III, with a further increase of *St*, the drag-force-related external body surface vortices become stronger again. In contrast, the jet vortices, the primary source of thrust production, fade in comparison with the body vortices. In consequence, there is no mean thrust generated in pattern III when the actuation frequency is high.

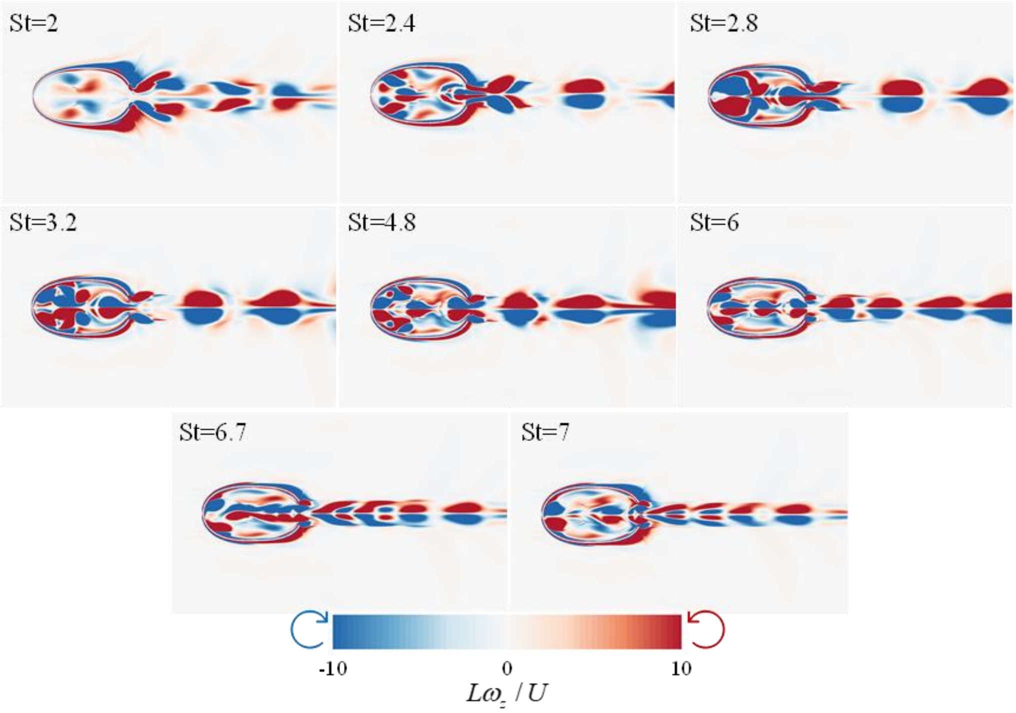

Fig. 5.13. The Z-vorticity contours around the swimmer at a fully deflated state at Re = 1×10^5.

With the proceeding of simulations, we find that the regular periodic deflation-inflation locomotion and resultant jet propulsion systems are not durable after several cycles, especially at high Reynolds numbers. To demonstrate the evolution to irregular vibration and symmetry breaking, the time history of the Y position of the co-vertex *A* and lift force C_y in the *y*-direction are plotted in Fig. 5.14. The irregularity of the body deformation is noticeable after about eight cycles at Re = 1×10^5, and one period later at Re = 3000. At lower Re, the periodic vibration is maintained within all ten periods. Another consequence of asymmetric deformation is the production of lift force. As shown in Fig. 5.14(b), during regular periodic deflation-inflation locomotion, the lift force C_y is negligible. However, the lift curves start to fluctuate from the seventh period at Re = 3000 and 1×10^5. The first peak lift of the former Re occurs slightly later than that of the latter Re. Generally, a higher Re leads to an earlier appearance of the symmetry-break instability. This is reminiscent that squid hatchlings that operate at laminar flow (Re = 1~100) employ continuous jet swimming more frequently than juveniles and adults which operate at higher Reynolds number (Re = 10^3~10^6) (Bartol et al., 2008). Burst-and-coast swimming by these juveniles and adult squids may help them avoid this symmetry-break instability in the turbulent flow.

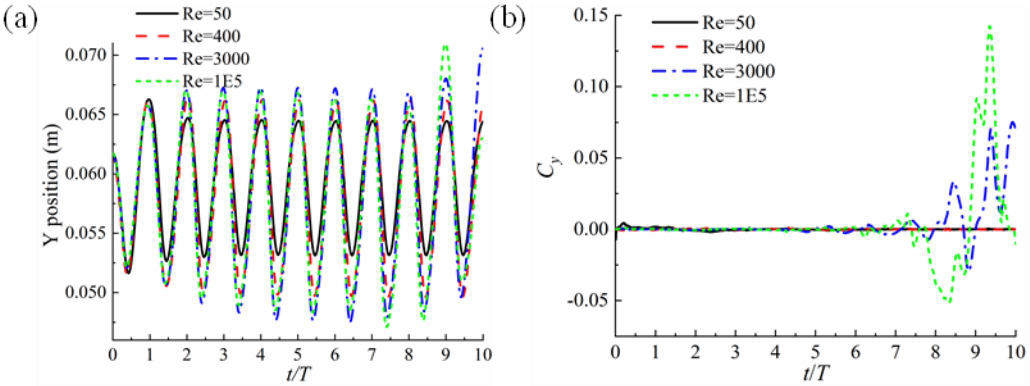

Fig. 5.14. The time history of the Y position of the co-vertex *A* (a) and C_y (b) at *St* = 3.2 for different Re.

The evolution of the *Z*-vorticity at Re = 1×10^5 is presented in Fig. 5.15 to showcase the development of the symmetry-breaking instability. The case at Re = 400 is also provided in Fig. 5.16 for a comparison. It can be found from Fig. 5.15 that before *t* = 6.60 *T*, all the three types of vortices, i.e., the internal body vortices, the outer body surface vortices, and jet vortices, are symmetric about the horizontal midline. From *t* = 7 *T* to 7.73 *T*, the symmetry of the vortices inside the mantle body is broken, while the symmetry of the other vortex pairs generally remains. A comparison of Fig. 5.14 and Fig. 5.15 reveals that the irregularity of the body deformation and the lift force production are firstly sourced from unstructured internal body vortices. Afterwards, the symmetry breaking of the jet vortices is induced, which becomes noticeable after *t* = 8.60 *T*. Similar wake symmetry breaking was reported in Bi and Zhu (2019b) at a much smaller Re of 400. In their study, the internal body vortices were not pronounced, and the deflation-inflation system instability was mainly due to the broken symmetry of the jet vortices in the wake. They expected that a smaller Reynolds number tended to delay the symmetry breaking. Indeed, our simulations indicate that the symmetry of the vortex pairs is well sustained at least for ten periods at Re=400 as shown in Fig. 5.16. Under this scenario, the existing vortices dissipate quickly, and newly formed vortices avoid colliding with them to cause disturbance inside and outside the mantle body. To the knowledge of the author, this result, for the first time, demonstrates the significant effect of internal body vortices on the system instability in jet propulsion at high Reynolds number conditions. It may provide implications for squid-inspired jet propulsion robots in turbulent flows: the internal body structure and related body deformation need to be carefully designed to avoid this symmetry-breaking of vortices. For example, a certain mechanism inside the body can be implemented to bar this instability by rearranging the internal vortices evolution.

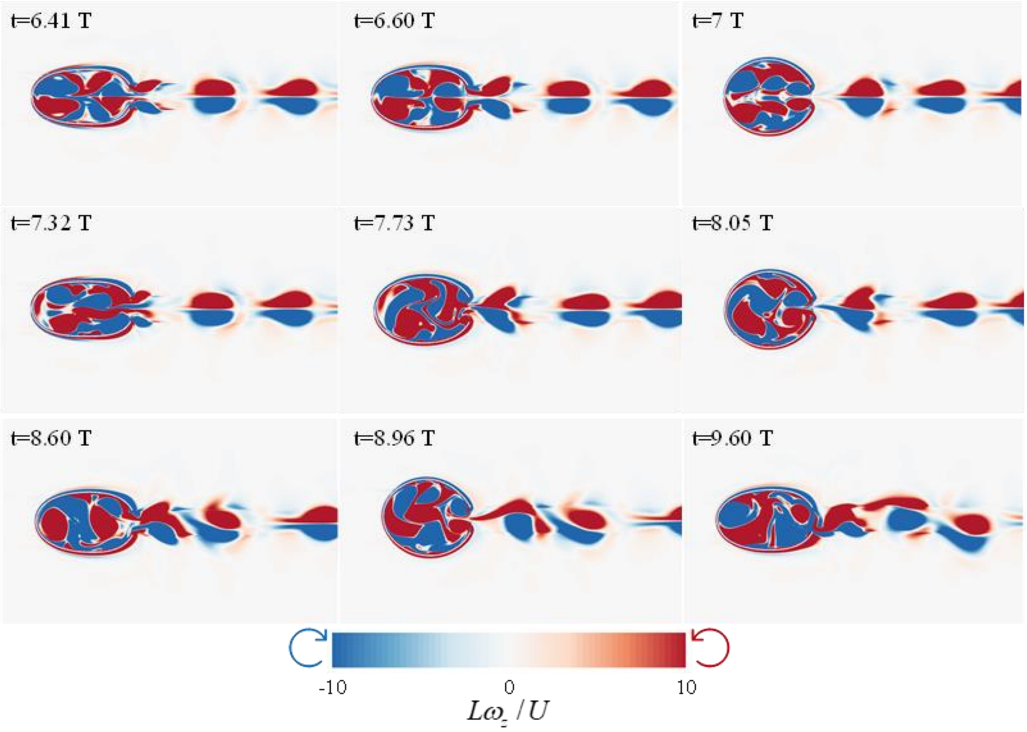

Fig. 5.15. The evolution of Z-vorticity contour around the swimmer at Re = 1×10^5 and *St* = 3.2.

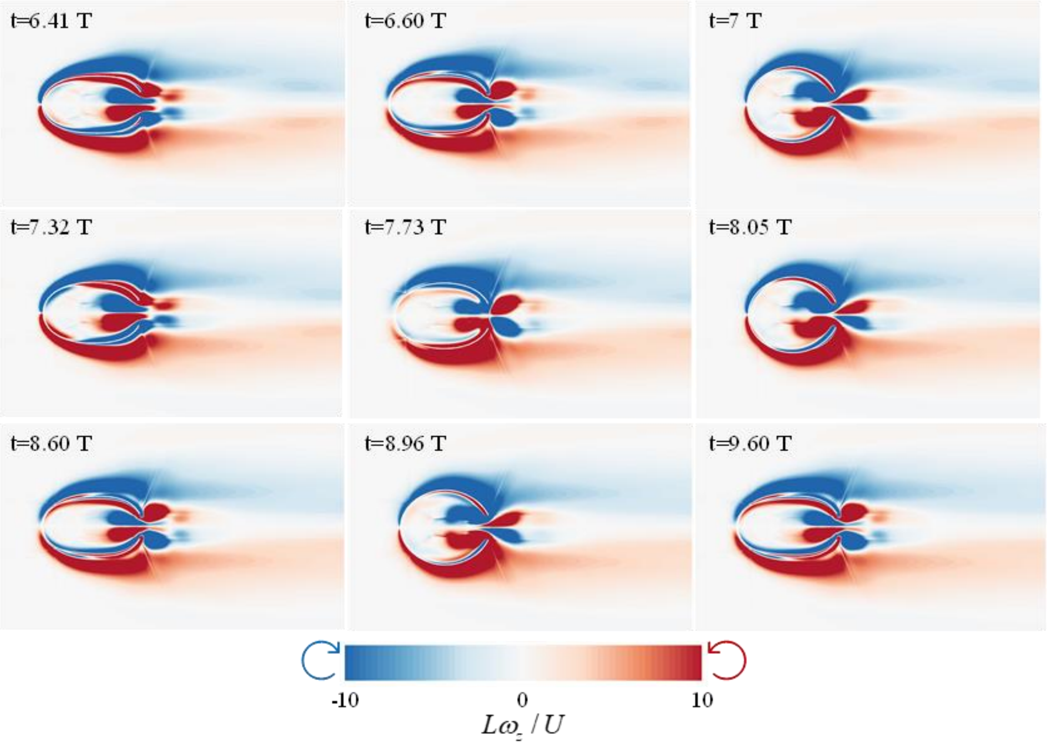

Fig. 5.16. The evolution of Z-vorticity contour around the swimmer at Re = 400 and *St* = 3.2.

5.1.4.4 Effect of the nozzle size

Jet flow, the main source of the thrust in jet propulsion, is directly influenced by the size of the nozzle which serves as the inlet and outlet. Here, two nozzle sizes, a large one with R =

0.14 L and a small one with R = 0.075 L, are considered. It is noted that the free vibration frequencies used for the inflation phase are different for the two nozzle sizes. They are obtained from the free vibration study introduced in section 5.1.2. The parameters in the simulations for the large and small nozzle sizes are listed in Table 5.2.

Table 5.2. List of parameters used in the simulations for the two different nozzle sizes.

Re	K	C_{ef0}	m^*	a	b	R (Large)	R (Small)
1×10^5	0.05	0.64	0.05	0.2 L	0.15 L	0.14 L	0.075 L

The time-averaged thrust, power expenditure coefficient, efficiency, and the instantaneous jet speed at St = 3.6 are plotted in Fig. 5.17. It can be seen that under the parameters studied, at low actuation frequency, the mean thrust of the jet swimmer with the small nozzle size is larger. With the increase of St, its time-averaged thrust becomes lower than that for a large nozzle size. The peak mean thrust of the swimmer with the large nozzle is 0.012 at St = 3.2, an increase by 27% from the peak thrust (0.0094) of the swimmer with the small nozzle. The power expenditure of the two cases monotonously increases as the external force actuation frequency increases. The swimmer with the large nozzle size is more energy-saving compared to that with a small one. As a result of more thrust and less power expenditure, the swimmer with a large nozzle is more efficient than the one with a small nozzle with the maximum efficiency difference of 98% between them (with the efficiency of the latter as reference) at St = 3.2, as shown in Fig. 5.17(c). The variation patterns of $\overline{C_T}$, $\overline{C_P}$ and η as a function of St suggest that the swimmer with a relatively large nozzle generally outperforms that with a small one in terms of propulsive capabilities. This may suggest that a relatively large nozzle size in the design of jet propulsion-based underwater vehicles can be generally favorable. Even the nozzle size can be changeable in the practical design so that it can match with specific jet frequency and flow conditions for best performance.

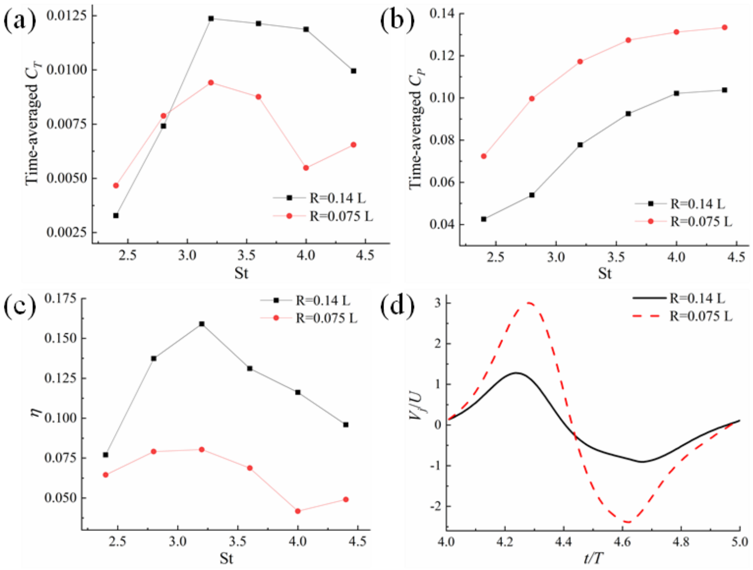

Fig. 5.17. The mean thrust (a), power expenditure coefficient (b), efficiency (c), and instantaneous jet speed within one period at *St* = 3.6 (d) of the squid-like jet swimmers with two different nozzle sizes.

Although the time-averaged thrust of the system with the small nozzle is lower, its maximum instantaneous thrust coefficient (0.61) is larger than that of the swimmer with the large nozzle (0.54). This implies that the swimmer with a small nozzle may achieve a larger instantaneous burst speed. As expected, a larger jet speed is also produced from the small nozzle as presented in Fig. 5.17(d). The large nozzle leads to the early emergence of peak jet velocity within a deflation-inflation locomotion period.

The vorticity patterns around the swimmers at different values of *St* for the two nozzle sizes are plotted in Fig. 5.18. At low frequency, e.g., *St* = 2.4, the internal body vortices and jet vortices are weak when the nozzle size is large. This is different from the small nozzle size case, whose vortices are much stronger. The main difference at this instant (*t* = 8 *T*) between the two vorticity patterns is that the symmetry of the vortex pairs around the swimmer with a large nozzle size is still well sustained. In contrast, the other vorticity patterns present fully developed intramantle disturbance and anti-symmetrical jet vortex pairs.

In addition to the fluid viscosity, the nozzle size also has a significant influence on the development of irregularity of the locomotion system as the cycle continues, which is presented by the lift force production in Fig. 5.19. As can be seen, before the occurrence of remarkable asymmetry of vortices at *t* = 8 *T*, the lift generation is noticeable from the sixth period.

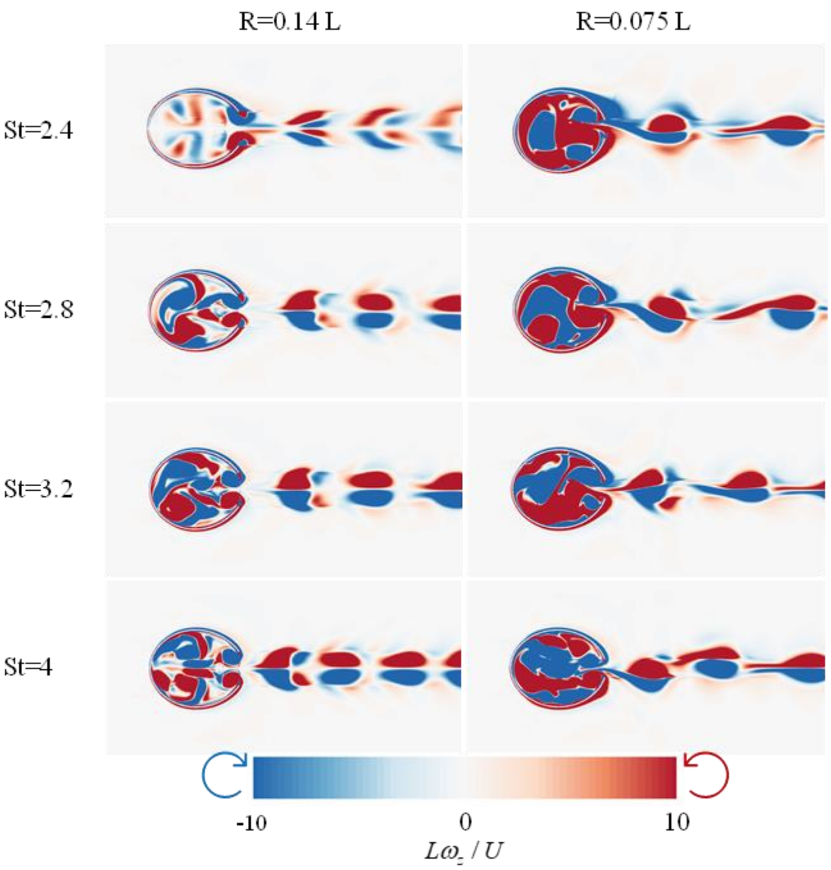

Fig. 5.18. *Z*-vorticity contour at t = 8 T for the two different nozzle sizes.

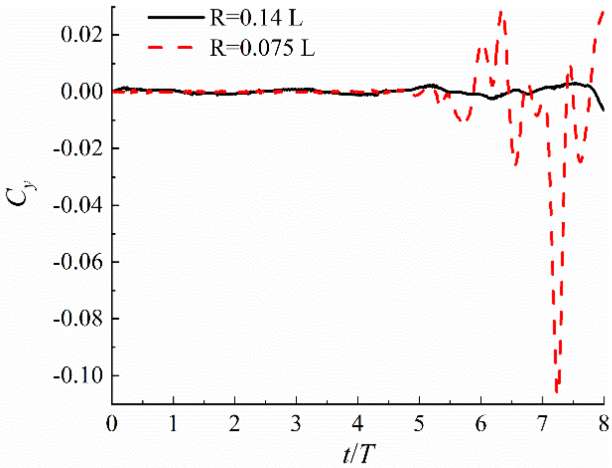

Fig. 5.19. The time history of C_y at *St* = 3.2 for the two different nozzle sizes.

The evolution of the *Z*-vorticity contour around the swimmer with the small nozzle size is presented in Fig. 5.20 to demonstrate the development of the symmetry-breaking instability of the vorticity patterns. Similar to the phenomenon shown in Fig. 5.15, the symmetry breaking of the vortex pairs firstly happens inside the mantle body at around t = 5.98 T. Afterwards, the internal body disturbance takes noticeable effect on the formation of jet vortices one period later, i.e., at about t = 7.67 T. Regarding the vorticity pattern for the cases with the large nozzle sizes at St = 3.2, the wake symmetry is sustained at least until t = 8 T, though the internal body vortices tend to become irregular at this instant as shown in Fig. 5.18. Consequently, the deformation of the body remains regular, and lift production is negligible until the end of the eighth period.

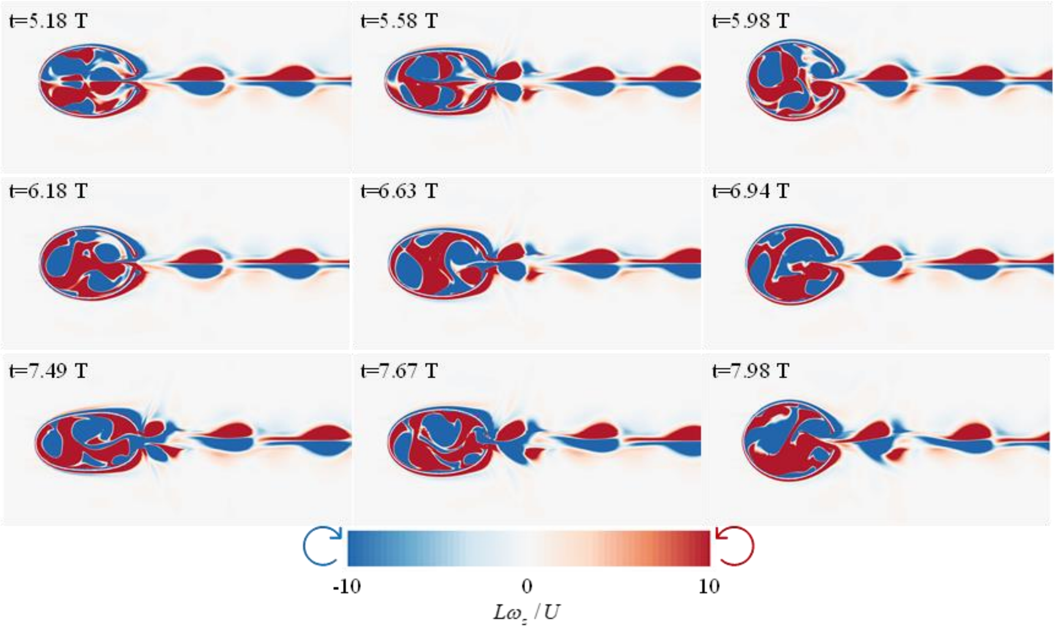

Fig. 5.20. The evolution of Z-vorticity contour at St = 3.2 around the squid-like swimmer with the small nozzle size.

5.1.5 Concluding remarks and discussions

Inspired by the jet propulsion of squid and other cephalopods, a deflation-inflation propulsion system is proposed in this section. The two-dimensional squid-like swimmer is simplified as part of a hemi-ellipse with an open end that serves as the nozzle. The external force is applied on the mantle body surface to actuate the deflation which mimics the constriction of the circular muscles of the squid. The mantle body shrinks under the actuation of the external force during the deflation phase. As a consequence, the fluid inside the chamber is ejected through the nozzle. After the external force is withdrawn, the mantle inflates as a result of the release of the elastic energy in the flexible body structure. During this inflation phase, the fluid enters the chamber through the nozzle, which will then be expelled in the next ejection. Our simulation results indicate that periodic deflation-inflation locomotion and thrust production (see Fig. 5.5 and Fig. 5.6) are achieved under this mechanism.

The effect of Reynolds number on jet propulsion is investigated systematically. Our results show that a higher Reynolds number yields larger mean thrust generation under the parameters studied. This thrust augmentation may be attributed to the suppressed body-generated vortices near the outer body surface, which is an indicator of drag force. Additionally, the resonant frequency of the mantle structure which was excluded in Bi and Zhu (2019b) is determined, and results indicate that although maximum vibration displacement is observed near the resonant frequency, it does not yield better propulsion performance. Peak time-averaged thrust is observed as the actuation frequency is varied for all four Reynolds numbers. The maximum efficiency is presented at a relatively low external force actuation frequency (see Fig. 5.9(c)). Within the range of parameters considered in this study, the peak efficiency reaches 25%, much higher than the one in Bi and Zhu (2019b) (15%). The visualization of flow patterns shows that three modes can be observed with the increase of *St*. In pattern I, the body-generated vortices are comparable in strength with the jet vortices. Pattern II is dominated by jet vortices, and the body-shed vortices become more dominating in pattern III. The most efficient jet propulsion is seen near the transition from pattern I to pattern II when jet vortices start to dominate, which is consistent with the findings by Bi and Zhu (2019b).

In Bi and Zhu (2019b), the symmetry-breaking instability at Re = 400 was demonstrated after the inflation-deflation locomotion proceeds several cycles. They expected that a higher Reynolds number tends to enhance instability. Indeed, our model shows that the higher the Reynolds number is, the earlier the irregular deformation and vortices patterns occur (see Fig. 5.14 and Fig. 5.15). However, their numerical model only emphasized the importance of wake instability. Instead, our simulation results indicate that the mechanism of the system instability seen at low Reynolds number (laminar flow) may not apply to the turbulent flow under high Re scenarios. Specially, under laminar flow scenarios, the asymmetry is mainly seen in the wake jet vortex pairs, while the effect of internal vortices remains insignificant. In comparison, at a much higher Reynolds number in this study, the disturbance occurs firstly in the intramantle vortices whose symmetry is broken during the collision between newly formed and vortices formed earlier. Around one cycle later, this disturbance is reflected in the wake jet vortices noticeably.

Despite the fact that the current study is strictly two-dimensional, the symmetry-breaking phenomenon may still have implications in the swimming of real squid, in which burst-and-coast jet along with the fin oscillation is employed. At low Re conditions where fluid viscosity is prominent, continuous swimming is more advantageous than burst-and-coast swimming (Weihs, 1974). Therefore, more frequent contractions with less coasting were predicted to be favored by squid hatchlings swimming in the laminar flow environment by Bartol et al. (2008), which was in line with biological measurement (Thompson and Kier, 2001). In comparison, fin activations are more frequently utilized by juvenile and adult squids at higher Reynolds numbers. Based on our results, it is sensible to conjecture that intermittent burst-and-coast swimming not only improves the efficiency but also suppresses the symmetry-breaking instability of the internal body vortices. As indicated by Bi and Zhu (2019b), some specific measures may be needed to mitigate the effect of this instability during the design of jet-propulsion inspired underwater vehicle or propulsors, e.g., via active control of the body deformation to change the evolution of the internal vortices pattern.

For the sake of completeness, the effect of nozzle size on propulsion performance is explored as well. The results indicate that although a narrow nozzle may increase the instantaneous thrust production, it does not always benefit the time-averaged thrust or efficiency. Besides, a small nozzle size leads to stronger vortices which are more likely to induce symmetry-breaking instability (see Fig. 5.19 and Fig. 5.20).

5.2 Pulsed-jet Propulsion of a 3D Squid-inspired Swimmer in the Presence of Background Flow

In section 5.1, the propulsion performance of a two-dimensional squid-like jet swimmer at a high Reynolds number is studied. The inflation-deflation of the mantle body is actuated by externally added force and the release of the elastic energy of the structure. Therefore, the fluid-structure interaction between the swimmer and surrounding fluid during the dynamic deformation is taken into consideration. Despite that this 2D model bears some resemblance to the jet propulsion of a squid, the exploration of the significant three-dimensional nozzle-shed vortex rings observed from live squid jetting is not possible for a two-dimensional model. Thus, in this section, a 3D squid-like swimmer model is considered. By prescribing the body deformation and jet velocity profile, we numerically investigate the jet flow field and propulsion performance at different jet velocity fashions under the influence of background flow during a single deflation procedure.

5.2.1 Problem statement

A squid-like swimmer consisting of a pressure chamber with an opening is considered in this section. This chamber mimics the mantle cavity of the squid, and its opening serves as both the inlet and outlet of fluid. During a typical deflation-inflation process, the chamber body shrinks so that the fluid inside the cavity is expelled through the nozzle, and then the fluid is sucked back into the chamber for the next jetting. In this particular study, we focus on a single deflation deformation that produces most of the thrust during the deflation-inflation propulsion cycle.

The geometry we consider is axisymmetric about the x-axis, as shown in Fig. 5.21(a). The body length of the swimmer is L, and the nozzle size is denoted by D. The upper surface (above the upper dash line in Fig. 5.21(a)), and lower surface (below the lower dash line in

Fig. 5.21(a)) are two halves of an ellipse, respectively. In a cylindrical coordinate system, the radial distance from the x-axis to a certain point on the body surface is given by

$$r = 0.5L\sqrt{\left(1-e^2\right)\left(1-4x^2/L^2\right)} + 0.5D, \tag{5.6}$$

where e is the eccentricity of the ellipse. It is worth noting that although the geometry itself is axisymmetric, there is no guarantee that the flow field remains axisymmetric at a relatively large Reynolds number (about 1000) considered in this study, unlike the cases with small Re (e.g., for flow over a static cylinder, the flow is assumed as axisymmetric below Re = 210 (Tomboulides et al., 1993)). Therefore, using 3D modeling in this work can avoid the possible inaccuracy due to axisymmetric simplification.

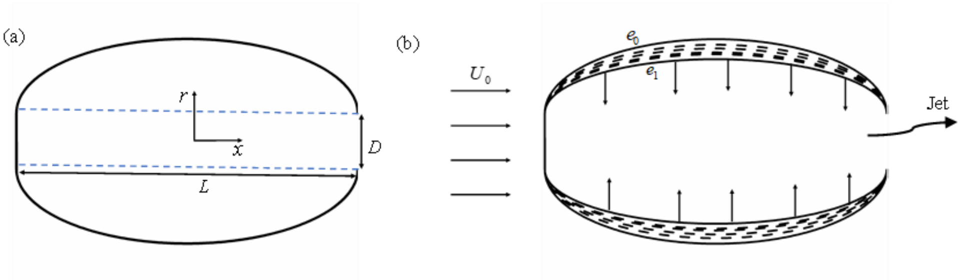

Fig. 5.21. The geometry (a) and deformation (b) of the profile of the wall (the starting (e_0) and ending (e_1) positions are shown in solid lines).

As shown in Fig. 5.21(b), during deflation, the length of the body L and nozzle diameter D = 0.2 L remain unchanged, while the eccentricity of the ellipse increases so that the volume of the internal body is reduced. This design is similar to an octopus-inspired robot in Weymouth et al. (2015) whose internal skeleton is rigid, and therefore the body length of the robot is constant. This is also in line with the jet locomotion of a squid, during which the body length remains almost unchanged, but the perimeter decreases as the body shrinks (Ward, 1972).

Fig. 5.22 shows the deflation process of the three-dimensional squid-like swimmer. During the deformation, the wall thickness h which equals 0.02 L at its depleted state is varied so that the overall volume of the solid body (excluding the fluid inside it) remains constant to avoid the mass change of the body itself. The two extreme states, i.e., the fully inflated and deflated, are denoted by $e = e_0$ and $e = e_1$, whose internal volumes (the volume of the fluid which fills in the chamber) are $V(e_0)$ and $V(e_1)$, respectively. The equivalent stroke ratio associated with the body deflation is defined as $\Gamma(t) = 4\Lambda(t)/(\pi D^3)$, where $\Lambda(t) = V(e_0) - V(e(t))$ ($e(t)$ is the instantaneous eccentricity). To characterize each case, we define the maximum equivalent stroke ratio Γ_m, which is closely related to body deformation and reached at the end of the body shrinking, as $\Gamma_m = 4(V(e_0) - V(e_1)/(\pi D^3)$. During the deflation, the spatially averaged speed of the ejected jet flow V_j at the nozzle can be determined by

$$V_j(t) = \frac{-4}{\pi D^2}\frac{dV}{dt} = \frac{d\Gamma}{dt}D. \tag{5.7}$$

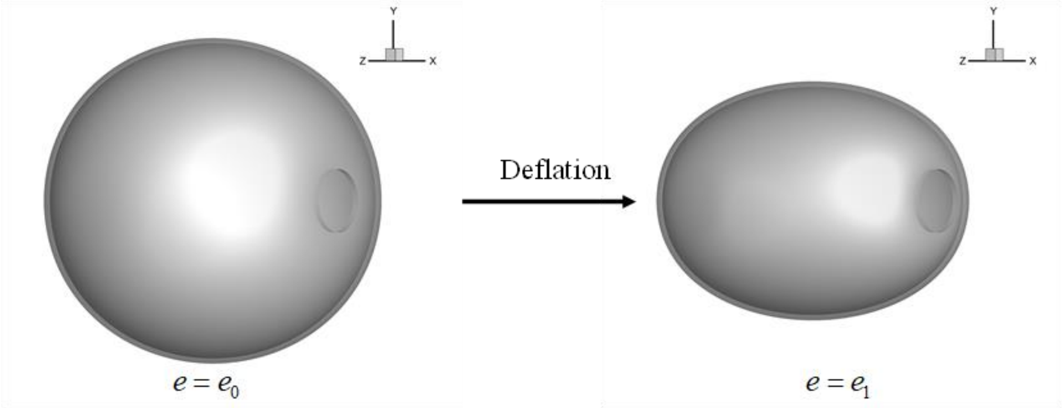

Fig. 5.22. The deflation during the cephalopod-inspired jet swimming.

Following the study by Bi and Zhu (2020), the jet speed $V_j(t)$ is prescribed to allow us to calculate the instantaneous internal volume $V(e)$ and equivalent stroke ratio $\Gamma(t)$ at the instant through Eq.(5.7), from which the eccentricity can also be determined. The maximum equivalent stroke ratio Γ_m which will be examined is listed in Table 5.3. The final deflated state is fixed herein, which is in line with some existing jet-propulsion systems (Christianson et al., 2020; Weymouth et al., 2015). In their designs, the deflated shape is the natural (or inactivated) shape, while the inflated form is the activated state. This is based on the burst-coast swimming mode in which the deflated profile is used for coasting motion since this shape is more streamlined than the inflated one.

Table 5.3. The maximum equivalent stroke ratio Γ_m for various initial eccentricities e_0 with the fully deflated state reached at $e_1 = 0.92$.

e_0	0.904	0.898	0.883	0.868	0.844
Γ_m	3.31	4.66	7.60	10.59	15.07

The jet-based Reynolds number is given by

$$\mathrm{Re}_j = V_{jm}D/\nu, \tag{5.8}$$

where V_{jm} denotes the maximum jet speed and ν is the kinematic viscosity. Simulations in this study will be conducted at $\mathrm{Re}_j = 980$.

To evaluate the performance of this propulsion system, we define the instantaneous thrust coefficient C_T and power expenditure coefficient C_P as

$$C_T = -\frac{F_x}{0.5\rho V_{jm}^2 D^2}, \tag{5.9}$$

and

$$C_P = \frac{P}{0.5\rho V_{jm}^3 D^2}, \tag{5.10}$$

where F_x is the total hydrodynamic force on the swimmer in the x-direction, ρ represents the fluid density, and P is the instantaneous power expenditure of the body, which can be calculated as

$$P = \int_{\Gamma_b} \boldsymbol{F}_{bs} \cdot \boldsymbol{U}(s) ds, \tag{5.11}$$

where $\boldsymbol{F}_{bs}$ denotes the fluidic force at node s on the body surface, $\boldsymbol{U}$ is the body velocity and Γ_b stands for the whole surface of the body (including both the inner and outer surfaces).

The propulsion factor quantifying the propulsive efficiency during the deformation is defined as

$$\eta = \frac{V_{jm} I}{P_{inp}}, \tag{5.12}$$

where I is the overall impulse during the deflation period T_d, calculated by $I = \int_0^{T_d} -F_x(t)dt$, and P_{inp} denotes the overall energy input which is given by $P_{inp} = \int_0^{T_d} P(t)\,dt.$

5.2.2 Mesh independence study

The computational domain and generated fluid mesh around the body surface are shown in Fig. 5.23. On the body surface, the no-slip condition is applied, while for the other boundaries, the non-reflective far-field boundary condition is imposed. A mesh independence study is performed to assess the appropriate mesh and time step resolution by solving the laminar flow for U_0 = 0.42 V_{jm} and Γ_m = 10.59. Specifically, three grids are generated: a coarse grid with 5109112 cells, a medium-size grid with 6437992 cells, and a fine grid with 8127368 cells. The minimum grid spacing for the three meshes is 3.5×10^{-3} L. Like the other simulations in this study, the body deformation is started after the surrounding quasi-steady flow field is fully developed at the presence of incoming background velocity U_0. Firstly, the mesh convergence test is performed in which three meshes are used along with the dimensionless time step size, defined as $\overline{\Delta t} = \Delta t V_{jm}/L$, $\overline{\Delta t} = 0.02$, as shown in Fig. 5.24(a). The required computational time for the fine mesh and medium mesh is 1.70 T_{coarse} and 1.34 T_{coarse}, respectively, where T_{coarse} is the computational time required for a coarse mesh using the same number of computer cores. It can be seen that the medium mesh yields a result that is very close to that of the fine mesh. Thereafter, the effect of the time step size is also studied, as shown in Fig. 5.24(b). These tests show that the results are not sensitive to the mesh size and time step size if they are sufficiently small. Therefore, the following simulations hereafter are carried out with a medium-size mesh at $\overline{\Delta t} = 0.025$ to reduce computational cost and ensure accuracy.

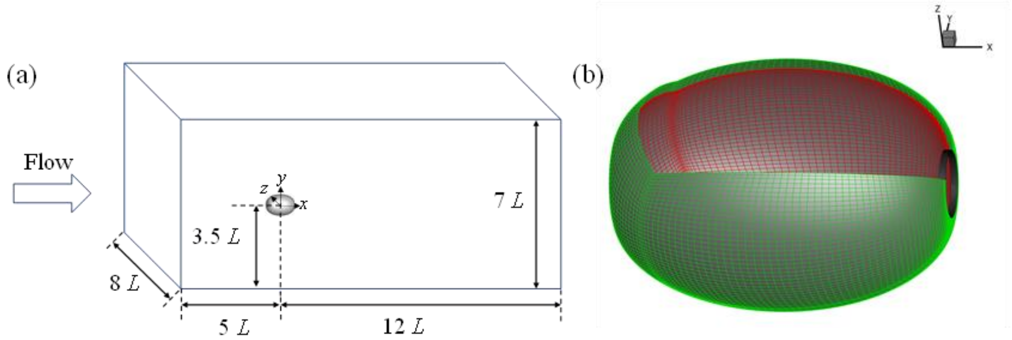

Fig. 5.23. Sketch of the computational domain (not in scale) (a) and the fluid mesh at the body surface (b). Only part of the mesh at the body surface is presented here to show the inner (red), outer (green), and nozzle (black) surface.

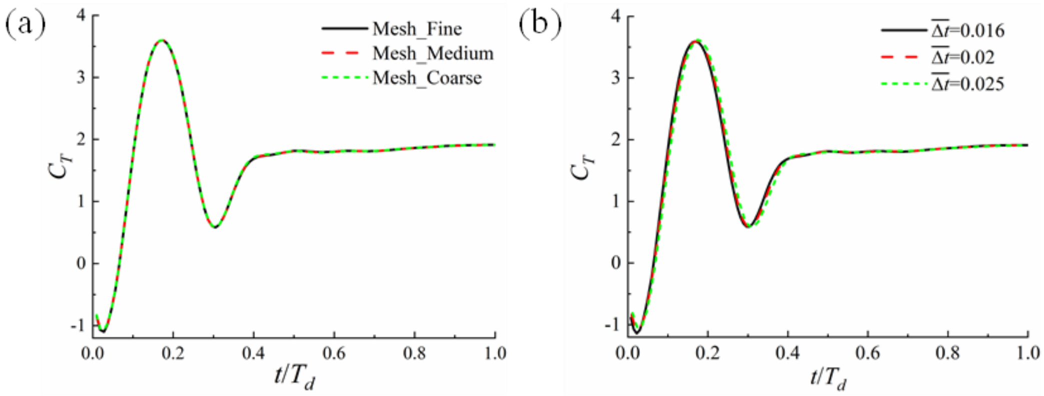

Fig. 5.24. Comparison of thrust coefficient C_T at Γ_m = 10.59 when three different meshes are used along with $\overline{\Delta t} = 0.02$ (a) and the medium-size mesh is used with three different time step sizes (b).

5.2.3 Results

Similar to Jiang and Grosenbaugh (2006), we initiate the body deformation after the external quasi-steady flow field is fully developed. To elaborate, the fluid field where the inflated body is at rest in the presence of incoming uniform flow is firstly simulated and then taken as the initial flow field for the following computations when the body deflation is included.

We start with a constant jet velocity profile for different maximum equivalent stroke ratios Γ_m at the same incoming velocity U_0 of the background flow, i.e., the time history of the spatially averaged jet speed is $V_j(t) = V_{jm}$, $t \in (0,T_d]$, where the duration of the deflation procedure is determined by

$$\int_0^{T_d} V_j dt = \Gamma_m D. \tag{5.13}$$

Afterwards, the cases at different incoming velocities with the constant jet velocity profile are studied. The ratio between incoming velocity to jet velocity U_0/V_{jm} is chosen as 0.42−0.69, consistent with the experimental measurement of live squids by Anderson and Grosenbaugh (2005). Then the effect of two additional jet velocity profiles is investigated.

5.2.3.1 Effect of maximum equivalent stroke ratio (body deformation)

To visualize the wake structure around the swimmer body at different maximum equivalent stroke ratios, we plot the *Z*-vorticity contour, streamline, and *Q* criterion distribution at the plane $z = 0$, as well as the wake structure by iso-surface of *Q* criterion, in Fig. 5.25. It can be seen from Fig. 5.25(a) and (g) that at a small maximum equivalent stroke ratio almost all of the ejected fluid is entrained into a single vortex ring. When Γ_m is increased to 10.59, on the other hand, the wake consists of a leading vortex ring followed by a trailing flow, as shown in Fig. 5.25(b). This is reminiscent of the two jet modes observed behind the jetting of squid, i.e., in mode I the ejected fluid rolls up into an isolated vortex ring, while in mode II a leading vortex ring pinches off from the trailing jet (Bartol et al., 2008). The cases for $\Gamma_m = 3.31$ and 10.59 show characteristics of these two modes, respectively.

Nevertheless, a close inspection of Fig. 5.25(f) and (h) reveals that there are no remarkable secondary vortices formed behind the leading vortex ring at $\Gamma_m = 10.59$, unlike what was observed in Gharib et al. (1998). This difference may be mostly attributed to the fact that larger jet-based Reynolds number Re_j (above 2500) was considered in the experiment, while at a small Reynolds number (below 1000), our results are consistent with numerical and experimental data in Bi and Zhu (2020) and Palacios-Morales and Zenit (2013). The interaction between the jet flow and background flow near the nozzle can be observed from the streamline distributions in Fig. 5.25(c) and (d), implying that the incoming flow may affect the wake flow field and vortex ring formation, which will be examined later.

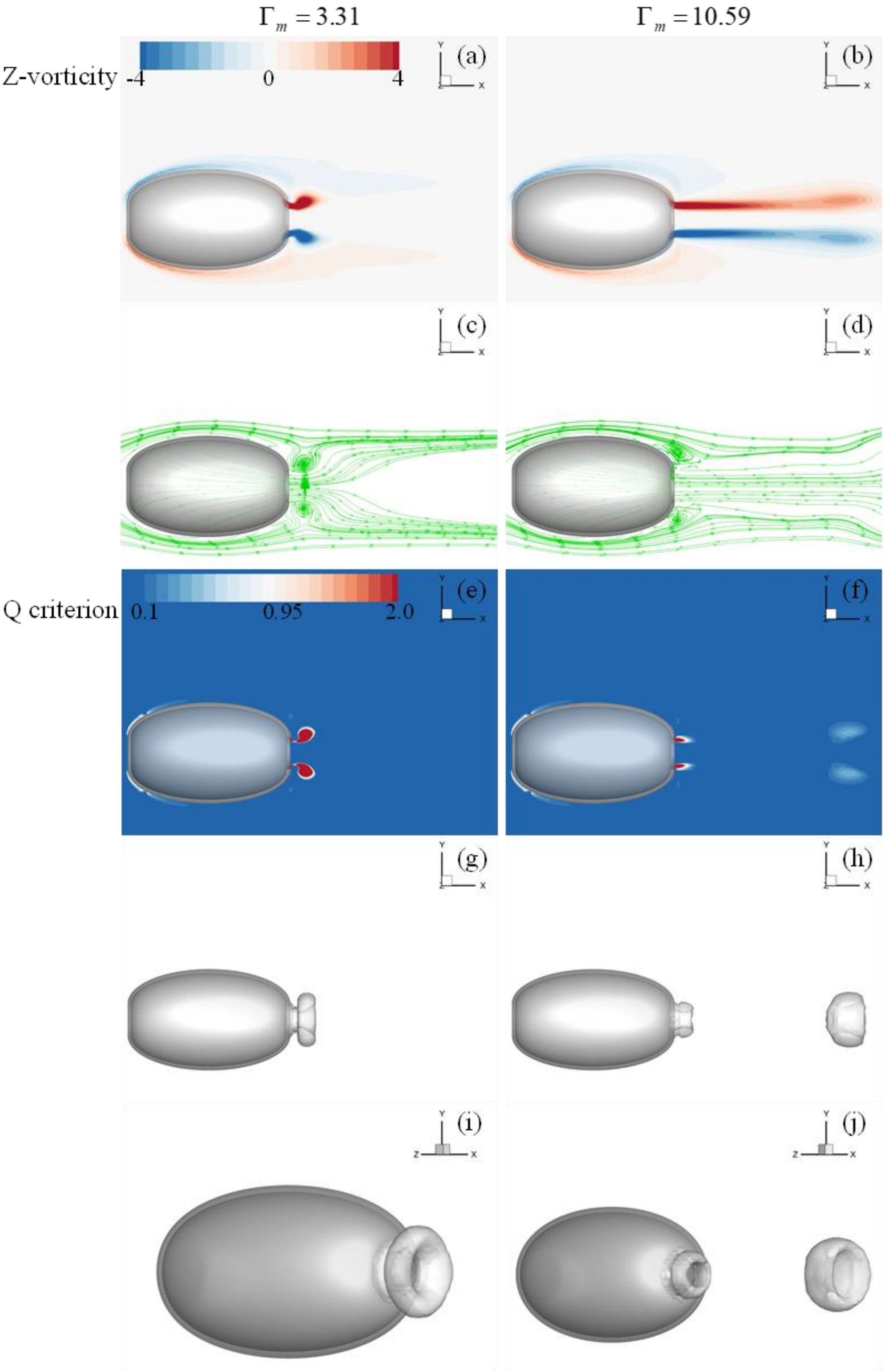

Fig. 5.25. The Z-vorticity contour ((a) and (b)), streamline distribution ((c) and (d)), Q criterion distribution ((e) and (f)) at plane $z = 0$, and wake structure visualized by iso-surface of Q criterion ($Q = 0.22$) ((g) ~(j)) at $\Gamma_m = 3.31$ and 10.59 and $U_0 = 0.42\ V_{jm}$. The Z-vorticity and Q criterion are normalized by V_{jm}/D and V_{jm}^2/D^2. The figures are captured at the end of the deflation.

For further insight into the evolution of the near-body flow field and vortex ring, the *Z*-vorticity contour and *Q* criterion distribution at the plane $z = 0$ and the wake structure at several instantaneous formation numbers during the jetting at $\Gamma_m = 10.59$ are presented in Fig. 5.26. However, it is important to note that the detachment of the leading vortex ring from its trailing jet cannot be determined by the *Q*-criterion contours presented here, as they exclude the region of the free shear layer which is the source of vorticity for the leading vortex ring growth. Although the critical value of stroke ratio was found to be around 4 by Gharib et al. (1998), some subsequent studies suggested that the critical stroke ratio may vary depending on specific conditions, e.g., velocity distribution at the nozzle plane and jet-based Reynolds number (Mohseni et al., 2001; Palacios-Morales and Zenit, 2013; Rosenfeld et al., 1998). For example, Bi and Zhu (2020) found that at $\mathrm{Re}_j = 150$, the trailing flow was not strong enough to induce a secondary vortex ring, and it remained connected with the leading vortex ring after $\Gamma = 4$ so that the trailing flow was still able to feed the leading vortex ring.

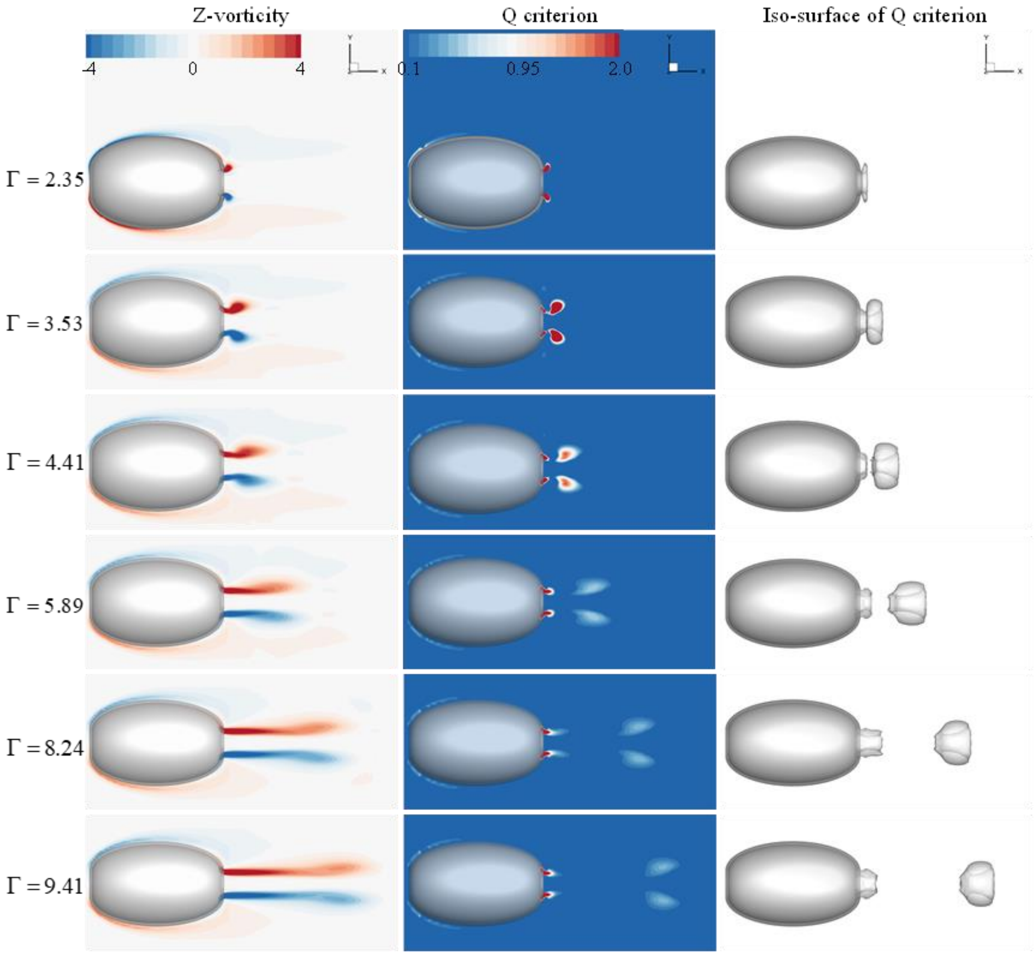

Fig. 5.26. Evolution of the *Z*-vorticity contour and *Q* criterion distribution at plane $z = 0$, and wake structure visualized by iso-surface of *Q* criterion ($Q = 0.22$) at $\Gamma_m = 10.59$ and $U_0 = 0.42\ V_{jm}$.

To understand the actual growth and decay of the leading vortex ring, we hereby calculate the circulation of the leading vortex ring. Following Palacios-Morales and Zenit (2013), we use the Q criterion to obtain a closed area where $Q > 0$ to integrate the vorticity and calculate the vortex ring circulation. The circulation C is obtained by

$$C = \int_{Q>0} \omega_z dS, \tag{5.14}$$

where ω_z is Z-vorticity at plane $z = 0$ given by

$$\omega_z = \frac{\partial u}{\partial y} - \frac{\partial v}{\partial x}. \tag{5.15}$$

It is noted that only the vorticity in the core of the vortex is considered using this method. Thus, the circulation values presented here may be lower than those reported by Gharib et al. (1998) and Mohseni et al. (2001). The vortex ring circulation with various maximum equivalent stroke ratios is plotted in Fig. 5.27. The normalized vortex ring circulation reaches a peak value of about 2.2 at around $\Gamma = 7.0$. However, it is important to note that this stroke ratio ($\Gamma = 7.0$) may not be the formation number defined by Gharib et al. (1998) (i.e., the maximum stroke ratio in which the circulation from the jet is completely enrolled into the leading vortex ring). In our study, this value corresponds to the time instant when the input from the jet is not able to keep up with the viscous dissipation so that the circulation of the leading vortex ring stops growing. At the relatively low Reynolds number considered in this work, the dissipation effect is pronounced. For example, the peak vortex ring circulation does not remain constant for a long time, as shown in Fig. 5.27. Instead, it decreases gradually due to viscous dissipation.

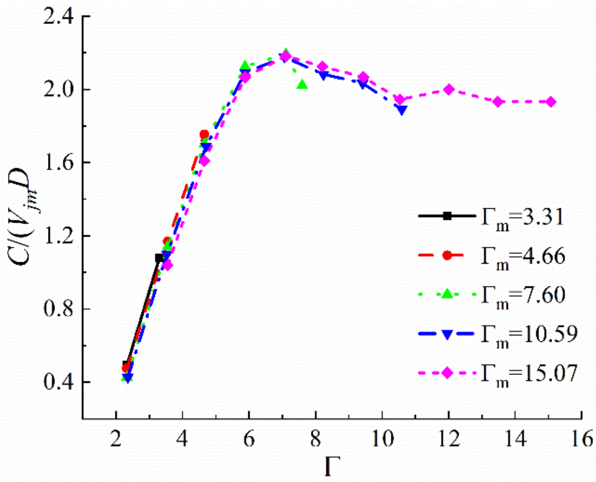

Fig. 5.27. Vortex ring circulation C as a function of equivalent stroke ratio Γ at $U_0 = 0.42\ V_{jm}$.

It is interesting to examine the effect of body deformation on the actual jet velocity profile. In most previous studies involving a piston arrangement (Gao et al., 2020; Gharib et al., 1998; Jiang and Grosenbaugh, 2006), the nozzle features a tubular shape so that the flow is mainly ejected in the axial direction. In comparison, our system is more like a conical nozzle as the lateral dimension decreases during the body's shrinking. For this reason, there may be a significant radial component in the jet velocity, as shown from the streamline distribution in Fig. 5.25(c) and (d). For further insight into the actual jet velocity profile at the exit plane, the distribution of axial and radial velocity is presented in Fig. 5.28. As shown in Fig. 5.28(b), a maximum radial velocity of around 0.3 V_{jm} is observed near the nozzle surface. On the other hand, we also observe a small peak of the axial velocity, which is larger than the jet speed near the position $r/D = 0.35 - 0.45$.

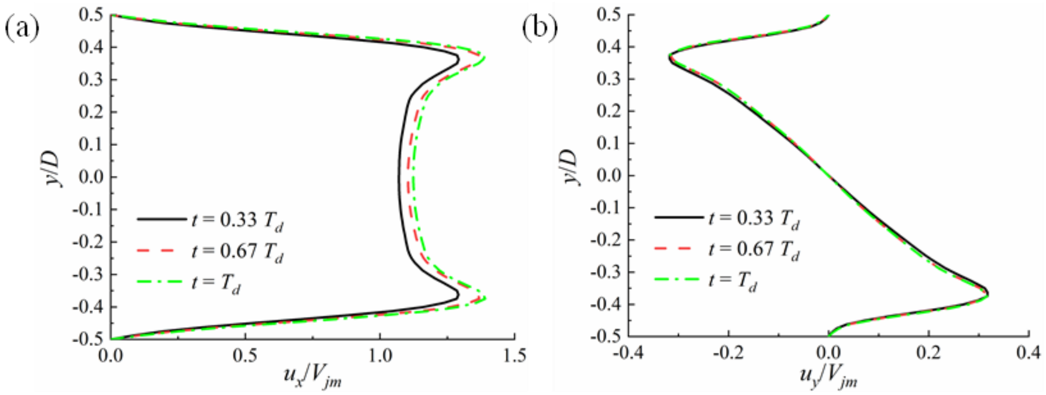

Fig. 5.28. The axial velocity (u_x) (a) and radial velocity (u_y) (b) distribution at the exit plane at $z = 0$ plane with $\Gamma_m = 10.59$ and $U_0 = 0.42\ V_{jm}$.

We then examine the jet thrust production with the fixed incoming flow velocity. The time history of the total thrust coefficient C_T at different maximum equivalent stroke ratios Γ_m is presented in Fig. 5.29(a). It can be seen that the total thrust arrives at a quasi-steady phase after reaching a peak value. This constant thrust is found to be reached after Γ is roughly beyond 4 when C_T is replotted against the instantaneous equivalent stroke ratio Γ in Fig. 5.29(b). For the interpretation of the observed temporal profiles of C_T, we analyze the thrust sources. By applying the momentum theorem, three thrust sources can be identified, i.e., the thrust source F_j attributed to jet momentum flux out of the nozzle plane, over-pressure F_p at the nozzle exit plane (Krueger and Gharib, 2003), and the thrust source F_m which equals the change rate of the horizontal momentum of the fluid inside the chamber (Bi and Zhu, 2020). Specifically, the thrust coefficient C_{Tj} attributed to jet momentum flux is calculated by

$$C_{Tj} = F_j / \left(0.5\rho V_{jm}^2 D^2\right), \tag{5.16}$$

where

$$F_j = \int_A \rho u_x^2 dS, \tag{5.17}$$

where A represents the nozzle plane. A comparison between Fig. 5.29(a) and Fig. 5.30(a) reveals that the jet momentum flux-related thrust is not the main contributor to the total thrust during the initial stage when C_T is much larger than C_{Tj}, although at the quasi-steady phase C_{Tj} approaches C_T.

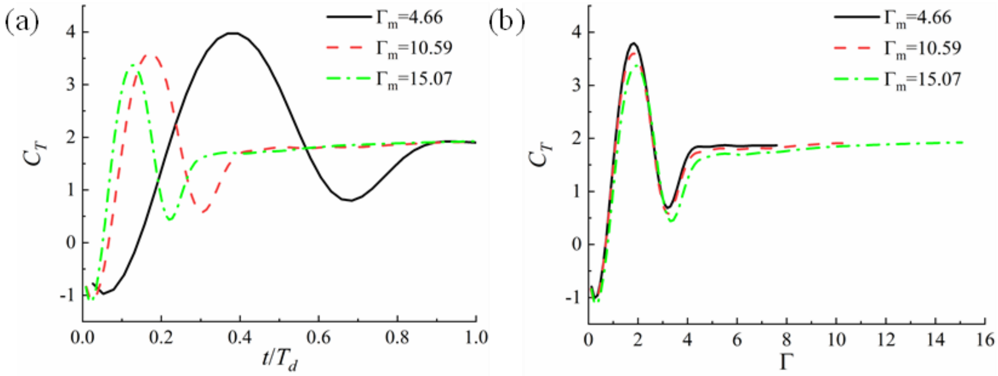

Fig. 5.29. C_T as a function of time (a) and instantaneous equivalent stroke ratio Γ (b) at $U_0 = 0.42\ V_{jm}$.

We further plot the excessive pressure-related thrust coefficient $C_{Tp} = F_p/(0.5\rho V_{jm}^2 D^2)$ in Fig. 5.30(b), where $F_p = \int_A \Delta p dS$ ($\Delta p = p - p_\infty$, with p_∞ being the pressure in the far-field) is the excessive pressure force at the nozzle plane. Nevertheless, by itself, C_{Tp} is not able to bridge the difference between C_{Tj} and the total thrust C_T, especially at its peak. For instance, at $\Gamma_m = 10.59$, the peak value of C_T is 3.37 while the maxima of $C_{Tp} + C_{Tj}$ is only 1.81. The remaining thrust comes from F_m, whose normalized form $C_{Tm} = F_m/(0.5\rho V_{jm}^2 D^2)$ is shown in Fig. 5.30(c). Taking $\Gamma_m = 15.07$ as an example, we find that the overall peak thrust at $t = 0.13\ T_d$ is mainly dominated by the horizontal momentum change of the fluid inside the chamber C_{Tm}, as shown in Fig. 5.29(a) and Fig. 5.30(c). By comparing Fig. 5.29(a) with Fig. 5.30(a), the thrust component attributed to jet momentum flux C_{Tj} dominates thrust generation roughly after $t = 0.4\ T_d$. Although previous studies suggested that the overpressure effect would enhance the generated thrust of the starting jet (Krueger and Gharib, 2003), we find its contribution C_{Tp} is relatively small during the whole procedure. In a comparison of Fig. 5.30(b) and (d), added-mass-related thrust (which will be discussed later) attributed to body deformation even contributes more thrust than C_{Tp}. The correlation of overall thrust production between the three thrust sources applies to other Γ_m as well.

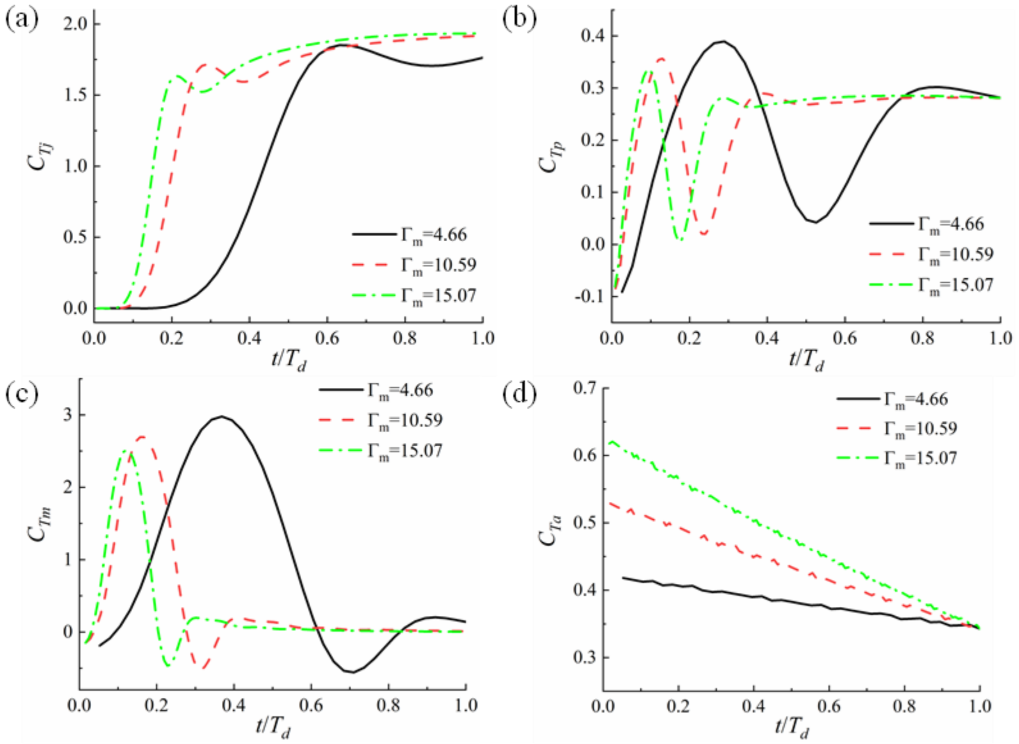

Fig. 5.30. Time history of C_{Tj} (a), C_{Tp} (b), C_{Tm} (c), and C_{Ta} (d) at $U_0 = 0.42\ V_{jm}$.

As mentioned before, due to the viscous dissipation effect, it is not straightforward to determine the traditionally defined formation number, corresponding to the last moment when the circulation supplied by the vortex generator is completely enrolled into the leading vortex ring, as proposed by Gharib et al. (1998). Nevertheless, for insights, we assume that the unsteady vortex ring dynamics mainly play roles in thrust production before C_T reaches constant to evaluate its contribution. Hereby, we define the impulse associated with vortex ring formation, i.e., the momentum flux I_j and the pressure impulse I_p, as

$$I_j = \int_0^{T_{ut}} F_{Tj} dt, \tag{5.18}$$

$$I_p = \int_0^{T_{ut}} F_{Tp} dt. \tag{5.19}$$

where T_{ut} is the instant when C_T approaches constant. Taking Γ_m = 4.66. 10.59 and 15.07 as examples, the values of I_j/I, I_p/I, and $(I_j + I_p)/I$ are compared in Fig. 5.31. It can be found that the unsteady vortex ring dynamics contribute substantially to the jet propulsion, especially at small Γ_m, i.e., small body deformation.

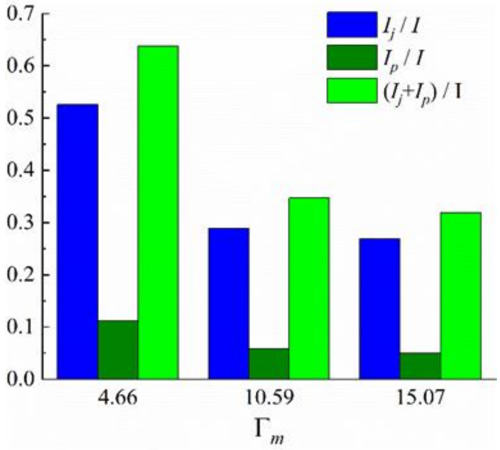

Fig. 5.31. Comparison of I_j, I_p, and their sum with the overall impulse I at $U_0 = 0.42\ V_{jm}$.

Besides, we further quantitively compare the three thrust components with the total thrust at $\Gamma_m = 15.07$ in Fig. 5.32(a). It can be seen that the peak value of the sum of the three parts matches well with that of the total thrust. However, during the quasi-steady phase, the combination of the three components overestimates the thrust production. The difference is partially attributed to the drag force on the body caused by the incoming flow. At $\Gamma_m = 15.07$, our simulations of a rigid body at its inflated state with $e_0 = 0.844$ in the incoming flow reveals that it sustains a drag coefficient $C_d = F_x/(0.5\rho V_{jm}^2 D^2) = 0.77$, as shown in Fig. 5.32(c). This value may decrease when the body shrinks as both the surface area and the projected area in the flow direction decrease, and the shape becomes more streamlined (for example, C_d drops to 0.54 at $e = e_1 = 0.92$). Meanwhile, the added-mass-related thrust F_a also contributes to the total thrust. We plot the dimensionless added-mass-related thrust coefficient $C_{Ta} = F_a/(0.5\rho V_{jm}^2 D^2)$ (its calculation is described in the next section) at different Γ_m in Fig. 5.30(d). As can be seen, larger body deformation (Γ_m) leads to a larger added-mass-related thrust. Now the added-mass-related thrust and the viscous drag force generally bridge the gap between the other three thrust components and the total thrust at the constant thrust phase, as shown in Fig. 5.32(b).

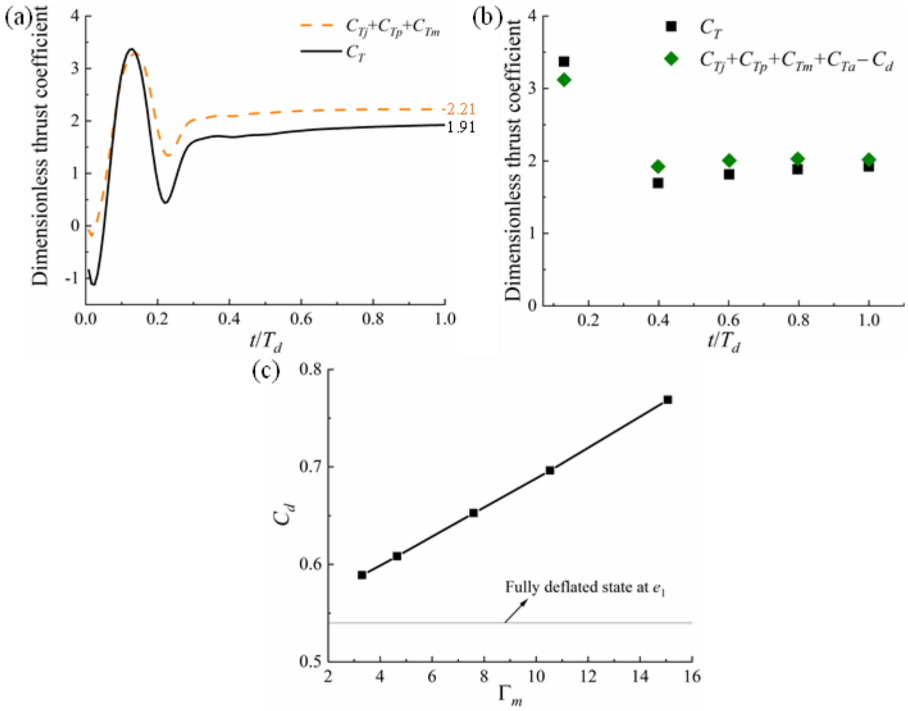

Fig. 5.32. Comparisons of total thrust C_T and the sum of C_{Tj}, C_{Tp} and C_{Tm} (a), and the sum of the four thrust component and drag force coefficient at Γ_m = 15.07 (b), and the drag force coefficient C_d of the swimmer at inflated state for different Γ_m (c) at U_0 = 0.42 V_{jm}.

Fig. 5.33 (a) presents the time history of the power expenditure coefficient C_P. It is found that there is an initial increase in power input, and it later approaches a plateau. In Fig. 5.33(b), we display the dependences of the time-averaged thrust coefficient and the propulsion factor of impulse generation upon Γ_m. In line with the previous study (Bi and Zhu, 2020), larger mean thrust production and propulsion factor are obtained at a small maximum equivalent stroke ratio Γ_m.

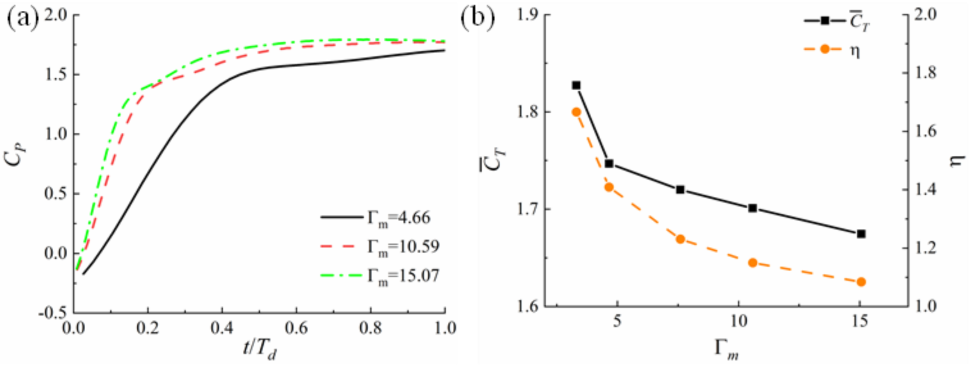

Fig. 5.33. Time history of the power expenditure coefficient C_P (a), and time-averaged thrust coefficient and propulsion factor (b) at different maximum equivalent stroke ratio Γ_m and U_0 = 0.42 V_{jm}.

5.2.3.2 Effect of background flow velocity

We first examine the effect of incoming flow on the starting process before the body deformation starts. The time histories of the drag force coefficient at several different incoming flow velocities are shown in Fig. 5.34(a). It can be found that after the initial phase, the drag force coefficient C_d eventually approaches a constant. The constant drag force coefficient is then plotted against the incoming velocity in Fig. 5.34(b). It roughly presents a linear correlation concerning U_0/V_{jm}. An inspection of the Z-vorticity contour, presented in Fig. 5.35, reveals that stronger vorticity is formed near the nozzle plane of the swimmer at a larger U_0. It is interesting to see how these enhanced vortices from incoming flow would influence the jet flow and thrust production when the body starts to deflate.

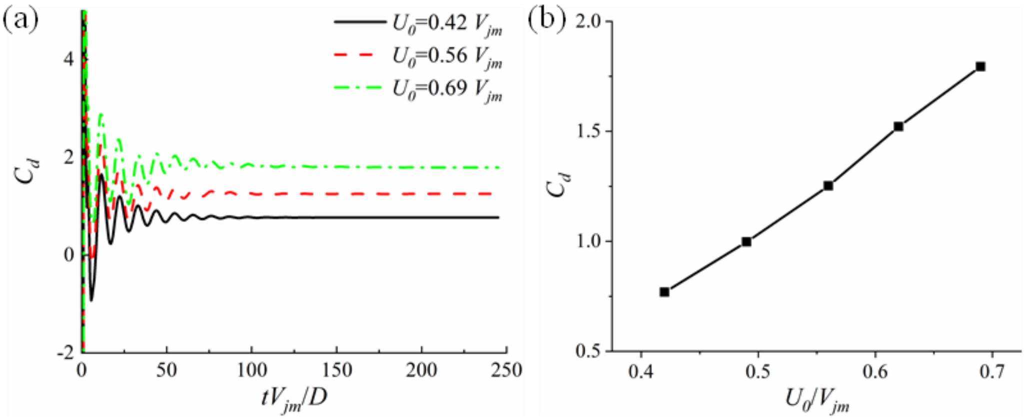

Fig. 5.34. Time histories of the drag coefficient C_d at several different U_0/V_{jm} (a) and the final converged values of C_d of the swimmer at rest as a function of incoming flow velocity (b).

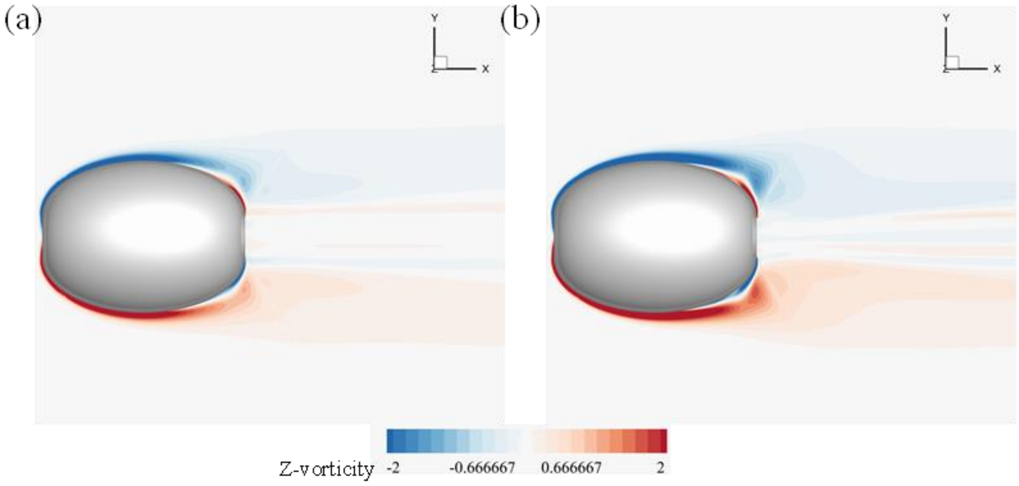

Fig. 5.35. The instantaneous Z-vorticity contour at plane $z = 0$ at $tV_{jm}/D = 245$ for $U_0/V_{jm} = 0.49$ (a) and $U_0/V_{jm} = 0.69$ (b) when background flow over the static swimmer with $e_0 = 0.844$.

To demonstrate the effect of incoming velocity during deformation, we first plot the normalized vortex ring circulation as a function of equivalent stroke ratio Γ at various U_0 with Γ_m = 15.07 in Fig. 5.36. The maximum circulation decreases with a larger incoming flow velocity. This may be due to the stronger interaction of the incoming flow and the jet flow near the nozzle at larger U_0 (as shown in Fig. 5.37), which consumes energy from the jet and makes it harder to feed the leading vortex ring. This is reminiscent of the phenomenon that the vortex ring observed in a squid jet is weaker than the formation of a vortex ring in still water (Anderson and Grosenbaugh, 2005). At a larger incoming velocity, more fluid ejected from the chamber is entrained into the vortices near the nozzle along with the background flow, instead of contributing to the growth of the vortex ring. Thus, stronger vortices are formed near the nozzle plane, while trailing vortices behind the leading vortex ring are more suppressed at an increased U_0, as shown in Fig. 5.38.

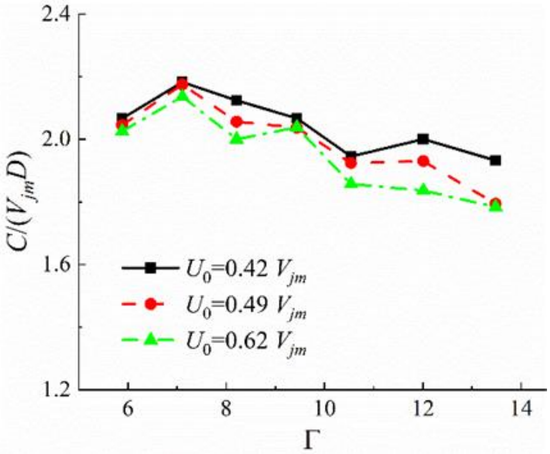

Fig. 5.36. The evolution of circulation at Γ_m = 15.07 for different background flow incoming velocity U_0.

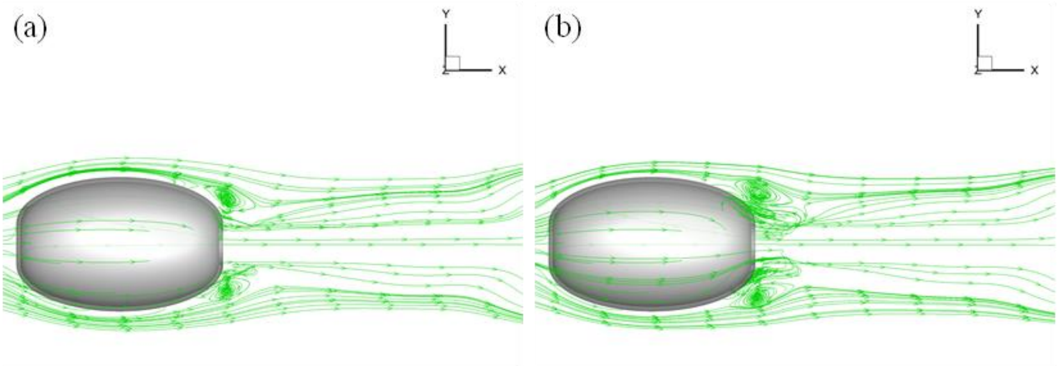

Fig. 5.37. Streamline distribution at plane z = 0 at t = 0.8 T_d for U_0/V_{jm} = 0.42 (a) and 0.62 (b) at Γ_m = 15.07.

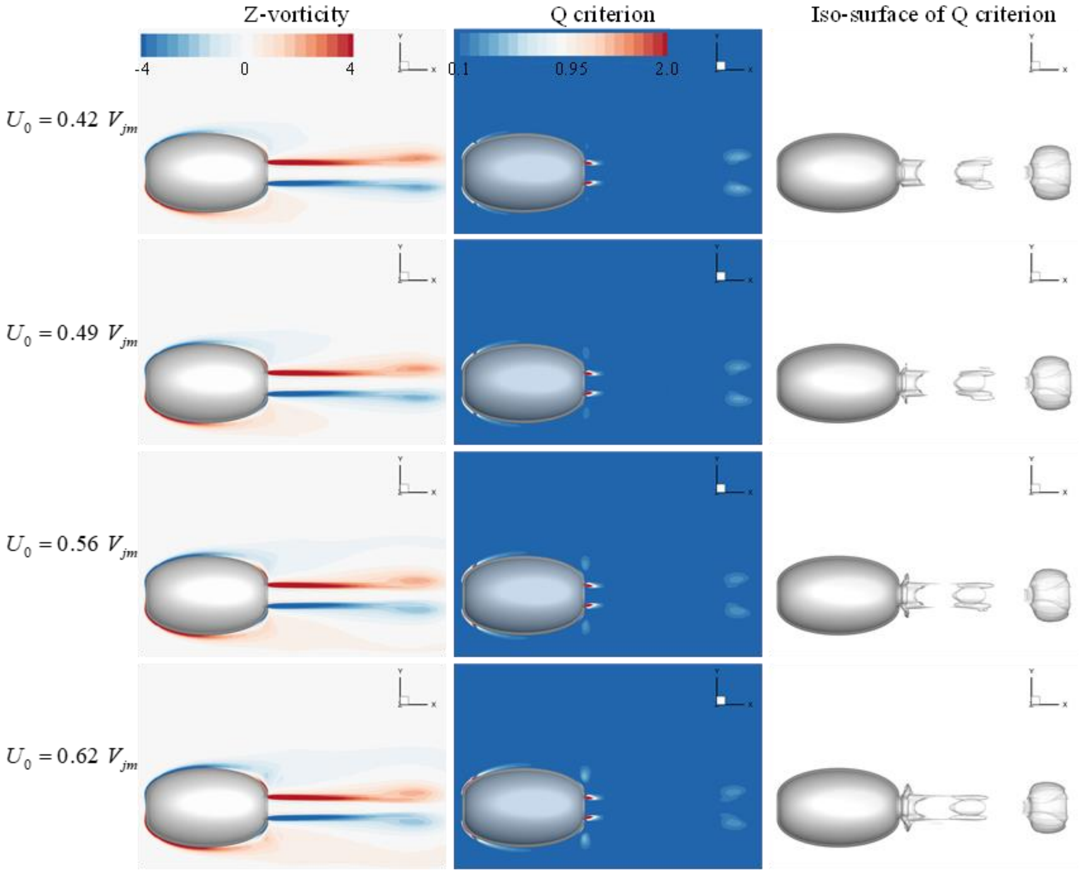

Fig. 5.38. The Z-vorticity contour and Q criterion distribution at plane z = 0, and wake structure visualized by iso-surface of Q criterion (Q = 0.037) at t = 0.8 T_d for different incoming flow speeds U_0 at Γ_m = 15.07.

Afterwards, the effect of the background flow velocity on the pulsed jet propulsion is examined. Fig. 5.39 presents the variation of thrust coefficient, mean thrust, and propulsion factor under different background flow velocities. It is shown that they all decrease with increased U_0. To explore the main cause of this total thrust reduction, we first compare C_{Tj}, C_{Tp}, and C_{Tm} at various U_0 in Fig. 5.40(a)−(c). As can be seen, the incoming flow velocity generally has negligible influence on the momentum flux-related thrust C_{Tj} and the thrust C_{Tm} sourced from the change rate of the horizontal momentum of the fluid inside the chamber, especially at the quasi-steady phase. It has a more noticeable effect on over pressure-related thrust C_{Tp}, mainly during the initial phase of the jetting near t = 0.2 T_d.

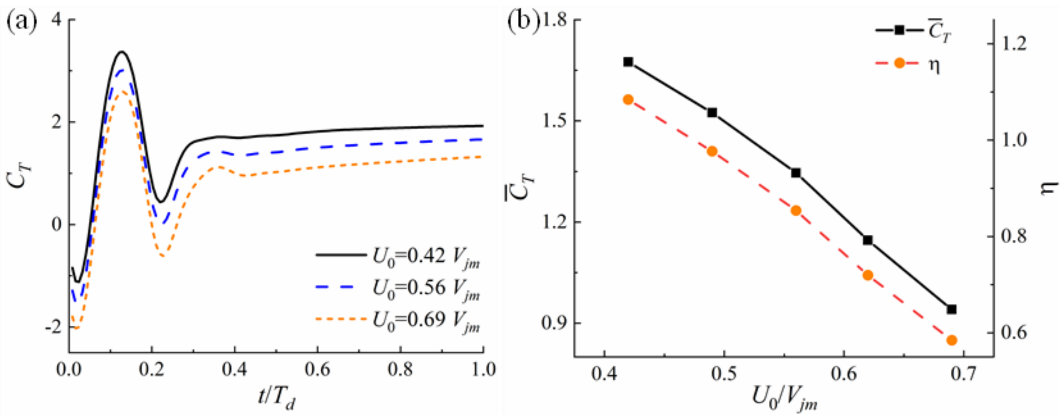

Fig. 5.39. Time history of C_T (a) time-averaged thrust coefficient and propulsion factor (b) at Γ_m = 15.07 for the different incoming velocities U_0 of the background flow.

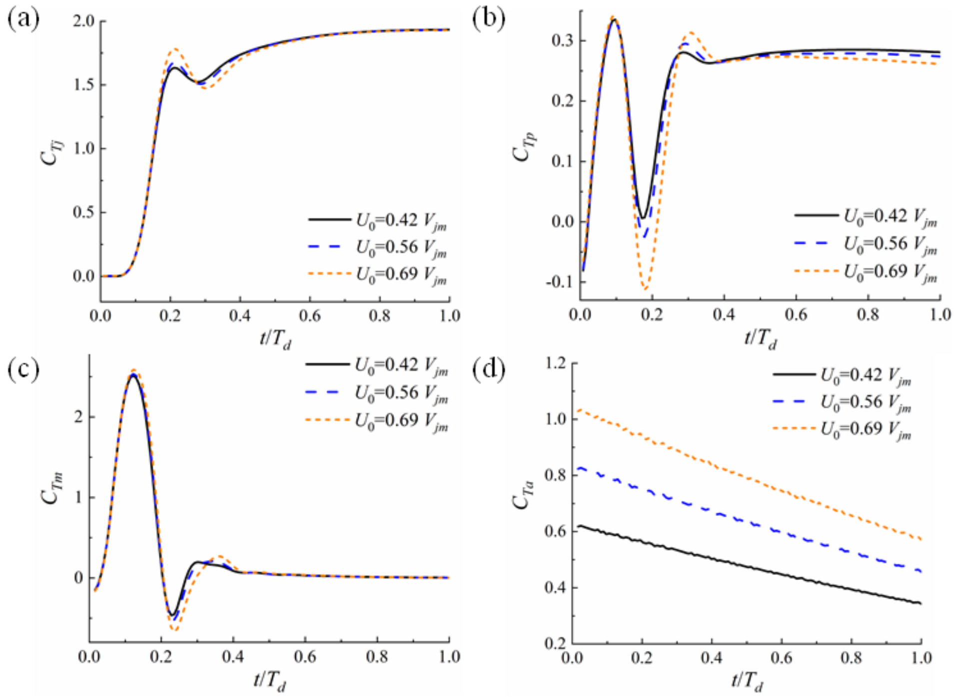

Fig. 5.40. Comparison of C_{Tj} (a), C_{Tp} (b), C_{Tp} (c), and C_{Ta} (d) at Γ_m = 15.07 at different U_0.

Indeed, these quantities are calculated from the fluid field at the exit plane and inside the chamber, where they are less likely to be affected by the background flow. Even so, background flow with larger incoming velocity enhances both axial and radial velocity at the exit plane in the initial phase of the jetting, as shown in Fig. 5.41. As a result, we observe an increase of C_{Tj} for a larger U_0 at the corresponding instant. Regarding the radial velocity that comes from body deformation, especially the shrinking in the radial direction, its initial increase may be caused by stronger induction of the recirculation formed by the interaction of background flow and pre-ejected flow near the nozzle. Afterwards, the axial velocity at the nozzle gradually plateaus and reaches similar steady values despite the difference in U_0.

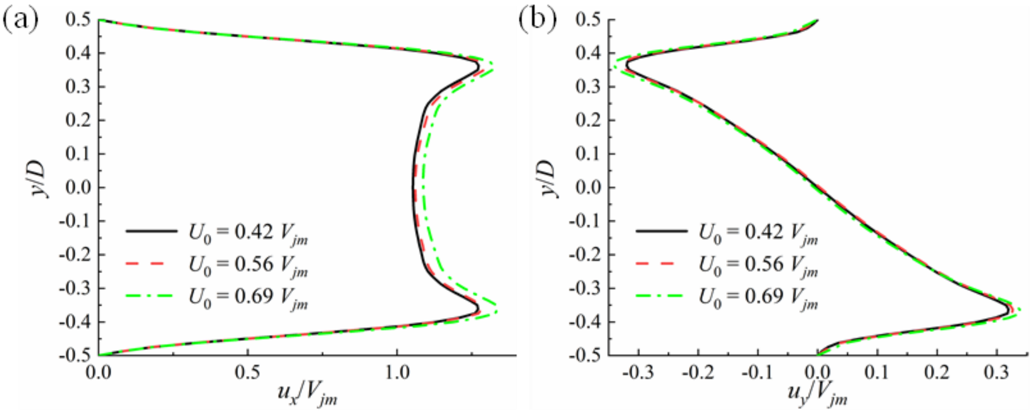

Fig. 5.41. The axial velocity (u_x) (a) and radial velocity (u_y) (b) distribution at the exit plane at z = 0 plane at t = 0.23 T_d with Γ_m = 15.07 for different U_0.

Excluding C_{Tj}, C_{Tp}, and C_{Tm} as the main cause for the overall thrust reduction at high incoming flow velocity, we further examine the added mass-related effect. As mentioned earlier, the lateral dimension of the swimmer decreases during the deflation, leading to added-mass-related force, $-\frac{d}{dt}\left(m_aV\right) = -\dot{m}_aV - m_a\dot{V}$ with V being the speed of the swimmer (for the present tethered mode, we use U_0 instead), in which the term $F_a = -\dot{m}_aV$ contributes positively to thrust generation. By approximating the shape of the swimmer as a prolate ellipsoid, we can calculate the instantaneous added mass as $m_a = C_a\frac{4}{3}\pi\rho a^3\left(1-e'^2\right)$ where $e' = \sqrt{1-\left(\sqrt{1-e^2}+D/L\right)^2}$. The added mass coefficient C_a is given by $C_a = \frac{\alpha}{\alpha-2}$ with $\alpha = \frac{2\left(1-e'^2\right)}{e'^3}\left(\frac{1}{2}\log\frac{1+e'}{1-e'}-e'\right)$ (Imlay, 1961). We plot the dimensionless added-mass-related thrust coefficient C_{Ta} in Fig. 5.40(d). Under the current tethered mode, C_{Ta} becomes larger with increased incoming flow velocity, and it decreases with the body approaching the deflated state. Nevertheless, the increased positive contribution from the added-mass-related force at larger U_0 does not overcome the rise of viscous drag. For example, the drag force coefficient C_d at the inflated static body shape is 0.77 when U_0 = 0.42 V_{jm}, while it increases significantly to 1.79 at U_0 = 0.69 V_{jm}, as shown in Fig. 5.34(b). Therefore, given the other three thrust components remain almost unchanged and F_a increases, we conclude that the reduction of overall thrust at high incoming flow velocity is caused mostly by viscous drag.

Besides, we are curious about the effect of the incoming velocity upon the unsteady impulse I_j and I_p related to vortex ring formation (see section 5.2.1 for the definition) as compared with the overall impulse production. For this purpose, we calculate the ratios between these unsteady impulses and the overall impulse I at different values of U_0/V_{jm} shown in Fig. 5.42.

With the increase of incoming flow velocity, the flux momentum and over-pressure associated with unsteady vortex ring dynamics become more crucial to the overall jet thrust production. Although the over-pressure effect at the nozzle plane would enhance the overall impulse, it is relatively small as U_0/V_{jm} is varied. In comparison, the flux momentum is of more importance in contributing to the overall thrust generation at a larger incoming flow velocity.

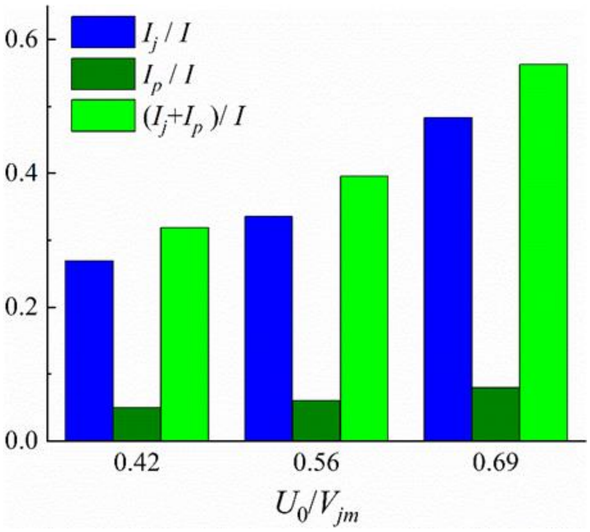

Fig. 5.42. Comparison of I_j, I_m, and their sum with the overall impulse at Γ_m = 15.07 for different incoming velocities U_0 of the background flow.

5.2.3.3 *Effect of the jet velocity profile*

Existing studies indicated that the jet velocity profile plays a non-negligible role in the vortex ring formation and dynamic performance in a jetting system. However, most of them ignored the effect of the horizontal momentum change of the fluid inside the system and the added mass effect involving body deformation in analyzing the jet propulsion performance (Jiang and Grosenbaugh, 2006; Querzoli et al., 2010; Rosenfeld et al., 1998). This would lead to underestimation of the actual pulsed propulsion capability. To further investigate these effects in the present squid-like swimmer propulsion, we consider two additional jet velocity styles, cosine, and half cosine, given by

$$V_j / V_{jm} = \begin{cases} 0.5\left[1-\cos\left(2\pi t / T_d\right)\right], \text{ cosine profile;} \\ 0.5\left[1-\cos\left(\pi t / T_d\right)\right], \text{ half cosine profile.} \end{cases} \tag{5.20}$$

The time evolutions of V_j for these two jet velocity patterns are shown in Fig. 5.43.

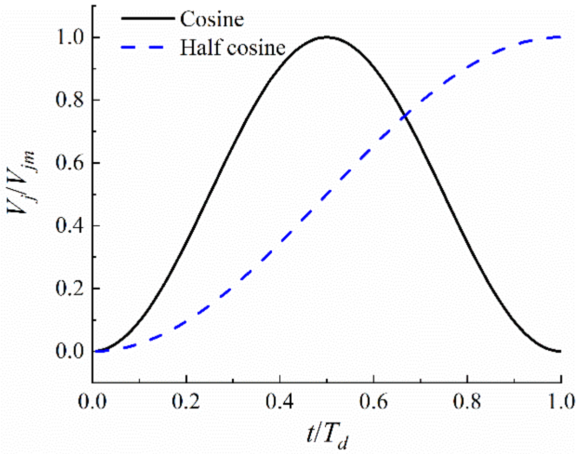

Fig. 5.43. Cosine and half cosine jet velocity profiles.

The time histories of the circulation of the vortex ring for the above two jet velocity patterns are presented in Fig. 5.44. Throughout the jetting procedure, for the half cosine profile, the circulation C with a smaller Γ_m is larger than that with a larger Γ_m at any instantaneous Γ. This is because the same amount of fluid mass (thus, the same Γ) is ejected with higher speed when Γ_m is smaller. For the same reason, the maximum circulation for the two jet velocity profiles is smaller than that for a constant jet velocity profile at the same Γ_m. As suggested by Bi and Zhu (2020), circulation C of the vortex ring at a certain instantaneous Γ is affected by the evolution of the jet speed before that instant. Therefore, even at the same equivalent stroke ratio Γ, the circulations for the two profiles may be different. In comparison, when a constant jet velocity is considered, the time histories of circulation C for different Γ_m are close to each other, as shown in Fig. 5.27.

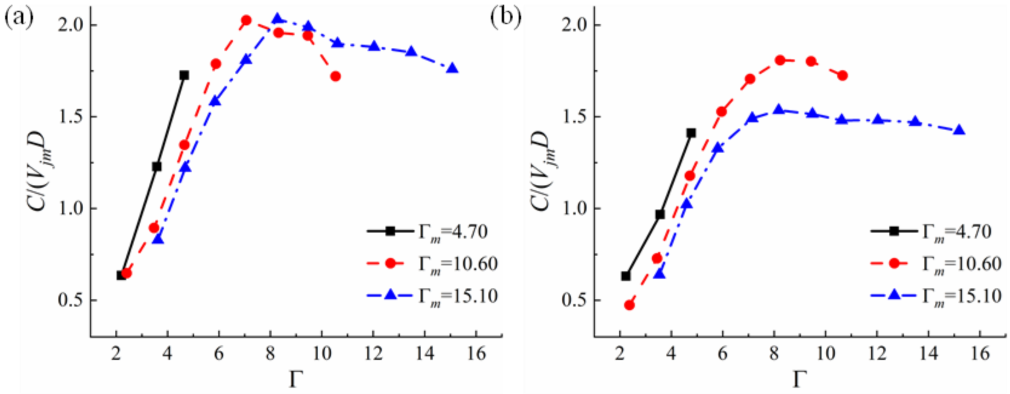

Fig. 5.44. The evolution of circulation C for the cosine (a) and half cosine (b) jet velocity profile.

Fig. 5.45 shows the time histories of C_T for the two jet velocity profiles. For the cosine jet velocity, a more significant acceleration of jet velocity results in a faster increase in C_T before t = 0.5 T_d compared with the half cosine profile. After the peak jet velocity is reached, the thrust production falls monotonically before a gradual increase at the late jetting. Negative thrust is yielded at the late jetting phase associated with the deceleration of the jet. In contrast, for the half cosine profile, C_T generally increases throughout the jetting process. In general, the overall thrust production for the constant fashion almost always surpasses those of the other two profiles. The underlying mechanism will be discussed in the following.

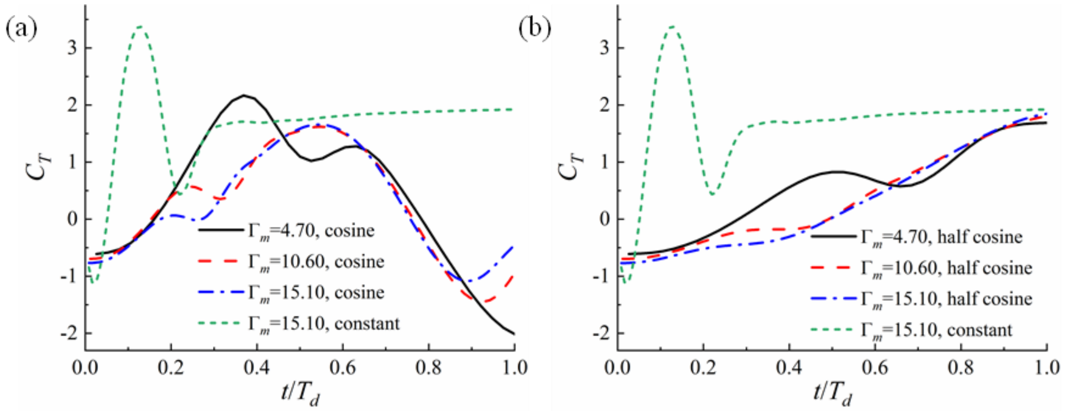

Fig. 5.45. Time histories of C_T for the cosine (a) and half cosine (b) jet velocity profiles. The case at Γ_m = 15.10 for the constant jet velocity profile is included for comparison.

To gain further insight into the sources of the overall thrust depicted in Fig. 5.45 for the two velocity profiles, we compare the time histories of C_{Tj}, C_{Tp}, C_{Tm}, and C_{Ta} in Fig. 5.46. By comparing Fig. 5.45(a) with Fig. 5.46(a), we find that the peak thrust for the cosine profile is dominated by the jet momentum flux out of the nozzle plane. After the peak roughly at $t = 0.6\ T_d$, C_{Tj}, C_{Tp}, and C_{Ta} start to decline as the jet velocity decreases. The thrust source C_{Tm} even becomes negative as the deceleration of the velocity of the fluid inside the chamber at the late phase of the jetting, which accounts for the negative total thrust C_T after $t = 0.8\ T_d$ along with the viscous drag force C_d.

Regarding the half cosine profile, all the values of the four thrust components remain positive due to the continuous acceleration of the jet velocity. Generally, the variation patterns of the C_{Tj}, C_{Tp} and C_{Ta} are similar at large Γ_m. The main difference among cases at different Γ_m is in C_{Tm}, especially the remarkable peak at $t = 0.5\ T_d$ for $\Gamma_m = 4.70$. This large peak of C_{Tm} is because the maximum jet velocity V_{jm} is reached faster for a smaller Γ_m with the same half cosine profile. It leads to a larger acceleration of the fluid inside the chamber. For the same reason, we see that the value of C_{Tm} at $\Gamma_m = 10.60$ is larger than that at $\Gamma_m = 15.10$. Thus, the small peak of the overall thrust C_T at $t = 0.5\ T_d$ and $\Gamma_m = 4.70$, as shown in Fig. 5.45(b), is dominated by C_{Tm}. Regarding the maximum total thrust C_T reached at the end of the deflation, they are all attributed to the thrust component C_{Tj} from jet momentum flux.

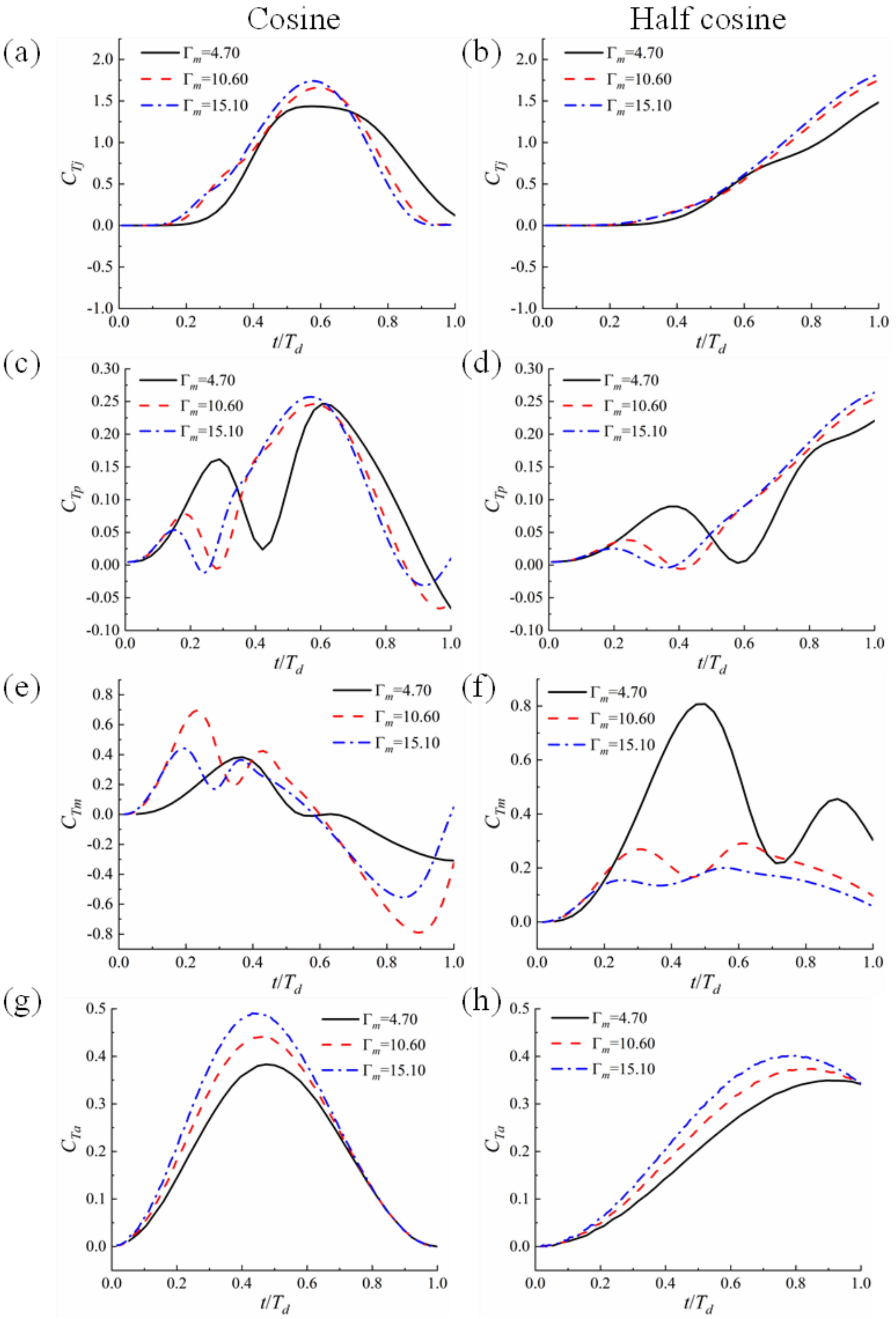

Fig. 5.46. Thrust components C_{Tj} (a-b), C_{Tp} (c-d), C_{Tm} (e-f) and C_{Ta} (g-h) for the cosine (left) and half cosine (right) velocity profile.

To interpret the different temporal variations of overall thrust for the three jet velocity patterns shown in Fig. 5.45, we replot their time histories of C_{Tj}, C_{Tp}, C_{Tm} and C_{Ta} at Γ_m = 15.10 in Fig. 5.47. Not surprisingly, the pattern of C_{Tj} is closely correlated with the specified jet velocity profile. In the constant jet profile, the large overall thrust C_T in the late stage of deflation is attributed to the relatively large jet velocity in that phase. The more distinct peak of C_T for the constant jet profile during the initial phase is closely related to C_{Tm} when the internal flow is quickly accelerated. Indeed, to reach the constant jet profile the fluid inside the chamber has to experience considerable acceleration from rest to establish the specified jet speed. In contrast, the variations of C_{Tm} of the other two jet velocity profiles are more gentle due to the slow change of V_j. The maximum C_{Tp} is close for the three jet velocity profiles but located at different time instants. Regarding the added-mass-related thrust F_a, although different variation patterns of C_{Ta} are presented for the three jet velocity profiles, it plays a non-significant role in the overall thrust generation. Their contribution may increase if large body deformation is considered.

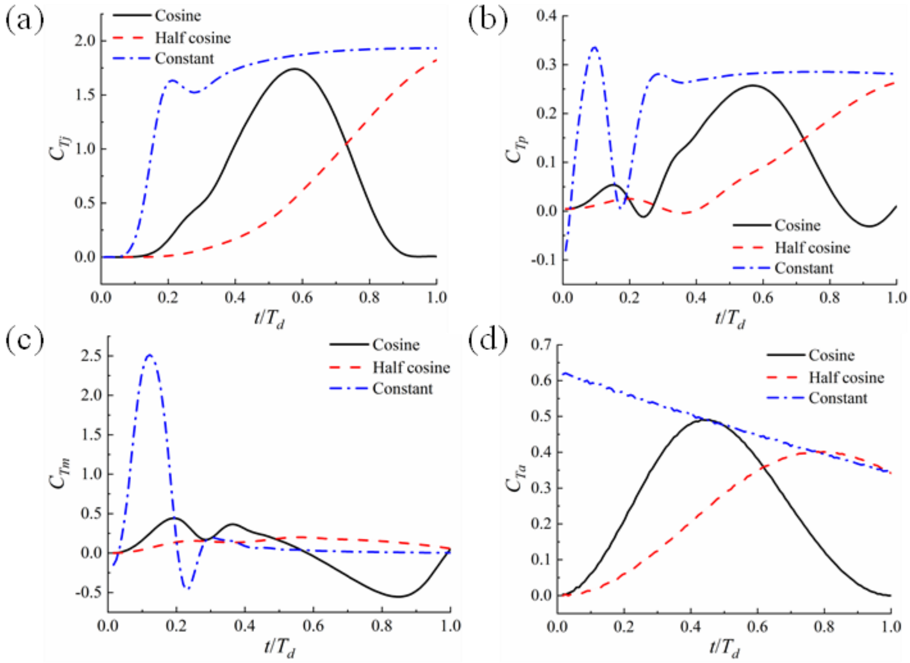

Fig. 5.47. Comparison of C_{Tj} (a), C_{Tp} (b), C_{Tm} (c) and C_{Ta} (d) at Γ_m = 15.10 for different jet velocity profiles.

5.2.4 Concluding remarks

Using a three-dimensional, unsteady, viscous, and compressible Navier-Stokes fluid solver based on the cell-centered finite volume method described in section 3.1, we numerically study squid-like jet propulsion through body deformation. The cephalopod-inspired swimmer is idealized as an ellipsoid-like pressure chamber with an opening serving as the outlet of jet flow. With the increase of the eccentricity of the body, the chamber deflates so that internal fluid is ejected. We focus on a single deflation deformation and systematically investigate the near-body fluid field, vortex ring formation, and jet propulsion performance with various background flow conditions and different jet velocity profiles.

For a constant jet velocity profile, the flow field visualization shows that no pronounced secondary vortices are observed behind the leading vortex ring at a relatively small jet-based Reynold number Re_j considered in this study, which is different from the high Reynolds number cases. The incoming flow speed U_0 of the background flow plays a role in the formation of the vortex ring. A larger U_0 leads to a stronger interaction between the background flow and jet flow near the nozzle. A pronounced recirculation zone is formed near the exit plane as the jet flow is entrained into these vortices, making it harder to feed the vortex ring and tailing vortices so that circulation of the vortex ring is reduced at high incoming velocity. The jet velocity profile is another significant factor determining the evolution of the vortex ring. In comparison with the cosine and half-cosine jet velocity profiles, a constant jet velocity profile produces larger peak values of C at a given formation number. This is explained by the fact that the fluid is initially ejected at a higher speed under a constant jet velocity profile without an acceleration phase.

Based on conservation of momentum, three distinctive thrust sources are identified, i.e., momentum flux-related thrust C_{Tj}, excessive pressure (at the nozzle exit) related thrust C_{Tp}, and thrust C_{Tm} due to time variation of the momentum of the fluid inside the pressure chamber. For a constant jet velocity pattern, total thrust peak is observed in the initial phase of the jetting and is mostly dominated by C_{Tm}, while C_{Tj} determines the thrust at the quasi-steady phase. For the cosine jet velocity profile, the jet momentum flux-related thrust C_{Tj} accounts for the overall peak thrust near the middle of the jetting phase. Regarding the thrust production for the half cosine profile, C_T generally experiences a continuous increase throughout the jetting mainly attributed to the growing C_{Tj}. By comparing thrust production for the three jet velocity profiles, we find that the thrust C_{Tj} from jet momentum flux, which is closely related to instantaneous jet speed, is essential to maintain a positive total thrust. For example, with the deceleration of the jet during the second half of the deflation period for a cosine jet velocity profile, the total thrust becomes negative. In terms of C_T, the constant profile outperforms the other two profiles during the later stage of deflation quasi-steady thrust phase due to larger jet velocity (thus, greater C_{Tj}). Our evaluation of added-mass-related thrust F_a due to the body deformation suggests that it contributes a non-negligible portion in the overall thrust for all the three jet velocity profiles for the body kinematics considered here.

Although larger incoming flow velocity U_0 would result in thrust reduction, the background flow is proven to have a negligible effect on momentum flux related thrust C_{Tj} and thrust C_{Tm} from the horizontal momentum change of the fluid inside the chamber. Increased incoming flow velocity results in greater added mass-related thrust F_a attributed to body deformation. Nevertheless, the rise of F_a is overweighted by the significantly increased viscous drag force at larger U_0. Therefore, the overall thrust declines at a large incoming flow speed. We also find that larger background flow velocity would increase the portion of C_{Tj} and C_{Tp} in the overall thrust generation.

5.3 Summary

In this chapter, the pulsed-jet propulsion inspired by squid and other cephalopods is numerically investigated. Two different models are considered depending on the research objectives. In section 5.1, a two-dimensional inflation-deflation propulsion system operating at high Reynolds number fluid conditions is considered. In order to explore the structural response of the flexible mantle structure under actuation force, the developed FSI solver is utilized. The simulation results reveal a different mechanism of symmetry-breaking instability under turbulent flow conditions compared with that reported in the laminar flow study. Specifically, this instability in turbulent flow stems from irregular internal body vortices, which cause symmetry breaking in the wake. A higher Reynolds number or smaller nozzle size would accelerate the formation of this symmetry-breaking instability.

Regarding the 3D jet swimmer model, we aim at investigating the effect of stroke ratio and jet velocity profiles on the jetting propulsion performance in the presence of background flow, a scenario consistent with live squids in nature. Therefore, the single deflation, which produces the most of the thrust during the inflation-deflation process, is prescribed, so that the problem is resolved using the fluid solver only. Based on conservation of momentum and by taking added-mass-related thrust into account, the thrust sources are analyzed at different maximum stroke ratios under different jet speed patterns. It is found that under the present tethered mode, the background flow has negligible influence on the thrust attributed to momentum flux and momentum change of the fluid inside the body. However, it indeed affects the over pressure-related thrust but its effect is relatively small. The overall thrust declines due to the significantly increased drag force at large incoming flow speed despite the rise of added-mass-related thrust.

Chapter 6 Motion Control of a Self-propelled Flexible Swimmer near a Rigid Body Utilizing PD Control

In chapter 4 and chapter 5, the fin propulsion and jet propulsion are investigated numerically, respectively. Nevertheless, the swimmer models considered in the above are under tethered mode in a uniform flow. In this chapter, the self-propulsion of a two-dimensional flexible swimmer is studied. Besides, the free-swimming motion of the swimmer is controlled by a feedback PD controller to instruct it to swim to a target position and hold the station near a fixed circular cylinder in the uniform flow. Through the coupling of the developed FSI solver with a PD controller, we are curious how effective this classic control would be in real-time control involving a complex fluid-structure interaction. Additionally, the research aim is to explore how much the energy benefit/saving would be when the swimmer is swimming and holding the station in the bow wake, as demonstrated in the biological experiment (Liao et al., 2003) where the energy consumption may not be straightforward to measure.

6.1 Problem Statement

The swimmer considered here is a two-dimensional flexible plate, as shown in Fig. 6.1. Inspired by the experimental study conducted by Liao et al. (2003), the swimmer is placed in front of a fixed cylinder. The initial distance from the swimmer to the cylinder is denoted by d_0. Distinct from most of the previous studies (e.g., (Dai et al., 2016; Kim et al., 2016)), the deformation of the swimmer is actuated by an external force in the transverse direction which is uniformly distributed on its surface that mimics the muscle forces applied on the fish fin. This actuation mechanism by adding external force on the body surface has been successfully implemented in the studies for a squid-like swimmer section 5.1 in this thesis, and a ribbon tail ray-like bio-inspired underwater robot (Shi and Xiao, 2021).

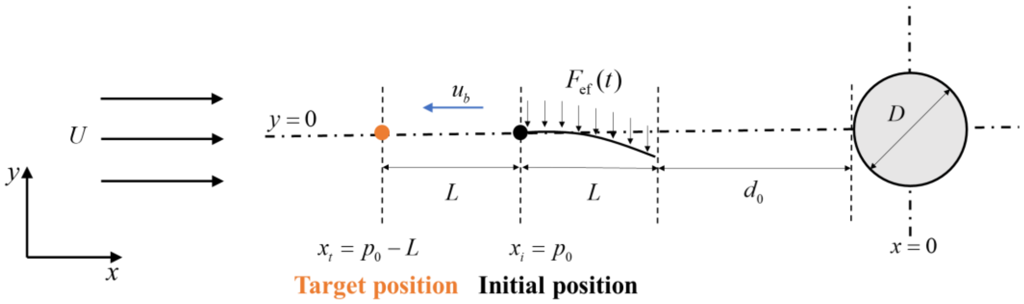

Fig. 6.1. Scheme diagram (not in scale) of a self-propelled flexible swimmer under force actuation in front of a cylinder in the uniform flow. The swimming is limited to the *x*-direction.

In structural dynamics, the leading edge of the swimmer is fixed (pinned) while the trailing edge is set as free. The swimmer is allowed for free-swimming in the horizontal direction, which is solely determined by the dynamic fluid-structure interplay between the surrounding fluid and the flexible swimmer locomotion under the action of added actuation force, fluidic force, and structural inertial force. The induced horizontal motion along the x-direction is given by Newton's second law

$$m_b \frac{du_b}{dt} = F_x, \tag{6.1}$$

where m_b is the mass of the swimmer, u_b is the swimming velocity in x-direction, and F_x represents the component of the overall fluidic force in the x-direction.

A feedback controller is implemented to dynamically adjust the actuation force and therefore, control the free-swimming motion of the swimmer. Specifically, the control scheme, which will be detailed in section 6.2 is derived to lead the swimmer to swim from an initial position $x_i = p_0$ (measured at the leading edge of the swimmer) to a target position $x_t = p_0 - L$ (see in Fig. 6.1), and remain there, balancing thrust and drag forces over one swimmer deflection cycle period. As a result, the actuation force is given by

$$F_{\mathrm{ef}}\left(t\right) = \alpha\left(t\right) \cdot F_{\mathrm{ef0}} \sin\left(2\pi f_{\mathrm{ef}} t + \varphi\right), \tag{6.2}$$

where α denotes the control variable ranging between [0,1] which serves as the adjustment factor of the actuation force amplitude, f_{ef} is the actuation frequency of the force and φ represents the phase shift of the actuation force. F_{ef0} is the maximum amplitude of the actuation force, given by $F_{\mathrm{ef0}} = 0.5\rho_f U^2 L \cdot C_{\mathrm{ef0}}$, where ρ_f is the fluid density, U is the free stream velocity, L is the chord length of the swimmer which is equal to the diameter of the cylinder D ($L = D$), and C_{ef0} denotes the actuation force coefficient. The adjustment factor α is the output of the feedback controller and its exact calculation will be described in the next section.

The Reynolds number is defined by

$$\mathrm{Re} = LU / \nu, \tag{6.3}$$

where ν is the kinematic viscosity of the fluid. The instantaneous thrust coefficient C_T is given by

$$C_T = -\frac{F_x}{\frac{1}{2}\rho_f U^2 L}. \tag{6.4}$$

To evaluate the swimming performance at different initial positions d_0, the time T_s which the swimmer takes to travel the same distance that equals L to reach the target location is recorded. The overall energy expenditure coefficient C_{Ps} required by the swimmer during T_s is defined as

$$C_{Ps} = \frac{\int_0^{T_s} P_{in}\left(t\right)dt}{\frac{1}{2}\rho_f U^2 L^2}, \tag{6.5}$$

where $P_{in}(t)$ stands for the instantaneous power input as $P_{in}\left(t\right) = \int_{\Gamma_f} \boldsymbol{F}_{\mathrm{ef}}\left(s,t\right) \bullet \boldsymbol{u}\left(s,t\right) ds$ with $\boldsymbol{u}(s,t)$ being the velocity of the grid node s where the actuation force is applied along the body surface Γ_f. Besides, the mean energy expenditure coefficient required to dynamically maintain near the target point is calculated by

$$C_{P_h} = \frac{\int_t^{t+T_h} P_{in}\left(t\right)dt}{T_h \bullet \frac{1}{2}\rho_f U^3 L}, \tag{6.6}$$

where T_h is the selected reference period when the swimmer lingers around the target after reaching the position $x_t = x_i - L$, which is a constant for all the cases considered. Through the evaluation of these two metrics, we can get an insight into how much energy consumption is during traveling the same distance and holding the position.

The dimensionless parameters governing the problems are as follows: the mass ratio $m^* = \rho_s h/\rho_f L$ with ρ_s denoting the density of the swimmer and h being the thickness of the body; the non-dimensional frequency of the actuation force $f^* = f_{\mathrm{ef}}L/U$; the dimensionless stiffness $K = EI/(\rho_f U^2 L^3)$, where E is Young's modulus and $I = h^3/12$ denotes the area moment of inertial of the cross-section; and the Poisson ratio v_s.

6.2 Scheme of the Feedback Controller

Control objectives are set for the swimming motion, i.e., swimming towards a target point from an initial point in front of the cylinder, and remaining at that target position. A feedback control system is developed for this purpose. Previous investigations of numerical simulations of fish swimming coupled with control have shown that the PID control is robust and effective (Gao and Triantafyllou, 2018; Hess et al., 2020). In this work, we neglect the integral (I) term and a general form of a PD controller considered is given as

$$C_v\left(t\right) = k_p e\left(t\right) + k_d \frac{d\left(e_t\right)}{dt}, \tag{6.7}$$

where $C_v(t)$ is the control variable which corresponds to the adjustment factor α of the force amplitude here, $e(t)$ is the tracking error, and k_p and k_d are the tuning gains.

The swimmer's body deformation and global motion are actively influenced by the actuation force. To achieve the control objectives, a control variable α is added to dynamically adjust the actuation force amplitude, as shown in Eq.(6.2). The control diagram of the selected PD controller coupled with the FSI solver is shown in Fig. 6.2.

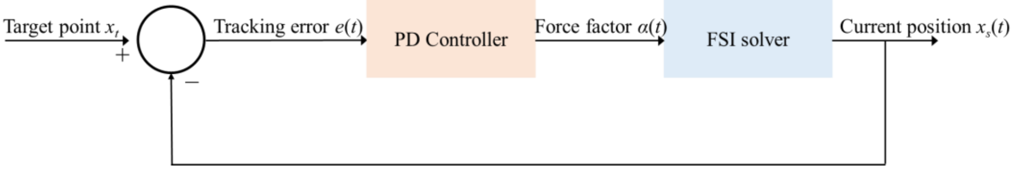

Fig. 6.2. The general feedback controller implementation schematic coupled with the FSI solver.

In a previous study on swimming motion control, the tracking error is calculated using the sign from the dot-product of the swimming velocity vector and the distance vector (Hess et al., 2020). This can avoid the overshoot that the swimmer is past the target but without stopping at the right time. Different from the above method, we propose to use the swimming speed for control, rather than the position tracking error as did in many previous studies (Kopman et al., 2014; Yen et al., 2018). This is because our numerical tests show that a tracking error that only considers the distance between the target position and the current position leads to a large overshoot in position control. Specifically, the PD controller is used to dynamically adjust the control variable α to match the swimmer's velocity to follow the desired velocity $u_{set}(t)$. u_{set} is dependent on the instantaneous gap G between the current swimmer position and the target, given by $G(t) = x_s(t) - x_t$ with $x_s(t)$ denoting the instantaneous position of the swimmer's leading-edge and x_t being the target position, as shown in Fig. 6.3. Given the periodic deformation of the oscillating swimmer, instead of using the instantaneous speed, we use the mean velocity of the swimmer averaged over one actuation period in the tracking error evaluation. This enhances numerical stability by avoiding high fluctuation of the error signal, which is essential to maintain stable control of the swimmer by balancing the thrust and drag forces over one cycle period at the target position, especially when approaching the target position.

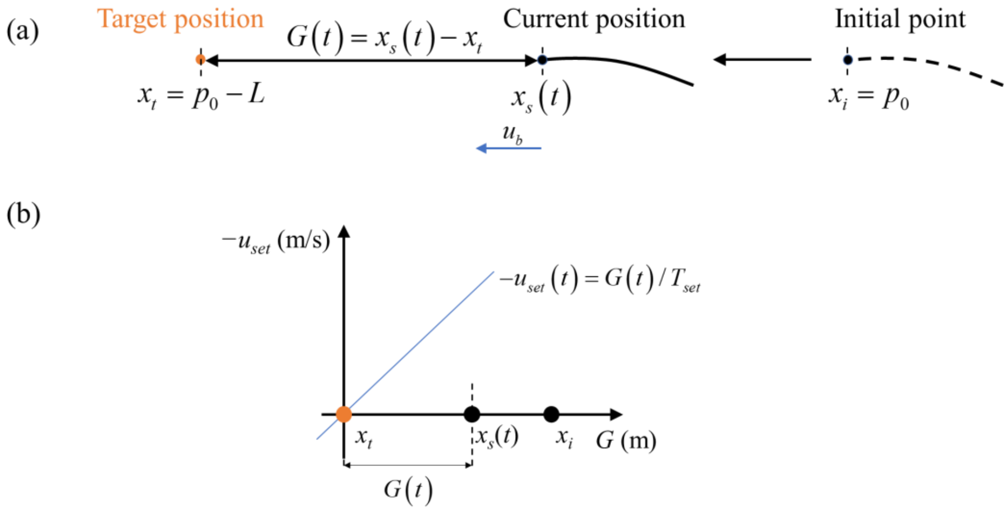

Fig. 6.3. Schematic illustration of the control scheme based on the horizontal motion of the flexible swimmer relative to the target (a), and the correlation of instantaneous u_{set} and gap G (b).

Following the above logic, the instantaneous control tracking error $e(t)$ is defined as

$$e(t) = \overline{u_b(t)} - u_{set}, \tag{6.8}$$

where $\overline{u_b(t)}$ is the time-average swimming velocity of the swimmer during one force actuation period T given by

$$\overline{u_b(t)} = \frac{1}{T}\int_t^{t+T} u_b(t)\,dt, \tag{6.9}$$

and the set velocity u_{set} associated with the gap G is defined as

$$u_{set}(t) = -G(t)/T_{set}, \tag{6.10}$$

where T_{set} denotes a constant period used to tune the magnitude of this set velocity. Since the desired swimming speed towards the target, relative to the initial location, is negative (along the negative x-direction) in the coordinate system (see Fig. 6.1), a negative sign is added to u_{set}. The value of T_{set} is obtained from numerical tests to yield stable control of swimming speed.

Based on the present scheme in Eq.(6.8), the swimmer would swim at a high velocity when distance $G(t)$ is large and slow down when approaching the target position, as demonstrated in Fig. 6.3(b). In case of overshoot in position, reversing the sign of u_{set} would lead to the reduction of tracking error, and thus subsequent deceleration due to reduced actuation force. And the swimmer would even be pushed back by the incoming flow if the produced thrust is overwhelmed by the drag. Nevertheless, after the swimmer is pushed from the target location, the gap value becomes positive and causes it to swim forward again. When the swimmer is very close to the target, the value of u_{set} is nearly zero so that the controller instructs the swimmer to maintain a nearly zero mean swimming speed during each actuation period at the target.

We employ an incremental calculation of the adjustment factor $\alpha(t)$, and the current value of $\alpha(t_n)$ is obtained by

$$\alpha\left(t_n\right)=\alpha\left(t_{n-1}\right)+\Delta\alpha\left(t_n\right), \tag{6.11}$$

where $\alpha(t_{n-1})$ denotes the value of the last time step and $\Delta\alpha(t_n)$ is the error increment which is calculated by

$$\Delta\alpha\left(t_n\right)=k_p\left[e\left(t_n\right)-e\left(t_{n-1}\right)\right]+\frac{k_d}{t_s}\left[e\left(t_n\right)-2e\left(t_{n-1}\right)+e\left(t_{n-2}\right)\right], \tag{6.12}$$

where t_s is the sampling period which corresponds to the time step size here, and $n-2$ denotes the time step before the last one step. The value of α calculated by Eq.(6.11) is limited to [0,1] so that the amplitude of the actuation force does not exceed the specified maximum while the force direction will not be changed. The values of k_p and k_d (listed in Table 6.1) are obtained from numerical tests using the Ziegler-Nichols method (Ziegler and Nichols, 1942) to yield agile response and small overshoot.

6.3 Mesh independence study

The computational domain is presented in Fig. 6.4(a). On the flexible swimmer surface, the non-slip/no-flux condition is imposed, while for the other boundaries, the non-reflective far-field boundary condition is applied. A multi-block overset grid system is utilized in this study to handle the relative motion between the swimmer and cylinder. This overset grid method is based on the implicit hole cutting (IHC) technique proposed by Lee and Baeder (2003) and improved by Liao et al. (2007). Specifically, there are two clusters of structured grids in this simulation, as shown in Fig. 6.4 (b), i.e., one is the background grid containing the cylinder (cluster 1), and the other one is the body-fitted grid around the body (cluster 2). In this way, the latter cluster can move relative to the former one without large mesh distortion or even the occurrence of negative cell volume. The details of this overset grid assembler are described in Shi et al. (2019).

A mesh independence study is conducted to assess the sensitivity to the mesh density and time step size by solving the laminar flow around a tethered flexible plate at Re = 500, $m^* = 0.5$, $K = 0.5$, $f^* = 2.5$, and $d_0 = 1.0\ L$. Three meshes are generated: a coarse mesh with 82574 cells, a medium-size mesh with 103888 cells, and a fine mesh with 130533 cells. The first grid height of the three meshes is 0.005 L. The structural mesh contains 132 fifteen-node wedge elements (Dhondt, 2004). First, the mesh convergence test is performed in which the three generated meshes are used along with the non-dimensional time step size, defined as $\overline{\Delta t} = \Delta t U/L$, $\overline{\Delta t} = 0.00333$. The required computational time of the fine and medium mesh is 1.32 T_{coarse} and 1.14 T_{coarse}, respectively, where T_{coarse} is the computational time required for a coarse mesh using the same number of computer cores. The results of C_T yielded by the three meshes are presented in Fig. 6.5(a). The medium-size mesh yields a result that is very close to that of the fine mesh. Thereafter, the effect of the time step size is also studied when the medium-size mesh is used, as shown in Fig. 6.5(b). These results suggest that the simulation results are not sensitive to the mesh size and time step size if they are sufficiently small. Therefore, the medium mesh is used for the following simulations to ensure computational accuracy, and meanwhile, reduce the computational cost.

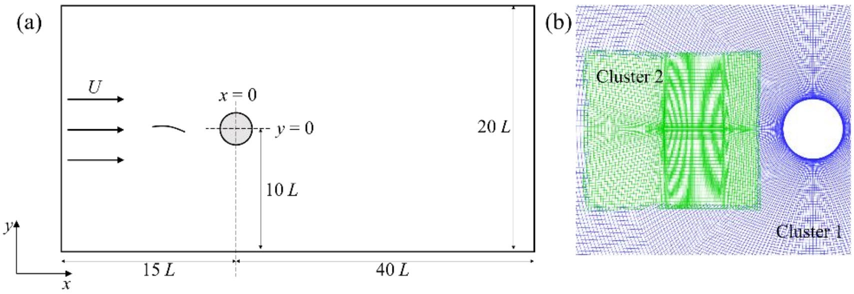

Fig. 6.4. Sketch of the computational domain (not in scale) (a) and the hole-cutting overset fluid mesh around the swimmer and cylinder at $d_0 = 1.0\,L$ (b).

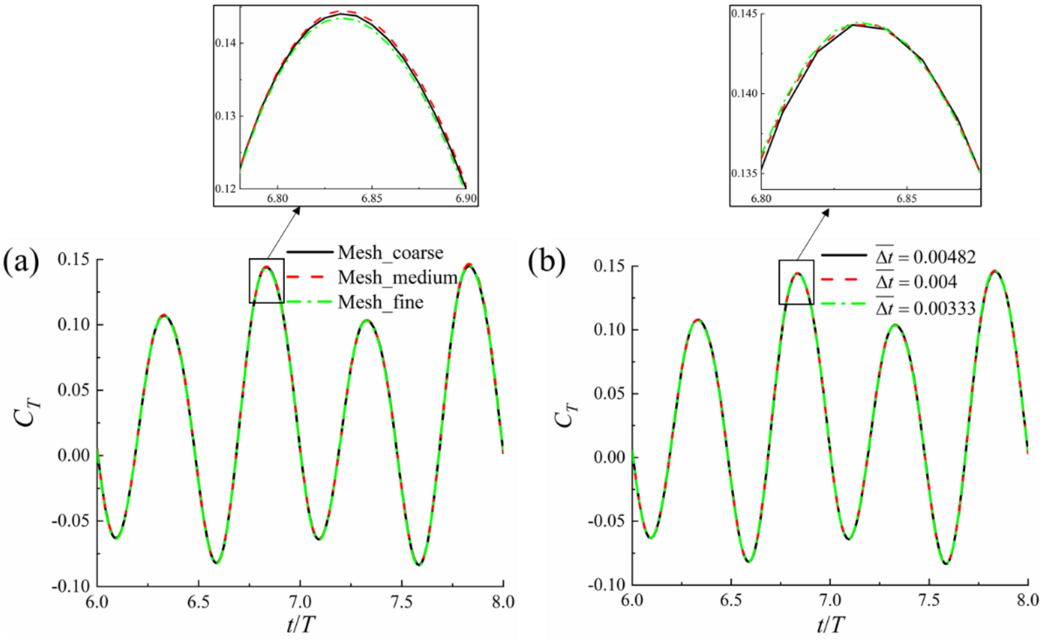

Fig. 6.5. The results of C_T yielded by three different meshes with $\overline{\Delta t} = 0.00333$ (a) and comparison of C_T for the medium-size mesh when three different time step sizes are used (b).

6.4 Results

Considering that a fish tends to hold station in front of the cylinder in a uniform flow, as reported in an experimental study by Liao et al. (2003), we focus on the swimming of a flexible swimmer whose actuation force amplitude is dynamically adjusted in front of a cylinder via a feedback controller, as shown in Fig. 6.1. The swimming and station-holding in the absence of a cylinder in a uniform flow condition are also considered for comparison. Before we start the FSI simulations involving motion control of the swimmer, the fluid field around a rigid and static swimmer near the cylinder is studied firstly. Then the effect of Reynolds number (Re = 500, 1000, and 2000) and initial distance between the swimmer and cylinder d_0 is considered with the fluid-only simulation results as the initial fluid field. Afterwards, we also explore how the actuation frequency f^* and phase shift φ of the actuation force would influence the swimming performance and control results. Some parameters remain unchanged for the following simulations, which are listed in Table 6.1. It is noted that the maximum magnitude of the actuation force C_{ef0} is obtained through numerical tests to bend the plate to produce a large enough thrust to swim forward, but meanwhile avoid a too large magnitude that yields exaggerated deformation which may cause numerical issues.

Table 6.1. The parameters used in the simulations of a self-propelled swimmer.

K	C_{ef0}	m^*	k_p	k_d	T_h	T_{set}
0.5	2.0	0.5	7, 15	0.05	20 T	4.2 U/L

6.4.1 Flow over the rigid swimmer at rest in front of a cylinder

Before initiating the actuation force to deform the flexible swimmer, the flow over the cylinder and swimmer at rest is firstly simulated. Taking Re = 1000 as the example, the mean drag coefficiency $\overline{C_d}$ of the cylinder and static swimmer at different d_0 is shown in Fig. 6.6. It can be seen that the presence of a cylinder in the wake results in the reduction of drag force of the static rigid swimmer compared with the cases when it is placed solely in the uniform flow. The closer the swimmer is to the cylinder, the more remarkable this drag decrease is. The cylinder also gains a similar drag reduction when it is placed behind the swimmer. Nevertheless, this benefit does not present a monotonous variation in correlation with the distance between the two bodies, but a maximum drag decrease is seen at $d_0 = 2\ L$. After this minimum value, $\overline{C_d}$ of the cylinder grows again as the swimmer is placed farther from it. This may be related to the unsteady vortex shedding of the cylinder which is influenced by the upstream plate in a complex way at different gaps. A similar variation pattern of drag force of the cylinder ahead of a plate was reported in Wu et al. (2014).

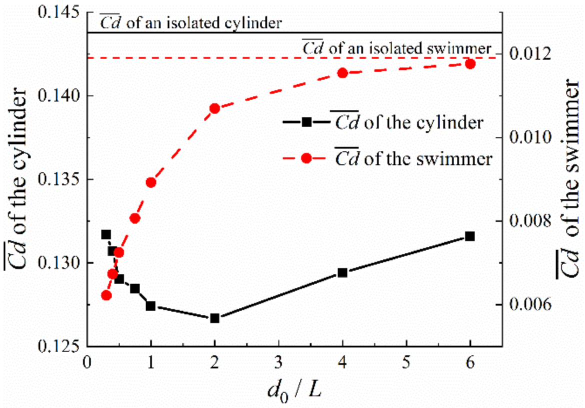

Fig. 6.6. The mean drag force coefficient $\overline{C_d}$ of the cylinder and static rigid swimmer at different distances d_0 at Re = 1000. The results of the isolated cylinder and swimmer are also included for comparison.

For insight into the surrounding fluid field, we plot the pressure distribution around the swimmer and cylinder in Fig. 6.7. It can be seen that the trailing part of the swimmer is exposed to the high-pressure attributed to the cylinder when it is placed near the cylinder, as shown in Fig. 6.7(a), which helps reduce the drag force. In comparison, when the swimmer is located further upstream of the cylinder, it loses the relatively high pressure which pushes it along the negative *x*-direction, as shown in Fig. 6.7(b). Meanwhile, the flow-incident surface of the cylinder also withstands larger pressure, which is close to the scenarios when it is solely in the uniform flow as shown in Fig. 6.7(c). This high pressure at the left side surface of the cylinder leads to a larger overall resistance compared with that when it is near the wake of the swimmer. It is interesting to further investigate how this hydrodynamic interaction between the swimmer and cylinder would influence the flexible deformation and free-swimming of the swimmer when the actuation force is applied under the control of a feedback controller.

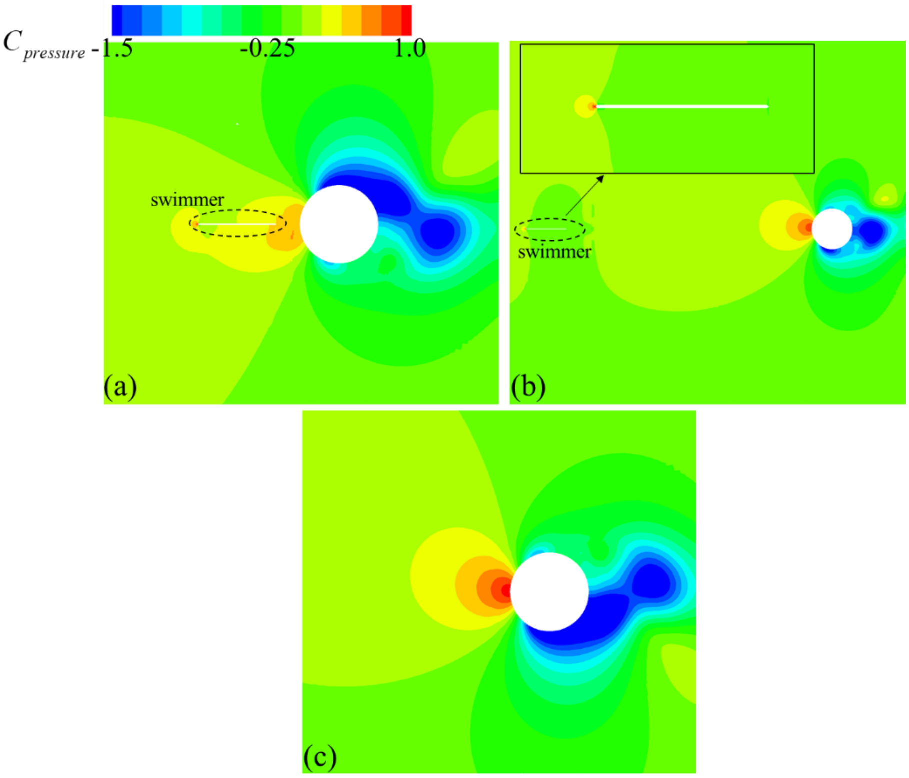

Fig. 6.7. The pressure distribution ($C_{pressure} = (p-p_\infty)/0.5\rho_f U^2$) where p_∞ is the pressure in the far-field) around the cylinder and static rigid swimmer in the uniform flow at $d_0 = 0.3\ L$ (a) and $d_0 = 6\ L$ (b), and around the isolated cylinder (c) at $tU/L = 104$ when Re = 1000.

6.4.2 The effect of Re and initial distance d_0

After the above simulations of the static swimmer without flexible deformation, we now start to explore the self-propulsion performance with the control objectives, ie., swimming to a target and station-holding, being implemented with $k_p = 7$ and $k_d = 0.05$. The results in section 6.4.1 when the swimmer is rigid and static are taken as the initial fluid field for the following simulations involving flexible flapping and self swimming. The overall energy expenditure coefficient C_{Ps} and time T_s required to travel the same distance (one body length L) from different initial positions, the mean energy expenditure coefficient C_{Ph}, and the converged force factor α_h when the swimmer holds the station near the target are shown in Fig. 6.8. The results for an isolated swimmer in the absence of the cylinder in the flow are also included for comparison. It can be found that under the present control scheme, generally, the less overall energy is consumed by the flexible swimmer to travel to the target position when it has an initial location closer to the behind cylinder. Besides, when the target position is closer to the cylinder, it is also more energy-saving for the swimmer to stay there, reflected by a smaller C_{Ph} compared with the cases with a larger d_0. The curves of swimming time T_s to reach the target position present more complex variation patterns as d_0 and Re vary.

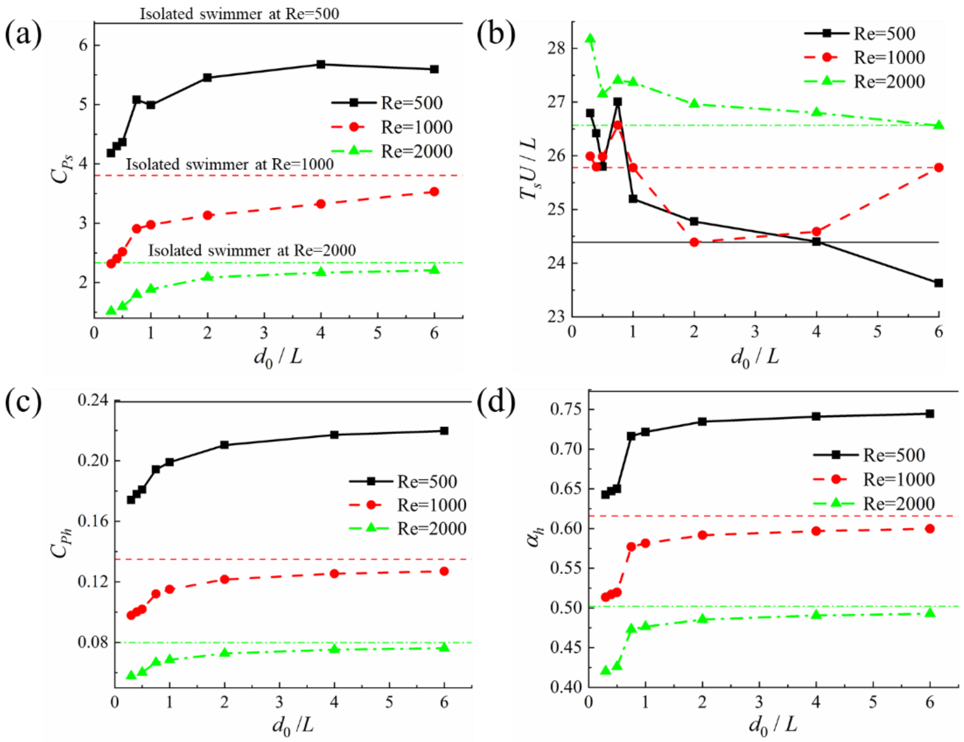

Fig. 6.8. The overall energy expenditure coefficient C_{Ps} (a) and time (b) required by the swimmer to reach the target by traveling the same distance L, the mean energy expenditure coefficient C_{Ph} (c), and the converged adjustment factor α_h of actuation force amplitude (d) when the swimmer holds station near the target at different initial distances relative to the cylinder d_0 and Re with f^* = 2.5 and φ = 0. The three straight lines represent the results when the swimmer is placed in the uniform in the absence of a cylinder at the respective Reynolds number.

A closer inspection on Fig. 6.8(a) reveals that the variations of C_{Ps} are more sensitive to the initial distance d_0 before the instantaneous distance d exceeds 1.0 L, after which the curves of C_{Ps} are flat as d increases. This trend is more noticeable for Re = 500, where C_{Ps} remains almost unchanged after d_0/L is larger than 2. The greatest saving of energy compared with that required by an isolated swimmer which travels the same distance is seen at d_0/L = 0.3 and Re = 1000, with a reduction of 39% in C_{Ps}. In addition to the initial position, the Reynolds number is also a significant factor in determining the swimming energy consumption. For example, 183 % more energy is needed to swim the same distance at d_0/L = 0.75 when Re decreases from 2000 to 500. Generally, it is more energy-efficient for the swimmer to swim in the flow condition with larger Re regardless of the departure positions and the presence of the cylinder. Nevertheless, T_s does not increase with a larger d_0 or smaller Re, unlike C_{Ps} does under the present control scheme, suggesting that energy-saving does not necessarily mean time-saving simultaneously. For example, T_s at Re = 2000 is even the largest at the same d_0 compared with the cases with lower Re where greater energy consumption (C_{Ps}) is seen when d_0 is fixed, as shown in Fig. 6.8(a) and (b).

The variation patterns of C_{Ps} generally apply to that of the mean energy cost coefficient C_{Ph} during the station-holding after reaching the target. The closer to the cylinder the target is, the less energy is required by the swimmer to stay there. A large Re also contributes to the reduction of energy consumption. Not surprisingly, the curves of the converged force adjustment factor α_h show similar styles as d_0 and Re are varied to that of C_{Ps} and C_{Ph} whose calculations are dependent on instantaneous force amplitude.

The instantaneous swimming distance relative to the initial position, swimming velocity, and force amplitude factor α produced by the controller at $d_0 = 0.3\ L$ and $d_0 = 6.0\ L$ are presented in Fig. 6.9, Fig. 6.10, and Fig. 6.11, respectively. It can be found that the swimming distance and velocity curves when $d_0 = 6.0\ L$ are close to that of an isolated swimmer, implying the hydrodynamic benefit from the cylinder upstream is rather weak at this remote initial position. The swimmer is firstly drifted downstream at the beginning of the swimming (before $t = 11\ T$) when the swimmer departs from a position far from the cylinder. This is related to the small force amplitude (α) in the early phase as presented in Fig. 6.11 so that the generated thrust is not large enough to overcome the drag. But this downstream drift is not seen at $d_0 = 0.3\ L$ and is significantly reduced at a higher Reynold number, 2000. Under the closed-loop feedback control, the swimmer experiences remarkable acceleration and reaches the maximum swimming speed at around $t = 17\ T$ as a larger actuation force is applied as shown in Fig. 6.9 and Fig. 6.10. After this peak swimming velocity, the exerted actuation force is reduced under the feedback control as the swimmer approaching the target. As a result, the swimmer decelerates and swims slowly towards the target to avoid significant overshoot.

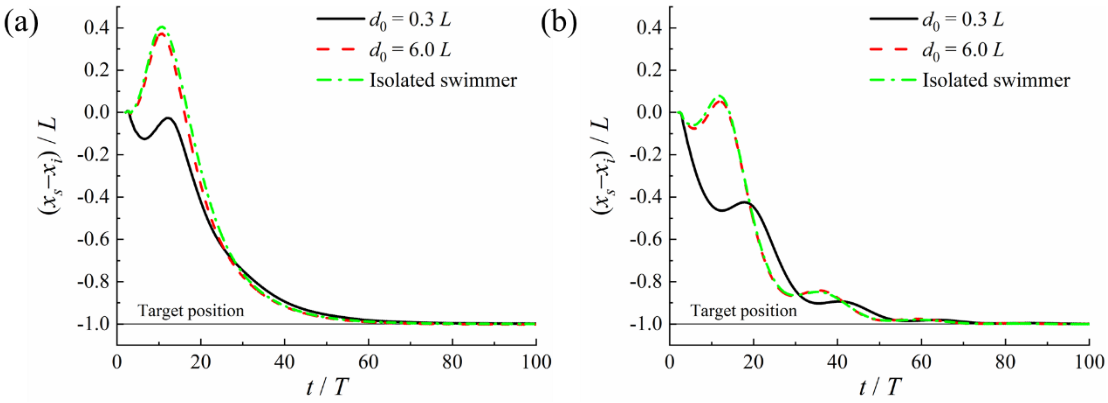

Fig. 6.9. The normalized instantaneous swimming distance $(x_s - x_i)/L$ at $d_0 = 0.3\ L$ and $d_0 = 6.0\ L$ at Re = 500 (a) and Re = 2000 (b) with $f^* = 2.5$ and $\varphi = 0$. The results for an isolated swimmer are also included for comparison.

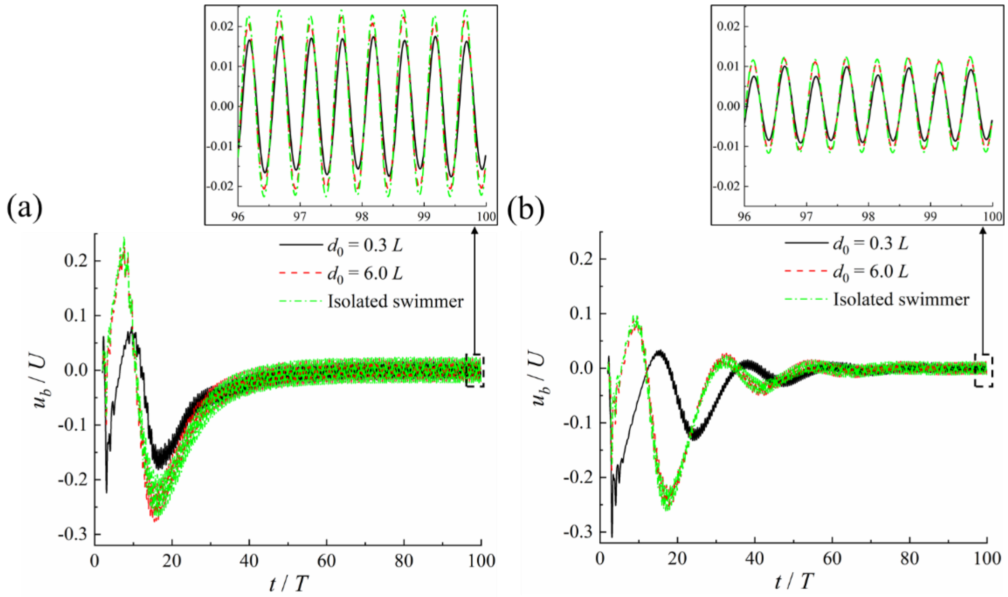

Fig. 6.10. The normalized instantaneous swimming speed u_b/U at d_0 = 0.3 L and d_0 = 6.0 L at Re = 500 (a) and Re = 2000 (b) with f^* = 2.5 and φ = 0. The results for an isolated swimmer are also included for comparison. A negative value of u_b implies upstream swimming approaching the target.

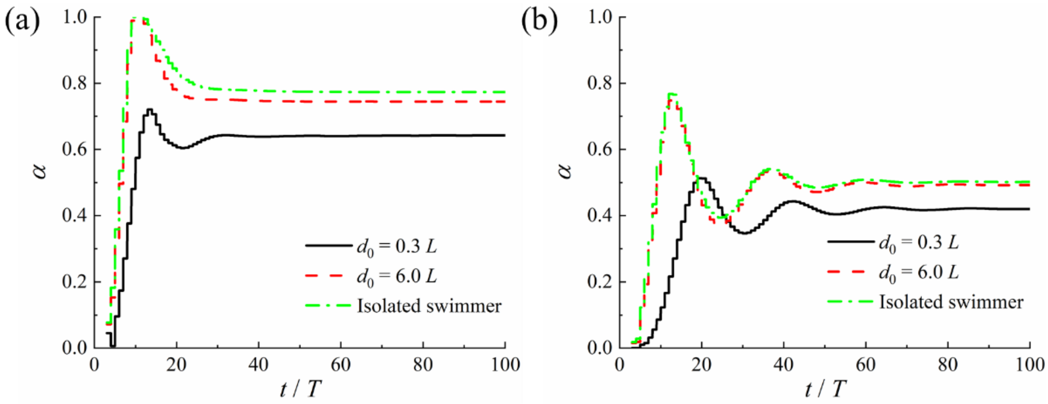

Fig. 6.11. The instantaneous force amplitude adjustment factor α yielded by the controller at d_0 = 0.3 L and d_0 = 6.0 L at Re = 500 (a) and Re = 2000 (b) with f^* = 2.5 and φ = 0. The results for an isolated swimmer are also included for comparison.

The eventual swimming speed during the holding station at the target is relatively small and fluctuates upstream and downstream symmetrically, as plotted in Fig. 6.10. In comparison between Fig. 6.9 and Fig. 6.10, we find that the converged swimming velocity at the larger Re (2000) during the position-holding phase seems more stable in contrast to a lower Re (500) in terms of smaller undulation amplitude (± 0.01 U versus ± 0.02 U). Furthermore, a smaller d_0 also yields fewer undulation amplitude of the swimming speed. In general, the implemented feedback controller here is proved to be effective in the motion control of the considered flexible swimmer involving dynamic fluid-structure interaction, reflected by the well-converged swimmer position, swimming speed, and actuation force amplitude factor as shown in Fig. 6.9 – Fig. 6.11.

In addition to the above swimming performance, we also study the flexible structural deformation due to the dynamic interplay of the structure and the fluid with the actuation force being applied. The tip displacement of the trailing edge of the swimmer is depicted in Fig. 6.12. The maximum tip displacement of the swimmer at Re = 500 is greater than that at Re =2000 attributed to a bigger actuation force applied on the surface during the station holding. A closer initial location, and thus a closer target position, relative to the cylinder seems to have little effect on the maximum amplitude of the displacement. Nevertheless, a more noticeable oscillation of the displacement amplitude is presented at d_0/L = 0.3 and 1.0, but not at d_0/L = 6.0 for both the two Reynolds numbers, which is marked in Fig. 6.12. Interestingly, we find that this normalized displacement oscillation period $T_{oscillation}U/L$, defined as the time interval of the maximum trailing-edge tip displacements of the plate as shown in Fig. 6.12, at d_0/L = 0.3 is 4.79 and 4.27 for Re = 500 and 2000, which is quite close to the vortex shedding period from the cylinder, i.e., 4.69 and 4.39, respectively. Therefore, we conjuncture that this displacement oscillation is mainly caused by the nearby downstream periodic vortex shedding from the cylinder surface. This demonstrates the interaction between the flexible deformation and nearby vortices, which is not present if the swimmer is far from the cylinder.

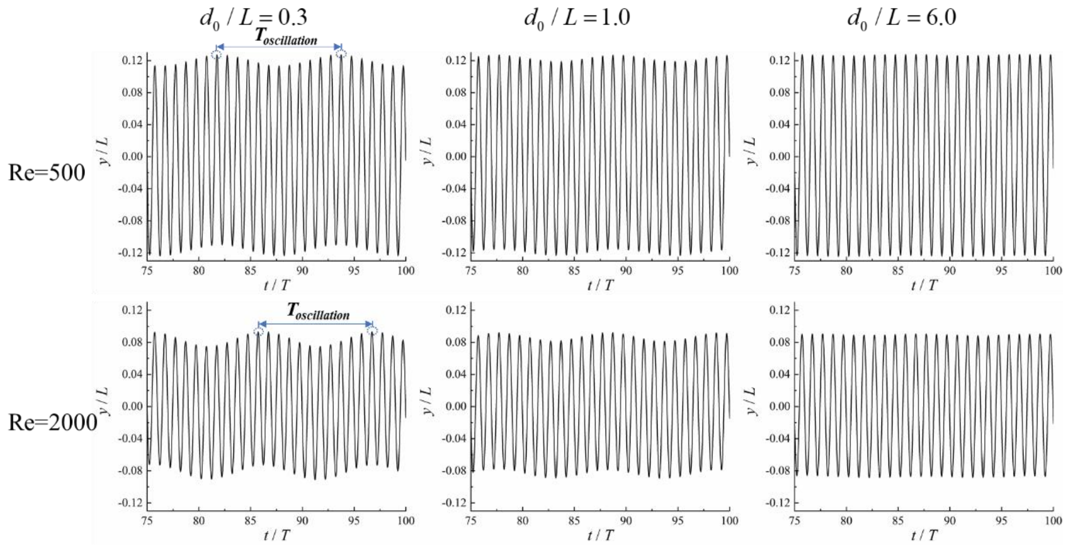

Fig. 6.12. The tip displacement of the trailing edge of the swimmer at d_0 = 0.3 L, d_0 = 1.0 L and d_0 = 6.0 L at Re = 500 and Re = 2000 with f^* = 2.5 and φ = 0.

For further insight into the flexible deformation of the swimmer under actuation force, we plot the envelope of the midline in one actuation period in Fig. 6.13. It can be found that the periodic body deformation is generally symmetric about the horizontal balanced position (y-axis), which shows similarity to the body deformation patterns of a real larval zebrafish

(Müller and van Leeuwen, 2004) under the present force actuation mechanism in terms of the arch-shaped midline at the posterior body (see Fig. 2 in their work). The observed tip deformation at Re = 500 is larger than that at Re = 2000 attributed to a larger actuation force as shown in Fig. 6.11. At $t = 0.5\ T$ and $t = T$ when the instantaneous force amplitude is zero, a more noticeable arch near the middle of the body length is seen at Re = 500. In comparison, the body at Re = 2000 presents a more flat profile at this instant.

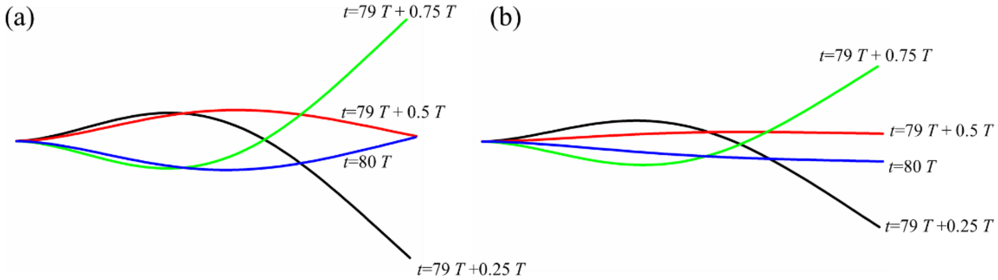

Fig. 6.13. Envelope trajectories of the midline of the flexible swimming at $d_0 = 0.3\ L$ for Re = 500 (a) and Re = 2000 (b) during one actuation period with $f^* = 2.5$ and $\varphi = 0$.

The instantaneous Z-vorticity contour around the swimmer during station-holding at two different d_0 is depicted in Fig. 6.14. A pair of vortices, each with clockwise and anti-clockwise direction, is shed from the trailing edge of the swimmer roughly at $t = 0.25\ T$ and $t = 0.75\ T$ when the swimmer flaps reversely from one extreme side to another side, respectively, during one period. The effect of the presence of the fixed cylinder is mainly reflected by the morphologies of the wake vortices. Namely, the vortices behind the swimmer are more compressed towards the negative x-direction at $d_0/L = 0.3$, which presents a "V" style layout from the swimmer tail to the downstream till the cylinder. In contrast, at $d_0/L = 6.0$ when the swimmer is far from the cylinder, the vortices show more regular patterns which have been seen behind a flapping foil or plate in static fluid and uniform flow (Kim et al., 2016; Zhu et al., 2014b). This difference is caused by the high pressure at the left-side surface of the cylinder, as shown in Fig. 6.15. Due to this high pressure, the low-pressure zone near the tail of the swimmer is reduced in size at $d_0/L = 0.3$ compared with that at $d_0/L = 6.0$, which can be found through a comparison of Fig. 6.15(a) and (b). Apart from this noticeable reduction of low-pressure, the other pressure distribution between these two is generally identical. This would help the swimmer gain a thrust boost and thus, less energy is required to hold the station there for $d_0/L = 0.3$ as presented in Fig. 6.8(c) and (d). The vortices patterns and pressure distribution at Re = 2000 are qualitatively similar to the counterparts at Re = 500. Therefore, they are not shown here.

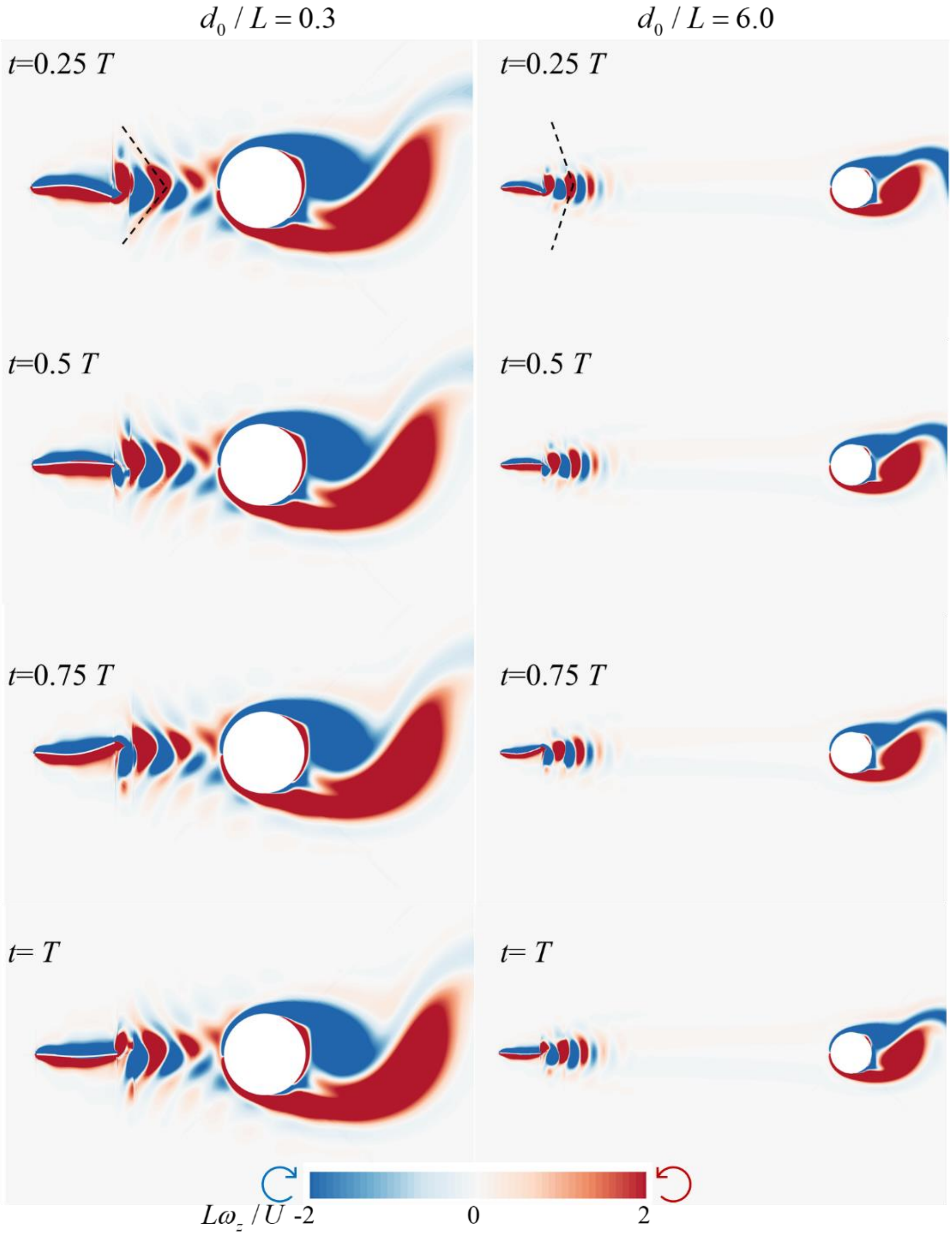

Fig. 6.14. The instantaneous Z-vorticity contour around the swimmer within one force actuation period during station-holding at d_0/L = 0.3 (left-hand column) and d_0/L = 6.0 (right-hand column) with Re = 500, f^* = 2.5 and φ = 0.

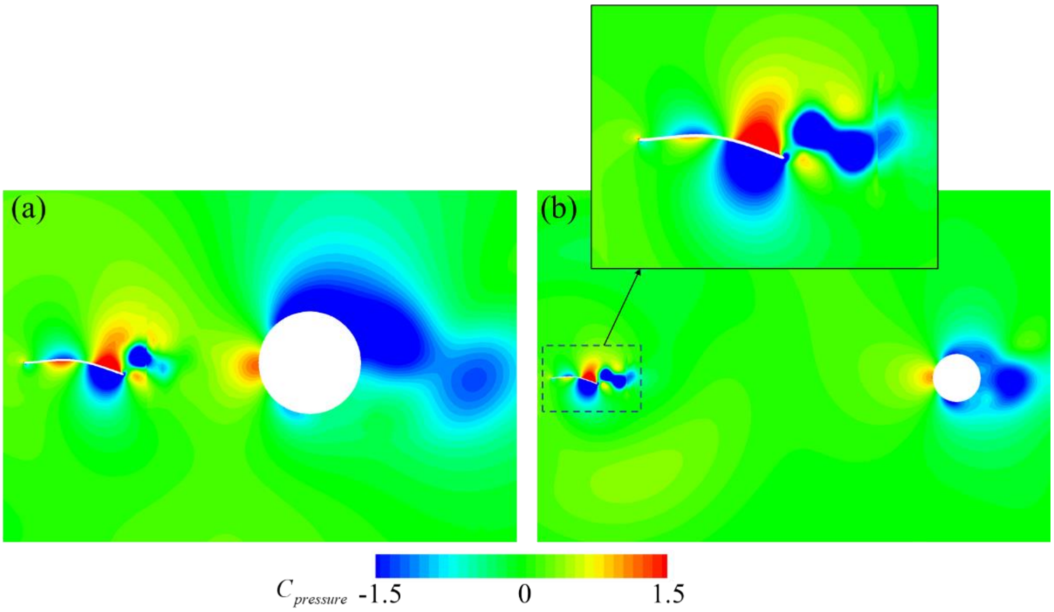

Fig. 6.15. The pressure distribution around the swimmer at t = 0.25 T during station-holding at d_0/L = 0.3 (a) and d_0/L = 6.0 (b) with Re = 500, f^* = 2.5 and φ = 0.

6.4.3 The effect of force actuation frequency f^* and phase shift angle φ

In this section, we study the effect of f^* and φ on the swimming performance and station-holding capability with Re = 500 and k_p = 15. We now use a larger k_p value than that (k_p = 7) in section 6.4.2 to yield fast initial acceleration of the swimmer to avoid the numerical divergence due to the clashes of the cylinder grid cluster and the swimmer grid cluster for some cases considered in this section. This clash is caused by the downstream drift of the swimmer by the incoming flow when the produced thrust is overwhelmed by the drag force at the initial swimming phase if a small k_p is used.

The results of C_{Ps}, T_s, C_{Ph}, and α_h at different force frequencies are summarized in Fig. 6.16. As can be seen, the actuation frequency has a significant effect on all four parameters. Specifically, much more energy and swimming time are required at f^* = 2.0 when d_0/L is beyond 1 for the swimmer to travel the same distance and hold the station from the same initial position compared with other f^*. The most energy savings and time savings are yielded at f^* = 2.5 for d_0/L > 1. Larger force amplitude is needed to swim forward and hold the station at f^* = 2.0, which even approaches the maximum allowed force amplitude with $\alpha \approx 1$ at a large d_0, e.g., 6.0. Our simulation also shows that an isolated swimmer in the absence of the cylinder is not able to swim forward or hold the position, which is drifted downstream, at f^* = 2.0 under the current control scheme even with the maximum force amplitude C_{ef0} = 2.0 (α = 1).

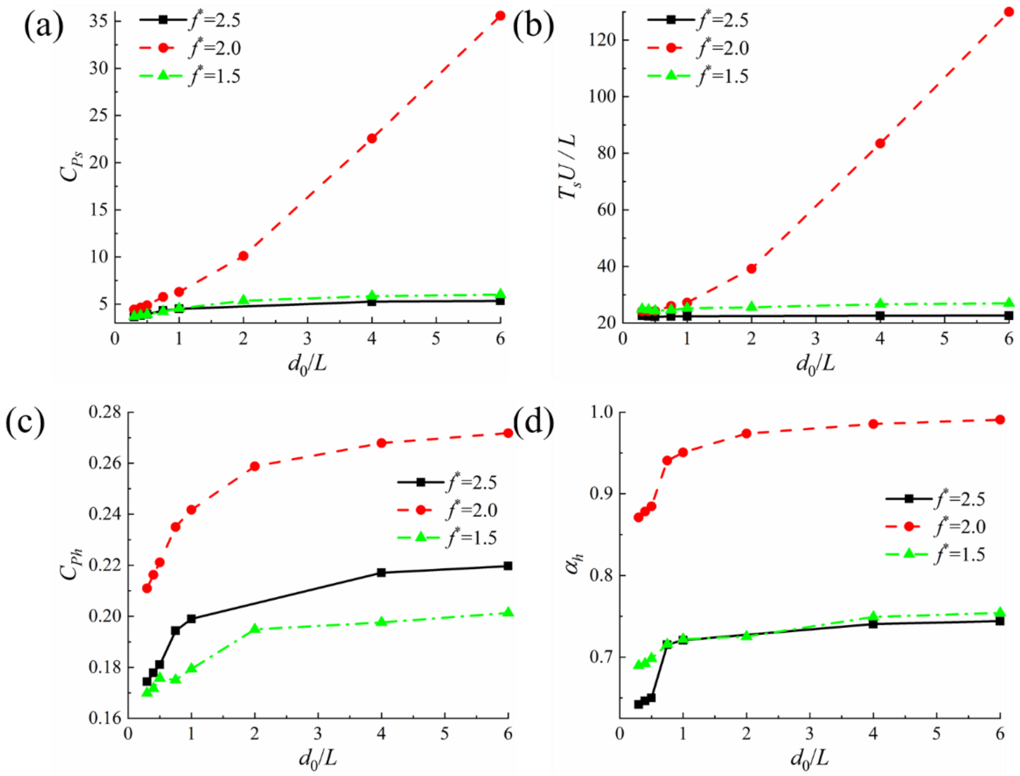

Fig. 6.16. The overall energy expenditure coefficient C_{Ps} (a) and T_s (b) required by the swimmer to reach the target by traveling the same distance L, the mean energy expenditure coefficient C_{Ph} (c), and the converged adjustment factor α_h of actuation force amplitude (d) when the swimmer hold station near the target at different initial distances relative to the cylinder d_0 at different f^* with Re = 500 and φ = 0.

A close inspection on Fig. 6.17(a) reveals that the reduced C_{Ps} at f^* = 1.5 compared with that at f^* = 2.0 may be attributed to a faster arrival at the target position, despite that a larger maximum swimming speed is seen at t = 10 T for f^* = 2.0. By comparing Fig. 6.17(c) and (d), we also find that a larger force amplitude and higher actuation frequency at f^* = 2.0 do not lead to greater tip amplitude than that at f^* = 1.5 as demonstrated in Dai et al. (2012b), implying a complex interaction between the flexible deformation and actuation parameters.

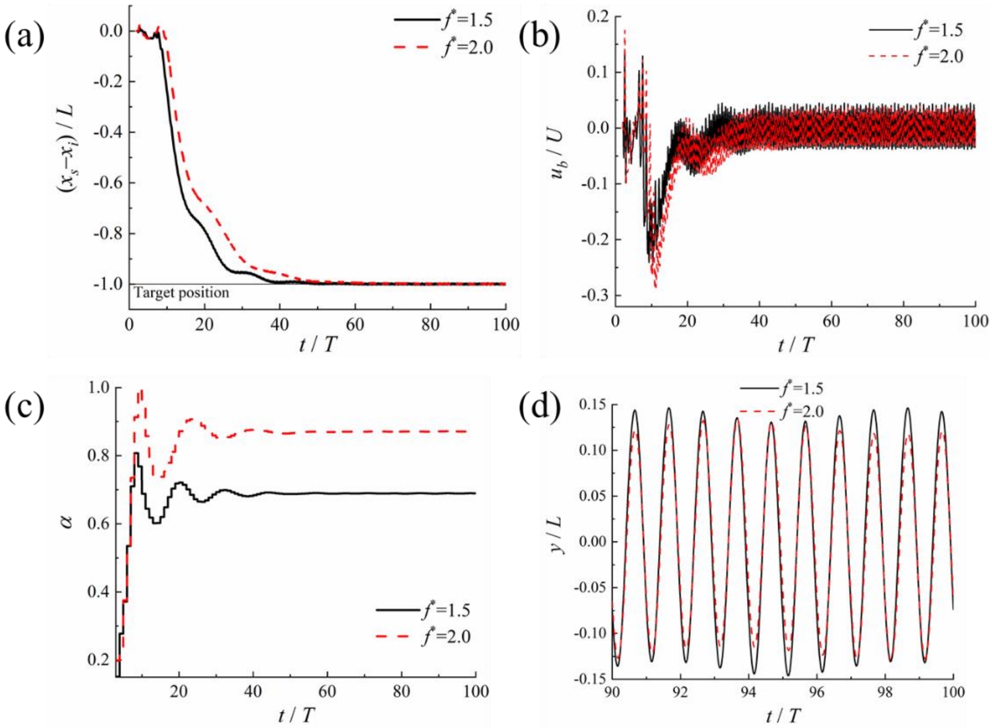

Fig. 6.17. The instantaneous normalized swimming distance (a), swimming speed (b), force amplitude factor (c), and the tip displacement (d) at f^* = 1.5 and 2.0 with Re = 500, d_0/L = 0.3 and φ = 0.

Fig. 6.18 depicts the instantaneous *Z*-vorticity contours around the swimmer and cylinder during it is holding station near the target at d_0/L = 0.3 for the two different actuation force frequencies. It can be seen that the vortices distribution around the left-side surface of the cylinder is more disturbed by the shedding vortices from the swimmer tail at f^* = 1.5. Thus, the shedding vortices by the cylinder have a less regular configuration compared with that behind the cylinder at f^* = 2.0 and 2.5, as shown in Fig. 6.18 and Fig. 6.14. It may be attributed to the greater oscillation amplitude of the swimmer's tip at f^* = 1.5. The peak tip displacements for the three frequencies are 0.147 *L*, 0.134 *L*, and 0.127 *L* at f^* = 1.5, 2.0 and 2.5, respectively. This larger flapping motion at the trailing edge enhances the capability of the swimmer to communicate momentum to the surrounding flow (Michelin and Llewellyn Smith, 2009), thus leading to a stronger influence on the vortices shed from the cylinder.

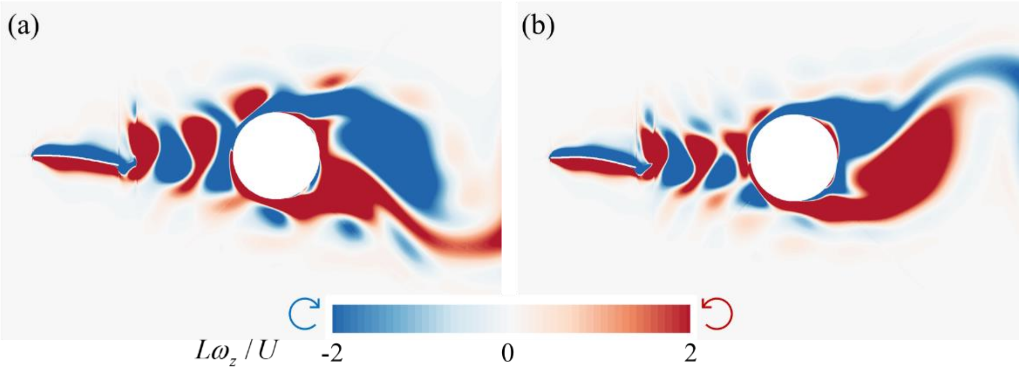

Fig. 6.18. The instantaneous *Z*-vorticity contour around the swimmer at t = 0.25 T during station-holding at f^* = 1.5 (a) and f^* = 2.0 (b) with Re = 500, d_0/L = 0.3 and φ = 0.

We now explore the effect of the phase shift φ of the actuation force in Eq.(6.2) at Re = 500, f^* = 2.5 and d_0/L = 1.0. The results of C_{Ps}, T_s, C_{Ph} and α_h are presented in Fig. 6.19. The phase shift has a similar effect on C_{Ps} and T_s whose curves have the same trend with φ being increased. Under the parameters studied, a maximum and minimum value of C_{Ps} and T_s are seen at φ = 60 and 120 deg. In comparison, the energy-saving and swimming time-saving are roughly 16% from φ = 60 deg to 120 deg. Nevertheless, the phase shift φ has a negligible effect on C_{Ph} and α_h in which the maximum difference caused by φ is below 1%. Therefore, the phase shift generally only affects the swimming phase from the initial location to the target, while the station-holding after reaching the target is far less sensitive to φ. Likewise, the influence of the phase shift on the instantaneous variations of swimming distance x_s, swimming speed u_b, and force adjustment factor α is mainly noticeable during the swimming phase, as shown in Fig. 6.20.

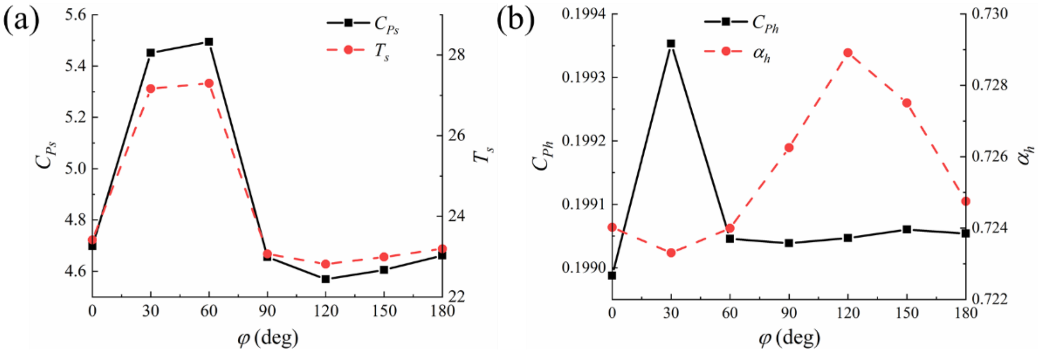

Fig. 6.19. C_{Ps} and T_s (a), and C_{Ph} and α_h (b) at different force phase shift φ with Re = 500, f^* = 2.5 and d_0/L = 0.3.

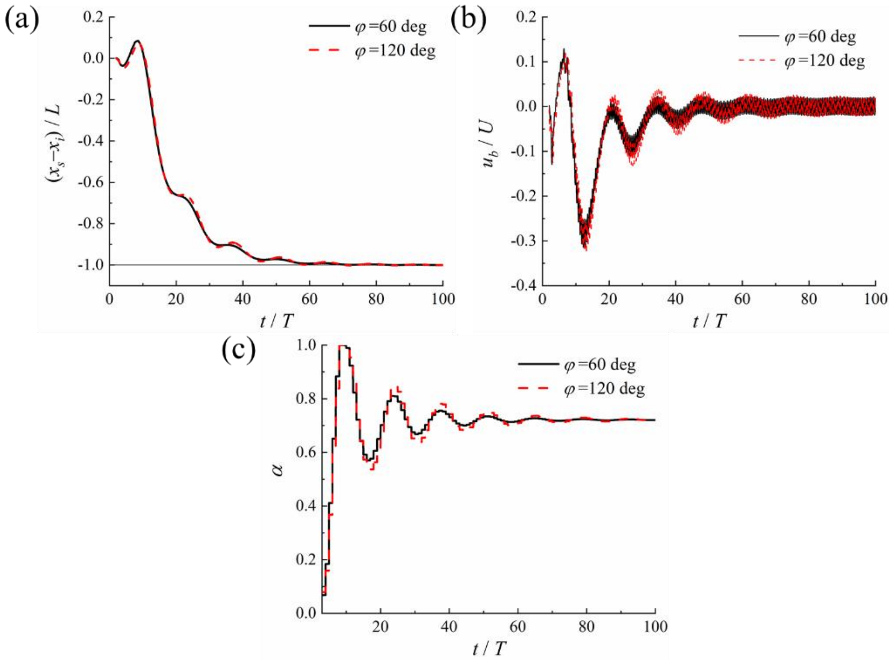

Fig. 6.20. The instantaneous normalized swimming distance (a), swimming speed (b), and force amplitude factor (c) for two different φ with Re = 500, f^* = 2.5 and d_0/L = 1.0.

6.5 Summary

The swimming and station-holding performance of a flexible swimmer in front of a fixed cylinder in the uniform flow is numerically studied by using the developed high-fidelity FSI solver. The two-dimensional fish-like swimmer is simplified as a flexible plate whose deformation is actuated by the imposed actuation force that mimics the muscle force of the fish body and fin. The amplitude of this actuation force is dynamically tuned by a feedback PD controller to achieve the control objective, i.e., swimming from the initial position to a designated target point and holding station there.

The simulation results show that the proposed control scheme to adjust the actuation force amplitude based on the instantaneous gap between the swimmer location and target and swimming speed is effective and robust. Specifically, the swimmer successfully achieves the control objectives. i.e., swimming to the target and holding the station stably despite the drag force due to the incoming flow at different flow environments (Reynold numbers, and initial position relative to the cylinder) and different actuation force formations (force frequencies and phase shift angles).

Nevertheless, these flow conditions and force actuation formulas indeed result in performance changes, in terms of swimming time T_s and energy consumption C_{Ps} during traveling the same distance (one body length) from the initial position to the target, and the energy expenditure C_{Ph} required to hold the station at the target. We find that energy consumption is reduced for swimming and holding the position at a higher Re compared with a smaller one. The swimmer which departs from an initial position d_0 closer to the cylinder can also enjoy energy savings reflected by smaller C_{Ps} and C_{Ph}, as well as a smaller actuation force, compared to that with larger d_0 at the same Reynolds number, force actuation formula, and control scheme. This may be attributed to the oppression of low pressure near the trailing edge of the swimmer (see Fig. 6.15) due to the downstream cylinder, which provides additional thrust boost (or drag reduction) to help save energy. Meanwhile, the flexible deformation of the swimmer is also affected by the nearby cylinder flow field, reflected by the frequency resonance of the oscillation of the maximum tip displacement with the shedding vortices from the cylinder (see Fig. 6.12). These benefits and influences are reduced when the swimmer is far away from the cylinder. And swimming time and energy consumption become almost the same as the counterparts of a swimmer swimming in the uniform flow in the absence of the cylinder if d_0 is large enough.

Besides, the frequency of the actuation force has a significant effect on swimming performance. Under the parameters studied, much more swimming time and energy consumption are required at $f^* = 2.0$ compared with other frequencies when other variables are the same. At this frequency, an isolated swimmer in the uniform flow even fails to produce enough thrust to overcome the drag force to swim forward despite the applied largest force amplitude allowed in this work. In comparison, the effect of the phase shift φ of the actuation force formula is less significant. Specifically, the difference in swimming energy consumption C_{Ps} from initial to the target position attributed to varied φ is below 16%, while it has a negligible effect on station-holding performance after the swimmer reaches the target.

It should be noted that although the present study is based on a two-dimensional model, the proposed method to calculate the tracking error with the time-averaged swimming speed may still have implications for the control design of underwater robots. The instantaneous distance is widely used as the tracking error in many existing underwater robotic systems when using PID control. It would be interesting to explore if the time-averaged swimming speed-based tracking error can enhance control stability and reduce overshoot in practice.

Chapter 7 Conclusions and Recommendations

7.1 Conclusions

Inspired by the previous biological, experimental, and numerical studies of caudal fin locomotion and jet propulsion in the uniflow flow and altered fluid conditions, this thesis aims at answering some fundamental questions proposed in section 1.2 through high-fidelity numerical modeling to investigate the hydrodynamics and propulsive performance of bio-inspired caudal fin and jet based propulsors. Possible answers to the raised questions are provided and the objectives are fulfilled. In this section, the main conclusions of this thesis are drawn as follows.

7.1.1 The Development of a Fluid-structure Interaction Solver (Chapter 3)

In this section, a numerical solver to simulate the fluid-structure interaction problems in aquatic propulsion was developed via the coupling of the existing in-house fluid code with a finite element method-based structural solver, CalculiX. Within this framework, the surrounding flow around the swimmer is resolved by the solution of three-dimensional, viscous, unsteady Navier-Stokes equations. The structural response is obtained by solving the equations of momentum balance in the weak form with a finite element method. The coupling is based on an open-source coupling library for partitioned multi-physics simulations, preCICE, that provides the main ingredients of an FSI coupling including data mapping, coupling scheme, and communications between solvers. Afterwards, through four properly selected validation cases, the accuracy of the developed FSI code is demonstrated via comparisons with other available numerical or experimental results. Compared with most of the existing numerical FSI solvers in the literature, the advantages of this FSI solver include: firstly, it is not limited to simple beam or shell structural models. As a universal three-dimensional finite element method, CalculiX can resolve nonlinear structures and nonlinear dynamics which may involve complex material behaviors along with large displacement and complex deformation, making it capable of simulating the fish body and fin structures. Additionally, thanks to the sophisticated and robust coupling algorithms implemented in preCICE, this new FSI solver enables to model strong coupling interaction between the swimmer and its immersed fluid efficiently. The development of this FSI solver provides a solid basis for the following numerical investigations of bio-inspired propulsion involving deformation and flexibility.

7.1.2 Investigation on Effects of Variable Stiffness Distribution on Propulsion Performance of Flexible Body and Fin (Chapter 4)

Two representative caudal fin-based swimmers, i.e., the sunfish and tuna fish, are chosen as prototypes. Distinct from previous numerical studies, the body and/or tail are composed of non-uniform stiffness distribution in this work. It is shown that it is feasible to replicate similar kinematics and propulsive capability to that of the real fish via purely passive structural deformations. For a sunfish-like caudal peduncle-fin model, consistent with the experimental measurements, the fin with a cupping stiffness profile generates the largest thrust and efficiency whereas a heterocercal flexible fin yields the least propulsion performance but has the best maneuverability.

However, the above does not apply to a highly-forked tuna-like tail model with a higher aspect ratio. The resulting asymmetric tail conformation from the heterocercal stiffness profile yields performance improvement at intermediate stiffness in comparison to the cupping and uniform stiffness. This may suggest that this asymmetrical tail movement does not only provides additional lift to balance the swimming body but may also contribute to efficient propulsion during steady swimming of scombrid fish. This heterocercal tail deformation has distinctive functions compared to that of a sunfish whose caudal fin has superior abilities in maneuvering. Besides, a bionic body stiffness profile results in better performance in most cases studied herein compared with a uniform stiffness commonly investigated in previous studies. Nevertheless, through the results, it is also found that it is impossible to achieve entirely real fish-like kinematics if only the passive control, via the variable body and fin stiffness proposed here, is adopted. This is reflected by the discrepancy of simulation results with biological measurements of real fishes.

7.1.3 Investigation on Jet Propulsion of a Squid-inspired Swimmer via Body Deformation (Chapter 5)

A two-dimensional inflation-deflation propulsion system inspired by the jet propulsion mechanism of squids and other cephalopods is proposed. It has a flexible mantle body with a pressure chamber and a nozzle that serves as the inlet and outlet of water. The fluid-structure interaction simulation results indicate that larger mean thrust production and higher efficiency can be achieved in high Reynolds number scenarios compared with the cases in laminar flow. The improved performance at high Reynolds number is attributed to stronger jet-induced vortices and highly suppressed external body vortices, which are associated with drag force. Maximum efficiency is reached when the jet vortices start to dominate the surrounding flow. The mechanism of symmetry-breaking instability under the turbulent flow condition is found to be different from that previously reported in laminar flow. Specifically, this instability in turbulent flow stems from irregular internal body vortices, which cause symmetry breaking in the wake. A higher Reynolds number or smaller nozzle size would accelerate the formation of this symmetry-breaking instability.

A three-dimensional jet propulsion system composed of an empty chamber enclosed within a deformable body with an opening is also proposed to focus on a single-cycle deflation process that produces the most thrust during periodic inflation-deflation phases. Distinct from the above 2D FSI model, the body deformation and jet velocity profiles are prescribed to investigate the jet flow and propulsion performance under the influence of background flow. Three jet velocity profiles, i.e., constant, cosine, and half cosine, are considered. We find that the maximum circulation of the vortex ring is reduced at a higher background flow velocity. This is because stronger interaction between the jet flow and background flow makes it harder to feed the leading vortex ring. Regarding thrust production, our analysis based on conservation of momentum indicates that with the constant profile the peak thrust is dominated by the time derivative of the fluid momentum inside the body, while momentum flux related thrust accounts for the quasi-steady thrust. For the cosine profile, its peak is mainly sourced from momentum flux associated with the unsteady vortex ring formation. No prominent thrust peak exists with the half cosine profile whose thrust continuously increases during the jetting. Under the present tethered mode, the background flow has negligible influence on the thrust attributed to momentum flux and momentum change of the fluid inside the body. However, it indeed affects the over pressure-related thrust but its effect is relatively small.

7.1.4 Investigation on Motion Control of a Self-propelled Flexible Swimmer near a Cylinder Utilizing PD Control (Chapter 6)

Inspired by a previous experimental study of fish swimming near a cylinder, we numerically investigate the swimming and station-holding behavior of a flexible swimmer ahead of a circular cylinder whose motion is controlled by a PD controller. Specifically, the deformation of this two-dimensional swimmer is actuated by a periodically varying external force applied on the body surface, which mimics the natural fish muscle force to produce propulsive thrust. The actuation force amplitude is dynamically adjusted by a feedback controller to instruct the swimmer to swim the desired distance from an initial position to a target location and then hold the station there. Our results show that the motion control of swimming and station holding has been achieved by this simple but effective feedback control without large overshoot when approaching the target at different flow conditions and actuation force formulas. Although the swimming distance remains the same, a swimmer whose initial position is closer to the cylinder requires less energy expenditure to swim to the target location and hold the station there. This is because the low pressure near the trailing edge of the swimmer is reduced in size, which provides drag reduction, contributing to reducing swimming energy. A higher Reynolds number also leads to energy savings. Under the same control strategy, the swimming performance is more affected by the force-frequency while the phase shift of the actuation force has a less significant impact.

7.2 Recommendations for Future Research

Fin propulsion and jet propulsion are big topics as they involve complex hydrodynamics, structural dynamics, and interaction between these two factors. Although this thesis focuses on numerical studies of caudal fin locomotion and jet locomotion and demonstrates some new findings involving fish and/or fin deformation and flexibility in uniform flows and altered flows, it has inevitable limitations due to limited research time and computational resources available. And there are some other interesting topics worth further investigation. Therefore, the following topics are recommended for future research.

I. In the present studies, the fluid solver is based on a multi-block structured grid system. The movement and deformation of the domain boundary are achieved by the arbitrary Lagrangian-Eulerian (ALE) formulation. It is usually challenging to generate a high-quality computation mesh for complex geometries like fishes with appendages. Besides, the mesh deformation during swimmer locomotion must be dealt with very carefully to avoid negative grid volume which causes numerical failures. In comparison, some CFD methods based on fixed and non-body-conformal grids are advantageous in handling complex/moving boundaries, such as the immersed-boundary method. Therefore, the capability of the present FSI solvers would be enhanced if an immersed-boundary method-based fluid solver is coupled with a universal finite element analysis code.

II. The geometries of the studied swimmers are simplified from a real streamlined body to a curved plate with uniform thickness despite non-uniform stiffness distribution. Future studies can take the streamlined fish body with complex curvatures into account as the body movement and tail movement interact with each other in real fish swimming. Besides, other fin types, such as dorsal fin, ventral fin, and pectoral fin, can also be considered to enable the investigation of the complex hydrodynamic interactions among them.

III. The present thesis concentrates on the fluid-structure interaction of fish fins while the undulating fish body also involves complex FSI problems. The undulation of the three-dimensional fish body can be actuated by active contractive strains/stress imposed on the two sides of the body that mimics the fish muscle constriction. In this way, more fish-like body deformation may be achieved compared with the cases in which only purely passive deformation is possible through the imposed simple heave or pitch movement. The actuation method by adding active strain/stress applies to the squid mantle deformation as well. This actuation mechanism needs further development of the structural solver.

IV. A unique symmetry-breaking mechanism of internal body vortices and subsequent jet vortices after continuous jets is found from the simulations of a 2D jetting model at high Reynolds numbers. It would be interesting to investigate if similar symmetry-breaking of vortex structures exists in a three-dimensional inflation-deflation jetting system after continuous jets in laminar and turbulent flows.

V. The effect of background flow on the vortex ring dynamics and jet propulsion performance is investigated. However, it is limited to a straight-line jetting scenario. The jet propulsion of squids is good at “vector-thrust” production by changing the angle of the nozzle relative to the flow directions. Thus, it is worth studying the vortex ring formation, jet propulsion, and turning performance when the nozzle has an angle with the swimming direction during maneuvering.

VI. In Chapter 6, a simple PD controller is used for motion control of a self-propelled swimmer ahead of a fixed cylinder. Although it is proved to be effective for the considered control objectives under the simulation environment, the control gains are not optimized for fast convergence and reduction of overshoot. Refined PD tuning and even optimization algorithms are anticipated for future studies to improve control performance. Besides, real-time control by the current PD controller requires a large number of iteration cycles to approach the target which is quite time-consuming and computational-resource-demanding. Some more intelligent control methods such as reinforcement learning based control may be more efficient to train the swimmers to reach the control targets without resolving complex Navier-Stokes equations throughout the control process.

References

Abbott, I.H., Von Doenhoff, A.E., 1959. Theory of wing sections, including a summary of airfoil data. Courier Corporation.

Abdel-Raouf, E., Sharif, M.A.R., Baker, J., 2017. Impulsively started, steady and pulsated annular inflows. Fluid Dynamics Research 49, 025511.

Advaith, S., Manu, K.V., Tinaikar, A., Chetia, U.K., Basu, S., 2017. Interaction of vortex ring with a stratified finite thickness interface. Physics of Fluids 29, 093602.

Akanyeti, O., Liao, J.C., 2013a. The effect of flow speed and body size on Kármán gait kinematics in rainbow trout. Journal of Experimental Biology 216, 3442-3449.

Akanyeti, O., Liao, J.C., 2013b. A kinematic model of Kármán gaiting in rainbow trout. Journal of Experimental Biology 216, 4666-4677.

Akhtar, I., Mittal, R., Lauder, G.V., Drucker, E., 2007. Hydrodynamics of a biologically inspired tandem flapping foil configuration. Theoretical and Computational Fluid Dynamics 21, 155-170.

Alben, S., Madden, P.G., Lauder, G.V., 2007. The mechanics of active fin-shape control in ray-finned fishes. Journal of the Royal Society, Interface 4, 243-256.

Aleev, I.U., 1969. Function and gross morphology in fish. Function and gross morphology in fish.

Anderson, E., Demont, M.E., 2005. The locomotory function of the fins in the squid Loligo pealei. Marine and Freshwater Behaviour and Physiology 38, 169-189.

Anderson, E.J., DeMont, M.E., 2000. The mechanics of locomotion in the squid Loligo pealei: locomotory function and unsteady hydrodynamics of the jet and intramantle pressure. Journal of Experimental Biology 203, 2851-2863.

Anderson, E.J., Grosenbaugh, M.A., 2005. Jet flow in steadily swimming adult squid. Journal of Experimental Biology 208, 1125-1146.

Anderson, E.J., Quinn, W., De Mont, M.E., 2001. Hydrodynamics of locomotion in the squid Loligo pealei. Journal of Fluid Mechanics 436, 249.

Arora, N., Kang, C.K., Shyy, W., Gupta, A., 2018. Analysis of passive flexion in propelling a plunging plate using a torsion spring model. Journal of Fluid Mechanics 857, 562-604.

Bao, Y., Tao, J., 2013. Active control of a cylinder wake flow by using a streamwise oscillating foil. Physics of Fluids 25, 053601.

Bartol, I.K., Krueger, P.S., Jastrebsky, R.A., Williams, S., Thompson, J.T., 2016. Volumetric flow imaging reveals the importance of vortex ring formation in squid swimming tail-first and arms-first. Journal of Experimental Biology 219, 392-403.

Bartol, I.K., Krueger, P.S., Stewart, W.J., Thompson, J.T., 2009a. Hydrodynamics of pulsed jetting in juvenile and adult brief squid Lolliguncula brevis: evidence of multiple jetmodes' and their implications for propulsive efficiency. Journal of Experimental Biology 212, 1889-1903.

Bartol, I.K., Krueger, P.S., Stewart, W.J., Thompson, J.T., 2009b. Pulsed jet dynamics of squid hatchlings at intermediate Reynolds numbers. Journal of Experimental Biology 212, 1506-1518.

Bartol, I.K., Krueger, P.S., Thompson, J.T., Stewart, W.J., 2008. Swimming dynamics and propulsive efficiency of squids throughout ontogeny. Integrative and Comparative Biology 48, 720-733.

Batina, J.T., 1990. Unsteady Euler airfoil solutions using unstructured dynamic meshes. AIAA Journal 28, 1381-1388.

Beal, D.N., Hover, F.S., Triantafyllou, M.S., Liao, J.C., Lauder, G.V., 2006. Passive propulsion in vortex wakes. Journal of Fluid Mechanics 549, 385.

Ben-Zvi, M., Shadwick, R.E., 2013. Exploring the mechanics of thunniform propulsion: a model study. Canadian Journal of Zoology 91, 741-755.

Bi, X., Zhu, Q., 2018. Numerical investigation of cephalopod-inspired locomotion with intermittent bursts. Bioinspiration & Biomimetics 13, 056005.

Bi, X., Zhu, Q., 2019a. Dynamics of a squid-inspired swimmer in free swimming. Bioinspiration & Biomimetics 15, 016005.

Bi, X., Zhu, Q., 2019b. Fluid-structure investigation of a squid-inspired swimmer. Physics of Fluids 31, 101901.

Bi, X., Zhu, Q., 2020. Pulsed-jet propulsion via shape deformation of an axisymmetric swimmer. Physics of Fluids 32, 081902.

Bone, Q., Pulsford, A., Chubb, A.D., 1981. Squid mantle muscle. journal of the Marine Biological Association of the United Kingdom 61, 327-342.

Borazjani, I., 2013. The functional role of caudal and anal/dorsal fins during the C-start of a bluegill sunfish. Journal of Experimental Biology 216, 1658-1669.

Borazjani, I., Daghooghi, M., 2013. The fish tail motion forms an attached leading edge vortex. Proceedings of the Royal Society B: Biological Sciences 280, 20122071.

Borazjani, I., Sotiropoulos, F., 2008. Numerical investigation of the hydrodynamics of carangiform swimming in the transitional and inertial flow regimes. Journal of Experimental Biology 211, 1541-1558.

Borazjani, I., Sotiropoulos, F., 2010. On the role of form and kinematics on the hydrodynamics of self-propelled body/caudal fin swimming. Journal of Experimental Biology 213, 89-107.

Boyer, F., Porez, M., Leroyer, A., Visonneau, M., 2008. Fast dynamics of an eel-like robot—comparisons with Navier–Stokes simulations. IEEE Transactions on Robotics 24, 1274-1288.

Bozkurttas, M., Mittal, R., Dong, H., Lauder, G.V., Madden, P., 2009. Low-dimensional models and performance scaling of a highly deformable fish pectoral fin. Journal of Fluid Mechanics 631, 311-342.

Buchholz, J.H., Smits, A.J., 2006. On the evolution of the wake structure produced by a low-aspect-ratio pitching panel. Journal of Fluid Mechanics 546, 433-443.

Bujard, T., Giorgio-Serchi, F., Weymouth, G., 2021. A resonant squid-inspired robot unlocks biological propulsive efficiency. Science Robotics 6, 50.

Bungartz, H.-J., Lindner, F., Gatzhammer, B., Mehl, M., Scheufele, K., Shukaev, A., Uekermann, B., 2016. preCICE–a fully parallel library for multi-physics surface coupling. Computers & Fluids 141, 250-258.

Carling, J., Williams, T.L., Bowtell, G., 1998. Self-propelled anguilliform swimming: simultaneous solution of the two-dimensional Navier-Stokes equations and Newton's laws of motion. Journal of Experimental Biology 201, 3143-3166.

Causin, P., Gerbeau, J.F., Nobile, F., 2005. Added-mass effect in the design of partitioned algorithms for fluid–structure problems. Computer Methods in Applied Mechanics and Engineering 194, 4506-4527.

Christianson, C., Cui, Y., Ishida, M., Bi, X., Zhu, Q., Pawlak, G., Tolley, M.T., 2020. Cephalopod-inspired robot capable of cyclic jet propulsion through shape change. Bioinspiration & Biomimetics 16, 016014.

Chung, H., Cao, S., Philen, M., Beran, P.S., Wang, K.G., 2018. CFD-CSD coupled analysis of underwater propulsion using a biomimetic fin-and-joint system. Computers & Fluids 172, 54-66.

Cinquegrana, D., Vitagliano, P.L., 2021. Validation of a new fluid—structure interaction framework for non-linear instabilities of 3D aerodynamic configurations. Journal of Fluids and Structures 103, 103264.

Coral, W., Rossi, C., Curet, O.M., Castro, D., 2018. Design and assessment of a flexible fish robot actuated by shape memory alloys. Bioinspiration & Biomimetics 13, 056009.

Dai, H., Luo, H., de Sousa, P.J.S.A.F., Doyle, J.F., 2012a. Thrust performance of a flexible low-aspect-ratio pitching plate. Physics of Fluids 24, 101903.

Dai, H., Luo, H., Doyle, J.F., 2012b. Dynamic pitching of an elastic rectangular wing in hovering motion. Journal of Fluid Mechanics 693, 473-499.

Dai, L., He, G., Zhang, X., 2016. Self-propelled swimming of a flexible plunging foil near a solid wall. Bioinspiration & Biomimetics 11, 046005.

Danaila, I., Vadean, C., Danaila, S., 2009. Specified discharge velocity models for numerical simulations of laminar vortex rings. Theoretical and Computational Fluid Dynamics 23, 317.

Das, P., Govardhan, R.N., Arakeri, J.H., 2018. Unsteady two-dimensional jet with flexible flaps at the channel exit. Journal of Fluid Mechanics 845, 462.

de Boer, A., van Zuijlen, A.H., Bijl, H., 2008. Comparison of conservative and consistent approaches for the coupling of non-matching meshes. Computer Methods in Applied Mechanics and Engineering 197, 4284-4297.

Degroote, J., Bathe, K.-J., Vierendeels, J., 2009. Performance of a new partitioned procedure versus a monolithic procedure in fluid–structure interaction. Computers & Structures 87, 793-801.

Degroote, J., Haelterman, R., Annerel, S., Bruggeman, P., Vierendeels, J., 2010. Performance of partitioned procedures in fluid–structure interaction. Computers & Structures 88, 446-457.

Delepine, M., 2013. Performance of thunniform propulsion: a high bio-fidelity experimental study. University of British Columbia.

Dettmer, W., Perić, D., 2006. A computational framework for fluid–structure interaction: finite element formulation and applications. Computer Methods in Applied Mechanics and Engineering 195, 5754-5779.

Dewar, H., Graham, J., 1994. Studies of tropical tuna swimming performance in a large water tunnel-Energetics. Journal of Experimental Biology 192, 13-31.

Dewey, P.A., Boschitsch, B.M., Moored, K.W., Stone, H.A., Smits, A.J., 2013. Scaling laws for the thrust production of flexible pitching panels. Journal of Fluid Mechanics 732, 29-46.

Dhondt, G., 2003. CalculiX CrunchiX USER'S MANUAL version 1.8. Mathematics Department, Macquarie University, Sydney.

Dhondt, G., 2004. The finite element method for three-dimensional thermomechanical applications. John Wiley & Sons.

Dong, H., Bozkurttas, M., Mittal, R., Madden, P., Lauder, G., 2010. Computational modelling and analysis of the hydrodynamics of a highly deformable fish pectoral fin. Journal of Fluid Mechanics 645, 345-373.

Donley, J.M., Dickson, K.A., 2000. Swimming kinematics of juvenile kawakawa tuna (Euthynnus affinis) and chub mackerel (Scomber japonicus). Journal of Experimental Biology 203, 3103-3116.

Drucker, E.G., Lauder, G.V., 1999. Locomotor forces on a swimming fish: three-dimensional vortex wake dynamics quantified using digital particle image velocimetry. Journal of Experimental Biology 202, 2393-2412.

Eldredge, J.D., 2008. Dynamically coupled fluid–body interactions in vorticity-based numerical simulations. Journal of Computational Physics 227, 9170-9194.

Eleni, D.C., Athanasios, T.I., Dionissios, M.P., 2012. Evaluation of the turbulence models for the simulation of the flow over a National Advisory Committee for Aeronautics (NACA) 0012 airfoil. Journal of Mechanical Engineering Research 4, 100-111.

Eloy, C., 2012. Optimal Strouhal number for swimming animals. Journal of Fluids and Structures 30, 205-218.

Enders, E.C., Boisclair, D., Roy, A.G., 2003. The effect of turbulence on the cost of swimming for juvenile Atlantic salmon (Salmo salar). Canadian Journal of Fisheries and Aquatic Sciences 60, 1149-1160.

Esposito, C.J., Tangorra, J.L., Flammang, B.E., Lauder, G.V., 2012. A robotic fish caudal fin: effects of stiffness and motor program on locomotor performance. Journal of Experimental Biology 215, 56-67.

Fausch, K.D., 1993. Experimental analysis of microhabitat selection by juvenile steelhead (Oncorhynchus mykiss) and coho salmon (O. kisutch) in a British Columbia stream. Canadian Journal of Fisheries and Aquatic Sciences 50, 1198-1207.

Feilich, K.L., Lauder, G.V., 2015. Passive mechanical models of fish caudal fins: effects of shape and stiffness on self-propulsion. Bioinspiration & Biomimetics 10, 036002.

Fernández, M.A., 2011. Coupling schemes for incompressible fluid-structure interaction: implicit, semi-implicit and explicit. SeMA Journal 55, 59-108.

Fierstine, H.L., Walters, V., 1968. Studies in locomotion and anatomy of scombroid fishes. Memoirs of the Southern California Academy of Sciences 6, 1.

Fish, F.E., 2020. Advantages of aquatic animals as models for bio-inspired drones over present AUV technology. Bioinspiration & Biomimetics 15, 025001.

Flammang, B.E., Lauder, G.V., 2008. Speed-dependent intrinsic caudal fin muscle recruitment during steady swimming in bluegill sunfish, *Lepomis macrochirus*. Journal of Experimental Biology 211, 587-598.

Flammang, B.E., Lauder, G.V., 2009. Caudal fin shape modulation and control during acceleration, braking and backing maneuvers in bluegill sunfish, *Lepomis macrochirus*. Journal of Experimental Biology 212, 277-286.

Flammang, B.E., Lauder, G.V., 2016. Functional morphology and hydrodynamics of backward swimming in bluegill sunfish, Lepomis macrochirus. Zoology 119, 414-420.

Flammang, B.E., Lauder, G.V., Troolin, D.R., Strand, T., 2011a. Volumetric imaging of shark tail hydrodynamics reveals a three-dimensional dual-ring vortex wake structure. Proceedings of the Royal Society B: Biological Sciences 278, 3670-3678.

Flammang, B.E., Lauder, G.V., Troolin, D.R., Strand, T.E., 2011b. Volumetric imaging of fish locomotion. Biology Letters 7, 695-698.

Förster, C., Wall, W.A., Ramm, E., 2007. Artificial added mass instabilities in sequential staggered coupling of nonlinear structures and incompressible viscous flows. Computer Methods in Applied Mechanics and Engineering 196, 1278-1293.

Free, B.A., Paley, D.A., 2018. Model-based observer and feedback control design for a rigid Joukowski foil in a Kármán vortex street. Bioinspiration & Biomimetics 13, 035001.

Fu, J., Liu, X., Shyy, W., Qiu, H., 2018. Effects of flexibility and aspect ratio on the aerodynamic performance of flapping wings. Bioinspiration & Biomimetics 13, 036001.

Gao, A., Triantafyllou, M.S., 2018. Independent caudal fin actuation enables high energy extraction and control in two-dimensional fish-like group swimming. Journal of Fluid Mechanics 850, 304-335.

Gao, L., Wang, X., Simon, C.M., Chyu, M.K., 2020. Development of the impulse and thrust for laminar starting jets with finite discharged volume. Journal of Fluid Mechanics 902.

Gatzhammer, B., 2008. A partitioned approach for Fluid-Structure Interaction on cartesian grids, Technische Universität München.

Gatzhammer, B., 2014. Efficient and flexible partitioned simulation of fluid-structure interactions. Technische Universität München.

Gharib, M., Rambod, E., Shariff, K., 1998. A universal time scale for vortex ring formation. Journal of Fluid Mechanics 360, 121-140.

Gibb, A.C., Dickson, K.A., Lauder, G.V., 1999. Tail kinematics of the chub mackerel Scomber japonicus: testing the homocercal tail model of fish propulsion. Journal of Experimental Biology 202, 2433-2447.

Gillis, G.B., 1996. Undulatory locomotion in elongate aquatic vertebrates: anguilliform swimming since Sir James Gray. American Zoologist 36, 656-665.

Giorgio-Serchi, F., Arienti, A., Laschi, C., 2016. Underwater soft-bodied pulsed-jet thrusters: Actuator modeling and performance profiling. The International Journal of Robotics Research 35, 1308-1329.

Gosline, J.M., DeMont, M.E., 1985. Jet-propelled swimming in squids. Scientific American 252, 96-103.

Gosline, J.M., Steeves, J.D., Harman, A.D., Demont, M.E., 1983. Patterns of circular and radial mantle muscle activity in respiration and jetting of the squid Loligo opalescens. Journal of Experimental Biology 104, 97-109.

Gosline, W.A., 1997. Functional morphology of the caudal skeleton in teleostean fishes. Ichthyological Research 44, 137-141.

Guinet, C., Domenici, P., de Stephanis, R., Barrett-Lennard, L., Ford, J.K.B., Verborgh, P., 2007. Killer whale predation on bluefin tuna: exploring the hypothesis of the endurance-exhaustion technique. Marine Ecology Progress Series 347, 111-119.

Habchi, C., Russeil, S., Bougeard, D., Harion, J.-L., Lemenand, T., Ghanem, A., Valle, D.D., Peerhossaini, H., 2013. Partitioned solver for strongly coupled fluid–structure interaction. Computers & Fluids 71, 306-319.

Haelterman, R., Bogaers, A.E.J., Scheufele, K., Uekermann, B., Mehl, M., 2016. Improving the performance of the partitioned QN-ILS procedure for fluid–structure interaction problems: Filtering. Computers & Structures 171, 9-17.

Han, P., Lauder, G.V., Dong, H., 2020. Hydrodynamics of median-fin interactions in fish-like locomotion: Effects of fin shape and movement. Physics of Fluids 32, 011902.

He, P., Wardle, n.C.S., 1986. Tilting behaviour of the Atlantic mackerel, Scomber scombrus, at low swimming speeds. Journal of Fish Biology 29, 223-232.

Heggenes, J., 1988. Effects of short-term flow fluctuations on displacement of, and habitat use by, brown trout in a small stream. Transactions of the American Fisheries Society 117, 336-344.

Heggenes, J., 2002. Flexible summer habitat selection by wild, allopatric brown trout in lotic environments. Transactions of the American Fisheries Society 131, 287-298.

Hess, A., Tan, X., Gao, T., 2020. CFD-based multi-objective controller optimization for soft robotic fish with muscle-like actuation. Bioinspiration & Biomimetics 15, 035004.

Hoover, A., Miller, L., 2015. A numerical study of the benefits of driving jellyfish bells at their natural frequency. Journal of Theoretical Biology 374, 13-25.

Hoover, A.P., Cortez, R., Tytell, E.D., Fauci, L.J., 2018. Swimming performance, resonance and shape evolution in heaving flexible panels. Journal of Fluid Mechanics 847, 386-416.

Hoover, A.P., Griffith, B.E., Miller, L.A., 2017. Quantifying performance in the medusan mechanospace with an actively swimming three-dimensional jellyfish model. Journal of Fluid Mechanics 813, 1112-1155.

Hou, T., Yang, X., Su, H., Jiang, B., Chen, L., Wang, T., Liang, J., 2019. Design and Experiments of a Squid-Like Aquatic-Aerial Vehicle with Soft Morphing Fins and Arms, 2019 International Conference on Robotics and Automation (ICRA). IEEE, pp. 4681-4687.

Hu, K., Ren, Z., Wang, Y., Wang, T., Wen, L., 2016. Quantitative hydrodynamic investigation of fish caudal fin cupping motion using a bio-robotic model, 2016 IEEE International Conference on Robotics and Biomimetics (ROBIO), pp. 295-300.

Huang, W.-X., Shin, S.J., Sung, H.J., 2007. Simulation of flexible filaments in a uniform flow by the immersed boundary method. Journal of Computational Physics 226, 2206-2228.

Imlay, F.H., 1961. The complete expressions for added mass of a rigid body moving in an ideal fluid. David Taylor Model Basin Washington D.C.

Isaacs, J.D., Seymour, R.J., 1973. The ocean as a power resource. International Journal of Environmental Studies 4, 201-205.

Jameson, A., 1991. Time dependent calculations using multigrid, with applications to unsteady flows past airfoils and wings, 10th Computational Fluid Dynamics Conference. American Institute of Aeronautics and Astronautics.

Jameson, A., Schmidt, W., Turkel, E.L.I., 1981. Numerical solution of the Euler equations by finite volume methods using Runge Kutta time stepping schemes, 14th Fluid and Plasma Dynamics Conference. American Institute of Aeronautics and Astronautics.

Jastrebsky, R.A., Bartol, I.K., Krueger, P.S., 2016. Turning performance in squid and cuttlefish: unique dual-mode, muscular hydrostatic systems. Journal of Experimental Biology 219, 1317-1326.

Jiang, H., Grosenbaugh, M.A., 2006. Numerical simulation of vortex ring formation in the presence of background flow with implications for squid propulsion. Theoretical and Computational Fluid Dynamics 20, 103-123.

Johnson, W., Soden, P.D., Trueman, E.R., 1972. A study in jet propulsion: an analysis of the motion of the squid, Loligo vulgaris. Journal of Experimental Biology 56, 155-165.

Kagemoto, H., Wolfgang, M.J., Yue, D.K.P., Triantafyllou, M.S., 2000. Force and power estimation in fish-like locomotion using a vortex-lattice method. Journal of Fluids Engineering 122, 239-253.

Kancharala, A.K., Philen, M.K., 2014. Study of flexible fin and compliant joint stiffness on propulsive performance: theory and experiments. Bioinspiration & Biomimetics 9, 036011.

Kancharala, A.K., Philen, M.K., 2016. Optimal chordwise stiffness profiles of self-propelled flapping fins. Bioinspiration & Biomimetics 11, 056016.

Kang, C.-K., Aono, H., Cesnik, C.E., Shyy, W., 2011. Effects of flexibility on the aerodynamic performance of flapping wings. Journal of Fluid Mechanics 689, 32-74.

Kier, W.M., Thompson, J.T., 2003. Muscle arrangement, function and specialization in recent coleoids. Berliner Paläobiologische Abhandlungen 3, 141-162.

Kim, B., Park, S.G., Huang, W., Sung, H.J., 2016. Self-propelled heaving and pitching flexible fin in a quiescent flow. International Journal of Heat and Fluid Flow 62, 273-281.

Kopman, V., Laut, J., Acquaviva, F., Rizzo, A., Porfiri, M., 2014. Dynamic modeling of a robotic fish propelled by a compliant tail. IEEE Journal of Oceanic Engineering 40, 209-221.

Krieg, M., Mohseni, K., 2013. Modelling circulation, impulse and kinetic energy of starting jets with non-zero radial velocity. Journal of Fluid Mechanics 719, 488-526.

Krueger, P.S., Gharib, M., 2003. The significance of vortex ring formation to the impulse and thrust of a starting jet. Physics of Fluids 15, 1271-1281.

Krueger, P.S., Moslemi, A.A., Nichols, J.T., Bartol, I.K., Stewart, W.J., 2008. Vortex rings in bio-inspired and biological jet propulsion. Advances in Science and Technology 58, 237-246.

Kurth, J.A., Thompson, J.T., Kier, W.M., 2014. Connective tissue in squid mantle is arranged to accommodate strain gradients. The Biological Bulletin 227, 1-6.

Küttler, U., Wall, W.A., 2008. Fixed-point fluid–structure interaction solvers with dynamic relaxation. Computational Mechanics 43, 61-72.

Lauder, G., Madden, P., Tangorra, J., Anderson, E., Baker, T., 2011a. Bioinspiration from fish for smart material design and function. Smart Materials and Structures 20, 094014.

Lauder, G.V., 1982. Structure and function in the tail of the Pumpkinseed sunfish (Lepomis gibbosus). Journal of Zoology 197, 483-495.

Lauder, G.V., 1989. Caudal fin locomotion in ray-finned fishes: historical and functional analyses. American Zoologist 29, 85-102.

Lauder, G.V., 2000. Function of the caudal fin during locomotion in fishes: kinematics, flow visualization, and evolutionary patterns. American Zoologist 40, 101-122.

Lauder, G.V., 2007. How fish swim: flexible fin thrusters as an EAP platform. International Society for Optics and Photonics, San Diego, California, United States, p. 652402.

Lauder, G.V., 2010. Swimming hydrodynamics: ten questions and the technical approaches needed to resolve them, Animal Locomotion. Springer, pp. 3-15.

Lauder, G.V., 2015. Flexible fins and fin rays as key transformations in ray-finned fishes. Great Transformations in Vertebrate Evolution 31.

Lauder, G.V., Drucker, E.G., 2004. Morphology and experimental hydrodynamics of fish fin control surfaces. IEEE Journal of Oceanic Engineering 29, 556-571.

Lauder, G.V., Lim, J., Shelton, R., Witt, C., Anderson, E., Tangorra, J.L., 2011b. Robotic models for studying undulatory locomotion in fishes. Marine Technology Society Journal 45, 41-55.

Lauder, G.V., Madden, P.G., 2006. Learning from fish: kinematics and experimental hydrodynamics for roboticists. International Journal of Automation and Computing 3, 325-335.

Lauder, G.V., Madden, P.G.A., 2007. Fish locomotion: kinematics and hydrodynamics of flexible foil-like fins. Experiments in Fluids 43, 641-653.

Lauder, G.V., Madden, P.G.A., Mittal, R., Dong, H., Bozkurttas, M., 2006. Locomotion with flexible propulsors: I. Experimental analysis of pectoral fin swimming in sunfish. Bioinspiration & Biomimetics 1, S25.

Lee, Y., Baeder, J., 2003. Implicit hole cutting-a new approach to overset grid connectivity, 16th AIAA Computational Fluid Dynamics Conference, p. 4128.

Li, C., Yang, W., Xu, X., Wang, J., Wang, M., Xu, L., 2017a. Numerical investigation of fish exploiting vortices based on the Kármán gaiting model. Ocean Engineering 140, 7-18.

Li, G., Kemp, G., Jaiman, R.K., Khoo, B.C., 2021. A high-fidelity numerical study on the propulsive performance of pitching flexible plates. Physics of Fluids 33, 051901.

Li, G., Law, Y.Z., Jaiman, R.K., 2019. A novel 3D variational aeroelastic framework for flexible multibody dynamics: Application to bat-like flapping dynamics. Computers & Fluids 180, 96-116.

Li, N., Liu, H., Su, Y., 2017b. Numerical study on the hydrodynamics of thunniform bio-inspired swimming under self-propulsion. PloS One 12, e0174740.

Li, R., Xiao, Q., Liu, Y., Hu, J., Li, L., Li, G., Liu, H., Hu, K., Wen, L., 2018. A multi-body dynamics based numerical modelling tool for solving aquatic biomimetic problems. Bioinspiration & Biomimetics 13, 056001.

Liao, J.C., 2004. Neuromuscular control of trout swimming in a vortex street: implications for energy economy during the Karman gait. Journal of Experimental Biology 207, 3495-3506.

Liao, J.C., 2006. The role of the lateral line and vision on body kinematics and hydrodynamic preference of rainbow trout in turbulent flow. Journal of Experimental Biology 209, 4077-4090.

Liao, J.C., 2007. A review of fish swimming mechanics and behaviour in altered flows. Philosophical Transactions of the Royal Society B: Biological Sciences 362, 1973-1993.

Liao, J.C., Akanyeti, O., 2017. Fish swimming in a Kármán vortex street: kinematics, sensory biology and energetics. Marine Technology Society Journal 51, 48-55.

Liao, J.C., Beal, D.N., Lauder, G.V., Triantafyllou, M.S., 2003. The Kármán gait: novel body kinematics of rainbow trout swimming in a vortex street. Journal of Experimental Biology 206, 1059-1073.

Liao, W., Cai, J., Tsai, H.M., 2007. A multigrid overset grid flow solver with implicit hole cutting method. Computer Methods in Applied Mechanics and Engineering 196, 1701-1715.

Lin, Z., Hess, A., Yu, Z., Cai, S., Gao, T., 2019. A fluid–structure interaction study of soft robotic swimmer using a fictitious domain/active-strain method. Journal of Computational Physics 376, 1138-1155.

Linden, P.F., Turner, J.S., 2001. The formation of 'optimal' vortex rings, and the efficiency of propulsion devices. Journal of Fluid Mechanics 427, 61.

Lindner, F., Mehl, M., Uekermann, B., 2017. Radial basis function interpolation for black-box multi-physics simulations, VII International Conference on Computational Methods for Coupled Problems in Science and Engineering, pp. 1-12.

Lindsey, C.C., 1978. Form, Function and Locomotory Habits in Fish. Fish Physiology VII Locomotion, 239-313.

Liu, F., Ji, S., 1996. Unsteady flow calculations with a multigrid Navier-Stokes method. AIAA Journal 34, 2047-2053.

Liu, F., Zheng, X., 1994. Staggered finite volume scheme for solving cascade flow with a k-omega turbulence model. AIAA Journal 32, 1589-1597.

Liu, F., Zheng, X., 1996. A strongly coupled time-marching method for solving the Navier–Stokes and k-ω turbulence model equations with multigrid. Journal of Computational Physics 128, 289-300.

Liu, G., Geng, B., Zheng, X., Xue, Q., Dong, H., Lauder, G.V., 2019. An image-guided computational approach to inversely determine in vivo material properties and model flow-structure interactions of fish fins. Journal of Computational Physics 392, 578-593.

Liu, G., Ren, Y., Dong, H., Akanyeti, O., Liao, J.C., Lauder, G.V., 2017. Computational analysis of vortex dynamics and performance enhancement due to body–fin and fin–fin interactions in fish-like locomotion. Journal of Fluid Mechanics 829, 65-88.

Liu, G., Ren, Y., Zhu, J., Bart-Smith, H., Dong, H., 2015. Thrust producing mechanisms in ray-inspired underwater vehicle propulsion. Theoretical and Applied Mechanics Letters 5, 54-57.

Liu, H., Wassersug, R., Kawachi, K., 1996. A computational fluid dynamics study of tadpole swimming. Journal of Experimental Biology 199, 1245-1260.

Liu, H., Wassersug, R., Kawachi, K., 1997. The three-dimensional hydrodynamics of tadpole locomotion. Journal of Experimental Biology 200, 2807-2819.

Liu, L., He, G., He, X., Wang, Q., Chen, L., 2021. Numerical study on the effects of a semi-free and non-uniform flexible filament in different vortex streets. Acta Mechanica Sinica, 1-9.

Liu, W., 2015. Numerical investigation into bio-inspired flow control for renewable turbine. University of Strathclyde.

Liu, W., Xiao, Q., Zhu, Q., 2016. Passive Flexibility Effect on Oscillating Foil Energy Harvester. AIAA Journal 54, 1172-1187.

Lolis, P., Guardino, C., Brown, T., Henson, J., 2016. Mechanical Integrity and Design Analysis Suite (MIDAS): A Tool for Rapid Finite Element Analysis (FEA) of Steam Turbine Blades, ASME Turbo Expo 2016: Turbomachinery Technical Conference and Exposition. American Society of Mechanical Engineers Digital Collection, Seoul, South Korea.

Low, K.H., 2011. Current and future trends of biologically inspired underwater vehicles, 2011 Defense Science Research Conference and Expo (DSR). IEEE, Singapore, pp. 1-8.

Lucas, K.N., Johnson, N., Beaulieu, W.T., Cathcart, E., Tirrell, G., Colin, S.P., Gemmell, B.J., Dabiri, J.O., Costello, J.H., 2014. Bending rules for animal propulsion. Nature Communications 5, 3293.

Lucas, K.N., Thornycroft, P.J., Gemmell, B.J., Colin, S.P., Costello, J.H., Lauder, G.V., 2015. Effects of non-uniform stiffness on the swimming performance of a passively-flexing, fish-like foil model. Bioinspiration & Biomimetics 10, 056019.

Luhar, M., Nepf, H.M., 2011. Flow-induced reconfiguration of buoyant and flexible aquatic vegetation. Limnology and Oceanography 56, 2003-2017.

Luo, H., Yin, B., Dai, H., Doyle, J., 2010. A 3D Computational Study of the Flow-Structure Interaction in Flapping Flight, 48th AIAA Aerospace Sciences Meeting Including the New Horizons Forum and Aerospace Exposition. American Institute of Aeronautics and Astronautics.

Lupandin, A.I., 2005. Effect of flow turbulence on swimming speed of fish. Biology Bulletin 32, 461-466.

MacIver, M.A., Patankar, N.A., Shirgaonkar, A.A., 2010. Energy-information trade-offs between movement and sensing. PLoS Computational Biology 6, e1000769.

Maertens, A.P., Gao, A., Triantafyllou, M.S., 2017. Optimal undulatory swimming for a single fish-like body and for a pair of interacting swimmers. Journal of Fluid Mechanics 813, 301-345.

Magnuson, J.J., 1973. Comparative study of adaptations for continuous swimming and hydrostatic equilibrium of scombroid and xiphoid fishes. Fish. Bull 71, 337-356.

Masoud, H., Alexeev, A., 2010. Resonance of flexible flapping wings at low Reynolds number. Physical Review E 81, 056304.

Matthies, H.G., Steindorf, J., 2003. Partitioned strong coupling algorithms for fluid–structure interaction. Computers & Structures 81, 805-812.

McHenry, M.J., Pell, C.A., Long, J., 1995. Mechanical control of swimming speed: stiffness and axial wave form in undulating fish models. Journal of Experimental Biology 198, 2293-2305.

McLaughlin, R.L., Noakes, D.L.G., 1998. Going against the flow: an examination of the propulsive movements made by young brook trout in streams. Canadian Journal of Fisheries and Aquatic Sciences 55, 853-860.

Mehl, M., Uekermann, B., Bijl, H., Blom, D., Gatzhammer, B., van Zuijlen, A., 2016. Parallel coupling numerics for partitioned fluid–structure interaction simulations. Computers & Mathematics with Applications 71, 869-891.

Michelin, S., Llewellyn Smith, S.G., 2009. Resonance and propulsion performance of a heaving flexible wing. Physics of Fluids 21, 071902.

Mittal, R., Dong, H., Bozkurttas, M., Lauder, G., Madden, P., 2006. Locomotion with flexible propulsors: II. Computational modeling of pectoral fin swimming in sunfish. Bioinspiration & Biomimetics 1, S35.

Mohseni, K., Gharib, M., 1998. A model for universal time scale of vortex ring formation. Physics of Fluids 10, 2436-2438.

Mohseni, K., Ran, H., Colonius, T., 2001. Numerical experiments on vortex ring formation. Journal of Fluid Mechanics 430, 267.

Morikawa, H., Yusa, K., Kobayashi, S., 2008. Mechanical Properties of the Caudal Fin Resulting from the Caudal Skeletal Structure of the Bluefin Tuna, Bio-mechanisms of Swimming and Flying. Springer, pp. 67-77.

Moslemi, A.A., Krueger, P.S., 2010. Propulsive efficiency of a biomorphic pulsed-jet underwater vehicle. Bioinspiration & Biomimetics 5, 036003.

Moslemi, A.A., Krueger, P.S., 2011. The effect of Reynolds number on the propulsive efficiency of a biomorphic pulsed-jet underwater vehicle. Bioinspiration & Biomimetics 6, 026001.

Müller, U.K., van Leeuwen, J.L., 2004. Swimming of larval zebrafish: ontogeny of body waves and implications for locomotory development. Journal of Experimental Biology 207, 853-868.

Muñoz-Benavent, P., Andreu-García, G., Valiente-González, J.M., Atienza-Vanacloig, V., Puig-Pons, V., Espinosa, V., 2017. Automatic Bluefin Tuna sizing using a stereoscopic vision system. ICES Journal of Marine Science 75, 390-401.

Nakata, T., Liu, H., 2012. A fluid–structure interaction model of insect flight with flexible wings. Journal of Computational Physics 231, 1822-1847.

National Agency for Finite Element, M., Standards, 1990. The standard NAFEMS benchmarks. NAFEMS.

Nauen, J.C., Lauder, G.V., 2000. Locomotion in scombrid fishes: morphology and kinematics of the finlets of the chub mackerel Scomber japonicus. Journal of Experimental Biology 203, 2247-2259.

Nauen, J.C., Lauder, G.V., 2001. Locomotion in scombrid fishes: visualization of flow around the caudal peduncle and finlets of the chub mackerel Scomber japonicus. Journal of Experimental Biology 204, 2251-2263.

Nauen, J.C., Lauder, G.V., 2002. Hydrodynamics of caudal fin locomotion by chub mackerel, Scomber japonicus (Scombridae). Journal of Experimental Biology 205, 1709-1724.

Nguyen, V.-T., Gatzhammer, B., 2015. A fluid structure interactions partitioned approach for simulations of explosive impacts on deformable structures. International Journal of Impact Engineering 80, 65-75.

Nguyen, V.L., Takamure, K., Uchiyama, T., 2019. Deformation of a vortex ring caused by its impingement on a sphere. Physics of Fluids 31, 107108.

Nichols, J.T., Krueger, P.S., 2012. Effect of vehicle configuration on the performance of a submersible pulsed-jet vehicle at intermediate Reynolds number. Bioinspiration & Biomimetics 7, 036010.

Nursall, J., 1963. The caudal musculature of Hoplopagrus guntheri Gill (Perciformes: Lutjanidae). Canadian Journal of Zoology 41, 865-880.

O'Dor, R.K., 1988. The forces acting on swimming squid. Journal of Experimental Biology 137, 421-442.

O’Dor, R.K., 2013. How squid swim and fly. Canadian Journal of Zoology 91, 413-419.

Olcay, A.B., Krueger, P.S., 2010. Momentum evolution of ejected and entrained fluid during laminar vortex ring formation. Theoretical and Computational Fluid Dynamics 24, 465-482.

Olivier, M., Dumas, G., 2016. A parametric investigation of the propulsion of 2D chordwise-flexible flapping wings at low Reynolds number using numerical simulations. Journal of Fluids and Structures 63, 210-237.

Olivier, M., Morissette, J.-F., Dumas, G., 2009. A Fluid-Structure Interaction Solver for Nano-Air-Vehicle Flapping Wings, 19th AIAA Computational Fluid Dynamics. American Institute of Aeronautics and Astronautics.

Packard, A., 1969. Jet propulsion and the giant fibre response of Loligo. Nature 221, 875-877.

Palacios-Morales, C., Zenit, R., 2013. Vortex ring formation for low Re numbers. Acta Mechanica 224, 383-397.

Paraz, F., Eloy, C., Schouveiler, L., 2014. Experimental study of the response of a flexible plate to a harmonic forcing in a flow. Comptes Rendus Mécanique 342, 532-538.

Paraz, F., Schouveiler, L., Eloy, C., 2016. Thrust generation by a heaving flexible foil: Resonance, nonlinearities, and optimality. Physics of Fluids 28, 011903.

Park, S.G., Kim, B., Sung, H.J., 2016. Self-propelled flexible fin in the wake of a circular cylinder. Physics of Fluids 28, 111902.

Peng, Z., Elfring, G.J., Pak, O.S., 2017. Maximizing propulsive thrust of a driven filament at low Reynolds number via variable flexibility. Soft Matter 13, 2339-2347.

Peppa, S., Triantafyllou, G.S., 2016. Sensitivity of two-dimensional flow past transversely oscillating cylinder to streamwise cylinder oscillations. Physics of Fluids 28, 037102.

Piperno, S., Farhat, C., Larrouturou, B., 1995. Partitioned procedures for the transient solution of coupled aroelastic problems Part I: Model problem, theory and two-dimensional application. Computer Methods in Applied Mechanics and Engineering 124, 79-112.

Porez, M., Boyer, F., Ijspeert, A.J., 2014. Improved lighthill fish swimming model for bio-inspired robots: Modeling, computational aspects and experimental comparisons. The International Journal of Robotics Research 33, 1322-1341.

Querzoli, G., Falchi, M., Romano, G.P., 2010. On the flow field generated by a gradually varying flow through an orifice. European Journal of Mechanics-B/Fluids 29, 259-268.

Radtke, L., Lampe, T., Abdel-Maksoud, M., Düster, A., 2018. A partitioned solution approach for the simulation of the dynamic behaviour of flexible marine propellers. Ship Technology Research, 1-14.

Reddy N, S., Sen, S., Har, C., 2018. Effect of flexural stiffness distribution of a fin on propulsion performance. Mechanism and Machine Theory 129, 218-231.

Ren, Z., Hu, K., Wang, T., Wen, L., 2016a. Investigation of fish caudal fin locomotion using a bio-inspired robotic model. International Journal of Advanced Robotic Systems 13, 87.

Ren, Z., Yang, X., Wang, T., Wen, L., 2016b. Hydrodynamics of a robotic fish tail: effects of the caudal peduncle, fin ray motions and the flow speed. Bioinspiration & Biomimetics 11, 016008.

Renda, F., Giorgio-Serchi, F., Boyer, F., Laschi, C., 2015a. Modelling cephalopod-inspired pulsed-jet locomotion for underwater soft robots. Bioinspiration & Biomimetics 10, 055005.

Renda, F., Serchi, F.G., Boyer, F., Laschi, C., 2015b. Structural dynamics of a pulsed-jet propulsion system for underwater soft robots. International Journal of Advanced Robotic Systems 12, 68.

Riggs, P., Bowyer, A., Vincent, J., 2010. Advantages of a Biomimetic Stiffness Profile in Pitching Flexible Fin Propulsion. Journal of Bionic Engineering 7, 113-119.

Rosenberger, L.J., 2001. Pectoral fin locomotion in batoid fishes: undulation versus oscillation. Journal of Experimental Biology 204, 379-394.

Rosenfeld, M., Rambod, E., Gharib, M., 1998. Circulation and formation number of laminar vortex rings. Journal of Fluid Mechanics 376, 297-318.

Rosic, M.-L., N., Thornycroft, P., J. M., Feilich, K., L., Lucas, K., N., Lauder, G., V., 2017. Performance variation due to stiffness in a tuna-inspired flexible foil model. Bioinspiration & Biomimetics 12, 016011.

Ryu, J., Byeon, H., Lee, S.J., Sung, H.J., 2019. Flapping dynamics of a flexible plate with Navier slip. Physics of Fluids 31, 091901.

Sadeghi, M., 2004. Parallel computation of three-dimensional aeroelastic fluid-structure interaction. University of California, Irvine.

Sadeghi, M., Yang, S., Liu, F., Tsai, H., 2003. Parallel computation of wing flutter with a coupled Navier-Stokes/CSD method, 41st Aerospace Sciences Meeting and Exhibit, p. 1347.

Salazar, R., Fuentes, V., Abdelkefi, A., 2018. Classification of biological and bioinspired aquatic systems: A review. Ocean Engineering 148, 75-114.

Salumäe, T., Chemori, A., Kruusmaa, M., 2017. Motion control of a hovering biomimetic four-fin underwater robot. IEEE Journal of Oceanic Engineering 44, 54-71.

Scholander, P.F., 1959. Wave-riding dolphins: How do they do it? Science 129, 1085-1087.

Serchi, F.G., Arienti, A., Laschi, C., 2012. Biomimetic vortex propulsion: toward the new paradigm of soft unmanned underwater vehicles. IEEE/ASME Transactions On Mechatronics 18, 484-493.

Sfakiotakis, M., Lane, D.M., Davies, J.B.C., 1999. Review of fish swimming modes for aquatic locomotion. IEEE Journal of oceanic engineering 24, 237-252.

Shahzad, A., Tian, F.-B., Young, J., Lai, J.C., 2018. Effects of Hawkmoth-like flexibility on the aerodynamic performance of flapping wings with different shapes and aspect ratios. Physics of Fluids 30, 091902.

Shao, X., Pan, D., Deng, J., Yu, Z., 2010. Hydrodynamic performance of a fishlike undulating foil in the wake of a cylinder. Physics of Fluids 22, 111903.

Shelton, R.M., Thornycroft, P.J., Lauder, G.V., 2014. Undulatory locomotion of flexible foils as biomimetic models for understanding fish propulsion. Journal of Experimental Biology 217, 2110-2120.

Shen, Q., Wang, T., Wen, L., Liang, J., 2013. Modelling and fuzzy control of an efficient swimming ionic polymer-metal composite actuated robot. International Journal of Advanced Robotic Systems 10, 350.

Shi, G., 2020. Fluid-Structure Interaction Simulations on Skeleton-Reinforced Biomimetic Fin Propulsion. University of Strathclyde (United Kingdom).

Shi, G., Xiao, Q., 2021. Numerical investigation of a bio-inspired underwater robot with skeleton-reinforced undulating fins. European Journal of Mechanics-B/Fluids 87, 75-91.

Shi, G., Xiao, Q., Zhu, Q., 2017. A Study of 3D Flexible Caudal Fin for Fish Propulsion, ASME 2017 36th International Conference on Ocean, Offshore and Arctic Engineering. American Society of Mechanical Engineers, p. V07AT06A052.

Shi, G., Xiao, Q., Zhu, Q., 2020. Numerical investigation of an actively and passively controlled skeleton-reinforced caudal fin. AIAA Journal 58, 4644-4658.

Shi, G., Xiao, Q., Zhu, Q., Liao, W., 2019. Fluid-structure interaction modeling on a 3D ray-strengthened caudal fin. Bioinspiration & Biomimetics 14, 036012.

Shoele, K., Zhu, Q., 2009. Fluid–structure interactions of skeleton-reinforced fins: performance analysis of a paired fin in lift-based propulsion. Journal of Experimental Biology 212, 2679-2690.

Shoele, K., Zhu, Q., 2010. Numerical simulation of a pectoral fin during labriform swimming. Journal of Experimental Biology 213, 2038-2047.

Shoele, K., Zhu, Q., 2012. Leading edge strengthening and the propulsion performance of flexible ray fins. Journal of Fluid Mechanics 693, 402-432.

Shuler, S.W., Nehring, R.B., Fausch, K.D., 1994. Diel habitat selection by brown trout in the Rio Grande River, Colorado, after placement of boulder structures. North American Journal of Fisheries Management 14, 99-111.

Siekmann, J., 1963. On a pulsating jet from the end of a tube, with application to the propulsion of certain aquatic animals. Journal of Fluid Mechanics 15, 399-418.

Smith, D.L., Brannon, E.L., Odeh, M., 2005. Response of juvenile rainbow trout to turbulence produced by prismatoidal shapes. Transactions of the American Fisheries Society 134, 741-753.

Spagnolie, S.E., Shelley, M.J., 2009. Shape-changing bodies in fluid: hovering, ratcheting, and bursting. Physics of Fluids 21, 013103.

Staaf, D.J., Gilly, W.F., Denny, M.W., 2014. Aperture effects in squid jet propulsion. Journal of Experimental Biology 217, 1588-1600.

Steele, S.C., Weymouth, G.D., Triantafyllou, M.S., 2017. Added mass energy recovery of octopus-inspired shape change. Journal of Fluid Mechanics 810, 155-174.

Stewart, W.J., Tian, F.-b., Akanyeti, O., Walker, C.J., Liao, J.C., 2016. Refuging rainbow trout selectively exploit flows behind tandem cylinders. Journal of Experimental Biology 219, 2182-2191.

Systèmes, D., 2010. ABAQUS 6.10 Benchmarks Manual. Abaqus 6.10 Documentation.

Taguchi, M., Liao, J.C., 2011. Rainbow trout consume less oxygen in turbulence: the energetics of swimming behaviors at different speeds. Journal of Experimental Biology 214, 1428-1436.

Tangorra, J.L., Davidson, S.N., Hunter, I.W., Madden, P.G.A., Lauder, G.V., Dong, H., Bozkurttas, M., Mittal, R., 2007. The development of a biologically inspired propulsor for unmanned underwater vehicles. IEEE Journal of Oceanic Engineering 32, 533-550.

Tangorra, J.L., Lauder, G.V., Hunter, I.W., Mittal, R., Madden, P.G., Bozkurttas, M., 2010. The effect of fin ray flexural rigidity on the propulsive forces generated by a biorobotic fish pectoral fin. Journal of Experimental Biology 213, 4043-4054.

Thandiackal, R., White, C.H., Bart-Smith, H., Lauder, G.V., 2021. Tuna robotics: hydrodynamics of rapid linear accelerations. Proceedings of the Royal Society B 288, 20202726.

Thompson, J.T., Kier, W.M., 2001. Ontogenetic changes in mantle kinematics during escape-jet locomotion in the oval squid, Sepioteuthis lessoniana Lesson, 1830. The Biological Bulletin 201, 154-166.

Thompson, J.T., Kier, W.M., 2006. Ontogeny of mantle musculature and implications for jet locomotion in oval squid Sepioteuthis lessoniana. Journal of Experimental Biology 209, 433-443.

Tian, F.-B., 2014. FSI modeling with the DSD/SST method for the fluid and finite difference method for the structure. Computational Mechanics 54, 581-589.

Tian, F.-B., Dai, H., Luo, H., Doyle, J.F., Rousseau, B., 2014. Fluid–structure interaction involving large deformations: 3D simulations and applications to biological systems. Journal of Computational Physics 258, 451-469.

Tian, F.-B., Luo, H., Song, J., Lu, X.-Y., 2013. Force production and asymmetric deformation of a flexible flapping wing in forward flight. Journal of Fluids and Structures 36, 149-161.

Tian, F.-B., Luo, H., Zhu, L., Liao, J.C., Lu, X.-Y., 2011. An efficient immersed boundary-lattice Boltzmann method for the hydrodynamic interaction of elastic filaments. Journal of Computational Physics 230, 7266-7283.

Tian, F.-B., Luo, H., Zhu, L., Lu, X.-Y., 2010. Interaction between a flexible filament and a downstream rigid body. Physical Review E 82, 026301.

Tomboulides, A., Orszag, S., Karniadakis, G., 1993. Direct and large-eddy simulations of axisymmetric wakes, 31st Aerospace Sciences Meeting. American Institute of Aeronautics and Astronautics, p. 546.

Toomey, J., Eldredge, J.D., 2008. Numerical and experimental study of the fluid dynamics of a flapping wing with low order flexibility. Physics of Fluids 20, 073603.

Triantafyllou, G.S., Triantafyllou, M., Grosenbaugh, M., 1993. Optimal thrust development in oscillating foils with application to fish propulsion. Journal of Fluids and Structures 7, 205-224.

Tsai, H.M., F. Wong, A.S., Cai, J., Zhu, Y., Liu, F., 2001. Unsteady Flow Calculations with a Parallel Multiblock Moving Mesh Algorithm. AIAA Journal 39, 1021-1029.

Tu, J., Yeoh, G.H., Liu, C., 2018. Computational fluid dynamics: a practical approach. Butterworth-Heinemann.

Tytell, E.D., 2006. Median fin function in bluegill sunfish Lepomis macrochirus: streamwise vortex structure during steady swimming. Journal of Experimental Biology 209, 1516-1534.

Tytell, E.D., Lauder, G.V., 2004. The hydrodynamics of eel swimming: I. Wake structure. Journal of Experimental Biology 207, 1825-1841.

Uekermann, B., Bungartz, H.-J., Yau, L.C., Chourdakis, G., Rusch, A., 2017. Official preCICE adapters for standard open-source solvers, Proceedings of the 7th GACM Colloquium on Computational Mechanics for Young Scientists from Academia.

van Ginneken, V., Antonissen, E., Müller, U.K., Booms, R., Eding, E., Verreth, J., van den Thillart, G., 2005. Eel migration to the Sargasso: remarkably high swimming efficiency and low energy costs. Journal of Experimental Biology 208, 1329-1335.

Vanella, M., Fitzgerald, T., Preidikman, S., Balaras, E., Balachandran, B., 2009. Influence of flexibility on the aerodynamic performance of a hovering wing. Journal of Experimental Biology 212, 95-105.

Videler, J.J., 1993. Fish swimming. Springer Science & Business Media.

Vierendeels, J., Lanoye, L., Degroote, J., Verdonck, P., 2007. Implicit coupling of partitioned fluid–structure interaction problems with reduced order models. Computers & Structures 85, 970-976.

Wainwright, D.K., Lauder, G.V., 2020. Tunas as a high-performance fish platform for inspiring the next generation of autonomous underwater vehicles. Bioinspiration & Biomimetics 15, 035007.

Wang, C., Tang, H., 2019. Influence of complex driving motion on propulsion performance of a heaving flexible foil. Bioinspiration & Biomimetics 14, 016011.

Wang, J., Wainwright, D.K., Lindengren, R.E., Lauder, G.V., Dong, H., 2020a. Tuna locomotion: a computational hydrodynamic analysis of finlet function. Journal of the Royal Society Interface 17, 20190590.

Wang, T., Lidtke, A.K., Giorgio-Serchi, F., Weymouth, G.D., 2019a. Manoeuvring of an aquatic soft robot using thrust-vectoring, 2019 2nd IEEE International Conference on Soft Robotics (RoboSoft). IEEE, Seoul, Korea (South), pp. 186-191.

Wang, W., Huang, H., Lu, X.-Y., 2019b. Self-propelled plate in wakes behind tandem cylinders. Physical Review E 100, 033114.

Wang, W., Huang, H., Lu, X.-Y., 2020b. Optimal chordwise stiffness distribution for self-propelled heaving flexible plates. Physics of Fluids 32, 111905.

Ward, D.V., 1972. Locomotory function of the squid mantle. Journal of Zoology 167, 487-499.

Ward, D.V., Wainwright, S.A., 1972. Locomotory aspects of squid mantle structure. Journal of Zoology 167, 437-449.

Webb, P., 1993. Is tilting behaviour at low swimming speeds unique to negatively buoyant fish? Observations on steelhead trout, Oncorhynchus mykiss, and bluegill, Lepomis macrochirus. Journal of Fish Biology 43, 687-694.

Webb, P.W., 1998. Entrainment by river chub Nocomis micropogon and smallmouth bass Micropterus dolomieu on cylinders. Journal of Experimental Biology 201, 2403-2412.

Weihs, D., 1974. Energetic advantages of burst swimming of fish. Journal of Theoretical Biology 48, 215-229.

Weihs, D., 1977. Periodic jet propulsion of aquatic creatures. Fortschritte der Zoologie 24, 171-175.

Wen, L., Lauder, G., 2013. Understanding undulatory locomotion in fishes using an inertia-compensated flapping foil robotic device. Bioinspiration & Biomimetics 8, 046013.

Wen, L., Ren, Z., Di Santo, V., Hu, K., Yuan, T., Wang, T., Lauder, G.V., 2018. Understanding fish linear acceleration using an undulatory biorobotic model with soft fluidic elastomer actuated morphing median fins. Soft robotics 5, 375-388.

Wen, L., Wang, T., Wu, G., Liang, J., Wang, C., 2011. Novel method for the modeling and control investigation of efficient swimming for robotic fish. IEEE Transactions on Industrial Electronics 59, 3176-3188.

Westneat, M.W., Thorsen, D.H., Walker, J.A., Hale, M.E., 2004. Structure, function, and neural control of pectoral fins in fishes. IEEE Journal of Oceanic Engineering 29, 674-683.

Weymouth, G.D., Subramaniam, V., Triantafyllou, M.S., 2015. Ultra-fast escape maneuver of an octopus-inspired robot. Bioinspiration & Biomimetics 10, 016016.

Weymouth, G.D., Triantafyllou, M.S., 2013. Ultra-fast escape of a deformable jet-propelled body. Journal of Fluid Mechanics 721, 367-385.

White, C.H., Lauder, G.V., Bart-Smith, H., 2021. Tunabot Flex: a tuna-inspired robot with body flexibility improves high-performance swimming. Bioinspiration & Biomimetics 16, 026019.

Wilson, M.M., Eldredge, J.D., 2011. Performance improvement through passive mechanics in jellyfish-inspired swimming. International Journal of Non-Linear Mechanics 46, 557-567.

Wise, T.N., Schwalbe, M.A.B., Tytell, E.D., 2018. Hydrodynamics of linear acceleration in bluegill sunfish, Lepomis macrochirus. Journal of Experimental Biology 221.

Wolfgang, M.J., Anderson, J.M., Grosenbaugh, M.A., Yue, D.K., Triantafyllou, M.S., 1999. Near-body flow dynamics in swimming fish. Journal of Experimental Biology 202, 2303-2327.

Wood, C., Gil, A.J., Hassan, O., Bonet, J., 2010. Partitioned block-Gauss–Seidel coupling for dynamic fluid–structure interaction. Computers & Structures 88, 1367-1382.

Wu, J., Shu, C., Zhao, N., 2014. Numerical study of flow control via the interaction between a circular cylinder and a flexible plate. Journal of Fluids and Structures 49, 594-613.

Xiao, Q., Hu, J., Liu, H., 2014. Effect of torsional stiffness and inertia on the dynamics of low aspect ratio flapping wings. Bioinspiration & Biomimetics 9, 016008.

Xiao, Q., Liao, W., 2010. Numerical investigation of angle of attack profile on propulsion performance of an oscillating foil. Computers & Fluids 39, 1366-1380.

Xiao, Q., Liao, W., Yang, S., Peng, Y., 2012a. How motion trajectory affects energy extraction performance of a biomimic energy generator with an oscillating foil? Renewable Energy 37, 61-75.

Xiao, Q., Liu, W., Hu, J., 2012b. Parametric study on a cylinder drag reduction using downstream undulating foil. European Journal of Mechanics-B/Fluids 36, 48-62.

Xiao, Q., Sun, K., Liu, H., Hu, J., 2011. Computational study on near wake interaction between undulation body and a D-section cylinder. Ocean Engineering 38, 673-683.

Yang, L., Su, Y.-m., 2011. CFD simulation of flow features and vorticity structures in tuna-like swimming. China Ocean Engineering 25, 73-82.

Yeh, P.D., Alexeev, A., 2014. Free swimming of an elastic plate plunging at low Reynolds number. Physics of Fluids 26, 053604.

Yeh, P.D., Alexeev, A., 2016a. Biomimetic flexible plate actuators are faster and more efficient with a passive attachment. Acta Mechanica Sinica 32, 1001-1011.

Yeh, P.D., Alexeev, A., 2016b. Effect of aspect ratio in free-swimming plunging flexible plates. Computers & Fluids 124, 220-225.

Yeh, P.D., Demirer, E., Alexeev, A., 2019. Turning strategies for plunging elastic plate propulsor. Physical Review Fluids 4, 064101.

Yen, W.-K., Sierra, D.M., Guo, J., 2018. Controlling a robotic fish to swim along a wall using hydrodynamic pressure feedback. IEEE Journal of Oceanic Engineering 43, 369-380.

Yeom, S.-W., Oh, I.-K., 2009. A biomimetic jellyfish robot based on ionic polymer metal composite actuators. Smart Materials and Structures 18, 085002.

York, C.A., Bartol, I.K., Krueger, P.S., Thompson, J.T., 2020. Squids use multiple escape jet patterns throughout ontogeny. Biology Open 9, bio054585.

Youngerman, E.D., Flammang, B.E., Lauder, G.V., 2014. Locomotion of free-swimming ghost knifefish: anal fin kinematics during four behaviors. Zoology 117, 337-348.

Yu, J., Tan, M., Wang, S., Chen, E., 2004. Development of a biomimetic robotic fish and its control algorithm. IEEE Transactions on Systems, Man, and Cybernetics, Part B (Cybernetics) 34, 1798-1810.

Yuen, H.S.H., 1961. Bow wave riding of dolphins. Science 134, 1011-1012.

Zhang, C., Huang, H., Lu, X.-Y., 2020a. Effect of trailing-edge shape on the self-propulsive performance of heaving flexible plates. Journal of Fluid Mechanics 887, A7.

Zhang, J.-D., Sung, H.J., Huang, W.-X., 2020b. Specialization of tuna: A numerical study on the function of caudal keels. Physics of Fluids 32, 111902.

Zhang, J., Liu, N.-S., Lu, X.-Y., 2010. Locomotion of a passively flapping flat plate. Journal of Fluid Mechanics 659, 43-68.

Zhang, X., Wang, J., Wan, D., 2020c. CFD investigations of evolution and propulsion of low speed vortex ring. Ocean Engineering 195, 106687.

Zhang, Y., Zhou, C., Luo, H., 2017. Effect of mass ratio on thrust production of an elastic panel pitching or heaving near resonance. Journal of Fluids and Structures 74, 385-400.

Zhao, W., Yu, J., Fang, Y., Wang, L., 2006. Development of multi-mode biomimetic robotic fish based on central pattern generator, 2006 IEEE/RSJ International Conference on Intelligent Robots and Systems. IEEE, Beijing, China, pp. 3891-3896.

Zhao, Z., Li, G., Xiao, Q., Jiang, H.-R., Tchivelekete, G.M., Shu, X., Liu, H., 2020. Quantification of the influence of drugs on zebrafish larvae swimming kinematics and energetics. PeerJ 8, e8374.

Zhu, J., White, C., Wainwright, D.K., Di Santo, V., Lauder, G.V., Bart-Smith, H., 2019. Tuna robotics: A high-frequency experimental platform exploring the performance space of swimming fishes. Science Robotics 4, 4615.

Zhu, Q., 2007. Numerical Simulation of a Flapping Foil with Chordwise or Spanwise Flexibility. AIAA Journal 45, 2448-2457.

Zhu, Q., Bi, X., 2017. Effects of stiffness distribution and spanwise deformation on the dynamics of a ray-supported caudal fin. Bioinspiration & Biomimetics 12, 026011.

Zhu, Q., Shoele, K., 2008. Propulsion performance of a skeleton-strengthened fin. Journal of Experimental Biology 211, 2087-2100.

Zhu, Q., Wolfgang, M., Yue, D., Triantafyllou, M., 2002. Three-dimensional flow structures and vorticity control in fish-like swimming. Journal of Fluid Mechanics 468, 1-28.

Zhu, X., He, G., Zhang, X., 2014a. How flexibility affects the wake symmetry properties of a self-propelled plunging foil. Journal of Fluid Mechanics 751, 164.

Zhu, X., He, G., Zhang, X., 2014b. Numerical study on hydrodynamic effect of flexibility in a self-propelled plunging foil. Computers & Fluids 97, 1-20.

Zhu, Y., 2020. A Numerical Study of Fish Adaption Behaviors by Deep Reinforcement Learning and Immersed Boundary-Lattice Boltzmann Method. The University of New South Wales.

Zhu, Y., Tian, F.-B., Young, J., Liao, J.C., Lai, J.C.S., 2021. A numerical study of fish adaption behaviors in complex environments with a deep reinforcement learning and immersed boundary–lattice Boltzmann method. Scientific Reports 11, 1-20.

Ziegler, J.G., Nichols, N.B., 1942. Optimum settings for automatic controllers. Transactions of the ASME 64.